Abstract

Angle resolved photoemission study of Fermi surfaces and single-particle excitations of quasi-low dimensional materials

by

Gey-Hong Gweon

Chair: James W. Allen

Using angle resolved photoemission spectroscopy (ARPES) as the main experimental tool and the single particle Green's function as the main theoretical tool, materials of various degrees of low dimensionality and different ground states are studied. The underlying theme of this thesis is that of one dimensional physics, which includes charge density waves (CDW's) and the Luttinger liquid (LL). The LL is the prime example of a lattice non-Fermi liquid (non-FL) and CDW fluctuations also give non-FL behaviors. The current importance of one dimensional physics is that non-FL physics is an emerging paradigm of condensed matter physics. Furthermore, it is thought by some researchers that one dimensional LL behavior is a key element in solving the high temperature superconductivity problem.

$TiTe_2$ is a quasi-2 dimensional (quasi-2D) Fermi liquid (FL) material very well suited for ARPES lineshape studies. Its ARPES lineshapes for the Ti *3d* band are an important reference to compare with non-FL ARPES lineshapes and also provide a valuable opportunity to examine the many body theoretical interpretation of ARPES spectra. I report ARPES spectra at 300 K which show an unusual behavior of a peak moving *through* the Fermi energy (E_F). An accurate value of the Fermi momentum, $\mathbf{k}_F$, can be obtained by analyzing the dispersion. I also report a good fit of the ARPES spectra at 25 K obtained by using a causal Green's function proposed by K. Matho. However, the $\mathbf{k}_F$ values found from the lineshape fits and from the 300 K dispersion are different by about 8 %, large enough to be significant for some issues. I discuss possible origins of this discrepancy. $SmTe_3$ is a quasi-2D CDW material. Resonant photoemission shows that Sm is trivalent. ARPES spectra show that its valence band electronic structure is 4 fold symmetric except for the states near E_F. The near E_F ARPES spectra and intensity map reveal rich details of an anisotropic gap and imperfectly nested Fermi surface

(FS) for a high temperature CDW. A simple model of imperfect nesting can be constructed from these data and predicts a CDW wavevector in very good agreement with the value known from electron diffraction. $NaMo_6O_{17}$ and KMo_6O_{17} are also quasi-2D CDW materials. The "hidden nesting" or "hidden 1 dimensionality" picture for the CDW, suggested for these materials by M. Whangbo, is confirmed very well by our direct image of the FS. I also point out anomalous ARPES lineshapes.

$K_{0.3}MoO_3$, the so-called "blue bronze," is a quasi-1 dimensional (quasi-1D) CDW material. Even in its metallic phase above the CDW transition temperature, its photoemission spectra show an anomalously weak intensity at E_F and no clear metallic Fermi edge, which are expected non-FL aspects of both the LL and the CDW fluctuations. I compare predictions of an LL model and a CDW fluctuation model regarding these aspects, and find that the LL scenario explains them better. But I also point out other difficulties that arise in the LL comparison. Despite the weak E_F intensity, the E_F intensity map shows a FS pattern in good agreement with the expected FS and the known CDW wavevector. $Li_{0.9}Mo_6O_{17}$ is a quasi-1D material, whose 24 K transition is incompatible with a CDW transition. Its near E_F ARPES spectra and intensity map show a nearly perfect 1D electronic structure. Its 200 K ARPES spectra are a unique example so far for studying non-FL ARPES lineshapes without concern about thermal CDW fluctuation effects. I compare the 200 K ARPES lineshapes with the LL lineshapes calculated using the spin-independent Tomonaga-Luttinger model. I point out both strong similarities and some significant differences.

Angle resolved photoemission study of Fermi surfaces and single-particle excitations of quasi-low dimensional materials

by

Gey-Hong Gweon

A dissertation submitted in partial fulfillment
of the requirements for the degree of
Doctor of Philosophy
(Physics)
in The University of Michigan
1999

Doctoral committee:

Professor James W. Allen, Chair
Associate Professor Meigan C. Aronson
Professor Joseph G. Conlon
Professor Martin B. Einhorn
Assistant Professor Alberto G. Rojo

To my parents,
my parents in law
and my wife.

Acknowledgments

I am much indebted to the excellent group of people that I have luckily come into contact with and benefited from in the course of this thesis work.

First of all, my deep thanks go to Prof. James Allen, my advisor, who set the topics, taught me, supported me and encouraged me throughout the program. His enthusiasm and understanding about physics was most inspiring. I also thank Prof.'s Meigan Aronson, Joseph Conlon, Martin Einhorn and Alberto Rojo, for dedicating time to serve on my committee. Special thanks go to Prof. Meigan Aronson, with whom I was lucky to collaborate on $SmTe_3$. Prof.'s Stephen Lee and Leonard Sanders initially served on the committee, but conflicting schedules did not allow them to serve on the committee at the time of my oral exam. I thank them for their kind guidance. Especially, I thank Prof. Stephen Lee for his generous support in the collaboration on $SmTe_3$.

Dr. Cliff Olson generously shared his expertise on photoemission and his equipment at the SRC/Ames-Montana beamline to make the large part of this thesis work possible. I thank him for his valuable contribution. Prof. Z.-X. Shen shared his apparatus at the SSRL beamline 5. I thank his hospitality. I thank Prof. Se-Jung Oh for starting up my research in this field by accepting me into his group. I thank Prof. Ralph Claessen for collaboration and stimulating interaction. I learned a great deal from his balanced understanding of experiment and theory. It is a great pleasure to acknowledge Dr. Jonathan Denlinger for the pleasant synchrotron runs that I had with him and interactions on various subjects. Dr. Walt Ellis has been a great companion during the synchrotron runs that I had been lucky to enjoy with him. I thank him for the role model he is and wish him continuing health. I thank Dr. Konrad Matho for sharing his unique thoughts and knowledge about the many body aspect of photoemission theory. I thank Prof. Claire Schlenker and Dr. Marcus for beautiful purple bronze samples and warm collaborative supports. I thank Dr. Lynn Schneemeyer who contributed blue bronze samples and collaborated with us so pleasantly. I thank Dr.'s Elaine DiMasi and Brendan Foran for doing pioneering work on $SmTe_3$ and giving me samples.

Dr. Jae-Hoon Park has supported and encouraged me warmly. I thank him for his care. I was very lucky to know Dr. Hao Tjeng whose dedication and energy engraved a deep impression on me. Many people have made the synchrotron runs enjoyable by sharing their expertise and also by simply being friendly. I thank Dr.'s Derrick Poirier, Paul Benning, Harmut Höchst, Dan Dessau, Chang-Young Kim, Chul-Hong Park, Dave

King, Dan Marshall, and Ann Matsuura. I enjoyed working with Dr. Friedel Reinert at the SSRL runs. I would not forget the warm hospitality that he and the group of Prof. Hüfner at Saarbrücken showed to me. I thank Jhules Clack for sharing his efforts with me on many experiments. Many compatriots have made my life in Ann Arbor more comfortable. They also helped me in time of need. I thank my cousin Donghoon Chen and his family, Sang Kyoung Kahng and his family, Hunsuk Kim and his family, Yun-Shik Lee and his family, Sang-Ho Lee and his family, Joon-Koo Kim, Jawhan Kim, Kyoungsik Kim, Jaewook Ahn, Han-bum Cho and Hyun-soo Ahn.

The support and love of my family have been the constant fuel of my life as a graduate student. I thank my parents and my parents in law. Especially, I thank my wife, Hee-sun Lee, for all the wonderful things that she gives. I also wish her the best with her own Ph. D. program.

Contents

Chapter

List of Figures

Chapter 1

Introduction: Experiment

Current quantum mechanical understanding of solids largely rests on the so called Fermi liquid (FL) theory, which explains why the large Coulomb interactions in the solid do not prevent the use of a much simpler picture of independent electrons. However, for quasi-low dimensional materials we may be observing an entirely new paradigm of non-Fermi liquid (non-FL) physics. Two prime examples of non-FL state in quasi-low dimensional systems are the Luttinger liquid (LL) and the charge density wave (CDW) fluctuations, both of which are strongly one-dimensional phenomena. The interest in the LL physics is currently very high because it is thought by some researchers that the one dimensional LL behavior is a key element in solving the high temperature superconductivity problem. Angle-resolved photoemission spectroscopy (ARPES) is a direct probe of the Green's function of the many body theory and has a potential to reveal the differences of these various ground states in details and without ambiguity. In this thesis, I study various quasi-low dimensional materials with ARPES to gain information about the FL, CDW and LL physics.

It may be helpful to explain what I mean by the title of this thesis. First, ARPES is the major experimental tool used in this thesis, and will be explained in this chapter. At the simplest level it could be envisioned as a tool for mapping the occupied part of an electron band, by pulling out an electron from the sample in a controlled manner. Second, the idea of the Fermi surface (FS) is easy in the Fermi gas model [1, 2] of electrons. It is a boundary region in momentum space which sharply distinguishes filled states and empty states. In correlated electron systems, however, this definition needs to be generalized, to be valid for a Fermi *liquid* [3] and even for a non-FL. Within the scope of this thesis, a general definition of the FS could be taken as the set of singular points of the function $n(\mathbf{k})$, the electron occupancy for momentum $\mathbf{k}$. Third, by "single-particle excitation" one means the excitation of a system by means of an electron addition or removal. In photoemission an electron is removed from the system to create a hole excitation. Therefore, a more semantically correct title probably would be "single-hole" rather than "single-particle." However, perhaps the use of a more general term is justified because we want to study general properties of single-particle excitations which happen to be more readily accessible in photoemission for technical reasons. Lastly, quasi-low dimensional materials are a class of materials with 3 dimensional crystal structures but with strong anisotropy in their electronic structure near the Fermi energy (E_F).

This is the first of two chapters in which background information essential for understanding the rest of this thesis is summarized. After two introductory chapters, specific materials are studied in chapters 3 through 7. These chapters are ordered in the decreasing order of the dimensionality as probed by photoemission. Each of them is concluded with a statement of my specific role in the work presented therein.

This chapter is organized as follows. In section 1.1, an idealized view of ARPES is presented. In section 1.2, a few realistic complications affecting the interpretation of ARPES measurements are discussed. In section 1.3, experimental setups are discussed. I will end this chapter with section 1.4 by showing key previous results which prompted this thesis work.

1.1 Principle of ARPES

Photoemission spectroscopy (PES), also sometimes called photoelectron spectroscopy, is an experiment in which photons are shot at a sample and out-coming electrons are analyzed. General reviews on the (AR)PES principles can be found in numerous references [4, 5, 6]. There are in principle many experimental variables. They include the photon energy $h\nu$, the photon incidence angle θ_p, the photon polarization $\hat{\epsilon}_p$, the sample temperature T, the photoelectron angles θ and ϕ, the photoelectron kinetic energy E_K, and the photoelectron spin quantum number σ_z. Therefore, the most general form of the photoemission intensity is written as

$$I(h\nu, \hat{\epsilon}_p, \theta_p; T; \theta, \phi, E_K, \sigma_z). \tag{1.1}$$

It is impractical to exploit all these degrees of freedom at the same time. Rather, only a few important ones are varied or resolved to suit the purpose at the time, with other variables fixed or integrated over. For example, ARPES experiments refer to photoe-

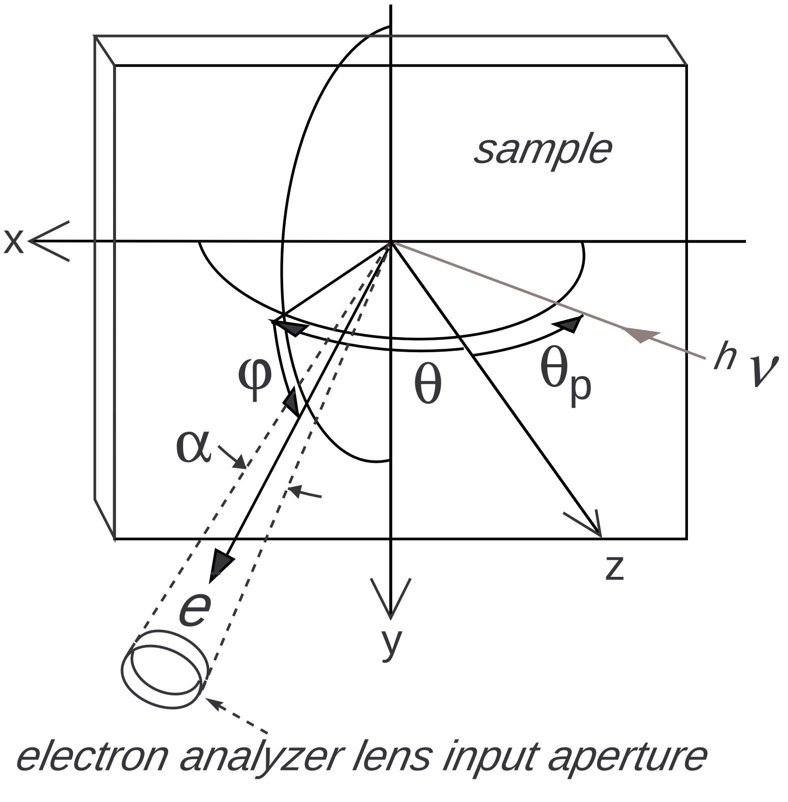

Figure 1.1: A schematic geometry of the photoemission experiment. z = sample normal. xy = sample cleavage surface. θ_p = photon incidence angle. (θ, ϕ) = electron energy analyzer direction. α = electron energy analyzer angular resolution.

mission experiments where the angle dependencies (θ,ϕ) are studied. If the $h\nu$ dependence across an absorption edge is exploited in order to enhance certain atomic orbital signals, then one is doing resonant photoemission spectroscopy (RESPES). If the spin states of the photoelectrons are resolved then one is doing spin resolved photoemission, most likely to study magnetic samples. In this thesis, spin is always integrated. All other variables in Eq. 1.1 do at least occasionally become important control variables.

Fig. 1.1 shows a schematic diagram that represents the angle resolved photoemission setups used in this thesis. In this setup, the sample is mounted with its flat surface vertical. In the figure, the x and z axes, the latter of which is the sample surface normal, define the horizontal plane in which the incoming photons propagate. Photons are radiated by relativistic electrons orbiting in a synchrotron storage ring, not shown here but contained in the xz plane. Light generated by synchrotron radiation is strongly, $\approx 85\%$, linearly polarized within this plane. The absorbed photon energy excites electrons – photoelectrons (e^-) – out of the sample. The electron analyzer catches those electrons coming out at angles θ and ϕ. These angles are related to the standard polar and azimuth angles of the spherical coordinates, θ_s and ϕ_s, by $\theta = \phi_s$ and $\phi = \pi/2 - \theta_s$, with the y axis as the polar axis of the spherical coordinate. The rather unconventional positive directions of the axes and the angles in the figure represents the major accessible directions in the experiment. Due to the space restrictions imposed by the direction of the incoming photon and the volume of the analyzer, the full range of angle variation covering the entire hemisphere is not available. Instead, the accessible ranges of the angles are: $\theta \approx -10^o$ to 90^o and $\phi \approx -10^o$ to 50^o. These ranges are usually more than sufficient to cover the whole Brillouin zone. The energy analyzer accepts those photoelectrons coming in a cone angle of α. In the setups used in this thesis, this angle is 2^o. As we will see below, the momentum value of the photoelectron depends on both the angle and the kinetic energy of the photoelectron. For the valence band structures probed by a photon energy $\sim$ 20 eV, the angle resolution translates to the momentum resolution of roughly 1/20 of the Brillouin zone dimension for typical unit cell dimensions.

With the photon variables $(h\nu,\theta_p,\hat{\epsilon}_p)$ and the sample temperature (T) made implicit, and with the spin quantum number (σ_z) summed over, the photoemission intensity is written in a simpler form

$$I(\theta,\phi,E_K). \tag{1.2}$$

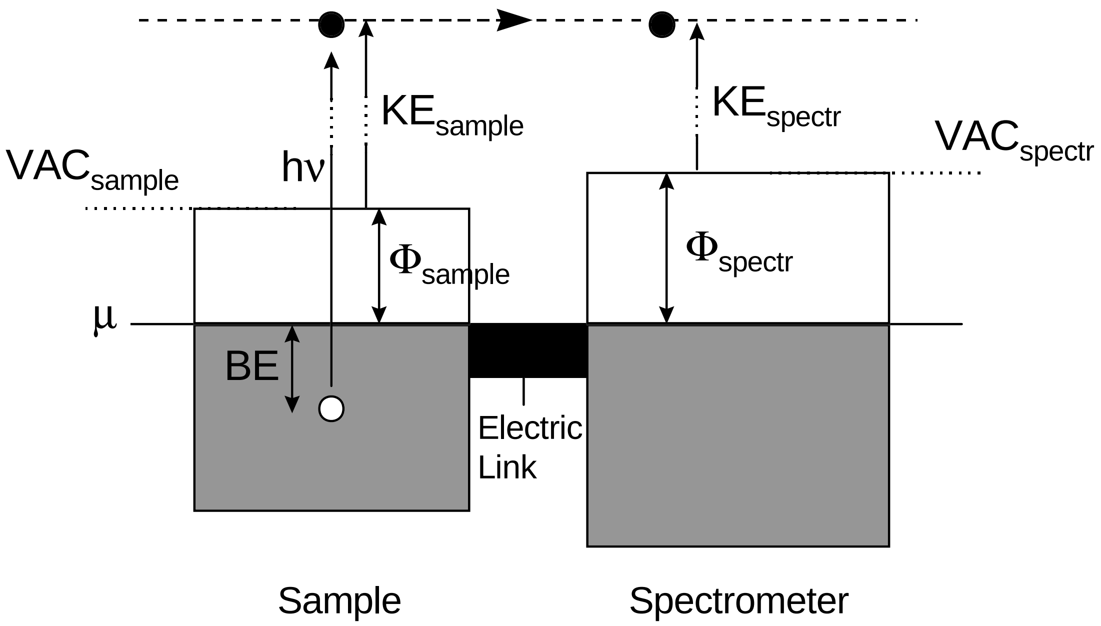

Figure 1.2: Energetics of photoemission experiment. An electron is excited from the sample by the photon hν. The vacuum levels (VAC) are the potential energy levels just outside the sample or the spectrometer. When the electron is ejected into the vacuum level of the sample, it acquires a kinetic energy = hν - binding energy (BE) - work function (Φ). See text for more discussion.

Kinetic energy and angles need to be transformed to binding energy and momentum to be useful for comparison with theory.

Fig. 1.2 shows the energetics of the usual photoemission experiment. The electrical contact made between the sample and the spectrometer means that their chemical potentials are equalized. With generally different work functions of the sample and the spectrometer, this means that the vacuum energies just outside the sample and the spectrometer are different. The photoelectron kinetic energy is measured relative to the spectrometer vacuum. This fact has the following two consequences. (1) To know the binding energy (BE in the figure), one needs to know the work function of the spectrometer[1], not of the sample. (2) The angle-momentum relation that we are going to discuss shortly is modified not only due to different kinetic energies but also due to a possible non-straight path of electrons from the sample to the spectrometer aperture. This effect has not been well analyzed by ARPES workers, but it is regarded to be small in general because typical work function differences ($<$ 1 eV) are small compared to kinetic energies ($>$ 10 eV).

The binding energy determination is most easily and accurately accomplished by measuring under the same conditions as for the sample a reference sample such as Pt

---

[1] A typical value of this work function for the setups used in this thesis is about 4.5 eV.

or Au, which shows a clear metallic Fermi edge at the chemical potential. It can also be shown that another way of looking at the binding energy is that it is the excitation energy of an $N-1$ state, relative to the $N-1$ ground state, where N is the initial number of electrons.

Now, I consider angle-momentum relations. The photoelectron momentum *outside* the sample can be worked out easily using the spherical coordinate transformation rule:

$$\begin{aligned} k_{x,out} &= 0.512\sqrt{E_K}\,\cos\phi\,\sin\theta, \\ k_{y,out} &= 0.512\sqrt{E_K}\,\sin\phi, \\ k_{z,out} &= 0.512\sqrt{E_K}\,\cos\phi\,\cos\theta. \end{aligned} \tag{1.3}$$

Here, the unit of momentum is Å^{-1}, and the unit of kinetic energy is eV. 0.512 is the numerical value of $\sqrt{2m_e}/\hbar$ in these units.

Because of diffraction at the surface, the photoelectron momentum outside sample is not the same as that inside. As a first approximation, let us assume that the photoelectron state in the sample is free-electron-like. Then one can envision free electron bands inside and outside of the sample. The free electron band inside the sample is lower in energy than that outside the sample. The energy difference is called the "inner potential" V_o. Details of the surface diffraction process should also depend on the surface morphology. At the simplest level, one might assume a perfectly flat surface, and model the surface potential as a perfectly sharp potential boundary. In this case, V_o modifies only the k_z value, and one obtains

$$\begin{aligned} k_{x,in} &= k_{x,out}, \\ k_{y,in} &= k_{y,out}, \\ k_{z,in} &= \sqrt{k_{z,out}^2 + 0.512^2 V_o}. \end{aligned} \tag{1.4}$$

Having made connections of the angles and the kinetic energy to the momentum and the binding energy of the hole (photohole) excitation, we can now ask "what do (AR)PES data mean?" A simplified but useful picture of ARPES is presented in Fig. 1.3. Electrons occupying the valence band (thick line) are excited to final states (shade), and escape from the sample to be detected. Due to the high energy of the photoelectrons, the density of states is large in the final states, i.e. there are many overlapping bands, which are represented as the shaded area. For a given angle, an energy distribution

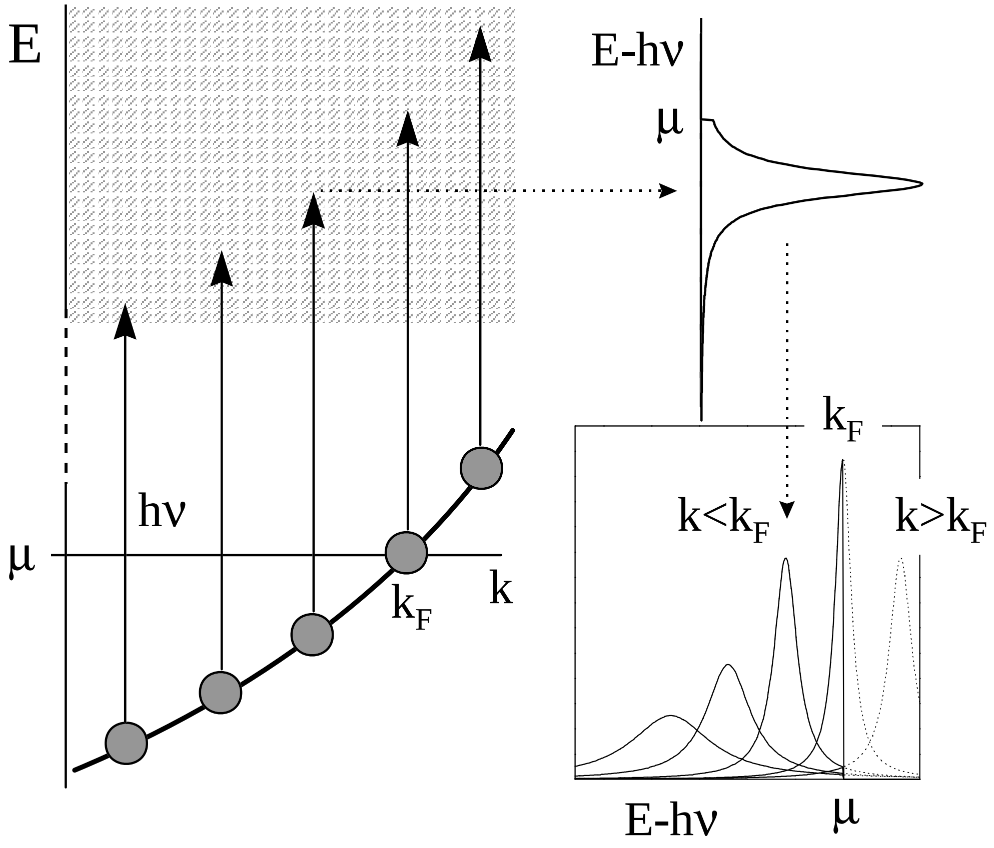

Figure 1.3: A simplified view of ARPES. The one particle spectral function is shown as a dotted line, and the ARPES spectrum is shown as a solid line. See the text for discussion.

curve (EDC) is obtained by scanning the detection energy of the photoelectrons. Within the independent electron theory, each band state would give rise to an EDC consisting of a single infinitely sharp peak. However, if electrons interact with each other and/or the lattice, complicated lineshapes can result. Here, a simple Lorentzian lineshape is shown. It should be emphasized that this lineshape serves only as an illustration and is not likely to be applicable to real problems. It merely serves the purpose of depicting general properties of line broadening and finite ARPES weight even for $k > k_F$.

Next I refine this picture and briefly discuss the widely used "sudden approximation" [7] of the photoemission theory and show how the single particle Green's function[2] (cf. Section 2.1) is related to the photoemission measurement. For simplicity, I set $c = \hbar = 1$ in this derivation.

The coupling between electrons and photons is given by

$$H_{int} = \frac{e}{2m_e}(\mathbf{p}\cdot\mathbf{A} + \mathbf{A}\cdot\mathbf{p}),$$

where $\mathbf{A}$ is the vector potential of the photon field and $\mathbf{p}$ is the momentum of an electron. For transverse fields, $\mathbf{A}$ and $\mathbf{p}(= -i\bigtriangledown)$ commute with each other[3]. Quantizing the photon field, one obtains

$$\begin{aligned} H_{int} &= \sum_{\mathbf{k}_p,\lambda} \frac{e}{m_e}\frac{1}{\sqrt{V\omega_p}} e^{i(\mathbf{k}_p\cdot\mathbf{x}-\omega_p t)}\, \hat{\epsilon}_\lambda \cdot \mathbf{p}\alpha_{\lambda,\mathbf{k}_p} + h.c. \\ &= \sum_{\mathbf{k}_p,\lambda} e^{-i\omega_p t}\,\alpha_{\lambda,\mathbf{k}_p} M + h.c., \text{ where} \\ M &= \frac{e}{m_e}\frac{1}{\sqrt{V\omega_p}} e^{i\mathbf{k}_p\cdot\boldsymbol{x}}\hat{\epsilon}_\lambda \cdot \mathbf{p}, \end{aligned}$$

and $\alpha_{\lambda,\mathbf{k}_p}$ is the annihilation operator for a photon with polarization vector $\hat{\epsilon}_\lambda$, momentum $\mathbf{k}_p$ and a corresponding frequency ω_p. For many electrons, the M operator becomes

$$M = \frac{e}{m_e}\frac{1}{\sqrt{V\omega_p}}\sum_i e^{i\mathbf{k}_p\cdot\mathbf{x}_i}\hat{\epsilon}_\lambda \cdot \mathbf{p}_i.$$

---

[2] From now on we will call this simply as Green's function, without the "single particle."

[3] Here we are considering the bulk value of the vector potential. At the surface, there can exist a strong discontinuity of $\mathbf{A}$, the derivative of which gives a surface term in the Hamiltonian. Such a term gives rise to an interference effect which can lead to an anomalous photoemission lineshape, as reported for a surface state in Ag [8].

The interaction term gives rise to transitions, the rate of which is given by the Fermi golden rule as

$$I(\mathbf{k},E) \;=\; 2\pi \sum_f |\, \langle f|H_{int}|i\rangle \,|^2 \; \delta(E_f - E_i),$$

where $|i\rangle$ is an initial state of the sample plus photon and $|f\rangle$ is a final state with photoelectron momentum $\mathbf{k}$ and energy E, . Plugging in H_{int} from above one obtains

$$I(\mathbf{k},E) \;=\; 2\pi \sum_f |\, \langle f|M|I\rangle \,|^2 \; \delta(E_f - E_I - \omega_p),$$

where $|I\rangle$ is now an initial state of the sample alone. At this step, we assume the sudden approximation that the photoelectron and the rest of the final state do not interact with each other because of the large kinetic energy of the photoelectron. Technically, this amounts to assuming

$$\begin{aligned} |f\rangle &= |N-1,m\rangle\, |\mathbf{k},E\rangle, \\ E_f &= E(N-1,m) + E, \end{aligned}$$

with N is number of electrons in the initial state and $|N-1,m\rangle$ is an eigenstate of the $N-1$ body Hamiltonian of the sample. The M operator can be written in second quantization as

$$\begin{aligned} M &= \sum_{\mathbf{k},r,\mathbf{l},s} M_{\mathbf{k},r,\mathbf{l},s}\, a^\dagger_{\mathbf{k},r} a_{\mathbf{l},s}, \\ M_{\mathbf{k},r,\mathbf{l},s} &= \frac{e}{m_e}\frac{1}{\sqrt{V\omega_p}} \langle \mathbf{k},r|e^{i\mathbf{k}_p\cdot\mathbf{x}}\,\hat{\epsilon}_\lambda\cdot\mathbf{p}|\mathbf{l},s\rangle, \end{aligned} \tag{1.5}$$

where $\mathbf{k}$ and $\mathbf{l}$ are crystal momenta and r and s are the band indices. By the sudden approximation, only the term with $(\mathbf{k}, r)$ corresponding to the photoelectron state survives, and we get

$$I(\mathbf{k},E) \;=\; 2\pi \sum_m |\, \langle N-1,m| \sum_{\mathbf{l},s} M_{\mathbf{k},r,\mathbf{l},s}\, a_{\mathbf{l},s}\, |i\rangle \,|^2 \; \delta(E + E(N-1,m) - E_i - \omega_p),$$

where now the index r is not dummy but constrained by $\epsilon_r(\mathbf{k}) = E$. In the momentum sum, the momentum conservation requires that $\mathbf{l} = \mathbf{k} - \mathbf{k}_p$. However, typically the photon momentum is an order of magnitude smaller than the electron momentum and in this case $\mathbf{l} \approx \mathbf{k}$, which we will assume from now on. By defining a new one electron operator,

$$\tau(\mathbf{k},E) = \sqrt{2\pi}\sum_s M_{\mathbf{k},r,\mathbf{k},s}a_{\mathbf{k},s}, \tag{1.6}$$

the equation above can be simplified as

$$I(\mathbf{k},E) = \sum_m |\langle N-1,m|\tau(\mathbf{k},E)|i\rangle|^2\ \delta(E+E(N-1,m)-E_i-\omega_p),$$

This can be further manipulated as

$$\begin{aligned} I(\mathbf{k},E) &= \langle i|\tau^\dagger(\mathbf{k},E)\sum_m |N-1,m\rangle\langle N-1,m|\tau(\mathbf{k},E)|i\rangle \times \\ &\quad \delta(E+E(N-1,m)-E_i-\omega_p) \\ &= \langle i|\tau^\dagger(\mathbf{k},E)\sum_m \delta(E+H-E_i-\omega_p)\,|N-1,m\rangle\langle N-1,m|\tau(\mathbf{k},E)|i\rangle \\ &= \langle i|\tau^\dagger(\mathbf{k},E)\,\delta(E+H-E_i-\omega_p)\,\tau(\mathbf{k},E)|i\rangle, \end{aligned}$$

where in the last step, the delta function is taken out of the m sum and the completeness relation $|N-1,m\rangle\langle N-1,m| = 1$ in $N-1$ particle space is used. It is customary to use the notation ω for $E-\omega_p$:

$$I(\mathbf{k},\omega) = \langle i|\tau^\dagger(\mathbf{k},\omega)\,\delta(\omega+H-E_i)\,\tau(\mathbf{k},\omega)\,|i\rangle.$$

So far, no definite statement has been made about the state $|i\rangle$, except that it is an eigenstate of the N electron Hamiltonian. At $T=0$, it should be understood as the ground state of the N particle system. At finite temperatures, we should consider an ensemble of eigenstates and therefore should replace the expectation value for the state $|i\rangle$ with an ensemble average:

$$I(\mathbf{k},\omega) = \langle\tau^\dagger(\mathbf{k},\omega)\,\delta(\omega+H-E_i)\,\tau(\mathbf{k},\omega)\rangle. \tag{1.7}$$

In chapter 2, I will discuss the Green's function, $G(\mathbf{k},\omega)$, the probability amplitude function for the propagation of an electron or a hole. Its imaginary part, called the spectral function, gives the probability for adding or removing an electron. Eq. 1.7 has the the same form as the spectral function for removing an electron, Eq. 2.5, except that the τ operator is in place of a one electron band operator $a_{\mathbf{k}}$. There are two differences to be noted. First, the τ operator here is ω-dependent. This is not a serious problem, however, because typically a photoemission spectrum with energy width (much) less than 1 eV is considered for lineshape analysis and the one electron transition matrix elements $M_{\mathbf{k},r,\mathbf{k},s}$ in Eq. 1.6 is not expected to be strongly energy dependent over such a small energy range. A more serious difficulty which is not easily overcome is that the τ operator is a linear combination of $a_{\mathbf{k},s}$ operators for different bands and therefore Eq. 1.7 involves non-diagonal (i.e. inter-band) as well as diagonal (i.e. intra-band) Green's functions. Furthermore, the relative weights of different matrix elements $M_{\mathbf{k},r,\mathbf{k},s}$ need to be known in order to calculate the photoemission current up to a constant numerical factor.

A favorable condition occurs if only a single initial band is relevant in the photoemission, i.e. if a single band appears in ARPES well separated from other bands. In such cases, $\tau_{\mathbf{k}} = \sqrt{2\pi} M_{\mathbf{k}} a_{\mathbf{k}}$ and Eq. 1.7 is directly proportional to the spectral function for removing an electron, Eq. 2.5. As a result, the photoemission intensity becomes

$$I(\mathbf{k},\omega) \;=\; |M_{\mathbf{k}}|^2 f(\omega-\mu)\,\mathrm{Im}G(\mathbf{k},\omega), \tag{1.8}$$

where the numerical factor of 2π is included in $|M_{\mathbf{k}}|^2$. The interpretation of this expression is simple. The imaginary part of the Green's function, i.e. the spectral function, gives the probability to remove or add an electron at $(\mathbf{k},\omega)$. Multiplication by the Fermi-Dirac function gives only the electron removal probability. The $|M_{\mathbf{k}}|^2$ factor gives the probability for a photon to excite the removed electron to a high energy photoelectron state. The clear separation of electron removal and excitation to a higher energy state is due to the sudden approximation.

A major goal of a photoemission experiment is to measure physics information contained in the Green's function term. On the other hand, the matrix element term, $|M_{\mathbf{k}}|^2$ is a determining factor for the strength of the photoemission signal. It is this term that has, for example, photon energy dependent crossection variations [9], photoemission selection rules [10, 11] determined by the photon polarization vector and band orbital symmetries, or intensity modulations across Brillouin zones ("Brillouin zone selection") [12, 13] due to interfering photoelectron waves originating from different atoms in the unit cell. In general, $|M_{\mathbf{k}}|^2$ is a difficult quantity to calculate theoretically because it is necessary to know the wave function for the final state as well as that for the initial state.

1.2 More principles of ARPES

In this section, I discuss departures from the idealized picture, which need to be taken into account for understanding ARPES data.

First, finite experimental angular and energy resolutions need to be taken into account. These resolutions can be defined by resolution functions W_k and W_ω for momentum and energy respectively. The theoretical ARPES intensity is obtained, for a single band, by integrating Eq. 1.8:

$$I(\mathbf{k},\omega) \;=\; \int d\omega'\, W_\omega(\omega-\omega')\, f(\omega'-\mu) \sum_{\mathbf{k}'} |M_{\mathbf{k}'}|^2 W_k(\mathbf{k}')\, \mathrm{Im}G(\mathbf{k}',\omega'),$$

The function W_ω is determined by convolution of the monochromator line profile and the analyzer response function. In practice, it is deduced from a Fermi edge reference spectrum, e.g. from Pt or Au, and is found to be close to Gaussian. The function W_k is determined by angular resolution through Eq.'s 1.3 and 1.4. It is helpful to note that it is very often the case that the Green's function depends on $\mathbf{k}$ only through $\epsilon(\mathbf{k})$, the one electron band energy. Then the above equation can be rewritten as

$$I(\mathbf{k},\omega) \;=\; \int d\omega'\, W_\omega(\omega-\omega')\, f(\omega'-\mu) \int d\epsilon(\mathbf{k}')\, |M_{\mathbf{k}'}|^2 W_\epsilon(\epsilon(\mathbf{k}'))\, \mathrm{Im}G(\epsilon(\mathbf{k}'),\omega')) \tag{1.9}$$

In general, $W_\epsilon(\epsilon(\mathbf{k}'))$ is expected to be a complicated function. However, for a low dimensional electronic structure (i.e. $\partial\epsilon(\mathbf{k})/\partial k_z = 0$) and under some simplifying assumptions it can be calculated as follows. First, we assume that the ARPES is performed along the x or y axis of Fig. 1.1. For definiteness, we pick the x axis, but an essentially same result is obtained for the y axis. Second, we assume that the photon spot on the sample is perfectly sharp. Then, the momentum distribution of the photoelectron at a fixed kinetic energy is determined by the uniform distribution of angles in the angular cone of Fig. 1.1. Because the width of the cone, α, is very small, the angle-to-momentum relation of Eq. 1.3 is linear to a good accuracy within the angular cone. Therefore, the angular cone translates directly to a momentum space cone. For a fixed kinetic energy E_K and a fixed value of $\mathbf{k}$, the momentum space area to sum over is then the section of the sphere of radius $\sqrt{2m_eE_K}/\hbar$ cut by the momentum space cone. Due to the smallness of the momentum resolution compared with typical values of the radius $\sqrt{2m_eE_K}/\hbar$, this section is a flat circular disk to a good approximation. Projecting this disk to the k_xk_y plane, one obtains an ellipse which gives the integral domain for

k_x and k_y. For $\mathbf{k}$ along the x axis, the momentum sum (integral) is therefore written as

$$\sum_{\mathbf{k}'} |M_{\mathbf{k}'}|^2 W_k(\mathbf{k}') \,\mathrm{Im}G(\epsilon(\mathbf{k}'), \omega')$$

$$= \frac{2}{(\frac{2\pi}{L})^2} \frac{1}{\cos\theta} \int_{k_1}^{k_2} dk'_x \int_{-\delta k\sqrt{1-\frac{4(k'_x-k_x)^2}{(k_2-k_1)^2}}}^{\delta k\sqrt{1-\frac{4(k'_x-k_x)^2}{(k_2-k_1)^2}}} dk'_y |M_{\mathbf{k}'}|^2 \,\mathrm{Im}G(\epsilon(\mathbf{k}'), \omega'),$$

where $\delta k = \sqrt{2m_e E_K/\hbar^2}\sin\frac{\alpha}{2}$, $k_x = \sqrt{2m_e E_K/\hbar^2}\sin\theta, k_1 = \sqrt{2m_e E_K/\hbar^2}\sin(\theta - \alpha/2)$ and $k_2 = \sqrt{2m_e E_K/\hbar^2}\sin(\theta + \alpha/2)$. For the narrow range of momentum within the disk, the dispersion relation $\epsilon(\mathbf{k}')$ can be linearized as

$$\epsilon(\mathbf{k}') \approx \epsilon(\mathbf{k}) + v_x(\mathbf{k})(k'_x - k_x) + v_y(\mathbf{k})(k'_y - k_y),$$

where $v_x(\mathbf{k}) = \partial\epsilon(\mathbf{k})/\partial k_x$ and $v_y(\mathbf{k}) = \partial\epsilon(\mathbf{k})/\partial k_y$. Further simplification occurs if we assume that $v_y(\mathbf{k}) = 0$, a condition satisfied often by materials with high enough symmetry and the usual alignment of the crystal to make the x axis parallel to a high symmetry direction of the crystal, and that $|M_{\mathbf{k}'}|^2$ is independent of k_y within the momentum resolution disk. Then the integral over k'_y becomes trivial because the integrand does not depend on k'_y. Also, the momentum variables can be easily converted to the $\epsilon(\mathbf{k}')$ variable. We have

$$\sum_{\mathbf{k}'} |M_{\mathbf{k}'}|^2 W_k(\mathbf{k}') \,\mathrm{Im}G(\epsilon(\mathbf{k}'), \omega')$$

$$= \frac{L^2}{\pi^2}\frac{1}{\cos\theta}\frac{1}{v_x(\mathbf{k})}\delta k(\epsilon_2 - \epsilon_1) \int_{\epsilon_1}^{\epsilon_2} \frac{d\epsilon'}{\epsilon_2 - \epsilon_1}\sqrt{1 - \frac{4(\epsilon' - \epsilon(\mathbf{k}))^2}{(\epsilon_2 - \epsilon_1)^2}} |M(\epsilon')|^2 \,\mathrm{Im}G(\epsilon', \omega')$$

$$= \frac{2L^2}{\pi^2}\delta k^2 \int_{\epsilon_1}^{\epsilon_2} \frac{d\epsilon'}{\epsilon_2 - \epsilon_1}\sqrt{1 - \frac{4(\epsilon' - \epsilon(\mathbf{k}))^2}{(\epsilon_2 - \epsilon_1)^2}} |M(\epsilon')|^2 \,\mathrm{Im}G(\epsilon', \omega')$$

where ϵ_1 and ϵ_2 are band energies corresponding to k_1 and k_2 respectively, and $\epsilon(\mathbf{k}) = (\epsilon_1 + \epsilon_2)/2$ by assumption. The $W_\epsilon(\epsilon')$ function is therefore an elliptical function

$$W_\epsilon(\epsilon') \propto \frac{1}{\epsilon_2 - \epsilon_1}\sqrt{1 - \frac{4(\epsilon' - \epsilon(\mathbf{k}))^2}{(\epsilon_2 - \epsilon_1)^2}}.$$

In a real experiment, the photon spot is not perfectly sharp, and gives rise to a substantial smearing of the resolution function. This additional broadening is particularly important for $\mathbf{k}$ in the vicinity of $\mathbf{k}_F$ where the small amount of tail in the resolution function can make a noticeable difference due to sharp peaks for $\mathbf{k}$ near $\mathbf{k}_F$. To include this smearing effect, a line profile with a tail instead of the sharp cutoff of the elliptical function, e.g. a Gaussian function, is better.

Second, the finite photoelectron lifetime should be taken into account. It is well-known [4] that photoelectrons strongly scatter with sample as they are leave the solid. The photoelectron mean free path is only $10 \sim 20$Åfor kinetic energies of $10 \sim 1000$ eV, making photoemission experiments surface sensitive. In EDC's, those photoelectrons that are scattered inelastically pile up in the low kinetic energy part of spectrum, giving rise to the so-called inelastic background. For an angle integrated photoemission spectrum, there is a well-established procedure, the Shirley background subtraction [14], to remove this inelastic background. In ARPES, there is no such established procedure due to the complexity of the situation [15]. In addition, there can be surprising effects in ARPES due to elastic momentum scattering of the photoelectrons, such as peak-*widening* [16] as the band approaches E_F.

In the description of the photoemission process using an optical potential [17], the finite photoelectron lifetime is modeled with an imaginary part in the momentum. In other words, the photoelectron is described as a wave packet rather than a plane wave. Due to the boundary condition at the surface the imaginary part can exist only in the momentum component perpendicular to the surface, $k_\perp$. A given finite state lifetime τ_e implies a width $\Delta k_\perp = 1/(\tau_e v_{e\perp})$, so that direct transitions between the initial state and the final state lead to an additional broadening in the ARPES spectrum [18],

$$\Delta E \approx v_{h\perp}\Delta k_\perp = \frac{v_{h\perp}}{v_{e\perp}}\frac{1}{\tau_e}, \tag{1.10}$$

where $v_{h\perp}$ and $v_{e\perp}$ are the group velocities perpendicular to the surface for the initial band and the final band respectively. For a material with large $v_{h\perp}$, i.e. with a strongly 3 dimensional electronic structure, this energy broadening can be quite large. In this case, a more proper description is to sum over $k_\perp$ in Eq. 1.9. Essentially, one must evaluate a sum $\sum_{k_\perp}\text{Im}G(k_{||}, k_\perp)$. One can then see that if $\Delta k_\perp$ is as large as the Brillouin zone width in the surface normal direction, this sum is a one dimensional density of states along this direction. For a material with strongly 3 dimensional electronic properties, this phenomenon can be often observable. One can calculate that in this case ARPES would still show strong dispersions as angles are changed, but no dispersions as photon energy is varied near normal emission.

Third and last, in a real experiment, the possibility of sample misalignment of a few degrees in mounting must be taken into account. When a sample is misaligned the ideal diagram in Fig. 1.1 does not hold true, because the sample normal axis and the analyzer

0 angle direction do not coincide. Fortunately correcting this sample misalignment is easy in the ARPES setup of Fig. 1.1. With misalignment, it is better to define θ and ϕ as the two angles of rotations for the two-axis goniometer on which the electron analyzer is mounted. That is, θ and ϕ are now defined with respect to an axis in the horizontal plane, not with respect to the sample normal. Now, the sample normal is given by finite values of θ and ϕ. Finite offset in θ is trivially renormalized to zero by a simple rotation along the vertical axis. This is not true for ϕ, however. Therefore a misaligned sample is characterized with a finite sample normal angle ϕ_N. With the (x, y, z) now defined in terms of the goniometer coordinates, the relation of the sample cartesian coordinates (x', y', z') to (x, y, z) is trivial. With this taken into account, the photoelectron momentum outside sample now reads

$$\begin{aligned}
k_{x,out} &= 0.512\sqrt{E_K}\,\cos\phi\,\sin\theta, \\
k_{y,out} &= 0.512\sqrt{E_K}\,(\sin\phi\,\cos\phi_N - \cos\phi\,\cos\theta\,\sin\phi_N), \\
k_{z,out} &= 0.512\sqrt{E_K}\,(\sin\phi\,\sin\phi_N + \cos\phi\,\cos\theta\,\cos\phi_N). \qquad (1.11)
\end{aligned}$$

For small values of θ, ϕ and ϕ_N, this correction can be approximated by simply putting $\phi - \phi_N$ in place of ϕ in Eq. 1.3, but such a quick fix is not acceptable when the angles become large.

Before closing this section, I point out important general advantages of ARPES for quasi-low dimensional systems. First, quasi-low dimensional systems are typically composed of layers with weak interactions between them. This means that the surface exposed by cleavage at these weak links is more stable than the surface of a 3 dimensional crystal and therefore surface sensitivity is less important. In contrast, surface peaks can complicate photoemission spectra severely for a 3 dimensional crystal [19]. Second, negligible dispersion perpendicular to the surface layer means small ΔE in Eq. 1.10. Third, for the same reason, the $k_\perp$ value is not of importance. This means that determining the inner potential V_o is not an important issue, while in a fully 3 dimensional crystal it is a crucial issue.

1.3 Experimental details

Most of the ARPES experiments reported in this thesis were done at the Ames/Montana beamline of the Synchrotron Radiation Center (SRC) at the University of Wisconsin. This beamline combined with its Ames group ARPES chamber was one of the most pioneering high resolution ARPES setups built in early '90s, and produced an extremely influential work [20], the discovery of the FS and the superconducting gaps in the high T_c superconducting cuprate material $Bi_2Sr_2CaCu_2O_8$. In a large sense, this thesis work is a result of issues raised by this past work and the excitement of the physics community that followed. Another source of the data presented here is the beamline 5 of the Stanford Synchrotron Radiation Laboratory (SSRL) which is equipped with an almost identical ARPES chamber. Over the last few years, this beamline has also produced very provocative data, mostly on $Bi_2Sr_2CaCu_2O_8$.

Synchrotron radiation is generated when electrons of relativistic energy ~ 1 GeV are forced to move in a curved orbit by a magnetic field. The unique capability of a synchrotron radiation source is that the continuous spectrum of a broad range of light is available for investigations in condensed matter physics, the biological sciences *etc*. The Ames/Montana beamline at the SRC is equipped with a combined Seya/Erg monochromator, which provides photons from ~ 10 eV up to ~ 1000 eV. For high resolution ARPES, the low energy monochromator, Seya, which provides photons from ~ 10 eV up to ~ 35 eV is exclusively used. There are two important reasons for favoring low energies in the UV region for a high resolution ARPES investigation. First, for a given resolving power, the energy resolution is better for low photon energies. Second, for a fixed angular resolution, the momentum resolution is better for low photon energies. Roughly, momentum resolution increases as the square root of the photon energy as can be seen from Eq. 1.3. At the SSRL, the beamline is equipped with an undulator which delivers a stronger beam intensity than the bending magnet beamline at the SRC. The photon energy range at this beamline is $20 \sim 35$ eV.

A hemispherical electron energy analyzer is used. A schematic diagram is drawn in Fig. 1.4. The main part of the equipment is two concentric hemispherical shells which are charged at different potentials. The resulting electro-static potential determines the kinetic energy (pass energy) of an incoming electron at the entrance slit which will be focussed at the exit slit. Therefore, before entering the hemisphere photoelectrons from the sample are decelerated or accelerated to the pass energy by the electro-static lens system, which also focuses the electrons at the entrance slit. The finite energy resolution

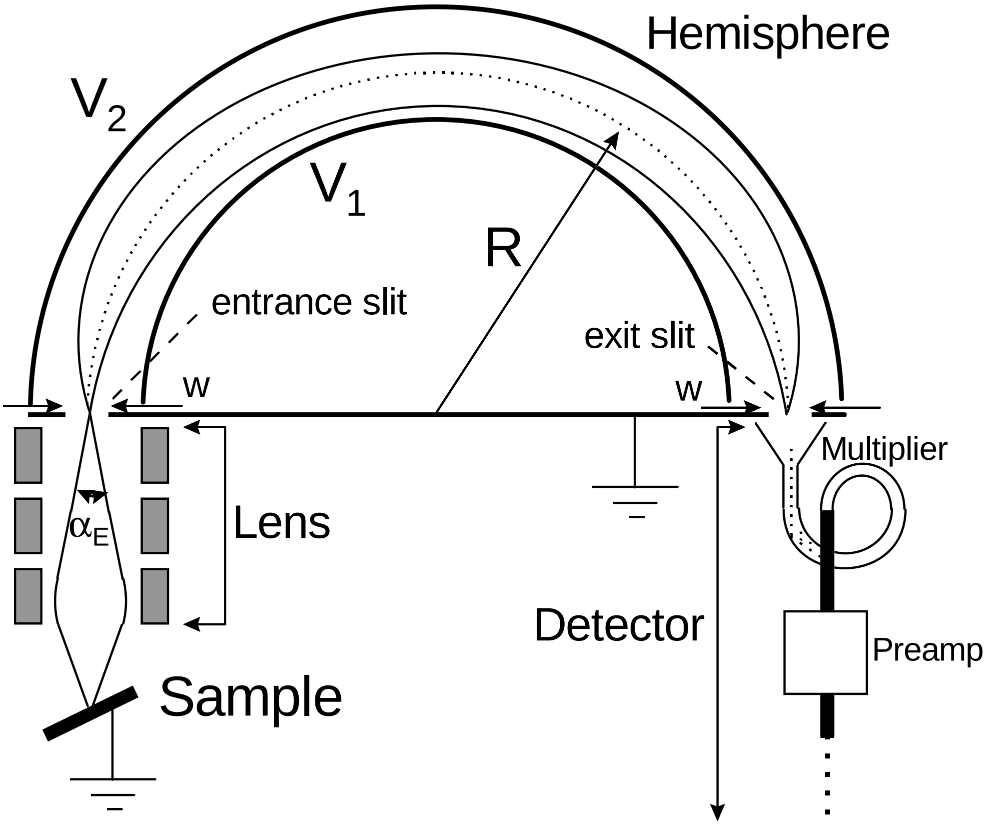

Figure 1.4: Schematic diagram of a hemispherical electron energy analyzer.

of the analyzer results from the finite widths of the entrance and the exit slits and the finite incident cone angle (α_E) resulting from the finite angle resolution.

In ARPES experiments, both the angle and energy of the detected photoelectrons are scanned. Conventionally, experiments are performed in the "EDC mode", in which EDC's are obtained for a few angles that define a path in momentum space. Recently, a new mode, the "map mode", has been gaining popularity for studying valence band electronic structure. In this mode, the kinetic energy of photoelectrons is fixed, very often at E_F, and wide ranges of angles are scanned to take an intensity map of the momentum space electron distribution. The two modes are quite complementary to each other: an E_F intensity map is extremely helpful to get an overview of the FS and the details of its connectivity, and EDC's are essential both for determining FS crossings exactly and for studying single-particle lineshapes. Usually an experimental setup with an automated rotatable sample holder is used for taking maps. In this thesis, however, the conventional movable analyzer setup of the Ames group ARPES chamber is used to take maps. This setup has a crucial advantage over a rotatable sample holder setup for the small samples used in this thesis, because it maintains the same detected spot on the sample over wide ranges of angles.

For angle integrated photoemission a Vacuum Generator (VG) ESCALAB MK II spectrometer in the home laboratory is used. For surface characterization, a Mg K_α source (1253.6 eV) or an Al K_α source (1486.6 eV) are used. For high resolution spectra the He I line (21.2 eV) from a gas discharge lamp is used.

The single crystalline samples used in this thesis all have layered structures and so have thin flake shapes. Typical dimensions are $\approx$ 2 mm×2 mm with thickness on the order of 0.1mm. The sample is mounted on a sample holder, which is then screwed into a hole in the cold tip of a closed cycle He refrigerator. The sample orientation needs to be determined before it is inserted into the cold tip, which goes into the ultra high vacuum chamber. For this purpose, a Laue diffraction photograph is taken. Because the probing depth of the photoemission experiment is only $\sim$ 10Å, and because the surface quality degrades over time even in ultra high vacuum, it is crucial to prepare a clean surface in the vacuum just before the photoemission measurement is made. This is done by gluing a thin and short post made of aluminum or copper onto the top of the sample and then knocking the post off in vacuum to peel off the top layers of the sample and expose a clean surface. The vacuum is typically $\sim 5 \times 10^{-11}$ Torr.

1.4 Previous results

In this thesis, I present an ARPES study of the lineshapes and FS's for molybdenum bron-zes, $SmTe_3$ and $TiTe_2$. The molybdenum bronzes are a family of quasi-low dimensional materials with the general formula $A_xMo_yO_z$, where A is an alkali metal or thallium. The work on the molybdenum bronzes and $SmTe_3$ was mainly my own project. However, the ARPES data on $Li_{0.9}Mo_6O_{17}$ are mainly credited to J.D. Denlinger. The $TiTe_2$ work is mostly "owned" by R. Claessen. At the beginning of Chapter 3 a short account of the $TiTe_2$ history within this group is presented. The $TiTe_2$ work reported in this thesis comprises my contributions in this field. I also collaborated in the work on the inorganic quasi-1D CDW compound Ta_2Se_8I [21], carried out mostly by R. Claessen and co-workers, by performing ARPES experiments. The results of this work, not presented here, differ in significant ways from the results [22] of a previous study. In the following, I discuss briefly the previous experimental work that motivated this thesis work. In chapter 2, I present the various conceptual issues in full detail.

The seminal work of Olson *et al.* [20] on $Bi_2Sr_2CaCu_2O_8$ has had a great influence on high resolution photoemission research. The data in Fig. 1.5 show dispersions along the ΓY $((0,0) \rightarrow (\pi,\pi))$ direction as a peak crosses E_F. Anderson [23] and Varma

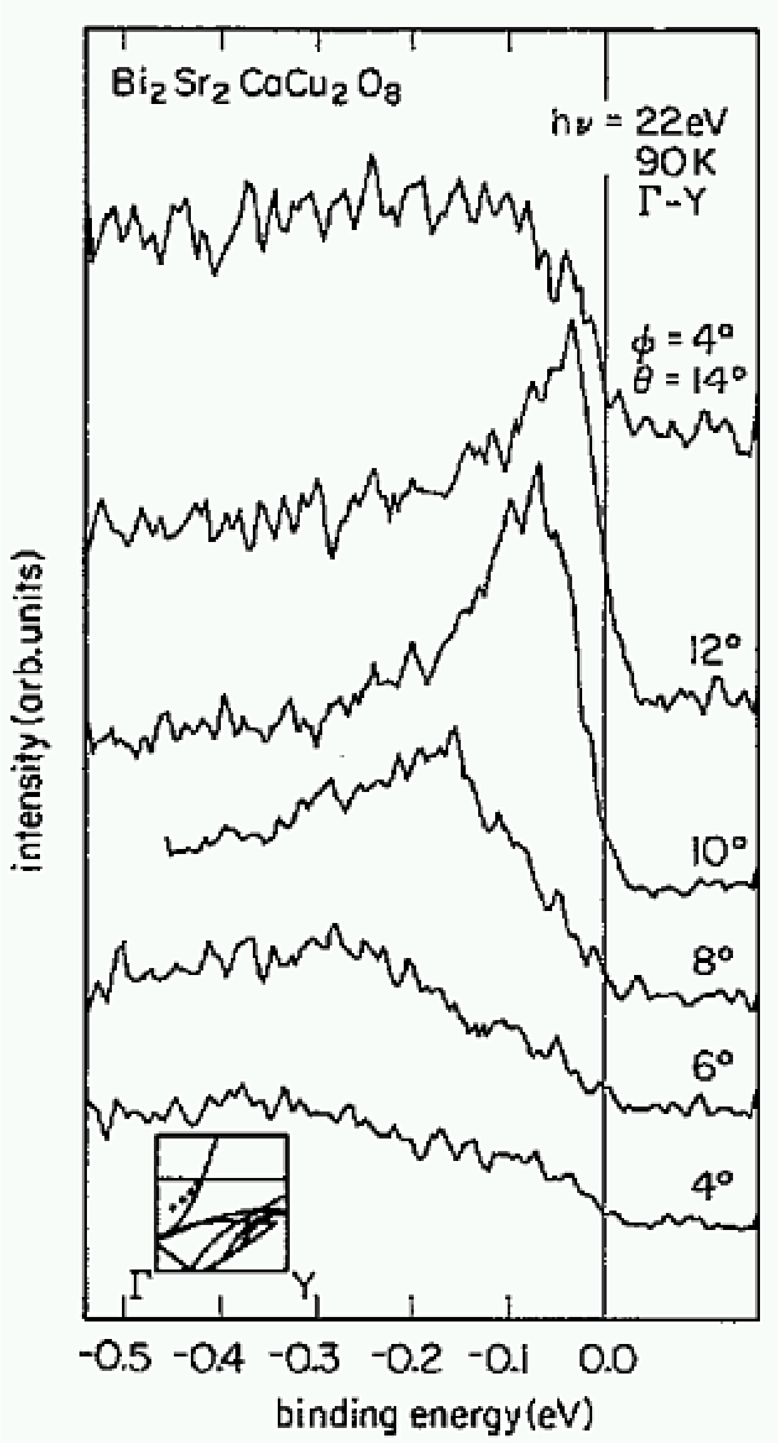

Figure 1.5: The ARPES data on $Bi_2Sr_2CaCu_2O_8$ by Olson *et al.* [20].

et al.[24] noted that the highly asymmetric non-Lorentzian lineshapes are incompatible with the Landau Fermi liquid. A great deal of work has been done on this material since Olson's work and many ARPES facts have been compiled concerning, e.g. the FS, the superconducting gap anisotropy, the existence of shadow bands and pseudo-gaps and most recently the controversial charge ordered stripes. However, a firm understanding of the lineshapes is still lacking [25, 26].

For a many body theoretical understanding of ARPES lineshapes, an examination of an established Fermi liquid compound is necessary. Work on $TiTe_2$ [27] provided such an example. Fig. 1.6 shows fits of the $TiTe_2$ ARPES data with a Fermi liquid spectral function (Eq. 2.13). Subsequently, the Fermi liquid model to be used for such analysis has been refined (section 2.2), and an attempt was made to relate ARPES findings to transport properties such as resistivity.

Several quasi-1D compounds including $K_{0.3}MoO_3$ [28], Ta_2Se_8I [28, 29] show greatly suppressed density of states at E_F. Fig. 1.7 shows angle integrated spectra from these materials. In contrast to quasi-2D $TaSe_2$ and 3D Rh metal showing a clear Fermi edge, these materials show anomalous behavior. As carefully discussed in Ref. [28], several mechanisms can possibly lead to a low density of states at E_F, including 1 dimensional CDW fluctuations and LL behavior. In this thesis, we systematically study quasi-1D and quasi-2D bronzes using ARPES and angle integrated PES to gain an insight into the cause of the E_F weight suppression and the interesting interplay between electronic properties and dimensionality.

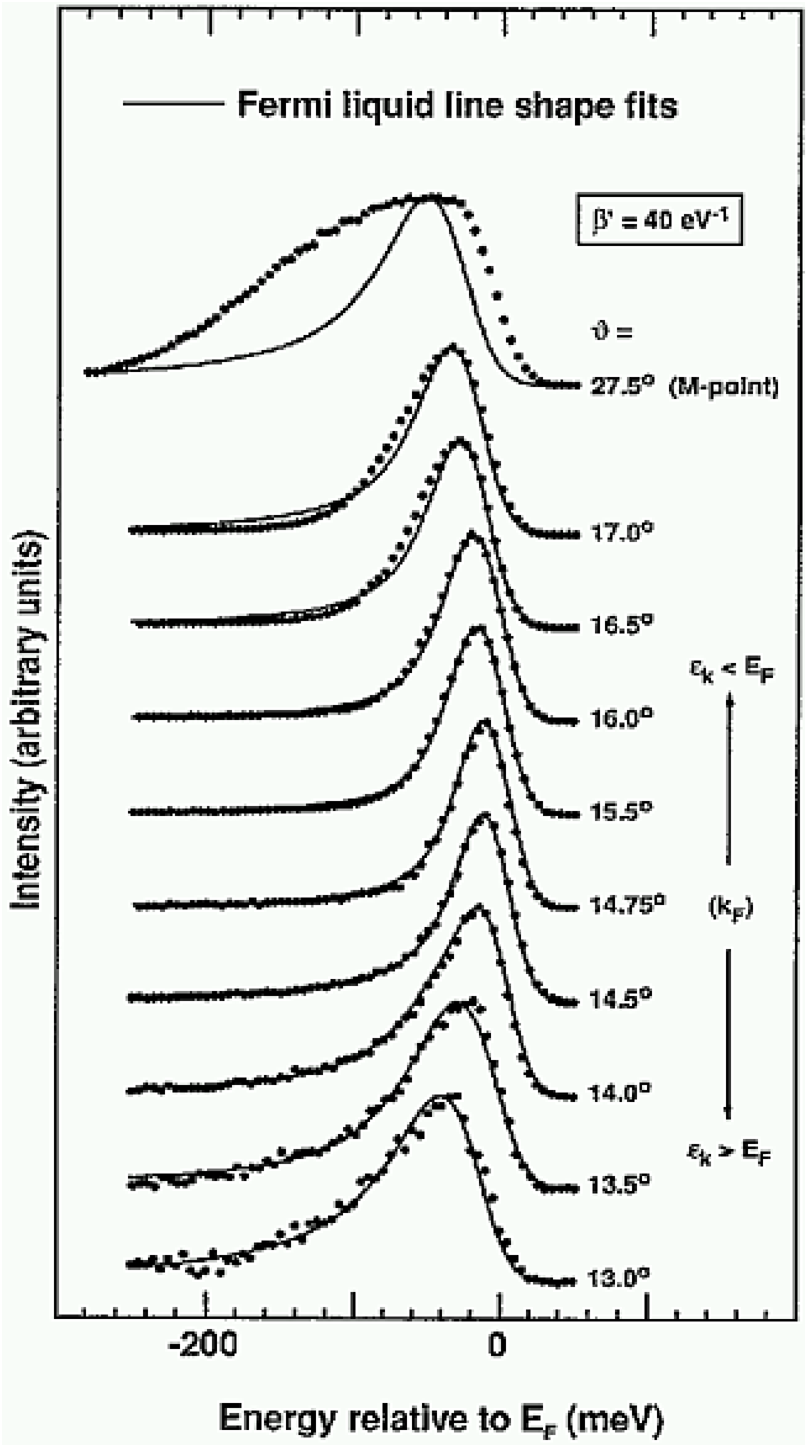

Figure 1.6: Fermi liquid fit of $TiTe_2$ lineshape by Claessen *et al.* [27].

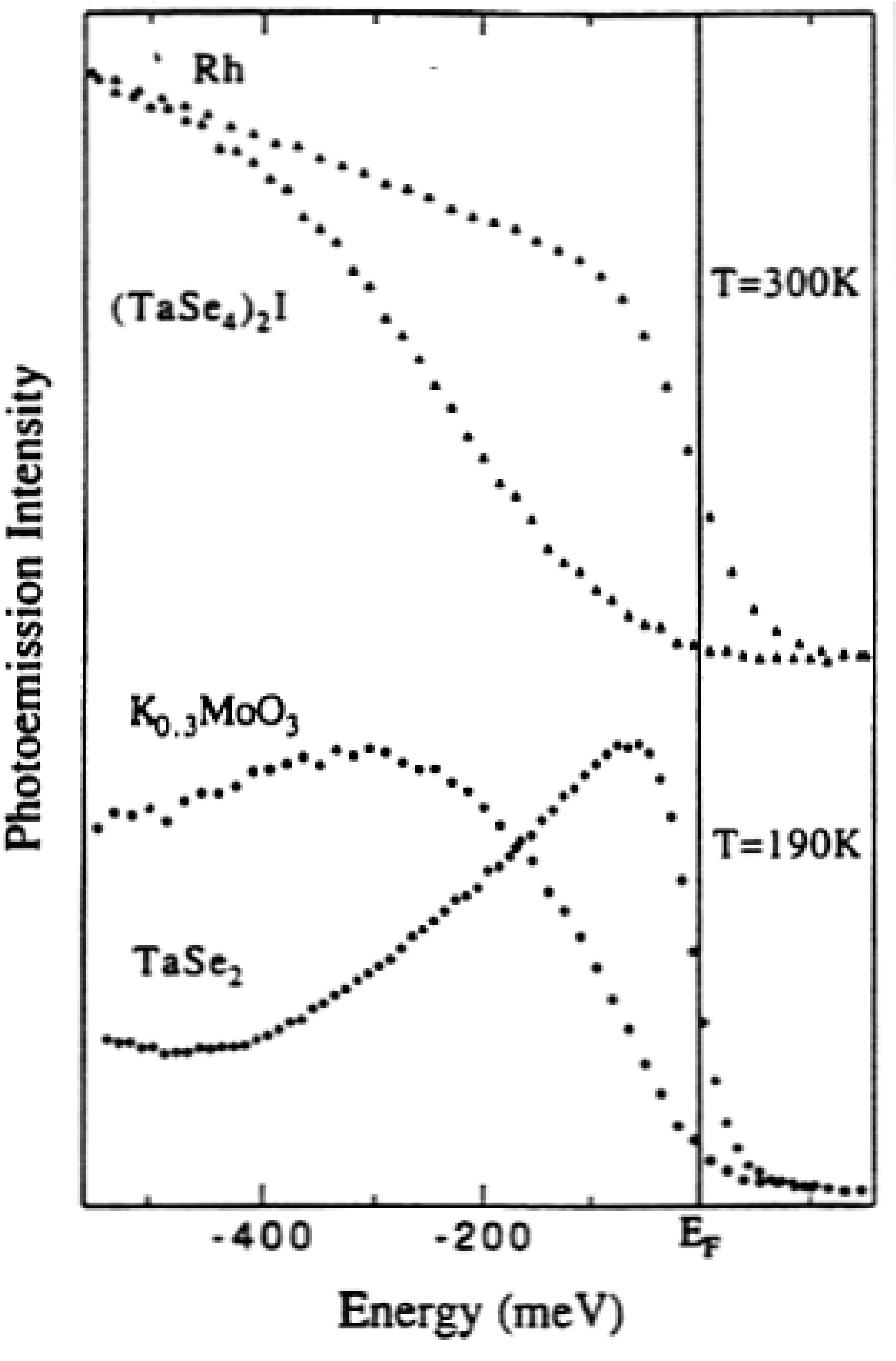

Figure 1.7: High resolution angle integrated photoemission spectra on quasi-low dimensional materials by Dardel *et al.* [28].

Chapter 2

Introduction: Theory

The Green's function is of central importance in interpreting ARPES. Therefore, its general properties are summarized here. I then discuss the theory of the FL, of CDW's and of the LL, with emphasis on spectral functions.

2.1 Green's function

The Green's function[1], or propagator, measures the probability amplitude for a particle to propagate from one point in space-time to another point. As a convention, we will use the advanced Green's function, defined as follows,

$$G(\mathbf{k},t) \quad = \quad i\theta(-t)\,\langle\{a_{\mathbf{k}}(t), a^{\dagger}_{\mathbf{k}}(0)\}\rangle, \tag{2.1}$$

where θ is the step function, $a_{\mathbf{k}}(t)$ ($a^{\dagger}_{\mathbf{k}}(t)$) is an electron annihilation (creation) operator in the Heisenberg representation, $\mathbf{k}$ is the (crystal) momentum label, $\{\}$ means anti-commutator, and $\langle\rangle$ means thermal average. The spin quantum number is omitted for simplicity. By definition, Eq. 2.1 is a sum of two probability amplitudes. The first is the complex conjugate of the probability that an electron with momentum $\mathbf{k}$ added to the system at time $t(<\,0)$ propagates to the same momentum state at $t = 0$. The second is the probability amplitude that a hole with momentum $-\mathbf{k}$ added at time $t(<\,0)$ propagates to the same momentum state at $t = 0$. For any N electron eigenstate, the addition of an electron or hole make the resulting state behave in a complicated way because it is no longer an eigenstate. In other words, the time evolution of such states involves a continuum of the energies for $N+1$ ($N-1$) eigenstates. More precisely, the

---

[1] The adjective phrase "single particle" is implied in the term Green's function. The same is implied for a spectral function.

Fourier transform of Eq. 2.1 yields information on the spectral distributions of $N+1$ and $N-1$ electron eigenstates:

$$\begin{aligned} G(\mathbf{k},\omega) &= \int_{-\infty}^{\infty} dt\, e^{i(\omega-i0^+)t}\, G(\mathbf{k},t) \\ &= i\int_{-\infty}^{0} dt e^{i(\omega-i0^+)t}\, \langle a^\dagger_{\mathbf{k}} a_{\mathbf{k}}(t) + a_{\mathbf{k}}(t) a^\dagger_{\mathbf{k}}\rangle \\ &= i\sum_{n,N}\int_{-\infty}^{0} dt \frac{e^{-\beta K_{n,N}}}{Z_G}\, \langle n,N|\, a^\dagger_{\mathbf{k}}\, e^{i(\omega-i0^+ + H - E_{n,N})t}\, a_{\mathbf{k}}\, |n,N\rangle + \\ &\quad\; i\sum_{n,N}\int_{-\infty}^{0} dt \frac{e^{-\beta K_{n,N}}}{Z_G}\, \langle n,N|\, a_{\mathbf{k}}\, e^{i(\omega-i0^+ - H + E_{n,N})t}\, a^\dagger_{\mathbf{k}}\, |n,N\rangle \\ &= G^-(\mathbf{k},\omega) + G^+(\mathbf{k},\omega), \\ G^-(\mathbf{k},\omega) &= \langle a^\dagger_{\mathbf{k}}\, \frac{1}{\omega - i0^+ + H - E_{n,N}}\, a_{\mathbf{k}}\rangle, \qquad (2.2) \\ G^+(\mathbf{k},\omega) &= \langle a_{\mathbf{k}}\, \frac{1}{\omega - i0^+ - H + E_{n,N}}\, a^\dagger_{\mathbf{k}}\rangle. \qquad (2.3) \end{aligned}$$

Here, 0^+ is inserted to make the t-integral well-behaved, $\beta = 1/(k_B T)$, $K_{n,N} = E_{n,N} - \mu N$, where $E_{n,N}$ is the energy for N particle eigenstate $|n,N\rangle$, μ is the chemical potential, and $Z_G = \sum_{n,N} e^{-\beta K_{n,N}}$ is the grand-canonical partition function. Operators with no explicit time argument are meant to be evaluated at $t=0$. If an identity operator $\sum_{n',N'} |n',N'\rangle\langle n',N'|$ is inserted before and after the operator $\frac{1}{\omega - i0^+ \pm H \mp E_{n,N}}$, then it is readily noted that the last two equations (2.2 and 2.3) represents a sum of (infinitely) many poles at energies $E_{n,N} - E_{m,N-1} + i0^+$ and $E_{o,N+1} - E_{n,N} + i0^+$. This is called the Lehman representation [30].

The strengths of these poles are given by the imaginary part of the Green's function, which is called the spectral function:

$$\begin{aligned} A(\mathbf{k},\omega) &= \frac{1}{\pi}\,\mathrm{Im}\, G(\mathbf{k},\omega) \qquad (2.4) \\ &= A^-(\mathbf{k},\omega) + A^+(\mathbf{k},\omega) \\ A^-(\mathbf{k},\omega) &= \langle a^\dagger_{\mathbf{k}}\, \delta(\omega + H - E_{n,N})\, a_{\mathbf{k}}\rangle, \qquad (2.5) \\ A^+(\mathbf{k},\omega) &= \langle a_{\mathbf{k}}\, \delta(\omega - H + E_{n,N})\, a^\dagger_{\mathbf{k}}\rangle. \qquad (2.6) \end{aligned}$$

By inserting the identity $\sum_{n',N'} |n',N'\rangle\langle n',N'|$ before and after the delta functions in the last two equations, and then noting that for $N \gg 1$, $\langle n', N+1|a_{\mathbf{k}}|n,N\rangle = \langle n', N|a_{\mathbf{k}}|n, N-$

$1\rangle$, it is easy to see that

$$A^{+}(\mathbf{k},\omega) \;=\; e^{\beta(\omega-\mu)}\, A^{-}(\mathbf{k},\omega).$$

From this, it follows immediately that

$$\begin{aligned} A^{-}(\mathbf{k},\omega) &= f(\omega-\mu)\, A(\mathbf{k},\omega), \\ A^{+}(\mathbf{k},\omega) &= (1-f(\omega-\mu))\, A(\mathbf{k},\omega), \end{aligned} \tag{2.7}$$

where $f(\omega-\mu) = 1/(1+e^{\beta(\omega-\mu)})$ is the Fermi-Dirac distribution function. $A^{-}(\mathbf{k},\omega)$ is the probability distribution for removing an electron with momentum $\mathbf{k}$ and energy ω, and $A^{+}(\mathbf{k},\omega)$ is the probability distribution for adding an electron with momentum $\mathbf{k}$ and energy ω. As explained in Section 1.1, $A^{-}(\mathbf{k},\omega)$ is directly related to the photoemission[2]. The spectral function satisfies a sum rule [30]

$$\int_{-\infty}^{\infty} d\omega\, A(\mathbf{k},\omega) \;=\; 1. \tag{2.8}$$

In the expressions for the spectral function, the chemical potential μ plays the role of the most natural origin of the energy axis. Therefore, we will take $\mu = 0$ throughout this thesis, unless otherwise noted. Also, it will often be identified with the Fermi energy, E_F. This is strictly true only for $T = 0$, as the chemical potential at finite temperature differs slightly [2] from its $T = 0$ value. The difference, which is of order $(k_BT/E_F)^2$, is negligible for a typical value of $E_F \sim 1$ eV and $k_BT \leq 300$ K = 25 meV.

Noting from Eq. 2.2 that $G(\mathbf{k},\omega)$ is analytic in the lower half plane[3], by contour integration, we get

$$G(\mathbf{k},\omega'') \;=\; \frac{1}{2\pi\, i}\int_{-\infty}^{\infty} d\omega' \frac{G(\mathbf{k},\omega')}{\omega''-\omega'},\;\; \mathrm{Im}(\omega'')<0.$$

Taking $\omega'' = \omega - i0^{+}$, with real ω, we get

$$G(\mathbf{k},\omega) \;=\; \frac{1}{\pi\, i} P\int_{-\infty}^{\infty} d\omega' \frac{G(\mathbf{k},\omega')}{\omega-\omega'},$$

where P means the Cauchy principal value. This equation implies the Kramers-Kronig relation for the real part and the imaginary part of the Green's function, and leads to

$$G(\mathbf{k},\omega) \;=\; \mathrm{Re}\, G(\mathbf{k},\omega) + i\, \mathrm{Im}\, G(\mathbf{k},\omega)$$

---

[2] Similarly, $A^{+}(\mathbf{k},\omega)$ is directly related to the inverse-photoemission .

[3] The Green's function has a branch cut just above the real axis, arising from (infinitely) many poles easily recognizable in the Lehman representation.

$$
\begin{aligned}
&= \frac{1}{\pi}P\int_{-\infty}^{\infty}d\omega'\frac{\mathrm{Im}\,G(\mathbf{k},\omega')}{\omega-\omega'}+i\,\mathrm{Im}\,G(\mathbf{k},\omega) \\
&= \int_{-\infty}^{\infty}d\omega'(P\frac{1}{\omega-\omega'}+i\pi\,\delta(\omega-\omega'))\frac{\mathrm{Im}\,G(\mathbf{k},\omega')}{\pi} \\
&= \int_{-\infty}^{\infty}d\omega'\frac{A(\mathbf{k},\omega')}{\omega-\omega'-i0^{+}}. \qquad (2.9)
\end{aligned}
$$

This last equation is a continuum version of the Lehman representation.

Another way of representing the Green's function is the Dyson equation [30],

$$
G(\mathbf{k},\omega) = \frac{1}{\omega-\epsilon(\mathbf{k})-\Sigma(\mathbf{k},\omega)}, \qquad (2.10)
$$

where $\epsilon(\mathbf{k})$ is one electron energy for the state created by $a^{\dagger}_{\mathbf{k}}$, and $\Sigma(\mathbf{k},\omega)$ is the self-energy term which contains all interaction effects. It can be shown [31] that the self energy also satisfies the Kramers-Kronig relation. The density of states is obtained by simply summing the spectral function over momenta,

$$
N(\omega) = \sum_{\mathbf{k}} A(\mathbf{k},\omega). \qquad (2.11)
$$

This quantity is related to angle integrated photoemission. An interesting relation[4] exists between $\Sigma(\mathbf{k},\omega)$ and $N(\omega)$: if $\Sigma(\mathbf{k},\omega)$ is $\mathbf{k}$-independent and vanishes at μ, then $N(\mu)$ is unchanged with or without $\Sigma(\mathbf{k},\omega)$. Conversely, if one finds that $N(\mu)$ changes dramatically due to interactions, as happens for CDW pseudo-gaps and the LL, then one must conclude that $\Sigma(\mathbf{k},\omega)$ is either $\mathbf{k}$-dependent or finite at $\omega=\mu$, or both. Another quantity of interest is the electron occupation number

$$
n(\mathbf{k}) = \int_{-\infty}^{\infty}d\omega\,A^{-}(\mathbf{k},\omega), \qquad (2.12)
$$

which gives the total probability to remove an electron with momentum $\mathbf{k}$. For non-interacting electrons, $n(\mathbf{k})$ is either 1 or 0 at $T=0$ K, and the sharp boundary between the region where $n(\mathbf{k})=1$ and the region where $n(\mathbf{k})=0$ defines the FS.

2.2 Fermi liquid

One of the most basic questions for a condensed matter physicist is "how can a system having a macroscopic number of electrons interacting with each other be described in

---

[4] Sometimes this relation is called "no-go" theorem [32].

a sensible way?." The answer from the Fermi liquid theory, or rather the Fermi liquid postulate, due to Landau [3], is surprisingly simple. In this theory, an interacting system is essentially the same as a non-interacting system and the low energy excitations of the system can be described as though the system consists of non-interacting electron-like particles – so called quasi-electrons, but with certain parameters like the mass having renormalized values. A quasi-electron can be visualized [33] as an electron moving in a cloud of other electrons, somewhat slowed down (heavier mass) but still retaining its identity as a Fermionic particle and also its charge and spin.

The quasi-particle concept can be brought into a mathematical formalism using the self-energy. For interacting electrons in 3-dimensions (3D), it was shown by Luttinger [31] that *if* perturbation theory in interaction strength is valid, then the lowest order term in an ω expansion of the imaginary part of the self energy is given *to all orders in perturbation theory* by a quadratic function of $(\omega - \mu)$. By a Kramers-Kronig transformation, it then follows that the self-energy can be written as

$$\Sigma(\mathbf{k},\omega) = \alpha\omega + i\beta\omega^2, \quad \alpha < 0, \beta > 0 \tag{2.13}$$

to lowest order in ω. As often demonstrated [34], the quadratic dependence of $\mathrm{Im}\Sigma(\mathbf{k},\omega)$ can be already seen in the 2nd order perturbation, and comes from the fact that the phase space volume available for the scattering of a quasi-particle decreases quadratically as a function of its energy, due to the Pauli exclusion principle and energy conservation.

Inserting Eq. 2.13 into Eq. 2.10, we have

$$\begin{aligned} G(\mathbf{k},\omega) &= \frac{1}{\omega - \epsilon(\mathbf{k}) - \alpha\omega - i\beta\omega^2} \\ &= \frac{Z}{\omega - \epsilon(\mathbf{k})' - i\beta'\omega^2}, \end{aligned} \tag{2.14}$$

where $Z = 1/(1-\alpha)$, $\epsilon(\mathbf{k})' = Z\epsilon(\mathbf{k})$ and $\beta' = Z\beta$. For $\omega \approx \epsilon(\mathbf{k})'$, one can approximate this expression as

$$G(\mathbf{k},\omega) \approx \frac{Z}{\omega - \epsilon(\mathbf{k})' - i\beta'\epsilon(\mathbf{k})'^2}. \tag{2.15}$$

This equation has the same form as that of the free electron Green's function,

$$G_o(\mathbf{k},\omega) = \frac{1}{\omega - \epsilon(\mathbf{k}) - i0^+}$$

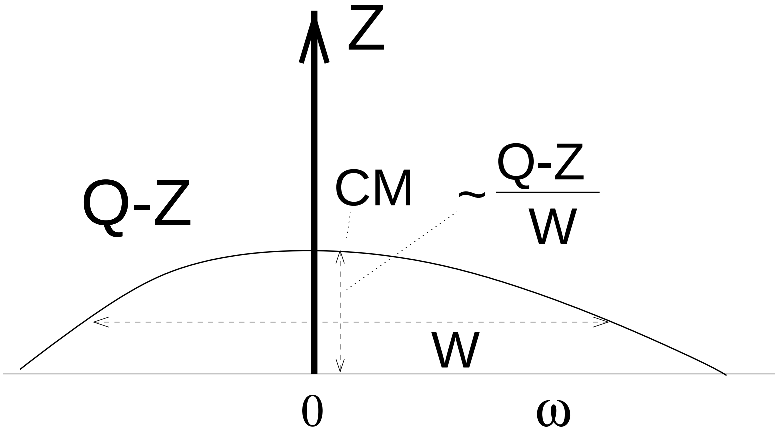

Figure 2.1: A generic Fermi liquid spectral function at Fermi wavevector. It consists of a quasi-particle peak at the chemical potential with weight Z and a smooth background function carrying the rest of the weight. Only the low energy part of the background function is drawn here, which carries weight $Q - Z$. The remaining weight $1 - Q$ is assumed to exist in higher energy structure, e.g. Hubbard satellite, not shown here.

except that the pole of the Green's function is shifted from $\epsilon(\mathbf{k})$ to $\epsilon(\mathbf{k})' + i\beta'\epsilon(\mathbf{k})'^2$, and its residue is reduced from 1 to Z. The finite imaginary part in the pole energy means a finite lifetime. As $|\epsilon(\mathbf{k})'|$ approaches 0, the pole approaches infinitesimally close to the real axis, signifying that the pole becomes a true eigenstate. This eigenstate is the quasi-particle state, whose dispersion relation $\epsilon(\mathbf{k})'$ is renormalized by $Z < 1$ relative to that of free electron, or equivalently whose mass is renormalized by $Z^{-1} > 1$ relative to that of free electron. Z is also the weight of the quasi-particle Green's function, i.e. the square of the overlap between the free electron and the quasi particle wave functions. I call the FL theory of Eq. 2.13 or Eq. 2.14 the "Taylor FL model", because it is a theory based on the lowest order Taylor series expansion in ω of the self energy.

The self energy of Eq. 2.13 shows pathological behaviors if it is used unconditionally. The form of Eq. 2.13 suggests that it is valid only for $\omega \ll 1/\beta'$, and therefore we define the Fermi liquid coherence energy scale $\Delta^* = 1/\beta'$. The pathology that occurs when this self energy is used for large energies on the order of Δ^* is easily noticed as follows. At the FS ($\epsilon(\mathbf{k}) = 0$) the Green's function of Eq. 2.14 has two poles $\omega = i0^+, -i\Delta^*$. Note that one is in the upper half plane while the other is below. By construction, our Green's function cannot have a pole in the lower half plane[5]. Therefore, the theory signals that it cannot be extended to the energy scale of Δ^*, because then the theory breaks the analytic property of the Green's function – in other words,

---

[5] On the other hand, in the upper plane poles are allowed. Note that the poles in the upper half plane appear only through an analytic continuation across the real axis. From the last section, we know that a branch cut exists along the real axis, so that the Green's function is well defined only in the lower half plane.

it breaks the causality principle.

In photoemission, however, we need a theory valid not only for the low energy scale but also for intermediate and high energy scales. How this can be done systematically was discussed by K. Matho [35], who proposed terminating a continued fraction expansion of the Green's function to obtain a Padé approximant. The underlying idea is that instead of expanding the self energy in ω, one considers a moment expansion of the spectral function. It is assumed that the spectral function at $\mathbf{k} = \mathbf{k}_F$ consists of a delta function at the chemical potential (the quasi-particle part of the spectral function) and a smooth function carrying the rest of the weight (the background spectral function), as shown in Fig. 2.1. Successive approximation of the true Green's function consists of taking more and more moments to describe the background spectral function better and better. Because one starts from a spectral function and gets the Green's function through the use of Eq. 2.9, the correct analytic property of the Green's function is automatically guaranteed.

The connection of a generic FL spectral function to the usual low energy expansion of the self energy is as follows. For a spectral function like that shown in Fig. 2.1, the Green's function is given by

$$\begin{aligned} G(\mathbf{k}_F,\omega) &= \frac{Z}{\omega - i0^+} + G_b(\mathbf{k}_F,\omega), \text{ where} \\ G_b(\mathbf{k}_F,\omega) &= \pi A_b(\mathbf{k}_F,\omega), \end{aligned}$$

and the subscript b stands for background. The self energy for this Green's function is easily obtained by inverting the Dyson's equation,

$$\begin{aligned} \mathrm{Re}\Sigma(\mathbf{k}_F,\omega) &= \omega\left[1 - \frac{Z + \omega\mathrm{Re}G_b(\mathbf{k}_F,\omega)}{|Z + \omega G_b(\mathbf{k}_F,\omega)|^2}\right], \text{ and} \\ \mathrm{Im}\Sigma(\mathbf{k}_F,\omega) &= \omega^2 \frac{\mathrm{Im}G_b(\mathbf{k}_F,\omega)}{|Z + \omega G_b(\mathbf{k}_F,\omega)|^2}. \end{aligned}$$

These equations imply that as long as $\omega G_b(\mathbf{k}_F,\omega) \to 0$ as $\omega \to 0$,[6] we get

$$\begin{aligned} \mathrm{Re}\Sigma(\mathbf{k}_F,\omega) &= \left(1 - \frac{1}{Z}\right)\omega, \text{ and} \\ \mathrm{Im}\Sigma(\mathbf{k}_F,\omega) &= \frac{\pi A_b(0)}{Z^2}\omega^2. \end{aligned}$$

---

[6] This is a perfectly reasonable condition, that the background spectral function is less singular than the quasi-particle spectral function.

Therefore, the quasi-particle part of the spectral function gives a linear ReΣ, regardless of the background spectral function. On the other hand, the background spectral function is directly related to the quadratic term of ImΣ. As long as $A_b(0)$ is neither 0 nor infinite, the usual FL self energy is recovered, with the FL coherence energy scale given by

$$\Delta^* = \frac{1}{\beta'} \quad = \quad \frac{Z}{\pi A_b(0)}. \tag{2.16}$$

The simplest model in the spirit of the spectral moment expansions of the background spectral function is the 2nd moment approximation, which gives the Green's function for $\mathbf{k} = \mathbf{k}_F$,

$$G(\mathbf{k}_F, \omega) \quad = \quad Q\left(\frac{z}{\omega - i0^+} + \frac{1-z}{\omega - \Omega_b}\right). \tag{2.17}$$

Here $Q < 1$ is the total weight in the energy range of interest, $z = Z/Q$, and Ω_b is a complex number describing the position of the "background pole." In this approximation, the background function is assumed to be a Lorentzian function, Re(Ω_b) describes the position of the background spectral function and Im(Ω_b) describes the width of the background spectral function. By construction, this approximation firmly links the high energy behavior of $A_b(\mathbf{k}_F, \omega)$, i.e. the coefficient of the quadratically falling tail, to the low energy behavior, i.e. the value of $A_b(\mathbf{k}_F, 0)$.

The self energy for this Green's function follows easily from the Dyson equation,

$$\Sigma(\mathbf{k}_F, \omega) \quad = \quad \frac{1}{Q}\left[(Q-1)\omega - (z-1)\Omega_b - \frac{z(z-1)\Omega_b^2}{\omega - z\Omega_b}\right]. \tag{2.18}$$

The linear term arises because $Q < 1$. It is a general property of the self energy that as $\omega \to \infty$ it should fall off faster than ω.[7] The linear term in the current self energy arises because we have ignored the high energy component of $A_b(\mathbf{k}_F, \omega)$, and therefore this self energy is invalid as $\omega \to \infty$. The next two terms give a self energy of Lorentzian shape.

We will call the Fermi liquid model defined by Eq. 2.17 the "Matho Fermi liquid model." This is a slight misnomer because Matho's theory [35] is not restricted to the 2nd moment expansion at all. However, in this thesis we will not concern ourselves

---

[7] This follows from the fact that $G(\mathbf{k}, \omega \to \infty) \to 1/\omega$, the property which can be seen by taking the $\omega \to \infty$ limit of Eq. 2.9 and using the sum rule $\int_{-\infty}^{\infty} A(\mathbf{k}, \omega) = 1$.

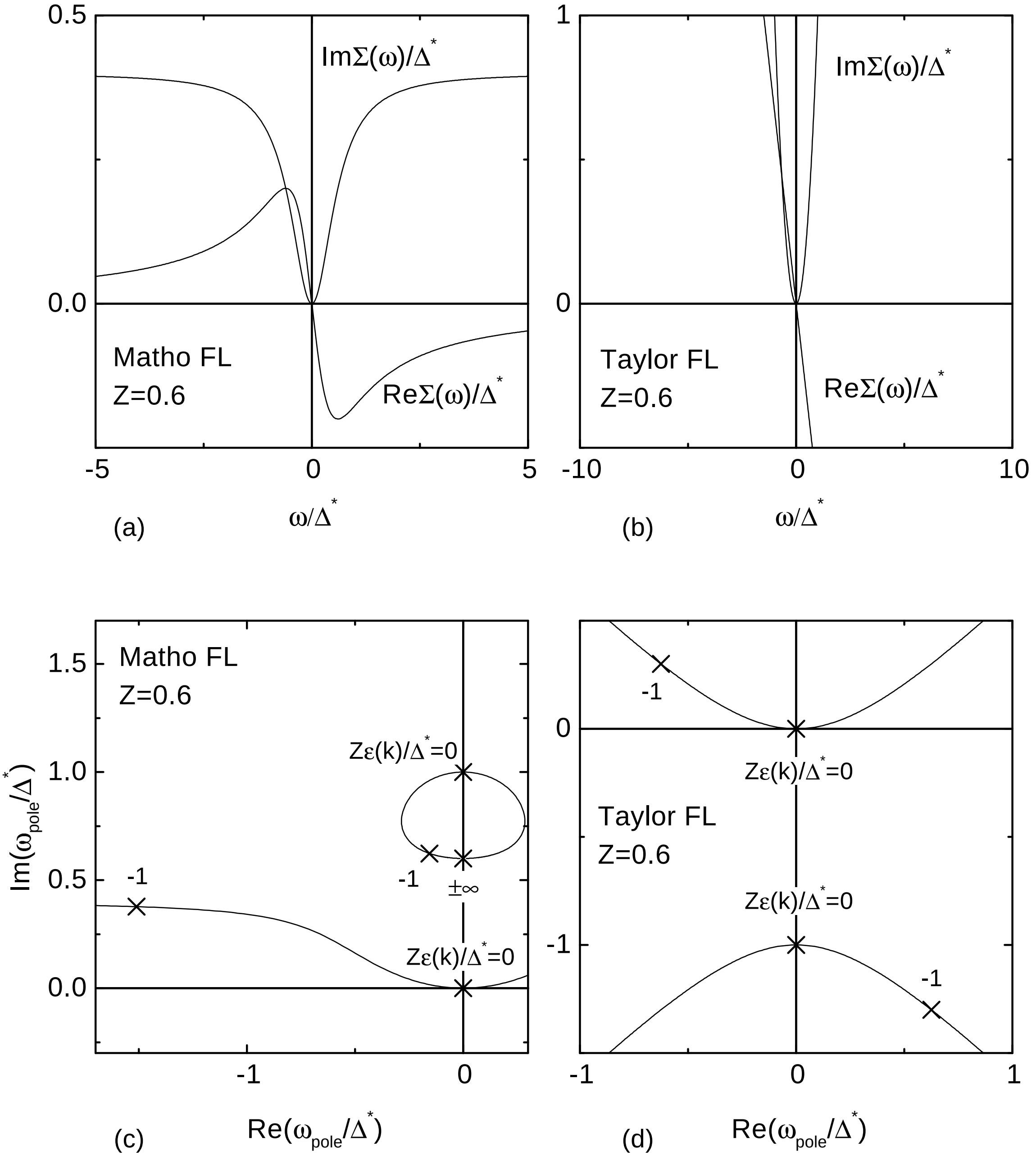

Figure 2.2: Self-energies (a and b) and poles (c and d) of FL model Green's functions. The imaginary part of the self energy of the Matho FL model is an inverted Lorentzian function.

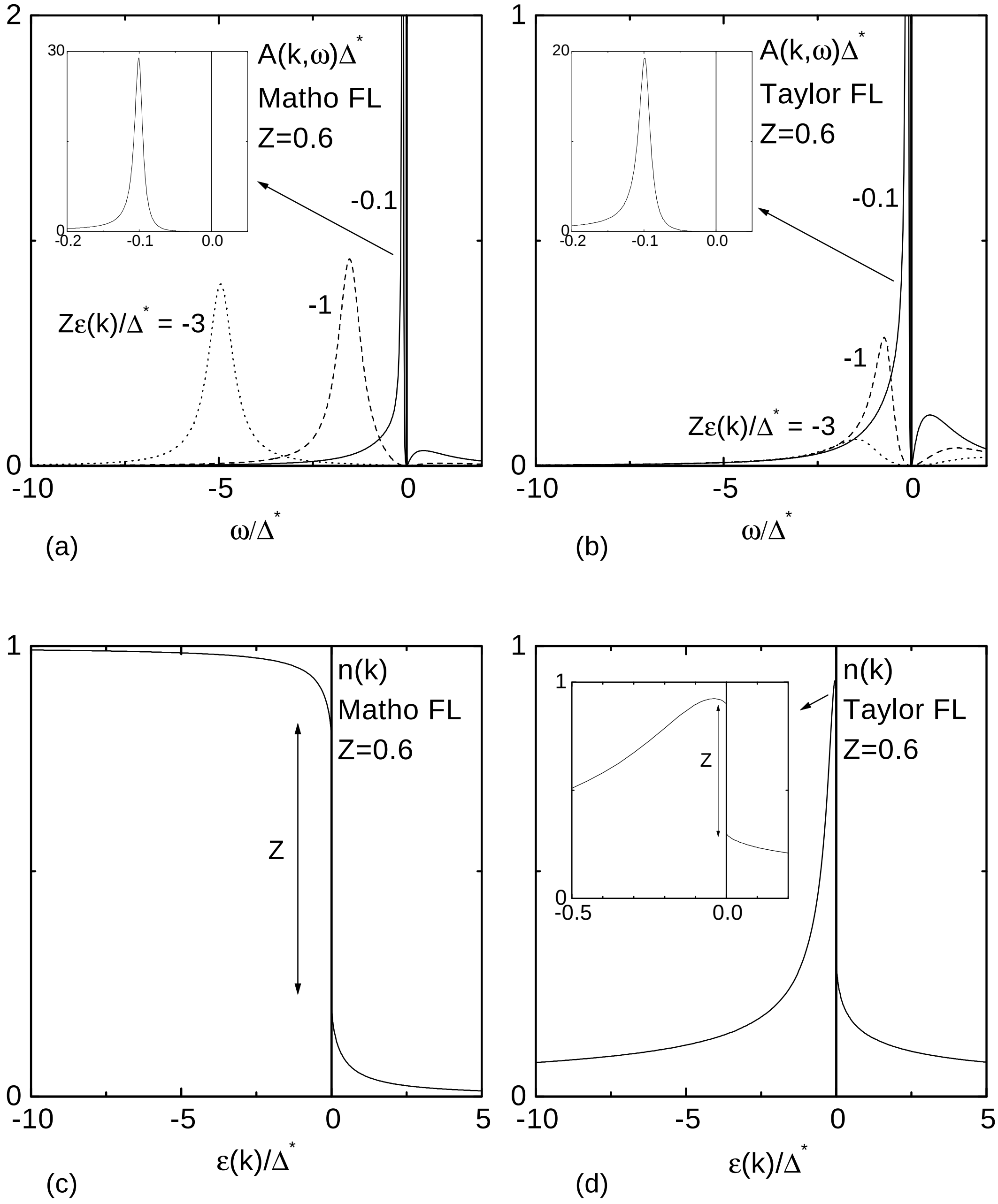

Figure 2.3: Spectral-functions (a and b) and electron occupation numbers (c and d) for FL models. Insets show a detailed view of an expanded scale.

with higher order theory. The Green's function can be extended to the case where $\mathbf{k} \neq \mathbf{k}_F$, e.g. by assuming a $\mathbf{k}$-independent self energy.

Fig.'s 2.2 and 2.3 show various quantities calculated within the Matho FL model. Also, we calculate the same quantities using the Taylor FL model of Eq. 2.14. In the Matho FL model, we used $\mathrm{Im}\Omega_b = 0$ which gives an electron-hole symmetric model and $Q = 1$. Fig. 2.2 (a) and (b) show self energies. The imaginary part of the self energy of the Matho FL model is an inverted Lorentzian shape, behaving quadratically near $\omega = 0$ and approaching constant as $\omega \to \infty$. The real part behaves linearly near $\omega = 0$ and falls off as $1/\omega$ as $\omega \to \infty$. The self energy for the Taylor model is quadratic in the imaginary part and linear in the real part. Therefore, in contrast to the Matho FL self energy, the Taylor FL self energy does not satisfy the general property that the self energy must decay faster than ω as $\omega \to \infty$. Fig. 2.2 (c) and (d) show the positions of the poles of the Green's function. The poles in the Matho FL model appear in the upper half plane. In contrast, the poles in the Taylor FL model appear in the upper and lower half planes, making the model analytically incorrect. Note also that for the $\epsilon(\mathbf{k})$ value different from 0, the real parts of the two poles of the Matho FL model have the same sign, while those of the Taylor FL model have opposite signs. Additionally, one pole for the Matho FL model bends back as $|\epsilon(\mathbf{k})|$ value increases and stays close to the $\mathrm{Im}(\omega)$ axis indefinitely. These two aspects are important in the lineshape study of Chapter 3. Fig. 2.3 (a) and (b) show spectral functions. For small values of $|\epsilon(\mathbf{k})|$ the lineshapes dominated by quasi-particle peak are rather similar for the two models, as shown in the insets. For a large value of $|\epsilon(\mathbf{k})|$, it can be shown that the spectral function for a large value of $|\epsilon(\mathbf{k})|$ has the center of mass at $\epsilon(\mathbf{k})$. This property is demonstrated well by the Matho FL spectral function for $Z\epsilon(\mathbf{k})/\Delta^* = -3$, i.e. $\epsilon(\mathbf{k})/\Delta^* = -5$, showing a symmetric peak centered at $\omega/\Delta^* = -5$. In contrast this property is poorly satisfied by the equivalent spectral function of the Taylor FL model. Fig. 2.3 (c) and (d) show the electron occupation numbers for the two models. Both of them show a step of height Z at the FS ($\epsilon(\mathbf{k}) = 0$). The origin of this step is the quasi-particle peak that passes through the chemical potential as the $\epsilon(\mathbf{k})$ value changes from -0 to $+0$. For large negative values of $\epsilon(\mathbf{k})$, $n(\mathbf{k})$ for the Matho FL model nicely approaches 1, while that for the Taylor FL model is abnormally small. It can be shown that the origin of this problematic behavior is the breakdown of the sum rule of Eq. 2.8 in the Taylor FL model. Overall, the Taylor FL model shows many pathological behaviors, which are nicely fixed by the Matho FL model.

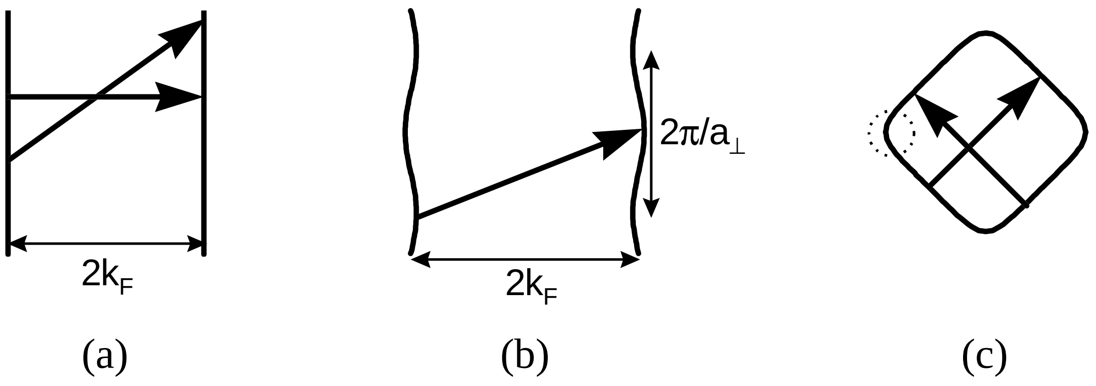

Figure 2.4: Examples of nesting FS's. For illustration a two spatial dimensional world is considered. (a) A 1 dimensional FS which is nested by an infinite number of vectors $(2k_F, x)$ for any value of x. (b) A small amount of modulation picks out the unique nesting vector $(2k_F, \frac{\pi}{a_\perp})$, where $a_\perp$ is the unit cell distance along the easy conducting direction. (c) A fully 2-dimensional FS with alternative partial nesting vectors. The states at corners are never nested in any case.

2.3 Charge density wave

Peierls [36] considered a system of independent electrons in one dimension and argued that there cannot be any metallic state at $T = 0$. He reasoned that any amount of electron-phonon interaction will gap the one dimensional FS, in much the same way as Bragg scattering gaps the electron bands at the zone boundaries. The new state is called a charge density wave (CDW) state. A similar argument was also made by Frölich [37].

At the heart of the CDW phenomenon is the Lindhard electric susceptibility [2],

$$\chi_L(\mathbf{q}, T) = \sum_{\mathbf{k}} \frac{f(\mathbf{k}) - f(\mathbf{k}+\mathbf{q})}{\epsilon(\mathbf{k}) - \epsilon(\mathbf{k}+\mathbf{q})}, \tag{2.19}$$

where $f(\mathbf{k})$ is the Fermi-Dirac distribution function and $\epsilon(\mathbf{k})$ is one electron band energy. χ_L gives the electron density modulation, $\delta\rho(\mathbf{q})$, due to an electro-static perturbation $V(\mathbf{q})$

$$\delta\rho(\mathbf{q}) = \chi_L(\mathbf{q})V(\mathbf{q}).$$

Under certain circumstances $\chi_L(\mathbf{q}, T \to 0)$ diverges at a certain wave-vector. A common example is when the FS has a "nesting" property, i.e. when part of the FS is related to another part of the FS by a constant wave-vector. Typical examples are shown in Fig. 2.4. Another possibility [38] for a diverging Lindhard susceptibility is to have a diverging density of states (van-Hove singularity) at two **k** points connected by q_{CDW}, a mechanism which was recently supported by ARPES [39]. In this thesis, we are concerned only with the nesting mechanism.

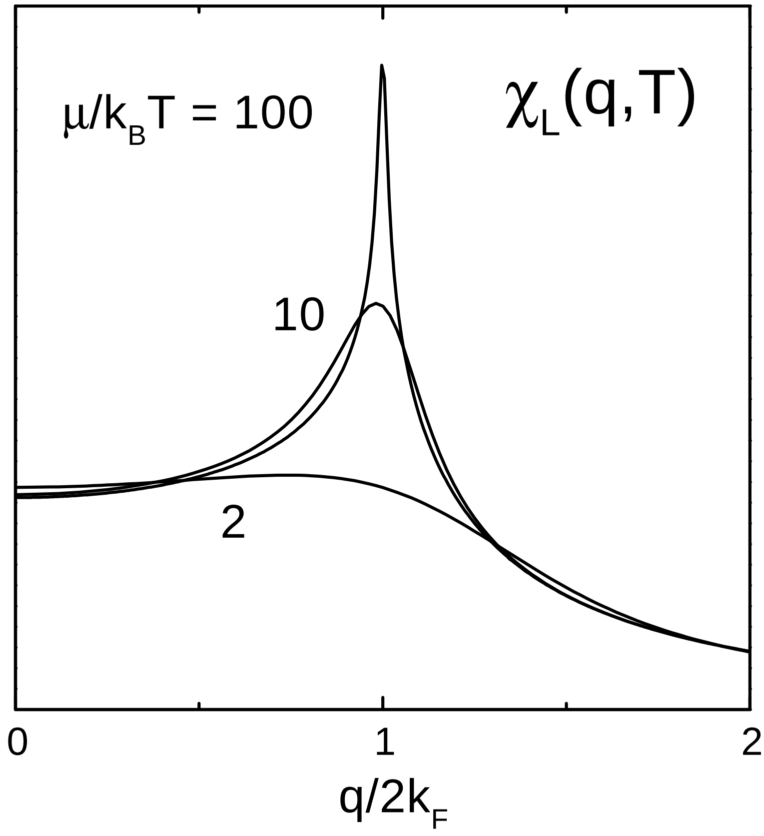

Figure 2.5: Lindhard susceptibility of one dimensional free electron gas as a function of temperature. Taken from Ref. [40].

The physics of the CDW transition can be summarized as follows. Let us assume that at $\mathbf{q} = \mathbf{q}_{CDW}$ and $T = 0$ χ_L diverges. At finite temperature, thermal broadening weakens the divergence but χ_L is still large for low T (Fig. 2.5). A large χ_L means that electrons can easily form the $\mathbf{q}_{CDW}$ density wave, either by the electron-phonon interaction or the electron-electron interaction. From the viewpoint of the lattice, this means that the lattice oscillation with $\mathbf{q} = \mathbf{q}_{CDW}$ is made easier because easy formation of electron density waves means good screening of lattice oscillations by electrons. As T is lowered, the screening by electrons becomes more and more effective, and therefore the phonon frequency at $\mathbf{q}_{CDW}$ becomes less and less (phonon softening). When the phonon frequency goes to 0, the crystal "freezes" into a new periodicity $\mathbf{q}_{CDW}$ (Peierls distortion) and a CDW phase transition occurs.

From the standpoint of electron spectroscopy, the electronic structure under the influence of the CDW is particularly interesting. The canonical Hamiltonian to describe CDW physics is the Frölich Hamiltonian [37],

$$H = \sum_k \epsilon(k)\, a_k^\dagger a_k + \sum_q \hbar\omega_q\, b_q^\dagger b_q + \sum_{k,q} g_q\, a_{k+q}^\dagger a_k (b_{-q}^\dagger + b_q),$$

where $\epsilon(k)$ is the one electron band energy, $a_k^\dagger(a_k)$ is the electron creation (annihilation) operator, ω_q is the phonon dispersion relation, $b_q^\dagger(b_q)$ is the phonon creation (annihilation) operator, and g_q is the electron-phonon interaction strength.

The mean-field theory solution for the Frölich Hamiltonian is obtained by decoupling the electron and phonon degrees of freedom. The electronic part of the Hamiltonian is given by

$$H = \sum_k \epsilon(k)\, a_k^\dagger a_k + \sum_{k,q} g_q\, a_{k+q}^\dagger a_k \langle b_{-q}^\dagger + b_q \rangle.$$

The expectation value, which is proportional to the permanent distortion of the lattice with wave-vector q, is zero for $q \neq q_{CDW}$. For $q = q_{CDW}$ it defines the order parameter of the CDW phase transition:

$$\Psi = g_{q_{CDW}} \langle b_{-q_{CDW}}^\dagger + b_{q_{CDW}} \rangle.$$

This order parameter is complex:

$$\Psi = \Delta\ \exp(i\,\phi).$$

For an incommensurate CDW, for which q_{CDW} is incommensurate with undistorted lattice periodicity, the mean field Hamiltonian approximately describes two states coupled by $\pm q_{CDW}$ for each k. This problem is trivial to solve, and yields a new band dispersion relation (Fig. 2.6 (a)) given by:

$$E_k = \frac{\epsilon(k) + \epsilon(k \pm q_{CDW})}{2} \pm \frac{\sqrt{(\epsilon(k) - \epsilon(k \pm q_{CDW}))^2 + \Delta^2}}{2}.$$

The modification of the band energy can be thought of as arising from the self energy

$$\Sigma_{MF}(k,\omega) = \frac{\Delta^2}{\omega - \epsilon(k \pm q_{CDW}) - i0^+}. \tag{2.20}$$

The order parameter is of course temperature dependent. The temperature dependence can be calculated [40] in the weak coupling limit, and yields exactly the same form (Fig. 2.6 (b)) as the BCS gap of superconductivity. In particular, the same energy gap expression

$$2\Delta(0) = 3.52 k_B T_{MF} \tag{2.21}$$

holds. In addition, note that the self energy of Eq. 2.20 is also the same form as the BCS self energy. The temperature dependent spectral function, $A(\mathbf{k},\omega)$, is shown in Fig.'s 2.6 (c) and (d).

Although this simple mean field theory provides a qualitative picture for a CDW transition, in reality it does not work well, because of the strong thermal fluctuation

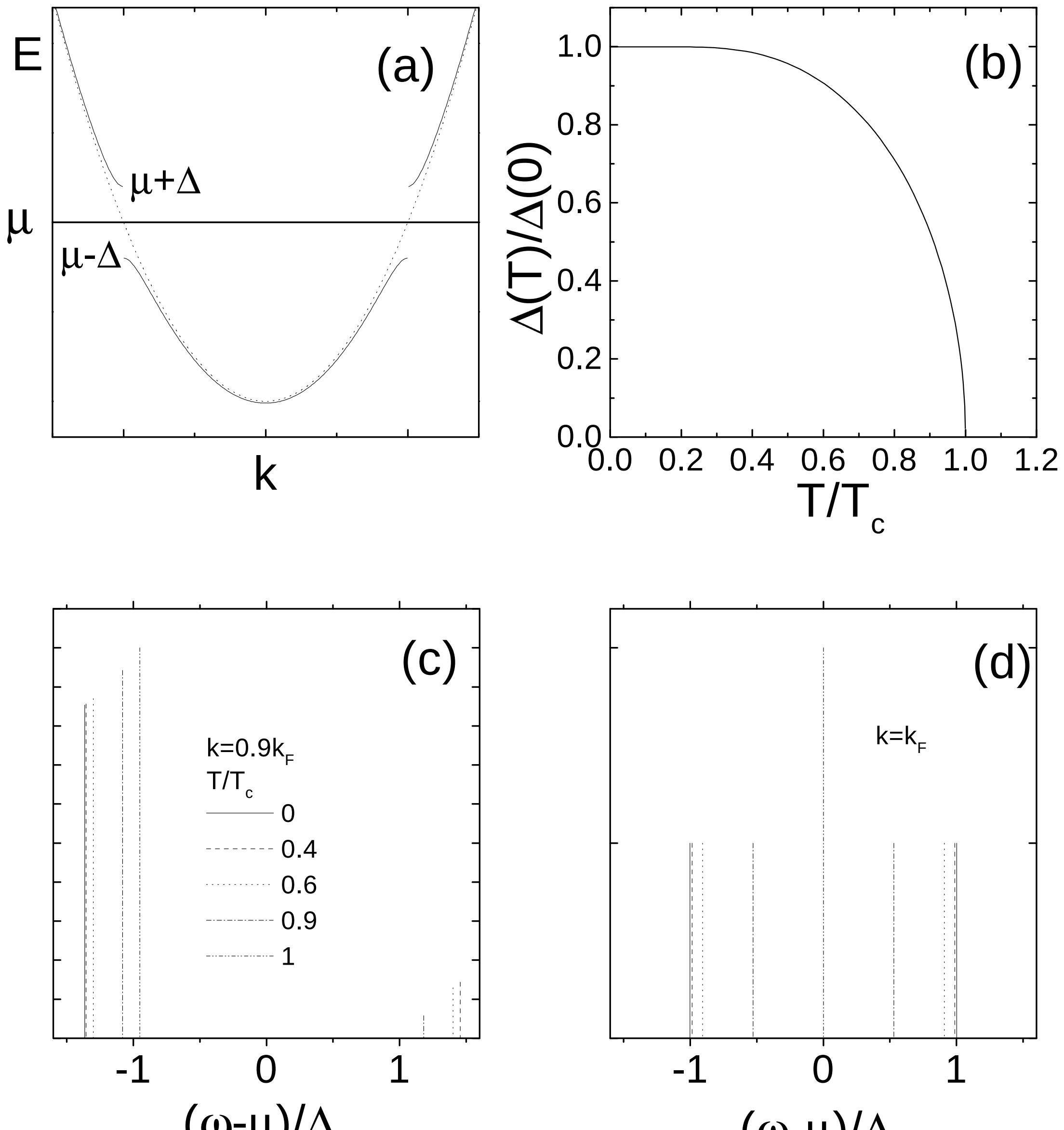

Figure 2.6: Mean field theory solution for the Frölich Hamiltonian. To demonstration the essential features of an incommensurate CDW, non-interacting band is taken to be a free electron band. (a) Gap opening in the energy dispersion. (b) Temperature dependence of the energy gap parameter Δ, calculated in the weak coupling limit. (c) Temperature-dependent spectral function $A(\boldsymbol{k},\omega)$ for $k = 0.9\,k_F$. (d) Same as (c), but for $k = k_F$. The vertical bars in (c) and (d) depict delta functions whose strengths are proportional to the bar heights.

effect in 1D. For example, the ratio of the transition temperature and the 2Δ gap often exceeds 3.52 greatly. This is because the transition is delayed as T is lowered through T_{MF}. It is well-known that thermal fluctuations prevent long range order in 1D [41, 42]. Breaking up long range order into many short range orders is always preferable in 1D because the entropy increase always over-compensates the energy increase. For example, the correlation length calculated for a Landau-Ginzburg theory of the CDW [43] remains finite at any finite temperature. However, real materials are seldom strictly one dimensional. There are weak but finite 3D couplings, an interchain hopping or a Coulomb interaction. As a result, phase transitions do occur for quasi-1D systems and they have full 3D character. A qualitative picture of the phase transition in a quasi-1D system can be described [40] in terms of the intrachain correlation length $\xi_{||}$ and the interchain correlation length $\xi_{\perp}$. As T_{MF} is approached from above, one dimensional fluctuations develop in each chain. They cannot form long range order, so $\xi_{||}$ is finite. For sufficiently weak interchain coupling, $\xi_{\perp}$ is negligible. As T is lowered, both correlation lengths increase, and $\xi_{\perp}$ becomes on the order of the interchain distance at a 1D to 3D crossover temperature $T^* < T_{MF}$. At transition temperature $T_c < T^*$, the system develops full 3D order, and $\xi_{||}$ and $\xi_{\perp}$ both become infinite.

Several authors have studied the CDW fluctuation problem theoretically. Lee, Rice and Anderson [44] applied 2nd order perturbation theory to obtain the Green's function in the presence of fluctuations. Their self energy is

$$\Sigma_{LRA}(k,\omega) = \frac{\psi(T)^2}{\omega - \epsilon(k \pm q_{CDW}) - i v_F/\xi(T)}, \tag{2.22}$$

where $\psi(T)^2$ is the mean-square fluctuation of the order parameter and $\xi(T)$ is the correlation length of the fluctuation. Comparing $\Sigma_{LRA}(k,\omega)$ with $\Sigma_{MF}(k,\omega)$, one finds that $\Sigma_{LRA}(k,\omega)$ has the same form if $\psi(T)^2$ is identified with Δ^2, except that the Lorentzian self energy has a finite width $v_F/\xi(T)$ for finite $\xi(T)$. It should be noted that this theory is still strictly 1 dimensional, and therefore, the correlation length $\xi(T)$ remains finite for any finite temperature, as in the work of Scalapino, Sears and Ferrel [43]. However, for a real order parameter, the thermal fluctuations require a finite amount of energy, and the correlation length becomes exponentially large at low temperature. Using this result, Lee, Rice and Anderson identified a phase transition at $\sim T_{MF}/4$. It is noteworthy that in general the CDW order parameter is *not* real, but complex. One way of characterizing this work is that it concerns amplitude fluctuation only, while neglecting phase fluctuations.

Rice and Strässler [45] studied CDW fluctuations *and* 3 dimensional coupling. Their

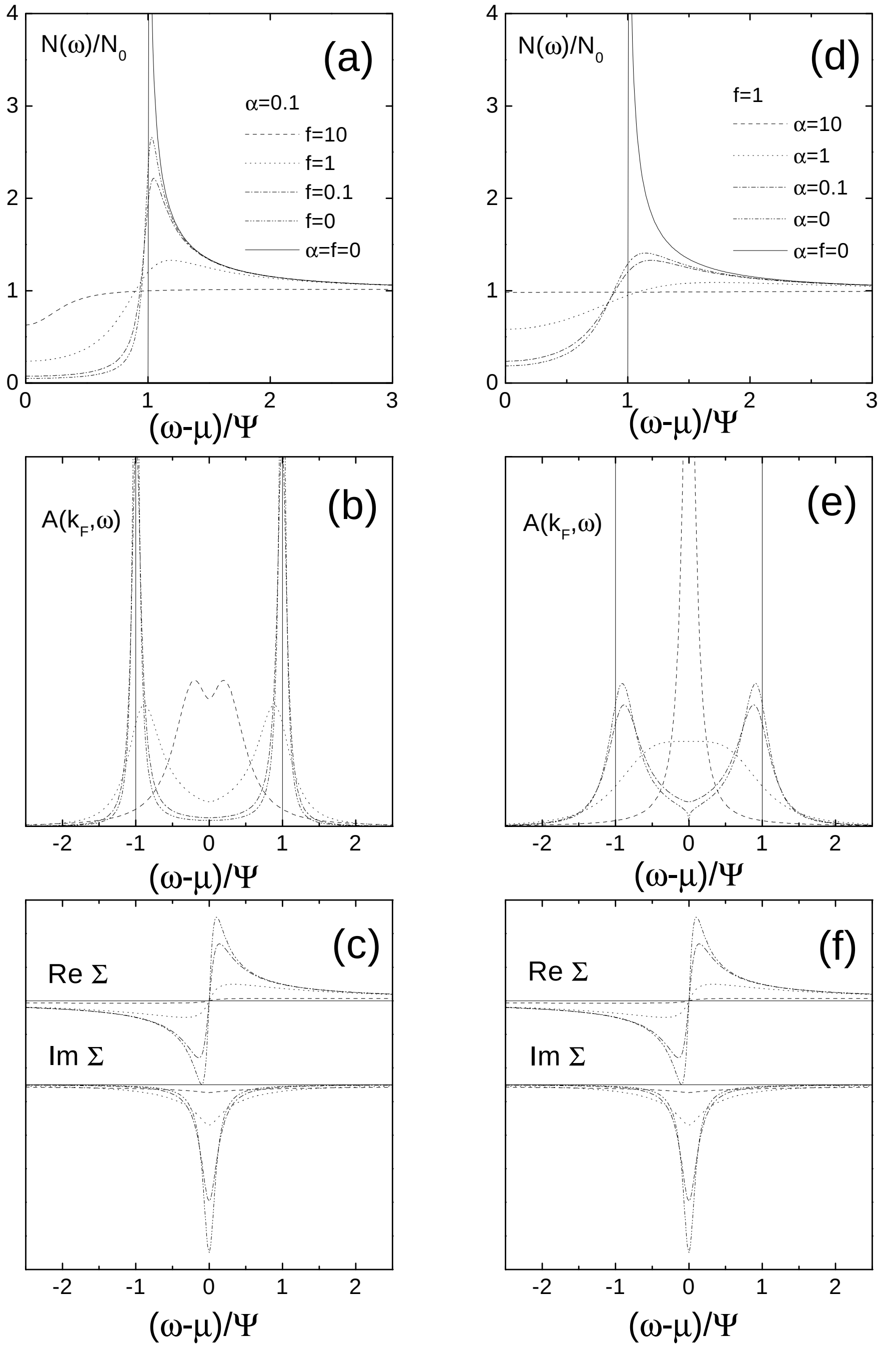

Figure 2.7: CDW pseudogap spectral function following the theory of Rice and Strässler [45]. (a) Density of states relative to the non-interacting density of states N_0, for $\alpha = 0.1$ and varying f. (b) $\boldsymbol{k}$-resolved spectral function at $\boldsymbol{k}_F$. (c) Real and imaginary parts of the self energy. (d),(e) and (f) are exactly the same as (a), (b) and (c) respectively, except that now $f = 1$ and α is varying. α is proportional to inverse correlation length and thus is a measure of the proximity to the phase transition. Bigger f means more 3 dimensionality.

results can be summarized by the self energy,

$$\Sigma_{RS}(\mathbf{k},\omega) = \frac{\psi(T)}{i\,f(T)}\,\log\left(1 + \frac{i\,f(T)\psi(T)}{\omega - \epsilon(\mathbf{k} \pm \mathbf{q}_{CDW}) - i\,\alpha(T)\psi(T)}\right), \tag{2.23}$$

where

$$\alpha(T) = v_F/(\xi(T)\psi(T)). \tag{2.24}$$

The new parameter $f(T)$ represents 3 dimensional coupling. As $f \to 0$, this self energy reduces to $\Sigma_{LRA}(\mathbf{k},\omega)$. The 3 dimensional transition temperature is given in this theory by

$$T_c = 0.26 f(T_c)^{1/3} T_{MF}. \tag{2.25}$$

For a typical value of order 1 for f, this equation gives $T_c \ll T_{MF}$, as qualitatively discussed above. At T_c, the correlation length $\xi(T)$ becomes infinite, and therefore, $\alpha(T) \to 0$. The spectral lineshapes and the self energies are shown in Fig. 2.7. Note that the real part of the self energy shows a positive slope at $\omega = \epsilon(\mathbf{k})$, in contrast to the the negative slope for a Fermi liquid (Fig. 2.2). Thus this system exhibits NFL behavior.

Sadovskii [46] considered a model in which the electron phonon interaction term in the Frölich Hamiltonian is modeled as a Gaussian random field, $\Psi(x)$ with correlation

$$\langle \Psi(x)\,\Psi(x')\rangle = \psi^2 \exp(-|x - x'|\xi^{-1})\,\cos(2k_F(x - x')).$$

The solution of Lee, Rice and Anderson follows exactly from the 2nd order perturbation theory of this model. Furthermore, Sadovskii showed that this model is exactly solvable and gave the solution in continued fraction form. McKenzie [47] noted that the solutions of this model contain many interesting properties, such as a pseudogap and non-FL behavior in the real part of the self energy, i.e. the positive slope. These features are actually already present in Rice and Strässler results (Fig. 2.7), although the origins are quite different. Relative to the theory of Lee, Rice and Anderson, the theory of Rice and Strässler represents inclusion of 3 D coupling, while the theory of Sadovskii represents an exact treatment of the fluctuation potential. It is quite interesting that the two results give apparently similar self energies and spectral functions. From a practical point of view, the theory of Rice and Strässler is more convenient to comparing to experiment because its solution is in a simpler form. Furthermore, it was recently claimed [48] that the solution of Sadovskii is flawed.

Finally, it is noted that the fluctuation theories outlined above apply to near the transition, where the expectation value of the order parameter is 0. The theory of fluctuations at low temperature, far away from the critical region, was also studied [49].

The result is interesting. Due to thermal fluctuations and zero point motion of the lattice the mean field theory gap is smeared out. That is, the density of states shows an intensity tail within the mean field gap region, extending all the way to E_F.

2.4 Luttinger liquid

In the previous section, we have left out the electron-electron interaction without any explanation. As a result, the system behaves as a collection of free electrons at temperatures well above the transition. What is implicitly assumed is not so much that electrons are literally free in the normal state, but rather that the normal state is described as a FL which is essentially like a free electron gas. An important question nowadays is "is there any normal state above the transition other than the FL?"

The answer is yes! The argument for a non-FL normal state is two-fold. First, it is noted [50] that FL theory is not in general provable. Only in the low density or weak interaction limit, can FL theory be proved rigorously. Second, theoretical studies show that many non-FL normal states [51, 52] do exist. In particular, in 1 dimension any amount of electron electron interaction gives rise to a LL, a term coined by Haldane [51] to designate a universality class of 1 dimensional systems which are characterized by gapless bosons. The fixed point Hamiltonian for the LL is the Tomonaga Luttinger (TL) model [53] just as that for the FL is the Fermi gas model. We now review some key features of the TL model in this section.

Before, delving into the TL model, it is helpful to get some hint of what is so special about 1 dimension. For this purpose, let us consider the energy diagram for general excitations of the free electron system, as Haldane does [51]. As shown in Fig. 2.8 (b), the one particle-hole excitation spectrum has a gap for momentum $q \neq 0, 2k_F$. The many particle-hole excitation diagram is similarly obtained as in Fig. 2.8 (c), where the low energy excitations near $2k_F n$ ($n =$integer) are bounded by two curves which can be approximated as two lines $\pm v_F(q - 2k_F n)$ at low energies. This diagram is more general than it might seem because an excitation diagram for a state with a net electron added to the system, for example, is simply obtained by shifting this diagram by k_F along the momentum axis. The low energy excitation diagram at each point $\pm v_F(q - k_F m)$ ($m =$ integer) is reminiscent of the low energy diagram of bosons with dispersion relation $v_F q$, hinting at a possible bosonic description of the free electron system in 1 dimension. As we will discuss shortly, this is actually correct, and by close inspection of the energy diagrams in Fig. 2.8 (c) and the energy diagram with odd number of added electrons one can write down the Hamiltonian for this system as follows,

$$H = v_F \sum_q |q| b_q^\dagger b_q + \frac{1}{2}\frac{\pi}{L}[v_F(\Delta N)^2 + v_F J^2], \tag{2.26}$$

where $q = 2\pi n/L$, $n = \pm 1, \pm 2, \dots$, ΔN and J are integers with the selection rule $(-1)^J = -(-1)^{\Delta N}$. Here ΔN is the change of the total number of electrons, and J is the difference between the number of the right moving electrons and that of the left moving ones. b_q and $b_q^\dagger$ are standard boson operators, whose details cannot be known just by the inspection of Fig. 2.8.

The bosonization [54, 55] of fermion operators in 1 dimension, as just described, is possible due to the following important, and highly nontrivial, property. In 1 dimension any electron-hole excitation near the FS can be described in terms of charge/spin density wave bosons. In other words, any state of the form $a_{k_2}^\dagger a_{k_1}|N\rangle_0$, where $|N\rangle_0$ is Fermi sea, can be expressed as $f(b_q^\dagger)|N\rangle_0$ where $b_q^\dagger$ is an operator $\propto \sum_k a_{k+q}^\dagger a_k$, and f is some function. Here, spin indices ($\pm 1/2$) in the summand $a_{k+q}^\dagger a_k$ are suppressed, but they are implied to be parallel for charge density and anti-parallel for spin density. It is not difficult to see that repeated application of $b_q^\dagger$ on $|N\rangle_0$ can give *some* $a_{k_2}^\dagger a_{k_1}|N\rangle_0$ state, but what is nontrivial is that one can generate *all* such states. This property leads immediately to the result that any *fermionic* excitation can be expressed by density wave bosons. For example, consider an electron with momentum k added to an N particle state. Relative to the $N+1$ particle Fermi sea $|N+1\rangle_0$, the resulting state can be described totally in terms of electron-hole excitations, which by the property stated above can be described fully in density wave bosons. It is stressed [55] that this bosonization holds regardless of Hamiltonian and one electron band dispersion $\epsilon(k)$, as long as $\epsilon(k)$ defines the FS.

Now we give the definition of the TL model. The TL model is defined as a one dimensional electron system with one electron band linearized at k_F and extended to $-\infty$ energy and with forward scattering electron-electron interactions. These conditions imposed on the model make it possible to solve this model exactly, as we will describe in the next 2 paragraphs. The point is that these conditions modify only the high energy scale physics of a particular physical system and therefore the TL model is well-suited for describing low energy processes. The form of the one electron energy band and its excitation energy diagram are shown in Fig. 2.9.

The density wave operators within the TL model are defined as

$$b_{q,r}^\dagger = \frac{i}{\sqrt{n_q}} \sum_{k=-\infty}^{\infty} a_{k+q,r}^\dagger a_{k,r},$$

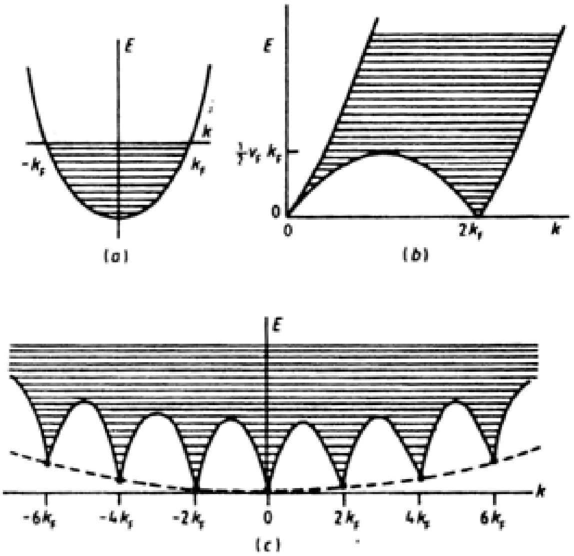

Figure 2.8: Excitation energies of a 1 dimensional free electron band. (a) Dispersion relation. (b) Single particle hole energy continuum. (c) Multiple particle hole energy continuum.

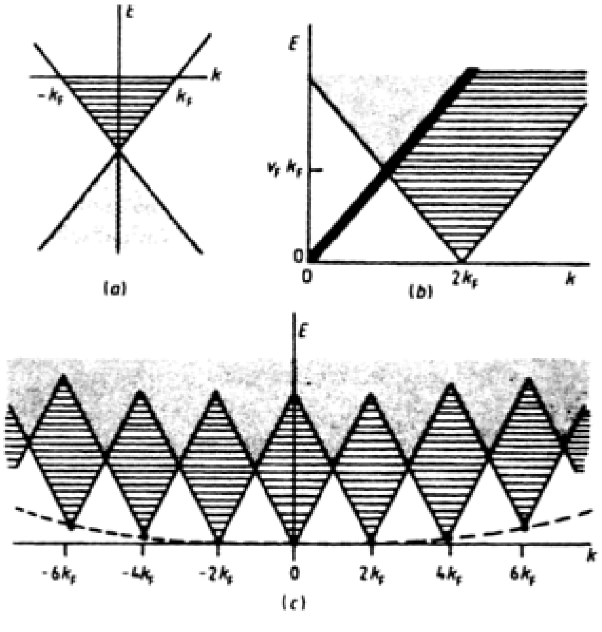

Figure 2.9: Excitation energies of a 1 dimensional Tomonaga-Luttinger electron band. (a) Dispersion relation. (b) Single particle hole energy continuum. (c) Multiple particle hole energy continuum.

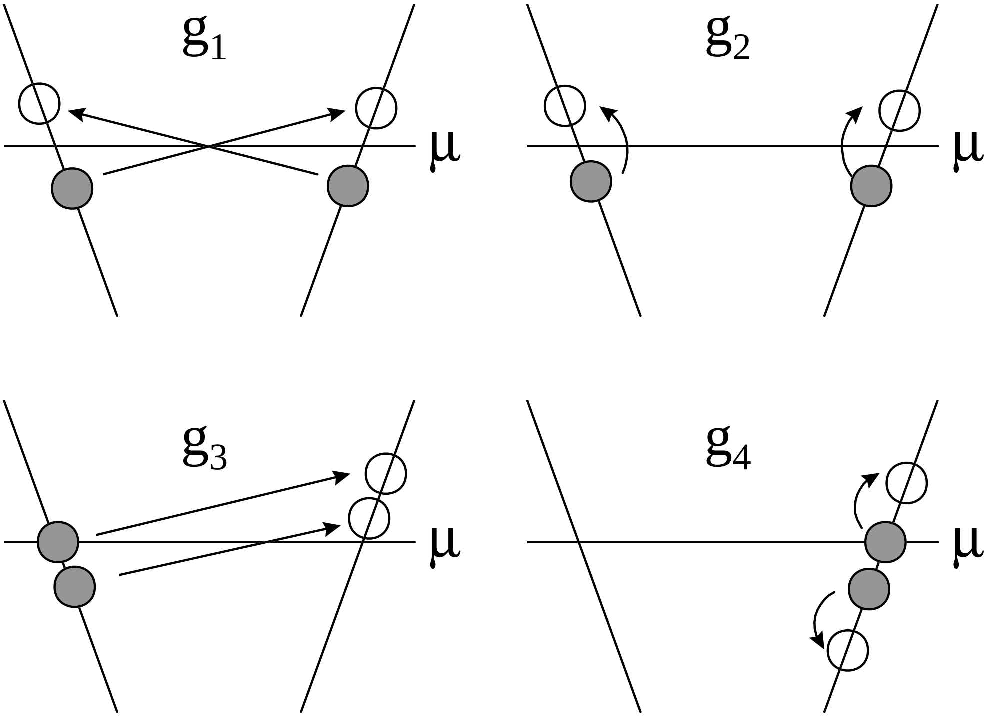

Figure 2.10: Electron electron interactions in 1 dimension (g-ology).

where $q = \frac{2\pi}{L} n_q$, $n_q > 0$, $L = \text{system length}$, and spin is ignored for the time being. Here the one electron band is divided into two branches, left-movers ($r = -1$) and right-movers ($r = 1$), and k stands for the magnitude of the momentum. The extension of the one electron band to $-\infty$ makes the following standard bosonic commutation rules become exact.

$$\left[b_q, b_{q'}^\dagger\right] = \delta_{q,q'}, \; [b_q, b_{q'}] = \left[b_q^\dagger, b_{q'}^\dagger\right] = 0.$$

In the so-called "g-ology", the general low-energy electron-electron interactions in 1 dimension are classified into 4 types as pictured in Fig. 2.10. The interactions are g_1: $2k_F$ back scattering, g_2: inter-branch forward scattering, g_3: Umklapp scattering, and g_4: intra-branch forward scattering. The Umklapp term is important only for special band fillings such as half filling. In the TL model, only the forward scatterings (g_2 and g_4) are kept. These terms have a simple property that they can be expressed as a quadratic form of density wave operators. So the TL Hamiltonian reads

$$H = v_F \sum_{k,b} |k| a_{k,r}^\dagger a_{k,r} + \sum_{q,r} g_2 b_{q,r}^\dagger b_{-q,-r} + \sum_{q,r} g_4 b_{q,r}^\dagger b_{-q,r}, \tag{2.27}$$

where $r = \pm 1$ is the branch index as before. Due to the linear dispersion, the first term of the Hamiltonian, which we call H_0, has a simple commutation relation,

$$[H_0, b_q] = v_F |q| \, b_q.$$

This suggests that $H_0 = \sum_q v_F |q| b_q^\dagger b_q + h$, where h is a term that commutes with all b_q. By the completeness of the b_q's, h must be a function of global quantum numbers ΔN and J. In fact, H_0 becomes exactly the same form as Eq. 2.26. The bilinear forms of the density operators are trivially diagonalized to give the TL Hamiltonian in a compact form:

$$H = v_b \sum_q |q| b_q^\dagger b_q + \frac{1}{2}\frac{\pi}{L}[v_N(\Delta N)^2 + v_J J^2], \tag{2.28}$$

where

$$v_N = v_b/K, \quad v_J = v_b K.$$

In other words, the TL model is an exactly solvable interacting electron model! Note that two interaction parameters g_2 and g_4 have renormalized three velocities v_b, v_N and v_J, resulting in a constraint that $v_N\, v_J = v_b^2$. Instead of g_2 and g_4, two equivalent parameters can be introduced

$$\begin{aligned} \beta &= v_b/v_F, \\ K &= v_N/v_b = v_b/v_J. \end{aligned}$$

Now we discuss electron spin, which has been ignored so far. In the g-ology, the terms that involve spin excitations are those that pull out an electron and flip its spin before inserting it into some unoccupied orbital. When the spin dependent interaction giving rise to such term is spin reversal invariant, the spin and charge degrees of freedom decouple, because then there cannot be any interaction term involving a product of spin density and charge density. This is the phenomenon of spin and charge separation. The TL Hamiltonian then becomes a simple sum of spin and charge Hamiltonians, each of which is of the same form as Eq. 2.27. The system is then characterized by four parameters – LL parameters – K_c,β_c, K_s, β_s with obvious notation. The spin parameters are determined by spin-dependent interactions and the charge parameters by spin-independent interactions. Therefore the spin and the charge bosons propagate with different velocities v_s and v_c. In addition to the spin charge separation, another key characteristics of LL is the so-called anomalous dimension, α, which is defined by

$$\begin{aligned} \alpha &= \alpha_c + \alpha_s \\ &= \frac{1}{4}(K_c + K_s + K_c^{-1} + K_s^{-1} - 4). \end{aligned}$$

Before discussing the meaning of α, a few special cases of electron-electron interaction are worth noting in relation to the LL parameters. First, if the interaction is spin rotation invariant (SU(2)), then $K_s = 1$. This is the case for the Hubbard model for example. Second, if the interaction is spin independent, then $K_s = \beta_s = 1$. Third, if $g_2 = g_4$, as would happen for a screened Coulomb interaction, then $K_s = \beta_s = 1$ and $K_c = \beta_c$, resulting in the following simple connection between α and β_c:

$$\alpha = \frac{1}{4}(\beta_c + \beta_c^{-1} - 2). \tag{2.29}$$

Now we discuss the meaning of α. The name "anomalous dimension" means that it enters into a scaling dimension which is different from physical dimension, e.g. for the Green's function,

$$G(\lambda\widetilde{k}, \lambda\omega) = \frac{1}{\lambda^{\alpha-1}} G(\widetilde{k}, \omega), \tag{2.30}$$

for small $\widetilde{k} = k - k_F$ and ω. By taking $\lambda = 1/\omega$, one obtains

$$G(\widetilde{k}, \omega) = \omega^{\alpha-1} f(\widetilde{k}/\omega).$$

Using Eq. 2.4, we have

$$A(\widetilde{k}, \omega) = \omega^{\alpha-1} g(\widetilde{k}/\omega). \tag{2.31}$$

Integrating this in $\widetilde{k}$ leads to the low energy behavior of the density of states,

$$N(\omega) \propto \omega^{\alpha}. \tag{2.32}$$

Therefore, density of states vanishes as ω approaches the chemical potential! The meaning of this is the absence of a quasi-particle ($Z = 0$), because if there were quasi-particles, then there would be delta function peaks dispersing near the chemical potential which would give rise to a finite density of states at the chemical potential. The absence of quasi-particles also means that $n(k)$ no longer has a finite step at the FS in contrast to that of the FL (Fig. 2.3 (c) and (d)). Instead, the leading singularity of $n(k)$ is given by

$$n(k) \propto |k - k_F|^{\alpha}. \tag{2.33}$$

This power law behavior can be obtained by inserting $\lambda = 1/\widetilde{k}$ in Eq. 2.30 and integrating over ω.

In Anderson's theory of high temperature superconductivity [50], the anomalous dimension α plays a crucial role. In his viewpoint, non-zero α arises from finite scattering phase shifts at k_F. In much the same way as in the Anderson orthogonality catastrophe problem [56] of X-ray absorption, the finite phase shifts mean that the overlap

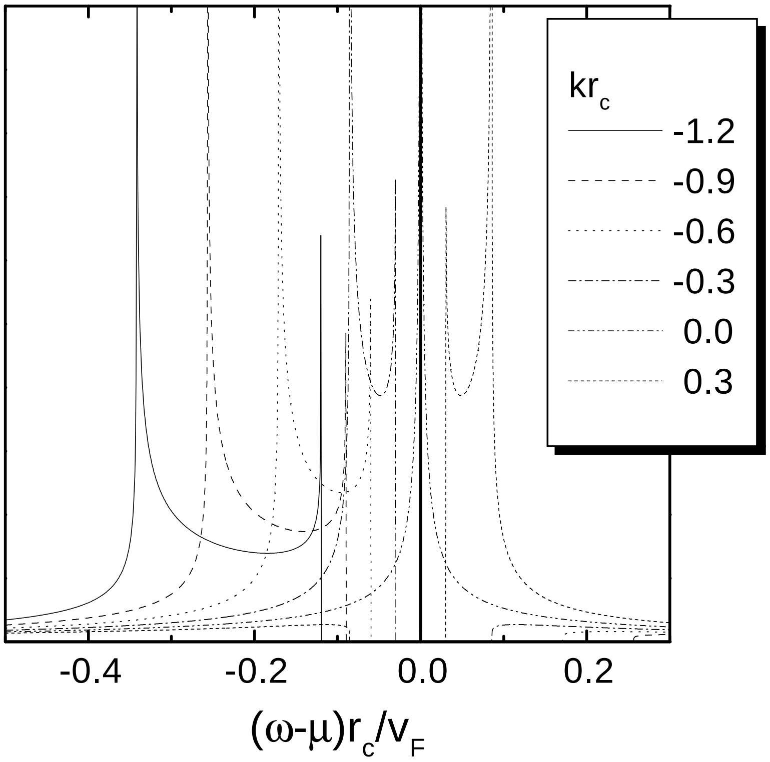

Figure 2.11: Spectral functions for spin-independent repulsive TL model.

between the many body wave functions before and after interactions are turned on is 0. This overlap is precisely the Z factor of FL theory. Anderson further notes that forward scatterings (and Cooper pair scatterings) are always the most important in any dimension and in particular it is singularly important [57] for a 2D Hubbard model which he argues to be a LL system and on which he bases his theory of high temperature superconductivity.

Fig. 2.11 shows spectral functions of the TL model [58, 59]. The integral of Eq. 45 in Ref. [58] is calculated to give these curves. Here the parameter r_c is the screening length of the two body potential [60], and defines the energy scale v_F/r_c over which the low energy LL behavior [58, 61], as described here, is valid. Differences of the TL lineshapes from FL lineshapes are obvious. First, there are two peaks dispersing instead of one peak[8], with different velocities. This is the phenomenon of spin and charge separation. Second, the peaks show power law divergences instead of the delta function singularity or Lorentzian lineshape of the Fermi liquid. There are three singularities:

$$(\omega - v_s\widetilde{k})^{\alpha_s/2+\alpha_c-1/2},\ (\omega - v_c\widetilde{k})^{\alpha_s+\alpha_c/2-1/2},\ (\omega + v_c\widetilde{k})^{\alpha_s/2+\alpha_c}. \tag{2.34}$$

---

[8] In the Matho Fermi liquid lineshape also, a two-peak structure can be observed for a particular parameter set (Section. 3.3). But this is not the underlying generic character of the FL model.

Here $v_s = v_F$ and $\alpha_s = 0$, due to the spin independent interaction assumed for Fig. 2.11. However, these expressions are valid even for spin dependent interaction. When the interaction is spin dependent, there is an additional singularity which is like that of the third term but with the roles of the spin and the charge exchanged. Third, there is a gap between $\omega = v_s\widetilde{k}$ and $\omega = -v_c\widetilde{k}$.

Some of these features – the positions of the singularities and the gap – can be qualitatively understood from simple kinematic considerations. This can be illustrated by considering the spectral function for the right moving ($r = 1$) branch, and positive $\widetilde{k}$. First, let us consider adding an electron and no inter-branch coupling ($g_2 = 0$). By bosonization, the ground state is a state that is annihilated by spin or charge density excitations, which we may call spinons and holons. To add an electron at $\widetilde{k}$ and ω is therefore to add an electron at $k = k_F$ and $\omega = \mu$ and add spinons and holons. The total momentum of the spinons and holons must be $\widetilde{k}$ and the total energy must be ω. From the linear dispersions of spinons and holons, it is easily seen that for given $\widetilde{k}$ the minimum energy cost is $v_s\widetilde{k}$, and the maximum energy cost is $v_c\widetilde{k}$ ($v_c > v_s$ is assumed). These two are the singularity positions for $g_2 = 0$, whose singularity indices are given as above and the spectral function is confined within $v_s\widetilde{k}$ and $v_c\widetilde{k}$. A special property of $g_2 = 0$ model is that $\alpha_c = \alpha_s = 0$ so that the two singularity indices are -1/2. Now, if g_2 is allowed to be finite, $a^\dagger_{k,r}$ is still bosonized by $b^\dagger_{\widetilde{k},r}$, but the boson operator that diagonalizes the Hamiltonian is $Ab^\dagger_{\widetilde{k},r} + Bb^\dagger_{-\widetilde{k},-r}$, where $A \gg B$ for weak interaction. Therefore, the ground state is now annihilated by $Ab_{\widetilde{k},r} + Bb_{-\widetilde{k},-r}$, not by $b_{\widetilde{k},r}$. In other words, the ground state has a small amount of $b^\dagger_{\widetilde{k},r}$ bosons. This means that now one can *remove* some electrons with positive $\widetilde{k}$. There is still a minimum energy cost for this process, which is $\min(v_s, v_c)\widetilde{k}$. However, note that when the interaction is spin independent this minimum energy is always $v_c\widetilde{k}$, because in this case the spin boson has zero B, i.e. no inter-branch mixing occurs for spin bosons[9]. Therefore, the gap feature in the spectral function is explained.

Various thermodynamic and transport properties of the TL model are renormalized [62] relative to those of free electrons. The specific heat for 1D bosons is linear and is given by

$$C(T) = \frac{1}{2}\left(v_F/v_s + v_F/v_c\right)\gamma_0 T, \tag{2.35}$$

where γ_0 is the free electron value $2\pi k_B^2/(3v_F)$. The spin susceptibility and compress-

---

[9] Or in other words, no anomalous dimension in the spin channel.

ibility are renormalized as

$$\begin{aligned} \chi &= \frac{v_F}{v_{N,s}}\chi_0, & (2.36) \\ \kappa &= \frac{v_F}{v_{N,c}}\kappa_0. & (2.37) \end{aligned}$$

The conductivity $\sigma(\omega)$ is again given by a Drude peak, but, as might be guessed, v_F is replaced by $v_{J,c}$:

$$\sigma(\omega) = 2v_{J,c}\delta(\omega). \tag{2.38}$$

So far, the pure TL model has been considered. It is interesting to comment on the results for the 1D Hubbard model, another exactly solvable model. The Hubbard model is defined by two parameters characterizing a tight binding band: the one electron hopping matrix element t to the nearest neighbors and Coulomb interaction U for two electrons occupying the same site. The 1D Hubbard model is an example of the LL because even though the model does not literally satisfy the conditions of the TL model, e.g. it has g_1 as big as g_2 and g_4, its low energy behavior is known [63] to be mapped to the TL model. Due to the SU(2) symmetry in the spin space, $K_s = 1$, and the low energy physics of the 1D Hubbard model is governed by three LL parameters K_c, β_c and β_s. Using renormalization group theory, these quantities have been calculated [63] as a function of U. In the large U limit, $K_c \to 1/2$, $\beta_c \to O(1)$ and $\beta_s \to O(t/U)$. The limiting value of K_c means that α approaches its maximum value of 1/8 as $U \to \infty$. Another interesting property of the 1D Hubbard model is that the LL energy scale is given by $\sim t^2/U$ for large U, which vanishes as $U \to \infty$! It is calculated [64] that due to the vanishing of the LL energy scale the density of states diverges rather than vanishes as $\omega \to 0$.

So far, strictly 1D theories have been discussed. However, real materials are almost never strictly 1D, but only quasi-1D. Therefore, it is important to consider 1D chains [60, 65, 66] coupled by Coulomb interaction and interchain hopping. The results of Ref. [60] are particularly enlightening, which we discuss now. In this work, the starting point for the electron-electron interaction is the bare Coulomb interaction, and the screened Coulomb interaction, which is regular at $\mathbf{q} = 0$ and which is usually the starting point for a 1D LL theory, is *calculated* using the random phase approximation (RPA). The input parameters for the theory are a dimensionless coupling constant $g = e^2/(\pi\hbar v_F)$, interchain lattice spacing $a_\perp$ and interchain hopping matrix element $t_\perp$. When $t_\perp = 0$, the system of coupled chains behaves as a LL, and its parameters α and

r_c can be calculated from g and $a_\perp$. It is especially notable that the anomalous dimension α can be as large as 1 or more. This is an important result that shows a way to get α larger than the 1D Hubbard model upper bound of 1/8 as mentioned above. The screening length r_c can also be calculated by the theory. In the limit $g|\log(a_\perp/a_0)| \ll 1$, where a_0 is a decay length of one-electron wave function perpendicular to the chains, it is given by the Thomas-Fermi wave vector $\kappa = a_\perp^{-1}\sqrt{8\pi g}$. Even when $g|\log(a_\perp/a_0)|$ is not small κ gives a rough estimate of r_c. With a finite $t_\perp$, the system loses the LL character in low energy below the energy scale $t_\perp$ but above this energy scale remains to show the LL behavior – anomalous dimension and spin-charge separation.

Chapter 3

$TiTe_2$: Fermi liquid

The section 3.3 of this chapter essentially reproduces the $TiTe_2$ part of the journal article: "Fermi liquids and non-Fermi liquids – the view from photoemission", J.W. Allen, G.-H. Gweon, R. Claessen and K. Matho, J. Phys. Chem. Solids **56**, 1849 (1995).

The history of the study on $TiTe_2$ in this group may be helpful. In 1992, a post-doc in our group, R. Claessen took ARPES data on this material and analyzed Ti $3d$ ARPES band lineshape with the Taylor FL model lineshapes, as explained in the previous chapter. In reaction to the publication of this work, K. Matho soon pointed out that the Taylor FL model is not analytically correct over the entire energy range used and proposed a simple fix, which is the Matho FL model that I summarized in the previous chapter. After I joined the group, I was introduced to this problem, and I did lineshape fitting of the Ti $3d$ band with the new model. Also, I collaborated in taking more data on $TiTe_2$ with R. Claessen, who had by then taken a new position in Germany, to explore its complete band structure. The next project of R. Claessen on $TiTe_2$ in collaboration with us, was to write a paper discussing the many body characteristics of $TiTe_2$ spectra without heavily replying on lineshape fitting but only with a semi-quantitative analysis. During this collaboration, the importance of the existing set of temperature dependent data of the Ti $3d$ band was recognized with respect to determining an experimental $\mathbf{k}_F$ value. I then proposed to take a more complete set of data at room temperature and low temperature, and I did the proposed experiments in collaboration with C. Olson at the SRC.

In this chapter, I present ARPES lineshape studies of the Ti $3d$ band of $TiTe_2$. I report temperature dependent ARPES measurement on the Ti $3d$ band of $TiTe_2$. The room temperature data shows a peak dispersing to well above E_F before losing amplitude, a very non-intuitive and surprising phenomenon in ARPES. I argue that the origin of this phenomenon is the small Fermi velocity. I also show a detailed lineshape fit analysis using the Matho FL model. The lineshape fit is both a conceptual and practical improvement over the original Taylor FL model fit. However, the Fermi wave vector determined by these lineshape fits is in disagreement with that determined from this dispersing peak at room temperature. Currently, this discrepancy remains a problem. I discuss a modified lineshape fitting method and some new results.

3.1 Introduction

TiTe$_2$ is a layered compound which is a semi-metal due to a small energetic overlap of a set of nominally Te $5p$ bands and one orbitally non-degenerate Ti $3d$ band [67]. Its transport properties give no indication of any behavior lying outside of the FL framework [68, 69]. Previously (Fig. 1.6) a set of high resolution data was obtained by our group to show the Ti $3d$ band as it crosses E_F. Because this band is well isolated from other bands and because TiTe$_2$ is quasi-2 dimensional, the situation is very favorable for studying the ARPES lineshape as an ARPES paradigm of FL behavior. In addition, the spectra are exceptionally clean, almost entirely free of an inelastic background signal. The overall band structure of this material is now well understood [67] both theoretically and experimentally. There is good agreement between the band calculation and the experiment regarding the number of bands and the character and the shape of the FS's, which have also been measured by a map method [70]. In this chapter, we concentrate on the high resolution data of the Ti $3d$ band.

A goal of ARPES research is the extraction of many body physics from measured lineshapes. Due to the simple FL properties and exceptionally clean ARPES data of TiTe$_2$, studying its lineshapes provides a very valuable opportunity to ask such basic questions about ARPES as "how do we define a Fermi wave vector from ARPES?" or "to what extent many body ground state properties can be extracted from ARPES?." In this chapter, answers to these questions are sought in the temperature dependent ARPES measurement and detailed lineshape fittings.

3.2 Temperature dependence

One of the most basic pieces of information that ARPES offers is the existence and the shape of the FS. A possibly optimum procedure for obtaining a FS from ARPES is as follows. First, a Fermi energy intensity map is taken to give a global view of a *possible* FS. Not all the patterns in a Fermi energy intensity map represent real FS, as we will see in Chapter 4. Second, EDC's are taken along representative directions in $\mathbf{k}$ space to allow judgment as to whether a specific part of the Fermi energy intensity map pattern really represents FS. Third, the exact locations of FS crossings are determined by examinations of EDC's or maps or both. Of these three steps, the last step is the most non-trivial, and no universal solution exists.

Ideally, one would like to find the best theory that fits the ARPES data and as a by-product one would be able to get $\mathbf{k}_F$ values. However, this is a difficult approach in general. We will see in this chapter the difficulty even for such a "simple" Fermi liquid case as TiTe$_2$. In practice, determination of $\mathbf{k}_F$ values relies on using some aspect of the data that the researcher deems to be most relevant. Examples of $\mathbf{k}_F$ criteria are the minimum peak binding energy [67, 71], the minimum peak width [27], the mid-point, or fixed point of the electron occupation number $n(\mathbf{k})$ [72] as a function of temperature, or the maximum derivative of -$n(\mathbf{k})$ [70, 73].

Each of these different criteria can be related to a certain aspect of a peak crossing E_F, where the peak is assumed to behave like a quasi particle peak. By definition, the peak for $\mathbf{k}$=$\mathbf{k}_F$ has the minimum binding energy, 0. The "lifetime" due to electron-electron interactions is minimum for $\mathbf{k}$=$\mathbf{k}_F$ because of phase space restrictions. The occupation number $n(\mathbf{k}_F)$ = 1/2 if $A(\mathbf{k}_F, \omega) = A(\mathbf{k}_F, -\omega)$, i.e. it is electron-hole symmetric. Lastly, the presence of the FS means that there is a peak that passes E_F at $\mathbf{k} = \mathbf{k}_F$, which means that $n(\mathbf{k})$ decreases the most steeply at $\mathbf{k}_F$. However, these criteria must be implemented with proper considerations of the Fermi-Dirac cutoff function and the experimental resolutions. Especially, the apparent binding energy and peak width can be affected by these additional factors. The criteria based on $n(\mathbf{k})$ do not suffer from distorting effects of the Fermi-Dirac distribution function or finite energy resolution. However, obtaining accurate $n(\mathbf{k})$ values can be problematic if multiple peaks are overlapping. The property that $n(\mathbf{k}_F) = 1/2$ is unaffected by finite angle resolution *if* the electron-hole symmetry condition is modified to mean that for any $\mathbf{k}$ belonging to the $\mathbf{k}$ resolution window there is a unique partner $\mathbf{k}'$ in the same window that satisfies $A(\mathbf{k}, \omega) = A(\mathbf{k}', -\omega)$. We further note that when this strong electron-hole symmetry condition is satisfied, $n(\mathbf{k}_F)$ is invariant as a function of T. Both the $n(\mathbf{k}_F) = 1/2$ condition and the $-n(\mathbf{k})$ derivative criterion are in principle susceptible to effects of matrix element variation, i.e. the lineshape area can vary also because the ARPES matrix element varies with $\mathbf{k}$.

Usually, the Fermi-Dirac distribution function plays the role of cutting the spectral function and putting the apparent ARPES peak positions below E_F. This is especially true because data for lineshape analysis are typically taken at the lowest temperature possible to avoid thermal broadening. However, a very favorable condition for $\mathbf{k}_F$ determination can occur if the Fermi-Dirac distribution function is wide enough to expose the dispersing peak both *below and above* the chemical potential. The possibility that this can happen can be seen as follows. Let us recall from section. 1.2 that the photoemission intensity with perfect energy resolution is given by

$$I(\mathbf{k},\omega) \;=\; M_{\mathbf{k}}^2 f(\omega) \sum_{\mathbf{k}} W_k(\mathbf{k}) A(\mathbf{k},\omega).$$

We consider perfect energy resolution because finite energy resolution does not affect the argument. For $\mathbf{k}$ outside the FS, the term $\sum_{\mathbf{k}} W_k(\mathbf{k})A(\mathbf{k},\omega)$ has a peak above E_F. The condition for observing a peak above E_F in $I(\mathbf{k},\omega)$ is then that the peak is narrow enough and/or the Fermi-Dirac function is varying slowly enough (i.e. the temperature is high enough) so that the product of the two still has a maximum above E_F. I illustrate this scenario in Fig. 3.1, where F represents $f(\omega)$ and G represents $\sum_{\mathbf{k}} W_k(\mathbf{k})A(\mathbf{k},\omega)$. As noted in the figure, the width of the peak G is given by $\approx v_F \Delta k$ where Δk is the momentum width due to experimental angle resolution and the width of the Fermi-Dirac distribution function is $\approx 4k_BT$. The intrinsic lifetime broadening due to the electron self energy is assumed to be much smaller than the width due to the angle resolution, because we are considering $\mathbf{k}$ near $\mathbf{k}_F$. For a Gaussian peak G centered at k_BT, the condition for the product of F and G to show a peak above E_F is roughly $v_F\Delta k < 4k_BT$.

Before showing our new temperature dependent data set, let us look at the previously obtained data at 25 K, because we will need this set for comparison with the new set. Fig. 3.2 (a) shows the data in Fig. 1.6, normalized to the photon flux. The exact $\mathbf{k}$ path arc tracked by these angles with $h\nu =$ 21.2 eV is explained in Ref. [67], but is not our major concern here. It is sufficient to note that 27.5^o and 0^o correspond to points somewhere along the vertical LM axis of the hexagonal Brillouin zone boundary and along the vertical ΓA axis at the zone center, respectively. For convenience, we will sometimes call 0^o the Γ point and 27.5^o the M point, but it should be born in mind these designations are only approximate. The Ti $3d$ band shown in Fig. 3.2 (a) forms small electron pockets near the zone boundaries. These electron pockets are compensated by the hole pockets at the zone center arising from Te $5p$ bands. A small amount

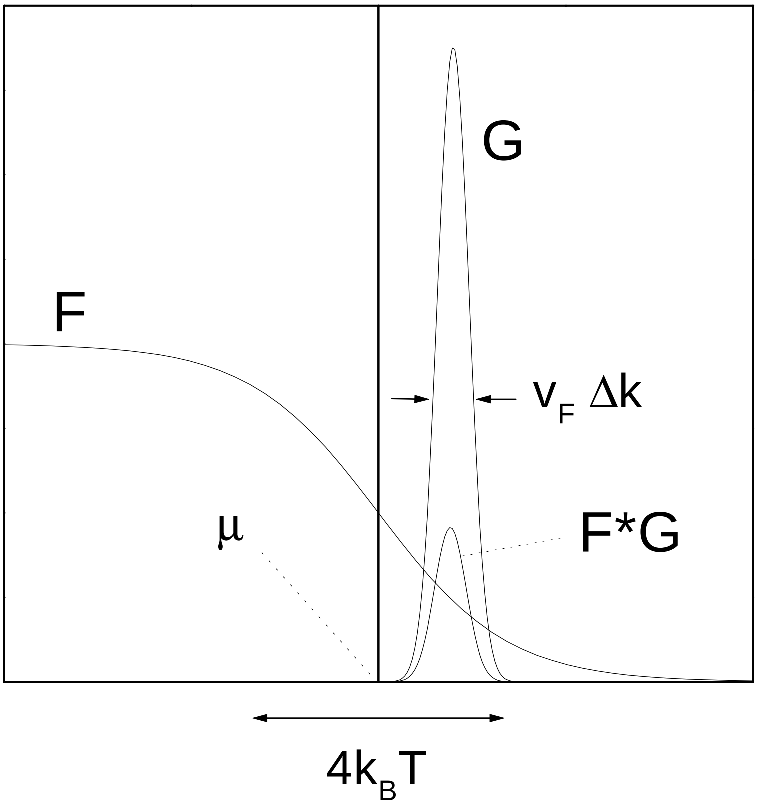

Figure 3.1: Scenario for a peak above chemical potential in photoemission. F = Fermi-Dirac function. G = momentum-summed spectral function. See text for discussion.

of uprising Te $5p$ emission is visible in the lower left corner of Fig. 3.2 (a).

The ARPES data in Fig. 3.2 (a) shows a shallow band with complex lineshapes. At the band bottom (M) the broad lineshape implies a two peak structure, one at ≈ 40meV and the other at $100 \sim 150$meV. As the band disperses towards E_F the lineshape develops into a single peak which sharpens up, crosses E_F and decreases rapidly in intensity. As shown in Fig. 1.6 the change in the spectral intensity after crossing is non-trivial, and shows a small peak dispersing backwards. So far, this data set is the best data obtained for $TiTe_2$, based on the sharpness of the peaks and the peak to background intensity ratio. The observed minimum peak width $\approx$ 45 meV is significantly larger than the energy resolution 35 meV. Successful fits of the lineshapes [27, 74] attributed the extra broadening to the effective energy broadening due to the finite angular resolution.

Fig. 3.3 shows new data of $TiTe_2$ taken at two different temperatures and with other conditions the same as in Fig. 3.2. It was already noted previously [67] that a peak does occur above E_F for $TiTe_2$ for the spectrum at $\theta = 15^o$ at room temperature. This finding is nicely reproduced by this new measurement. In addition, the new data show the full dispersion at room temperature. Between 25 K and 300 K, the data show quite a

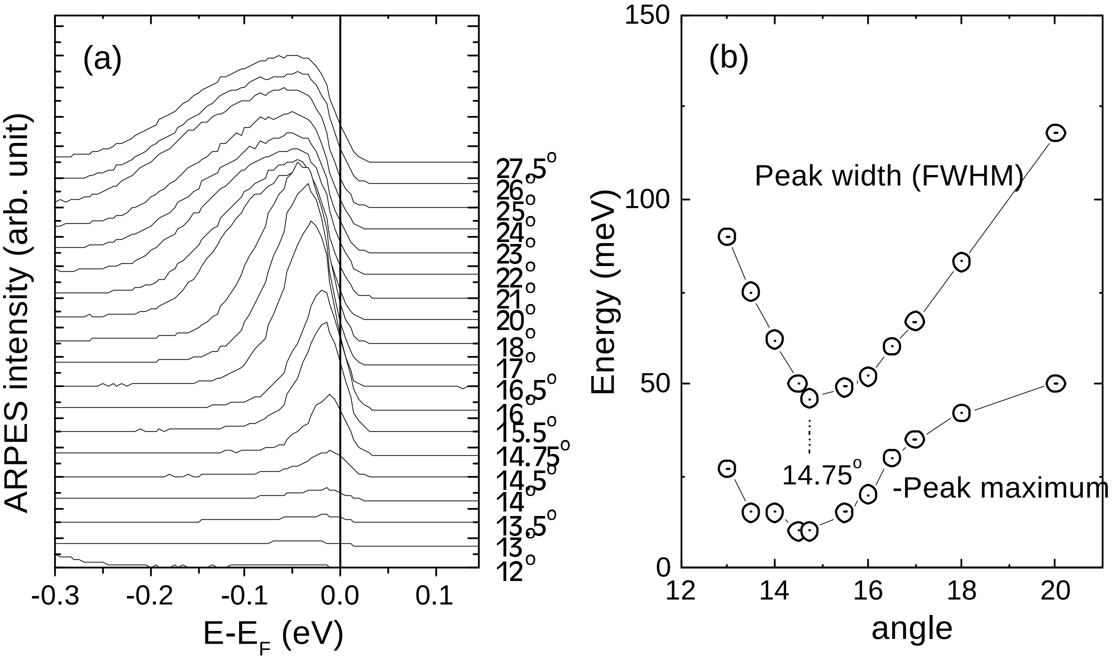

Figure 3.2: (a) High resolution ARPES data of the Ti $3d$ band of TiTe$_2$ at T=25K, hν=21.2eV, ΔE=35meV FWHM and full angular acceptance 2^o. The data are the same as those in Fig. 1.6. (b) Peak positions and widths extracted from the data.

dramatic temperature dependence, which we will argue below comes from the temperature dependence of the Fermi-Dirac distribution function. The data at T = 25 K are consistent with the previous data of Fig. 3.2, and show a minimum in binding energy and peak width at $\theta = 14.5^o$. In contrast, at T = 300 K peak widths show a minimum at $\theta = 15 \sim 16^o$ and the peak position varies linearly across E_F for angles down to $\theta = 14^o$ and then turns back. The v_F value measured from the peak dispersion is ≈ 0.5eVÅ, which implies that $v_F \Delta k \approx 35\mathrm{meV}$ for the given total angular resolution of 2^o and kinetic energy of $\approx$ 16.8 eV. On the other hand, room temperature gives $4k_BT = 100\mathrm{meV}$, much larger than $v_F \Delta k$. Therefore, the condition for a peak above E_F discussed in the previous paragraph is indeed satisfied.

The quantity $n(\mathbf{k})$ as a function of temperature is plotted in Fig. 3.3 (d). To compare the two temperatures, each $n(\mathbf{k})$ curve was normalized to its area. This normalization also makes the $n(\mathbf{k})$ values near the band minimum for the two temperatures agree well with each other. A fixed point occurs at $\theta = 15.5^o$ where the $n(\mathbf{k})$ value is about 0.4 of the value near the band minimum. Near this fixed point, the slope of $n(\mathbf{k})$ is observed to decrease at high temperature.

To determine the Fermi level crossing point at 300K, we choose the peak position as the best criterion, because peak positions are determined with higher accuracy than intensities and are not influenced by the photoemission matrix element. In Fig. 3.3 (c),

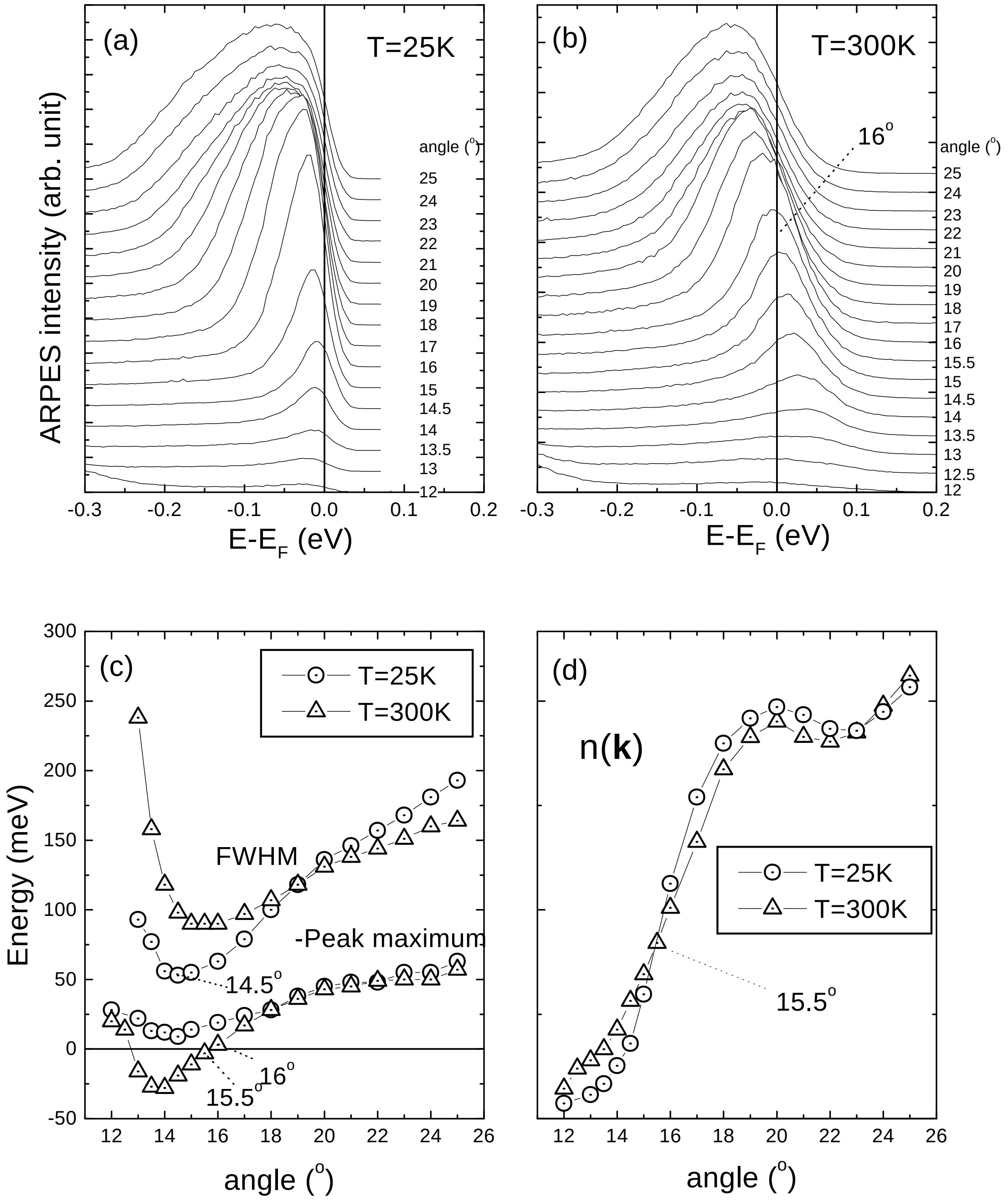

Figure 3.3: TiTe$_2$ ARPES data at 25 K and 300 K and peak positions, widths and areas derived from them.

the peak position determined from the peak maximum is observed to pass through E_F between 16^o and 15.5^o. Noting that the high but still finite temperature means that the Fermi-Dirac function gives slightly more weight to low binding energy, as is confirmed by the simulation to be discussed in the next paragraph, the best estimate of the Fermi level crossing point is 16^o. An important fact to notice regarding the $\mathbf{k}_F$ determination is that multiplication by the Fermi-Dirac distribution function never shifts a peak position to a lower binding energy. This means that the angles at which the peak is observed above E_F cannot correspond to $\mathbf{k}_F$.

Fig. 3.4 shows a simple theoretical simulation of the temperature dependent data. The electron-hole symmetric Matho FL model as described in section. 2.2 is used for the calculation. In principle, the spectral function $A(\mathbf{k},\omega)$ can be strongly temperature dependent. An example is the charge density wave spectral function presented in Section. 2.3. Another typical example is the spectral function of the Kondo model [75]. These systems are characterized by phase transition or cross-over phenomenon. For TiTe$_2$, there is no known phase transition or cross-over behavior. Therefore, we assume that $A(\mathbf{k},\omega)$ is temperature independent[1]. The temperature dependence in Fig. 3.4 then comes entirely from the Fermi-Dirac distribution function in Eq. 1.9. Also, a Gaussian $\epsilon(\mathbf{k})$ profile function W_ϵ and a Gaussian ω profile function W_ω are used in Eq. 1.9 to take the experimental resolutions into account.

The model parameters for the theoretical curves are chosen so as to approximately account for the dispersions and the peak widths near 16^o in Fig. 3.3. Major aspects of the temperature dependence, i.e. the back-bending dispersion at 25K below E_F and the linear dispersion extending to above E_F at 300K, is reproduced well. Within the current theory, this is entirely due to the Fermi-Dirac distribution function. The maximum of the $\mathbf{k}_F$ peak at $T = 300$ K has its energy just slightly below E_F, in good agreement with our experimental determination of $\mathbf{k}_F$ at 16^o. Apart from these main features, there are noticeable differences between the model calculation and the experiment. They are the structured lineshape in Fig. 3.4 (b) for $\mathbf{k} \gg \mathbf{k}_F$, not observed in Fig. 3.3 (b), and the positions of the minima in the peak position curve and the peak width curve at 25 K which differ by 1^o and 1.5^o respectively. The origins for these differences are not clear at the moment. Another noticeable difference is the small difference of the fixed

---

[1] A moderate temperature dependence in the self energy is actually expected to exist, but it is neglected here. In the low energy and temperature scales the FL self energy is written as $\mathrm{Im}\Sigma = \beta(\omega^2 + (\pi k_B T)^2)$ [77]. In this form, the temperature dependent part broadens $A(\mathbf{k},\omega)$ uniformly, and will not alter the discussion presented below in any essential way. The assumption is that this remains true even at high temperatures and with the presence of electron-phonon interactions.

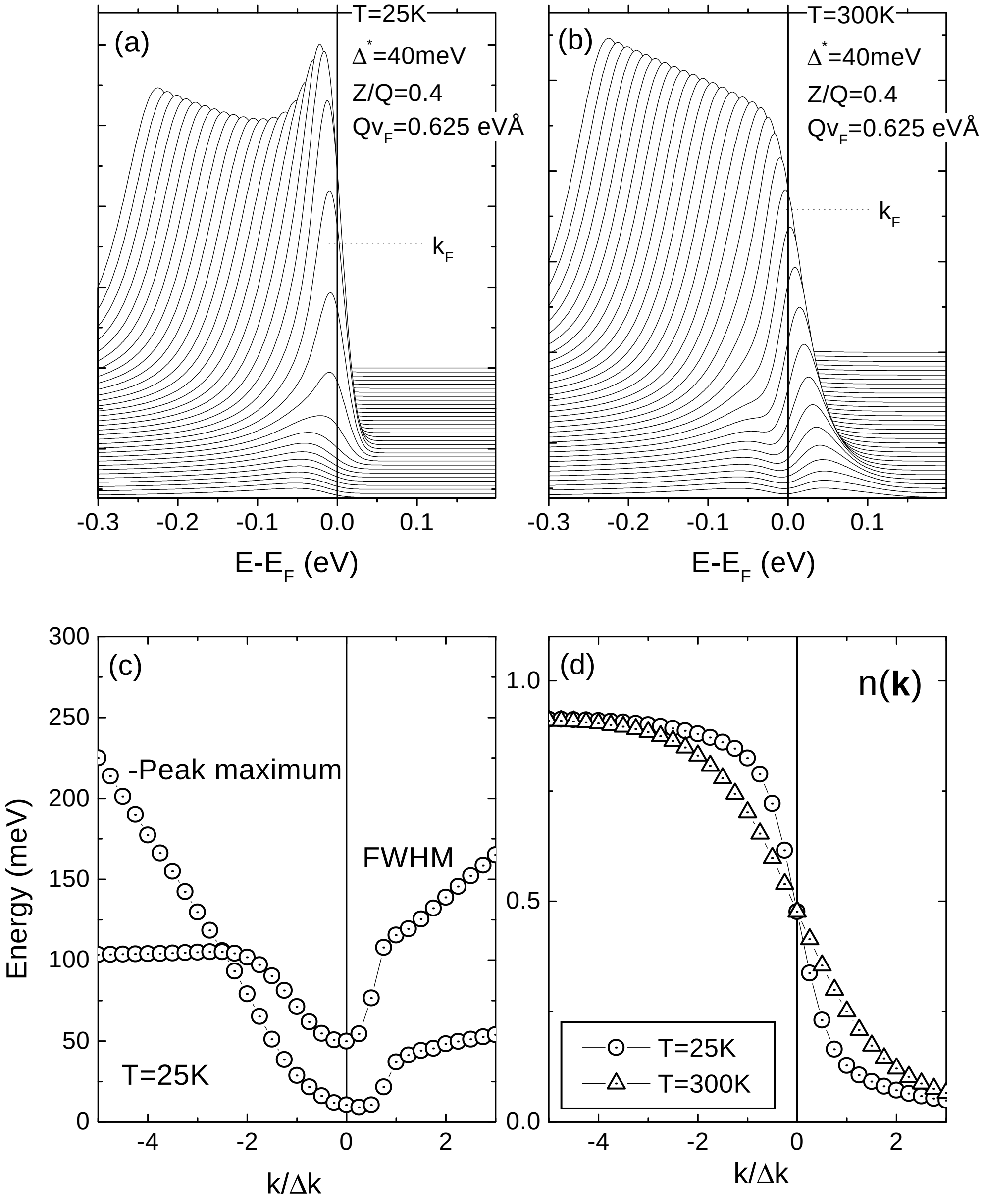

Figure 3.4: Theoretical modeling of Fermi liquid lineshapes at 25 K and 300 K with linear dispersion. The increment of k values is $1/4$ of Δk, the width due to the angle resolution, and corresponds to 0.5^o. See text for more discussion.

point position of $n(\mathbf{k})$, 15.5^o, and $\mathbf{k}_F$, 16.0^o. A possible explanation for this is a slight electron-hole asymmetry.

We now discuss various criteria for the $\mathbf{k}_F$ determination, applied to the current data. The dispersion at 300 K assigns $\mathbf{k}_F$ to angle 16^o. The $\mathbf{k}_F$ angle determined by the minimum peak width or the minimum binding energy at 25 K is 14.5^o, substantially different from 16^o. However, at 300 K, the 16^o spectrum is one of the spectra that give the minimum peak width, whereas 14.5^o has a bigger width. The $n(\mathbf{k}) = 1/2$ criterion assigns the $\mathbf{k}_F$ angle to ≈16^o. As noted above, the fixed point of $n(\mathbf{k})$ assigns $\mathbf{k}_F$ to ≈15.5^o. The $-n(\mathbf{k})$ derivative criterion is not ideal due to the small number of data points, but when it is applied it assigns $\mathbf{k}_F$ to ≈15.5^o at 25 K and ≈16.5^o at 300 K. Therefore, except for the peak width/energy criterion at 25 K, all other criteria give, or are not contradictory with, $\mathbf{k}_F \approx 16^o$. The general agreement of $\mathbf{k}_F$ determined by the criteria based on $n(\mathbf{k})$ with that determined by the 300 K dispersion means that the overall ARPES matrix element variation with $\mathbf{k}$ is rather weak.

3.3 Lineshape fit

In this section, our goal is now to fit the lineshape with the Matho FL model as discussed in section 2.2. It is important to make clear the philosophy of the fit efforts described here. First of all, the current fit is not intended to prove FL physics for TiTe$_2$. Such a proof, if it is to be made using photoemission alone, must prove that the FL fit is superior to non-FL fits. This was actually done early in Ref. [27]. There, it was shown that the marginal FL gives a noticeably worse fit than the FL fit. Second, the fits described here are fits over a large energy scale and a large momentum scale. Binding energies up to 250 meV and momentum values from the band minimum up to those past the Fermi level crossing are included in the fits. This means that the fits do not necessarily concentrate on the low energy features of the spectra, which are crucial in view of the low energy Fermi liquid parameters. In fact, the ARPES spectra reveal the high energy tails and the peak shapes better than the low energy lineshapes which are almost entirely obscured by the finite energy/momentum resolutions. The accuracy to which the low energy Fermi liquid parameters in Eq. 2.13 are obtained from these fit efforts is determined precisely by the extent to which the Matho Green's function approximation is good. Therefore, we here have two objectives, which are closely related in fact. First, we would like to see how well the Matho Fermi liquid theory describes the ARPES spectra. Second, we would like to see how well the resultant parameters describe the transport properties of TiTe_2.

In this section, we summarize the fits that were reported in Ref. [74]. The theory used for the fits is the electron-hole symmetric Matho FL model of Eq. 2.17. The theoretical parameters are Z/Q, $Q\epsilon(\mathbf{k})$, and Δ, where we write $\Omega_b = i\Delta$ (electron-hole symmetry). Additional experimental broadening effects were included by using a Gaussian energy broadening function and an elliptical momentum broadening function in Eq. 1.9. Using Eq. 2.16, the relation between Δ and the Fermi liquid coherence energy Δ^* is easily found: $\Delta^* = \frac{\Delta}{\frac{Q}{Z}-1}$. In the original fit [27] using the Taylor series FL model of Eq. 2.14, the fit parameters were $Z\epsilon(\mathbf{k})$ and Δ^*. The fit was made with $\Delta^* = 25$meV for all $\mathbf{k}$ and varying only $Z\epsilon(\mathbf{k})$. Good fits can be found only near the E_F crossing (Fig. 1.6). In the current effort, a similar fit was tried first. Fig. 3.5 show the fit made with a $\mathbf{k}$-independent self energy, optimized to fit the 14.75^o spectrum best. The $\mathbf{k}$-independent parameters are $Z/Q = 0.44$ and $\Delta^* = 36$ meV. The fit of Fig. 3.5 is quite similar to that of Fig. 1.6. It gives a good fit near the 14.75^o spectrum, but near the zone boundary, 27.5^o, the fit fails to produce the qualitative features of the lineshape at all.

Unlike the Taylor FL model, Matho FL model has an inherent capability to fit the structured lineshape for $\mathbf{k}$ far from $\mathbf{k}_F$. This was demonstrated previously by Harm *et al.* [76], without further elucidation of how it is possible. Fig. 3.6 shows our fit result and Fig. 3.7 summarizes the fit parameters. In these fits, the fit parameters are now allowed to vary as a function of $\mathbf{k}$. Overall, excellent fits are obtained for all the spectra. The fit procedure was as follows. First, the entire fit parameter space was explored by choosing randomly selected initial fit parameters within the expected parameter ranges and then letting a non-linear least square fit program using the Levenberg-Marquardt algorithm find its solution. The range for Δ was $10 \sim 100$ meV and that for Z/Q was $0.1 \sim 0.9$. The range of $Q\epsilon(\mathbf{k})$ was chosen depending on the angle. In particular it was chosen to be $-20 \sim 20$ meV for the 14.75^o spectrum and $-60 \sim -10$ meV for the 16^o spectrum. When ≈ 100 random fit results were collected for each angle, they defined unique optimum values of Δ, Z/Q and $Q\epsilon(\mathbf{k})$, and these optimum values were well within the prescribed ranges, showing no sign of a χ^2 minimum point lying outside. Using these fit results as a starting point, several iterations were performed until convergence in $Q\epsilon(\mathbf{k})$ was obtained. This is necessary because each spectrum is individually fitted and thus, to find an optimum value of $Q\epsilon(\mathbf{k})$ for the spectrum itself, one needs to know the range of $Q\epsilon(\mathbf{k})$ to include to account for finite angle resolution *before* the fit is made. The input for the range of $Q\epsilon(\mathbf{k})$ was determined by $Q\epsilon(\mathbf{k})$ parameters

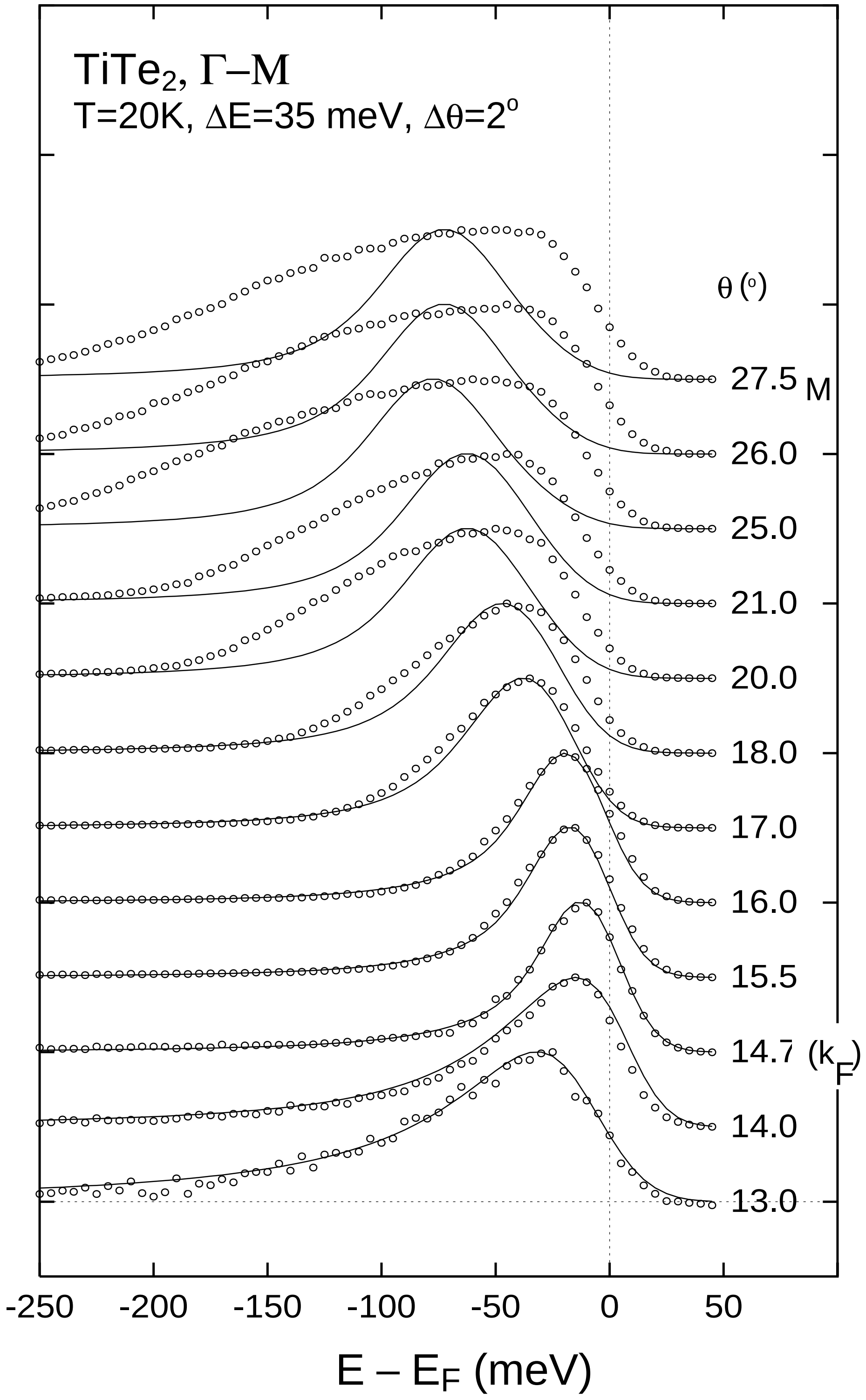

Figure 3.5: Matho FL model fit with momentum independent fit parameters.

for the adjacent angles in the previous iteration. Note that in Fig. 3.7 the LDA band calculation [67] is plotted with $Q\epsilon(\mathbf{k})$ parameter values. The shape of the fit parameter $Q\epsilon(\mathbf{k})$ is in excellent agreement with the theory, and the bandwidth is about 75% of the theoretical bandwidth. The spectra for angles 13.0^o and 14.0^o had enough noise to randomize the fit results. In order to fix this problem, Z/Q values for these angles were equalized with the value for 14.75^o.

Note that when $Z/Q = 0.5$ the Matho FL theory and the Taylor FL theory give exactly the same spectral functions at **k**=$\mathbf{k}_F$. But as soon as **k** departs from $\mathbf{k}_F$, the two theories produce different lineshapes. The fit parameters tend to show some similarity to those of the Taylor FL model fit in the sense that the fit produces a Z/Q value somewhat smaller than, but close to, 0.5 in the vicinity of 14.75^o and Δ^* ~20 meV for most angles except 14.75^o. However, occasional irregularities in Z/Q and Δ^* values make the comparison difficult. It is noticeable that Z/Q tends to decrease and Δ tends to increase as the angle increases. These trends are closely related to the structured lineshape observed for large angles. The origin of the structured lineshape is as follows. As shown in Fig. 2.2, as $\epsilon(\mathbf{k})$ changes from 0 the poles of $G(\mathbf{k}, \omega)$ move in an interesting way with one of the poles[2] remaining close to the Im(ω) axis. Because in addition, the residues become complex, there is interference between the contributions to $A(\mathbf{k}, \omega)$ from each pole, with the details depending mostly on Z/Q. For Z/Q roughly in the range of that for the fit near the 14.75^o spectrum, one finds that as $|\epsilon(\mathbf{k})|$ increases from zero, the moment of the poles and the effect of interference in the weights conspire so that there is a single peak moving away from E_F and broadening. However, for small Z/Q one finds a sharing of weight between the two poles so as to produce a two-peak lineshape having considerable weight near E_F even for **k** far away from $\mathbf{k}_F$, just as occurs in the data. Varying Δ tunes the separation of the two structures to produce a good fit.

Another non-trivial aspect of the data as pointed out in the last section is the back bending of the residual weight after the peak has crossed E_F. This feature is well reproduced by the fit. The residual weight is a direct consequence of correlated electron states in the model. Due to electron-electron interactions the ground state has many electron-hole excitations relative to the non-interacting ground state. Therefore, from **k** outside FS, an electron *can* be removed, and therefore there exists a small weight in the electron removal spectrum.

---

[2] When Z/Q $<$ 0.5, this pole is the pole evolving from the quasi-particle pole.

.

Having obtained good fits, one can then extract information such as the normalized occupation number $n(\mathbf{k})/Q$ and the matrix element $|M_\mathbf{k}|^2Q$. The result for $n(\mathbf{k})/Q$ is plotted as the solid line in the lower panel. Also plotted are the actual measured areas of the spectra. The difference reveals the fact that the data fitting requires also an overall scale factor which, in this ansatz, must be attributed to the normalized ARPES matrix element $|M_\mathbf{k}|^2Q$, plotted in the upper panel. This is the effect on $n(\mathbf{k})$ of the ARPES matrix element mentioned above.

In principle an energy dependence of ImΣ implies a temperature dependence of the dc resistivity $\rho(T)$. For the case Im$\Sigma = \beta\omega^2$, FL arguments lead to $\rho = (1/ne^2)(m^*/\tau)$ with $m^* = m/Z$ and $(1/\tau) = 2Z\text{Im}\Sigma = 2\beta Z[\omega^2 + (\pi k_B T)^2]$. Then one has $\rho(T) = 2(m/ne^2)(\pi k_B)^2\beta T^2$. The authors of [77] have calculated $\rho(T)$ for TiTe$_2$, assuming our Taylor FL model self energy Σ_T applies to the entire FS, computing from an LDA band structure the average Fermi velocity which gives n/m, and taking for β our experimental β'. They compared their result with experimental data [68] and found a large disagreement at high T, a result reproduced in Fig. 3.9(a). Fig. 3.9(b) shows the large difference at large ω between the purely ω^2-dependence of ImΣ_T from [27] and that of the Matho self energy Σ obtained above. Fig. 3.9(a) also shows the $\rho(T)$ obtained if the Matho self energy Σ is used in place of Σ_T, again taking $\beta = \beta'$ for a consistent comparison, if one is willing to speculate that the ω-dependence of ImΣ can be a guide to the T dependence of $\rho(T)$ even away from the ω^2 regime. The Matho self energy Σ essentially eliminates the large disagreement with experiment implied by Σ_T. However, the numerical agreement should not be taken too seriously because a detailed treatment should account for the probably different lifetimes on the Te p and Ti d parts of the FS, as well as for the considerable difference between β and β'.

3.4 Discussion

The lineshape fit results reported in the last section are in disagreement with our result in section 3.2 regarding the $\mathbf{k}_F$ value. In the fit, the $\mathbf{k}_F$ value lies where the $n(\mathbf{k})$ value is very small (Fig. 3.8) while the $\mathbf{k}_F$ value determined from the 300 K dispersion is near the midpoint of $n(\mathbf{k})$ curve. The $\mathbf{k}_F$ value away from the midpoint of the $n(\mathbf{k})$ curve implies a strong matrix element modulation (Fig. 3.8). Currently there is no clear explanation about the disagreement of the two results. In this section, we point out possible solutions.

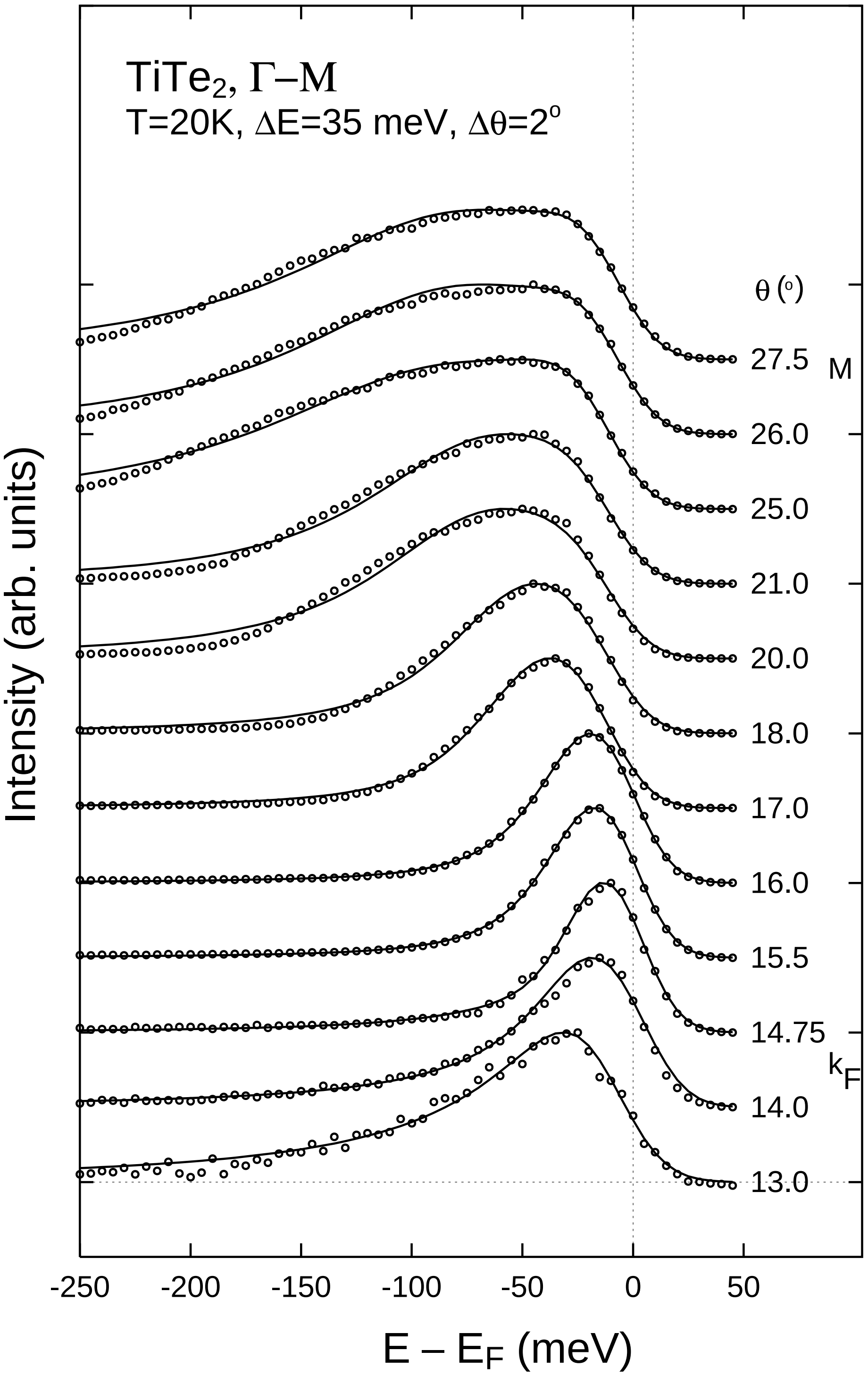

Figure 3.6: Fit of the Ti 3d band of TiTe$_2$ using the Matho FL model. The spectra are normalized to the same maximum height.

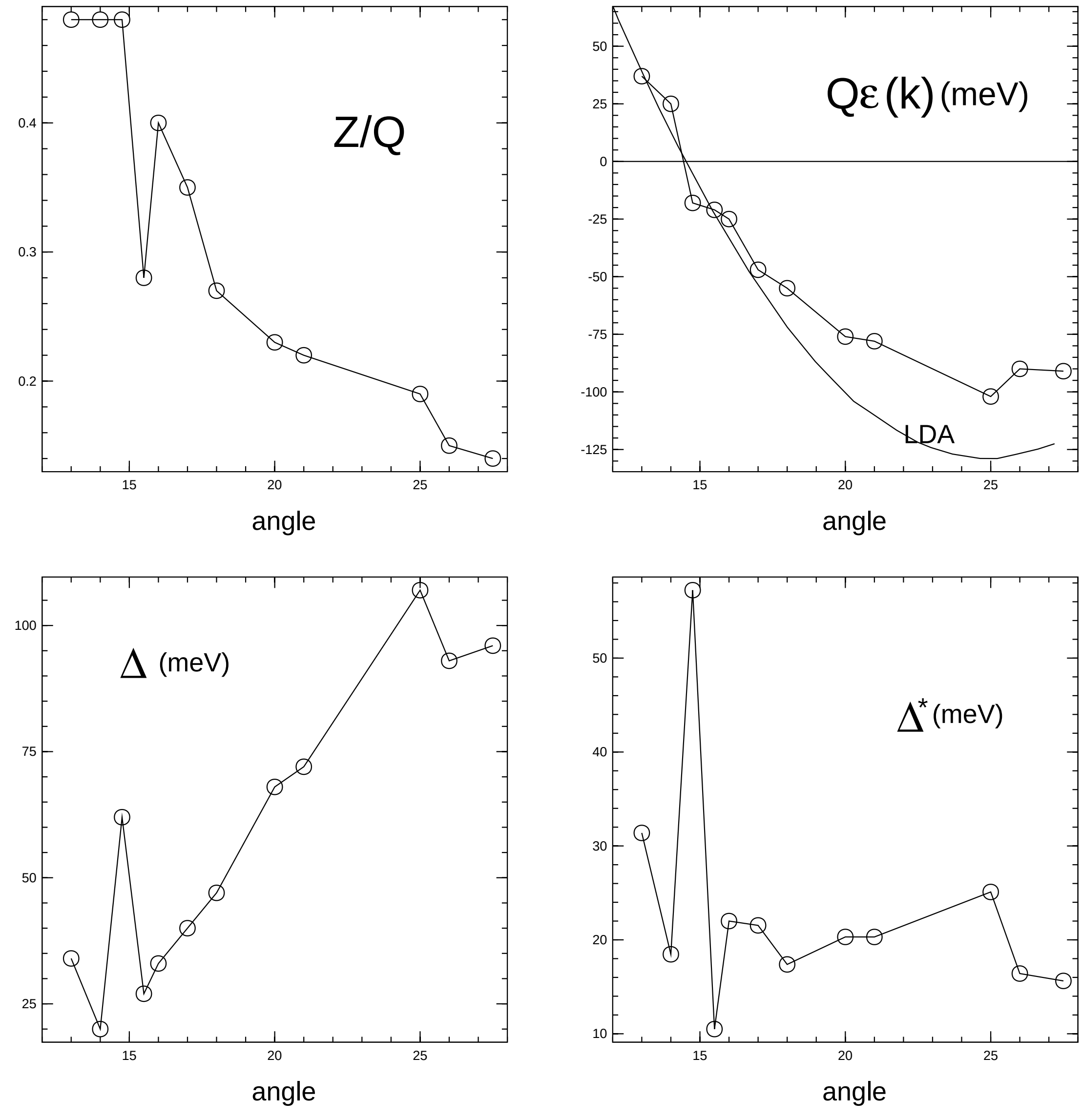

Figure 3.7: Fit parameters for Matho FL fit.

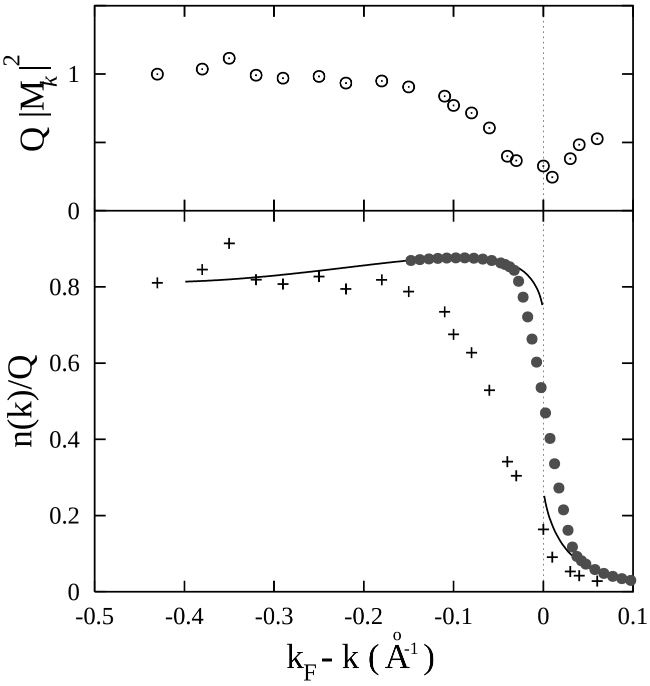

Figure 3.8: Normalized matrix element $|M_{\mathbf{k}}|^2 Q$ and occupation number $n(\mathbf{k})/Q$ determined from the fit of Fig. 3.6. The solid line for $n(\mathbf{k})/Q$ shows a polynomial fit to the fit parameters, and the filled circles show the effect of our finite angular resolution. The pluses show the (scaled) areas from ARPES.

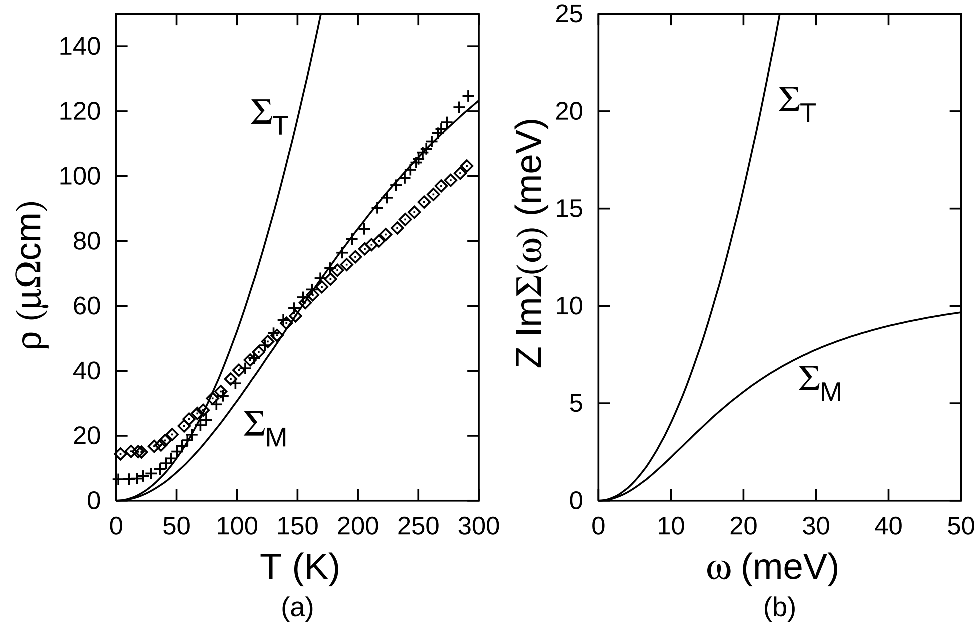

Figure 3.9: Comparison of the resistivity and the self energy for TiTe$_2$. (a) The resistivities calculated (solid lines) for TiTe$_2$ with Σ_T in [77] and with the Matho Σ, compared to experiment (data points) [68], as explained in the text. (b) $Z\mathrm{Im}\Sigma(\omega)$ for the Σ_T fit in [27] and the Matho fit.

One possibility is that there is non-trivial temperature dependence so that the $\mathbf{k}_F$ value is temperature dependent. One obvious candidate is that the chemical potential changes so that the band effectively moves up or down with respect to the chemical potential. That this does not happen can be seen from Fig. 3.3 (c), where the peak positions for the two temperatures agree well for angles $\geq 18^o$.

Another possibility is that the model used in the last section is insufficient. Possible extensions of the theory are the following. We call the new model the "extended Matho FL model."

- **k mass** In the fit of the previous section, the fit parameters were $Q|M_{\mathbf{k}}|^2$, Z/Q, Δ^* and $Q\epsilon(\mathbf{k})$. In addition to the **k** dependence of the Matho FL model parameters, there can be additional **k** dependence in the self energy. Following Ref. [78], we assume an additional term in the self energy $\Sigma(\mathbf{k}, 0) = \gamma\epsilon(\mathbf{k})$. This in effect introduces an additional renormalization factor for $\epsilon(\mathbf{k})$ in the Green's function. Therefore, the previous fit parameter $Q\epsilon(\mathbf{k})$ becomes $Q(1+\gamma)\epsilon(\mathbf{k})$. Actually, the addition of γ does not add a new fit parameter. It only means that the previously called $Q\epsilon(\mathbf{k})$ should be reinterpreted. The term $m_k = (1+\gamma)^{-1}$ defines the so-called "**k**-mass" [79, 80]. As described below, the new test fit used the LDA band calculation as a reference for determining $\epsilon(\mathbf{k})$ and its width due to the angular resolution. Despite the fact that conceptually no new fit parameter has been added, the procedural differences in determining $\epsilon(\mathbf{k})$ do seem to impart some importance to the **k**-mass parameter $Q(1+\gamma)$. This means that the exact role of this term in the new fit scheme may not be purely that of the **k**-mass and has to be investigated carefully.

- **electron hole asymmetry** In the previous section, electron-hole symmetry was assumed. As we discussed above, some electron hole asymmetry is implied by Fig. 3.3 (d). Therefore, we assume that the background pole Ω_b is fully complex, given by

$$\Omega_b = i\Delta^*(Q/Z - 1)\cos(\psi)\exp(i\psi)$$

  where ψ is the electron asymmetry parameter, $-\pi/2 \sim \pi/2$.

- **impurity scattering** Impurity scattering certainly exists in this material, as seen for example in the $T = 0$ value of the resistivity [68]. The effect of impurity

what	range
$Q(1+\gamma)$	$0.1 \sim 20$
Z/Q	$0.05 \sim 0.95$
Δ^*	$0 \sim 300\mathrm{meV}$
δ_L	$1 \sim 20\mathrm{meV}$
ψ	$-\pi/2 \sim \pi/2$
E_F	$-5 \sim 5\mathrm{meV}$
M^2Q	$20 \sim 1500$

Table 3.1: Fit parameters and ranges for an extended Matho FL model fit.

scattering in the Green's function was discussed by Lloyd [81], who showed that the net effect is to replace ω by $\omega - i\delta_L$ in the Green's function. By this replacement, the Matho FL self energy acquires a constant term in the imaginary part , of the order of δ_L/Z. Assuming that the lifetime $\tau_{transport} = \tau_{spectroscopy}$, and using the known plasma frequency [77] one gets the resistivity and self energy relation $\rho(\mu\Omega cm) = 2 \times 8.56 \times 10^2 \times \mathrm{Im}\Sigma(eV)$. Using our measured value of the $T = 0$ resistivity of $\sim 13\mu\Omega cm$, one obtains $\mathrm{Im}\Sigma(0) \approx 8\mathrm{meV}$. Therefore, one estimates δ_L to be on the order of a few meV.

- **Fermi energy calibration** In the previous fit, E_F was fixed at a value taken from a reference spectrum. However, it was found that the χ^2 is reduced substantially if it is varied as a free fit parameter.

As a test, the spectra for five angles, 14.75^o, 15.5^o, 16.0^o, 17.0^o, 18.0^o, 21.0^o and 25.0^o were fitted with the parameter ranges shown in Table 3.1. The fit parameters were selected randomly for the initial values within these ranges, and were also constrained within these ranges during the fit. Another difference between the previous fit and the new fit is in the determination of $Q(1+\gamma)\epsilon(\mathbf{k})$ parameter. In the new fit, the LDA band calculation is used as a reference during the fit. Because we do not want the LDA band calculation to determine the $\mathbf{k}_F$ value, the LDA band calculation is trusted only up to an arbitrary offset along the $\mathbf{k}$ axis. This offset defines a fit parameter controlling $\epsilon(\mathbf{k})$. The advantage of using the LDA band in this way is that the range of $\epsilon(\mathbf{k})$ corresponding to the angular resolution can be also taken from the LDA band, without need of the iteration mentioned in the previous section. This procedure then separates $Q(1+\gamma)$ and $\epsilon(\mathbf{k})$ in the $Q(1+\gamma)\epsilon(\mathbf{k})$ parameter during the fit.

Fig. 3.10 shows the fits to the spectra and Fig. 3.11 shows the fit parameters. The results are certainly encouraging in that the $\epsilon(\mathbf{k})$ parameters determine the FS crossing

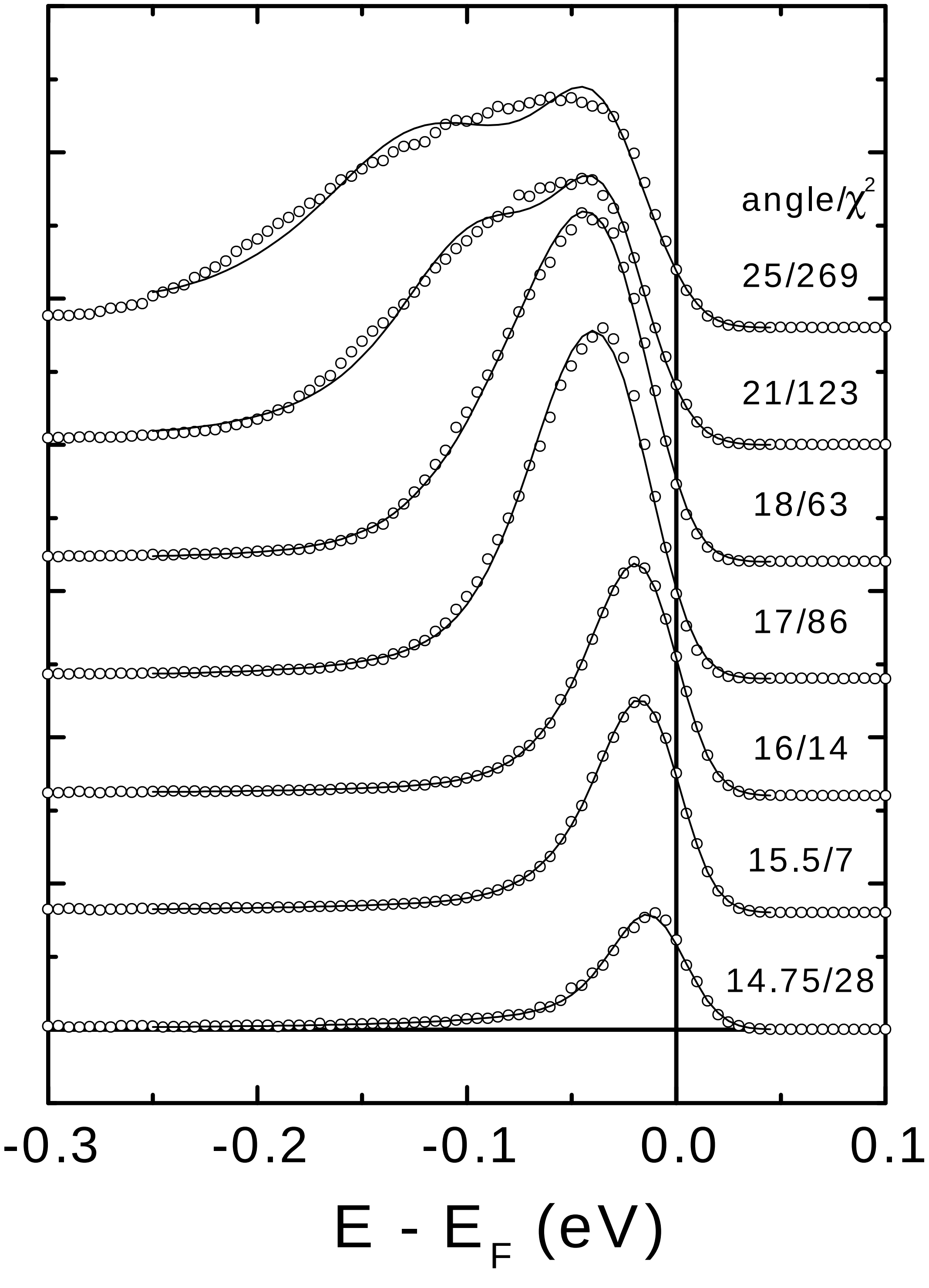

Figure 3.10: Sample fit result for the extended Matho FL fit

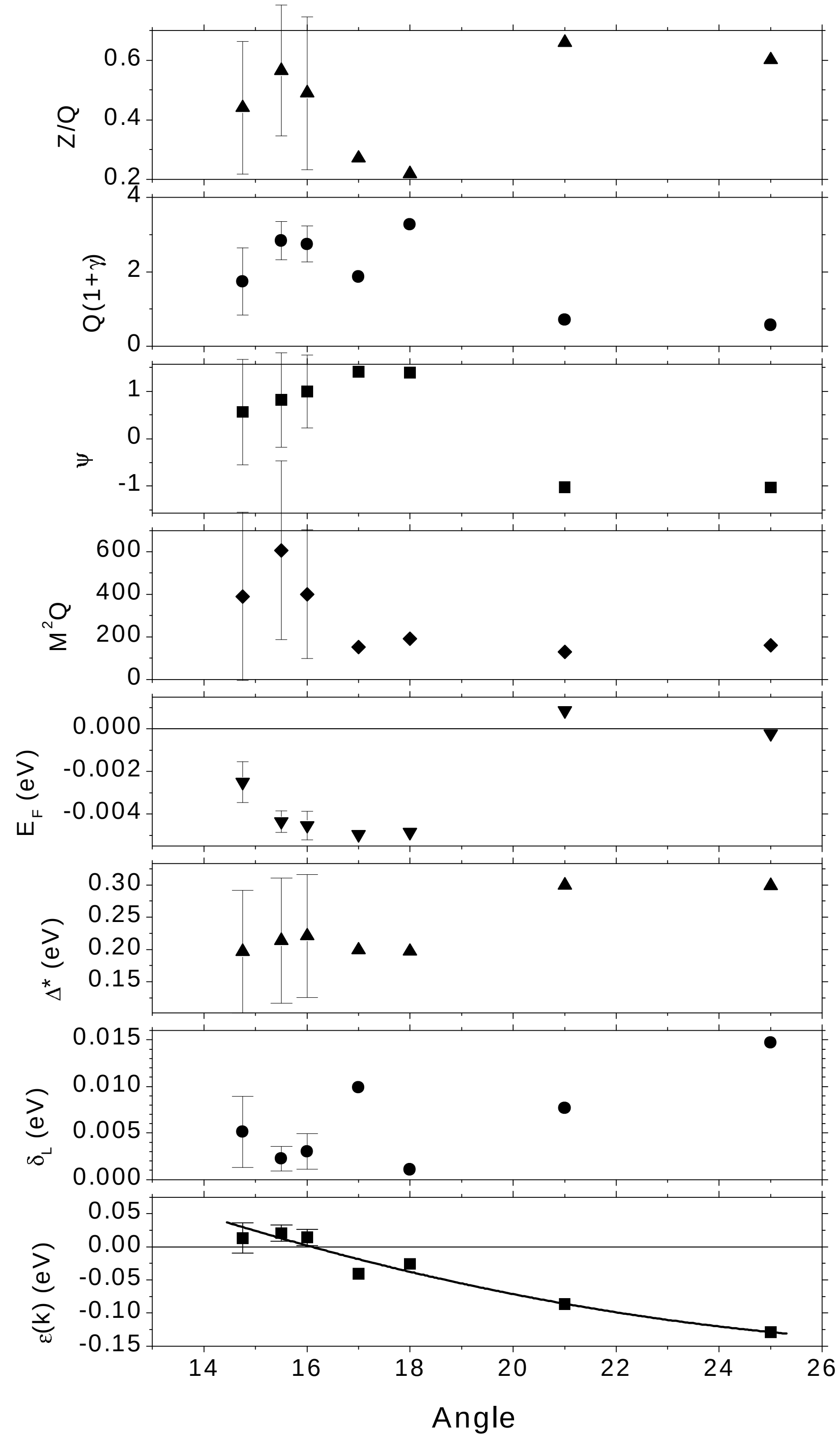

Figure 3.11: Fit parameters for the extended Matho FL model fit

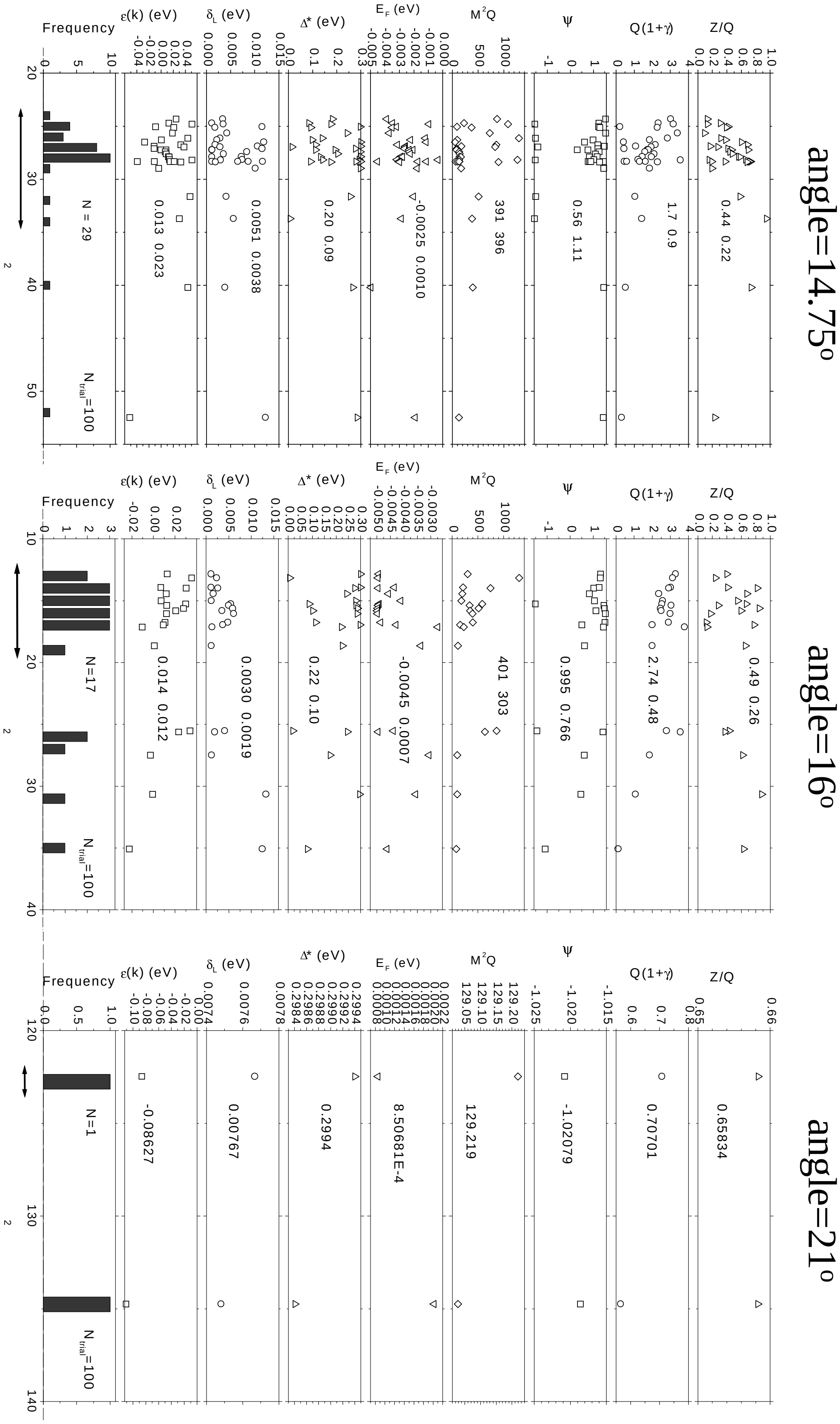

Figure 3.12: Fit parameter distributions for three representative angles

to be $\approx 16^o$. The precise origin of the new finding is not known clearly at the moment. Tests of turning on only one at a time of the additional parameters relative to the fit of the previous section imply that the separation of the $\mathbf{k}$-mass term $Q(1+\gamma)$ from the term $Q(1+\gamma)\epsilon(\mathbf{k})$ and the E_F parameter play an important role. Fig. 3.12 shows the distribution of fit parameters determined by the random fit process for three representative angles, 14.75^o, 16^o and 21^o. The fit parameter distribution for the 15.5^o spectrum shows behavior similar to that for the 14.75^o spectrum or the 16^o spectrum, and that for the spectrum for angle 17^o or higher shows behavior similar to that for the 21^o spectrum. For each angle, the frequency distribution of χ^2 is plotted at the bottom. By inspection, the "best group" of successful fits in the low χ^2 region is identified and marked with an arrow. For each fit parameter, the average and the standard deviation within the best group is written inside the plot. Also, these numbers are used to plot the position and error bars in Fig. 3.11. The parameter distributions indicate that more work is needed. The number of successful fits collected so far is rather small. There are only 29 and 17 successful fits in the best group for 14.75^o, 16^o and only one successful fit for 21^o. This means that as the number of parameters increases it becomes harder to sample the "good parameter region" with the same number of trials. Also, the wide distributions of fit parameters mean that more statistics is needed or perhaps that there are more parameters than can be reliably determined by the data.

3.5 Conclusions

The ARPES spectra for the Ti 3*d* band of TiTe_2 were studied. At room temperature the dispersion is observed to move *across* the Fermi edge, essentially due to the slow dispersion of the Ti *3d* band. The observation of a band below and above the Fermi edge gives the most accurate criterion for the Fermi level crossing position. We find that Matho's FL model gives a good description of the ARPES lineshapes. However, the $\mathbf{k}_F$ values determined from the room temperature dispersion and from the lineshape fit are significantly different. To find the origin of this problem, the lineshape fit model was extended to include an electron-hole asymmetry, impurity scattering and a possible E_F miscalibration. Inclusion of these effects gives some preliminary fit results in agreement with the room temperature dispersion data. However, more work is needed because of the great statistical uncertainty introduced by the increased number of fit parameters. It is clear from this work that a rather large uncertainty can exist in a fit parameter obtained by the ARPES lineshape fit, despite the apparent small uncertainty determined by the fit process.

My role in the work described in this chapter was to measure the temperature dependent ARPES data, to analyze them, to do lineshape fits of the previous ARPES spectra, and to participate in the comparison of the fit results with the resistivity.

Chapter 4

SmTe$_3$: Imperfectly nested CDW

The section 4.5 of this chapter essentially reproduces the journal article: "Direct Observation of Complete Fermi Surface, Imperfect Nesting, and Gap Anisotropy in the High-Temperature Incommensurate Charge-Density-Wave Compound SmTe$_3$", G.-H. Gweon, J.D. Denlinger, J.A. Clack, J.W. Allen, C.G. Olson, E. DiMasi, M.C. Aronson, B. Foran and S. Lee, Phys. Rev. Lett. **81**, 886 (1998).

We report photoemission spectroscopy of SmTe$_3$, a quasi-two dimensional material with an incommensurate high temperature charge density wave. We show by resonant photoemission that Sm is trivalent, in a good agreement with a previous finding by magnetic susceptibility measurement [82]. Valence band photoemission shows four-fold symmetric bands on the energy scale of a few eV from the Fermi energy, consistent with the near-tetragonal symmetry of the crystal. However, the electronic structure within a few hundreds of meV of E_F is found to be strongly 2 fold symmetric. We trace this reduced symmetry to the formation of a highly anisotropic charge density wave gap. From the FS geometry obtained in our experiment, we find an imperfect nesting condition. We illustrate how this condition determines the periodicity of the charge density wave in very good agreement with the observed periodicity.

4.1 Introduction

FS energy gap formation is a fundamental quantum phenomenon in solids because thereby the system of interacting electrons can stabilize a broken symmetry ground state. Two important examples of such ground states are the superconducting state and the CDW [36, 40] state. In the superconducting state, the gap opens up due to formation of Cooper pairs. In the CDW state, the gap opens up due to formation of

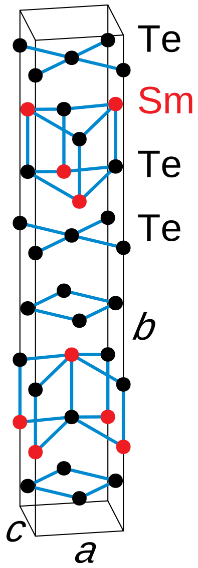

Figure 4.1: Schematic diagram for the one-face centered orthorhombic unit cell of SmTe$_3$ [82]. The dimensions are $a = 4.3326$ Å, $b = 25.6970$ Å and $c = 4.3363$ Å.

electron-hole pairs with wave vector $\boldsymbol{q}_{CDW}$. As discussed in section 2.3, the wave vector connects ("nests") one large portion of FS with another and dictates a new periodicity in the CDW state. In both cases the gap momentum dependence is of central theoretical importance.

ARPES is a beautifully direct method to measure the momentum dependence of the gap if the gap is large enough to be energy-resolved and if the material surface is stable for a long enough time to make the measurement. For a very few of the high temperature superconducting cuprates it has been possible to measure [83] the gap momentum anisotropy so well as to permit meaningful comparison to microscopic theories. However, in spite of continuing efforts in various materials [84, 85, 39], comparably detailed ARPES studies of CDW gaps have not yet been made successfully. This is largely due to the lack of a material with both a big enough gap and a sufficiently stable surface.

This chapter reports a detailed ARPES study of the valence band electronic structure and the CDW gap in SmTe$_3$, a novel incommensurate CDW material with a large anisotropic gap and very stable surface. We show below that the observed gap size implies a mean field transition temperature $\approx$ 1300 K, even larger than the melting temperature 1096 K [86], making SmTe$_3$ truly a "high temperature CDW material." This is the first time that the nesting condition and the momentum-dependence of a CDW gap have been tracked over the entire FS.

SmTe$_3$ is a layered material with conductivity anisotropy as big as 5000 [82]. The crystal structure as probed by X-ray diffraction [82] belongs to the orthorhombic group

$Cmcm$, and consists of alternating SmTe and double Te layers, as shown in Fig. 4.1 (a). The quasi-two dimensional metallic conduction is attributed [82] to the double Te layers. The structural motifs of $SmTe_3$ are practically identical with those of $SmTe_2$ and Sm_2Te_5, except that in $SmTe_2$ the double Te layers of $SmTe_3$ are replaced by single Te layers, and in Sm_2Te_5 by alternating single and double Te layers. Resistivity measurements [82] show $SmTe_3$ and Sm_2Te_5, which have double Te layers, to be quasi-two dimensional conductors while $SmTe_2$ is an insulator. The magnetic susceptibility and electric conductivity of $SmTe_3$ [82] did not show any anomaly from room temperature down to 1.2 K, thus failing to signal the CDW transition which was expected from a nesting FS found in a band calculation. A later transmission electron microscope (TEM) diffraction study [87] showed that this is because the CDW is already present at room temperature, giving rise to satellite spots[1] corresponding to an incommensurate $\boldsymbol{q}_{CDW}\approx \frac{2}{7}a^*$ or $\frac{2}{7}c^*$. The results reported below give strong evidence that the CDW is even stable up to the crystal melting temperature.

The single crystal samples were grown in RbCl-LiCl flux by our collaborators at the University of Michigan as described in Ref. [82]. The ARPES was performed at the Ames-Montana beamline of the Synchrotron Radiation Center (SRC) at the University of Wisconsin and at beamline 5 of the Stanford Synchrotron Radiation Laboratory (SSRL). The resonant photoemission experiment was performed at the Dragon beamline of Brookhaven National Laboratories (BNL) and at the Ames/Montana beamline of the SRC. Our sample orientation by Laue diffraction did not distinguish the very slight orthorhombicity (Fig. 4.1 caption). The sample was cleaved *in situ* just before the measurement, which was done at room temperature and at pressure $\approx 4 \times 10^{-11}$ Torr (SRC, SSRL) and $\approx 2 \times 10^{-10}$ Torr (BNL). The Fermi energy (E_F) and instrumental energy resolution were calibrated with a reference spectrum taken on a freshly sputtered surface of Pt foil (SRC) or a freshly evaporated Au surface (SSRL). At BNL, E_F was self-referenced and the energy resolution was known taken from an empirical calibration table for the monochromator and the analyzer. The angular resolution for the ARPES spectrometer was $\pm 1^o$, which amounts to ± 5 % of the distance from Γ to X in the Brillouin zone. Other detailed information, such as the instrumental energy resolution, for each data set will be reported as appropriate below.

---

[1] As often happens, the CDW satellites are too weak to be observed in X-ray diffraction, which lacks the sensitivity that multiple scattering imparts to electron diffraction.

4.2 Sm valency

The Sm valency in SmTe$_3$ is important in understanding the valence band electronic structure, because it determines the filling of the valence band. Previously [82], the temperature dependent magnetic susceptibility was fitted with a theoretical equation of a local moment magnetic susceptibility to show that Sm is nearly trivalent. We have performed a resonant photoemission spectroscopy (RESPES) study at the Sm $4d$ edge to obtain the valency information. In RESPES, the photon energy is tuned across an atomic absorption energy to enhance the intensity of a certain atomic character. In the current case, the absorption edge is that of the Sm $4d \to 4f$ transition. The photoelectrons (e^-) excited by photons near this absorption energy can be classified as coming from two channels. One channel is direct emission from the valence band:

$$4d^{10}4f^n + h\nu \to 4d^{10}4f^{n-1} + e^-.$$

Another channel is the so-called Auger emission preceded by resonant absorption of photons:

$$4d^{10}4f^n + h\nu \to 4d^9 4f^{n+1} \overset{(e^2/r)}{\longrightarrow} 4d^{10}4f^{n-1} + e^-.$$

As the photon energy is swept from below the edge, the interference between these two channels leads to a pre-edge minimum (“anti-resonance”) followed by a resonant enhancement of the $4f$ photoemission signal [88]. At this resonance, the $4f$ component of the photoemission is greatly enhanced compared to other features. The resonantly enhanced $4f$ intensity for Sm ions shows distinct features well separated for 2+ and 3+ Sm ions, each with its own resonant energy because the $4d \to 4f$ edge varies with valency. These spectra are well documented for the so-called mixed-valent materials, SmB$_6$ [89] or the Sm metal surface [89, 90], which show characteristic multiplet structures of the 2+ and 3+ Sm ions at the same time.

Fig. 4.2 shows Sm $4d$ resonance photoemission spectra for SmTe$_3$, obtained at BNL. The energy resolution is 150meV FWHM. The resonant enhancement of the $4f$ photoemission signal which maximizes at $h\nu = 140$ eV is quite obvious. The data show the general behavior found for RESPES, an anti-resonance minimum ($h\nu \approx 130$ eV) followed by a resonance enhancement ($h\nu \approx 140 \sim 150$ eV). On resonance, the spectra show a characteristic 4 peaks [89, 90] at binding energies 6.0 eV, 7.7 eV, 8.4 eV, and 10.0 eV, which corresponds to the well known multiplet structure of the $4f^4$ final state configuration of a $4f^5$ Sm^{3+} ion. The $4f$ emissions from Sm^{2+}ions of the Sm metal surface

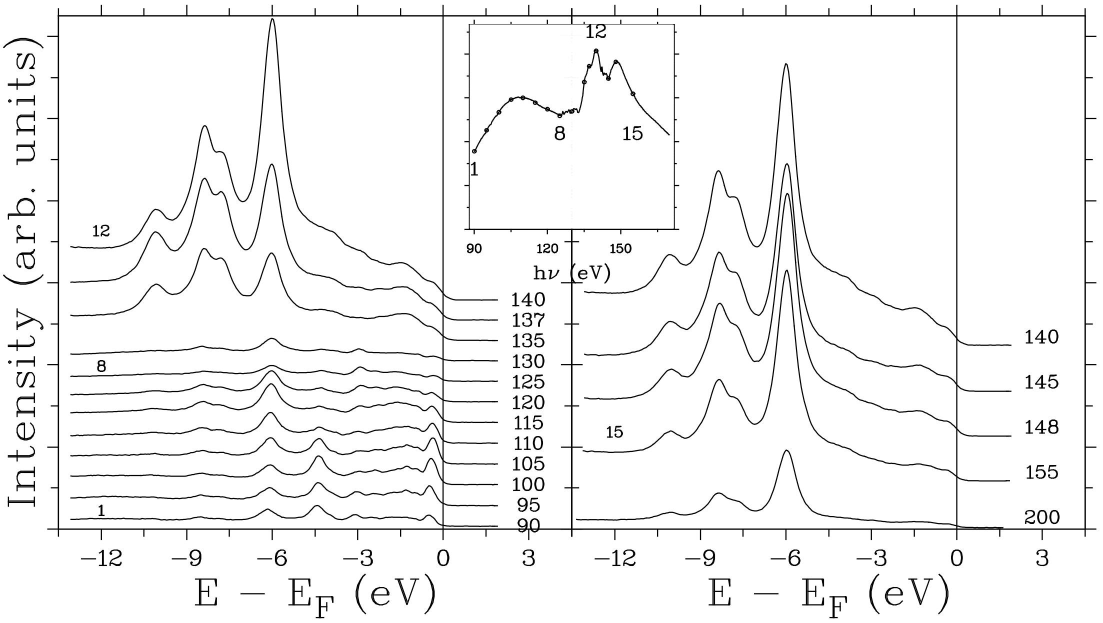

Figure 4.2: Resonant photoemission at Sm $4d$ edge for SmTe$_3$. Inset shows absorption spectrum.

show [89, 90] strong double structure near E_F and extend downward to show a small peak which overlaps with the lowest binding energy peak of the Sm^{3+} multiplet structure. For SmB$_6$ [89], the Sm^{2+} $4f$ emissions have a similar lineshape but they are farther away from the Sm^{3+} $4f$ emissions. Current data for SmTe$_3$ do not show any emission characteristic of the multiplet structure of Sm^{2+} $4f$ emissions. The general increase of intensity in the region of binding energy < 5 eV for $h\nu \approx 140$ eV is attributed to non-f emissions, possibly emissions from Sm $5d$.

Fig. 4.3 shows RESPES data obtained at the SRC. Fig. 4.3 (a) shows the constant initial-state spectroscopy (CIS) results, obtained by monitoring the intensity at a fixed binding energy as a function of photon energy. Fig. 4.3 (b) shows EDC's at two representative photon energies. The total instrumental energy resolution is 550 meV FWHM here, and explains less well resolved f peaks in this figure compared to the data in Fig. 4.2. The CIS spectrum of the peak at the binding energy A, shown in Fig. 4.3 (a) shows the well-known behavior [90] for Sm$^{3+}4f$ emission: the fine structure at the anti-resonance followed by two resonance peaks. On the other hand, the CIS at peak B shows a pattern which is quite different from the known resonance behavior of Sm^{2+} $4f$ emission. For example, the CIS spectrum for Sm^{2+} $4f$ emission shows a strong peak at $h\nu = 135$ eV followed by a weaker and broad peak at $h\nu = 142$ eV, none of which is observed in our CIS for the peak B.

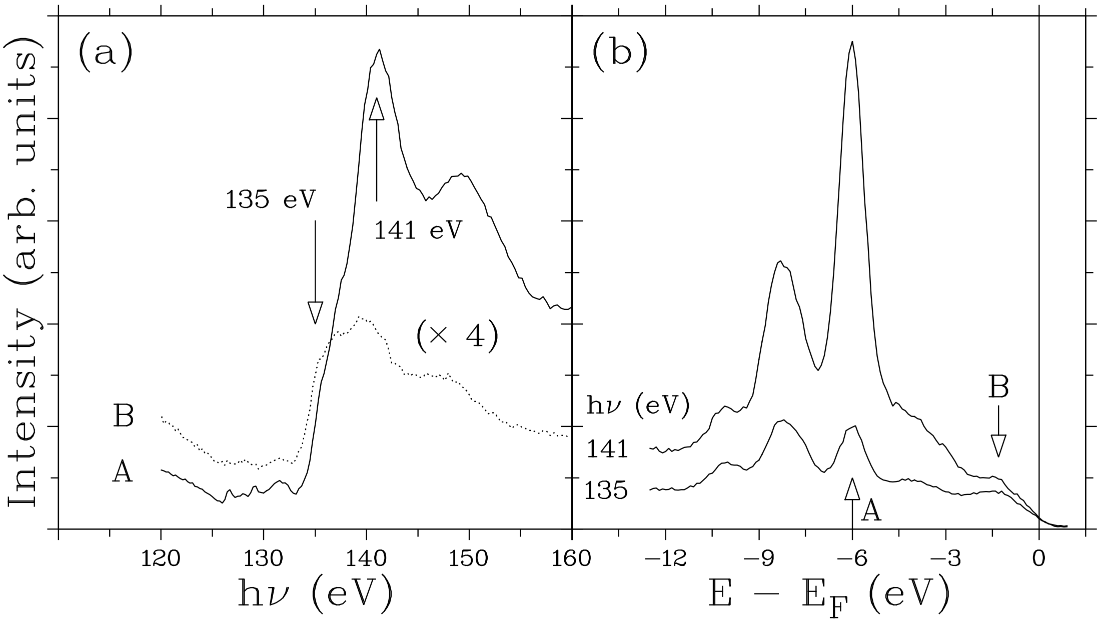

Figure 4.3: (a) Constant initial-state spectroscopy (CIS) at two binding energies A and B and (b) EDC's at two selected photon energies of 141 eV and 135 eV.

In short, we conclude that the Sm ion in SmTe3 is tri-valent because Sm^{2+} $4f$ emissions are simply undetectable in our data. This finding is in good agreement with the previous estimate of Sm valency [87] obtained from magnetic susceptibility measurement.

4.3 Band Structure

We summarize the band structure of the Te layer in SmTe3, as calculated by an extended Hückel [91] tight binding model. A similar report was already made in Ref.'s [87] and [92]. Here we discuss the bands with a little more details. As in previous reports, the calculation is performed for Te $5sp$ bands in the single Te layer of the SmTe3 structure. In Ref. [87] it was shown that this approximation is good enough to show the nesting property of the calculated FS by the CDW wave-vector implied by the satellite spots in the transmission electron microscope (TEM) diffraction pattern. In section 4.5, we will see that this nesting scenario is confirmed by our direct FS image. We will also find that the band splittings due to the Te layer-Te layer interaction in the double Te layer is of little importance.

Fig. 4.4 shows the band calculation result along high symmetry directions. The calculation was done using the EHMACC program [91] with extended Hückel parameters taken from the work on ZrTe3 [93]. To determine the Fermi energy, 6.5 electrons were

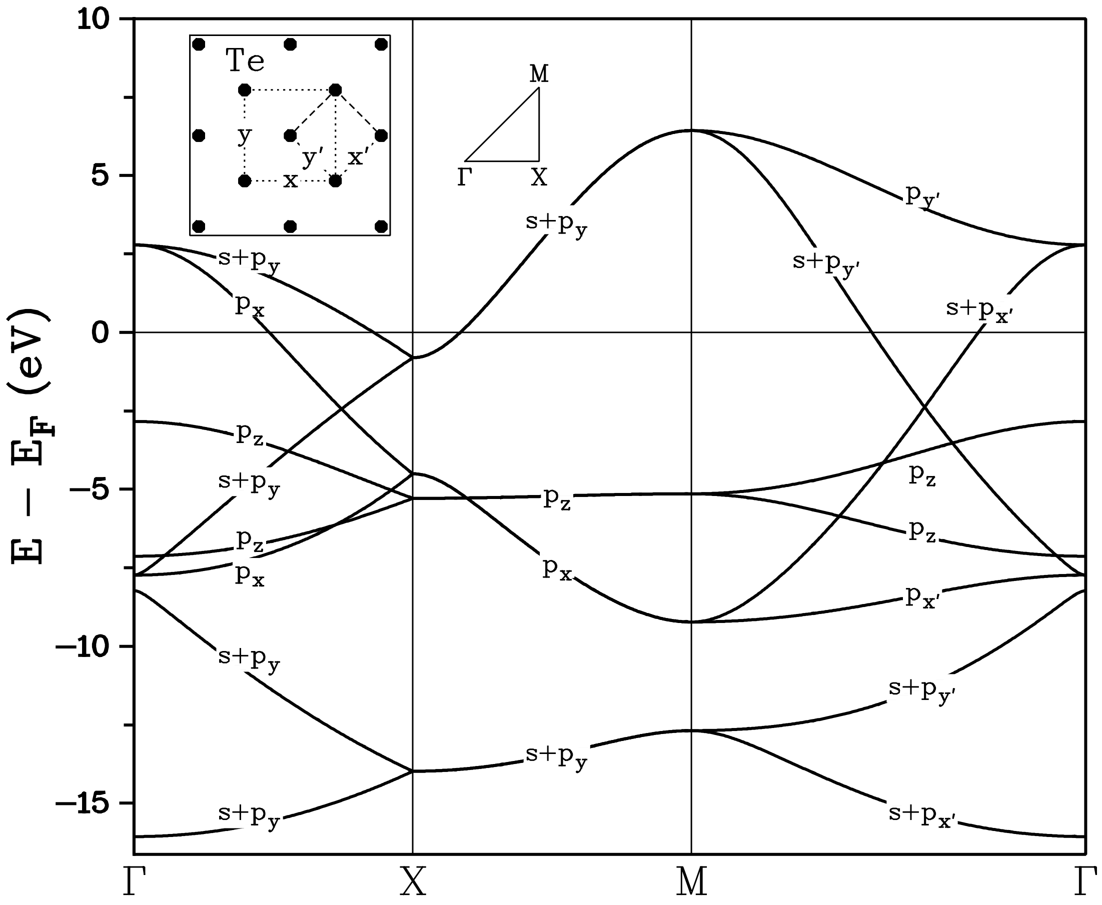

Figure 4.4: Valence band structure of SmTe$_3$ within the single Te layer approximation. The Te layer is shown in the inset with a unit cell shown with dotted lines. High symmetry directions Γ-X-M-Γ are also shown. Bands are labeled with atomic orbital names where "+" means hybridization. The coordinate systems xy and $x'y'$ are defined in the inset.

assigned per Te in the $5sp$ orbitals. This follows from having trivalent (3+) Sm as discussed in the last section and divalent (2-) Te as appropriate for insulating Te bands in the SmTe layer.

To understand the band structure, it is helpful to note that to a very good approximation the structure of the Te layer can be viewed as a perfect square net. The unit cell dimensions along the x and y directions (see inset of Fig. 4.4) are different only by 0.09 % and the angle between the two consecutive nearly collinear nearest neighbor Te pairs is 179.877^o, deviating only by 0.123^o from a perfect plane. These slight deviations from the square net structure are included in the calculation, but their effects are practically invisible. Within the square net approximation, the unit cell is halved compared to the real Te layer unit cell, and is most conveniently chosen to be the dashed square shown in the inset of Fig. 4.4. This means that the BZ for the real Te layer is half the size of the BZ for the square net. Therefore, the bands for the real Te layer can be obtained from those of square Te layer by band back-folding.

As shown in Ref. [92], group theory tells much about the *sp* band structure of a square net. In Fig. 4.4, we show the atomic character deduced for each band. In addition, a few symmetry related properties are worth mentioning specifically. First, the p_z orbital does not hybridize with any other orbital because it is odd under reflection through the plane, while other orbitals are even. For the the band filling appropriate for SmTe$_3$, the p_z band is completely filled and therefore irrelevant for the FS. Second, non-zero hybridization between $p_{x'}$ and $p_{y'}$ occurs only at the next nearest neighbor and beyond. Third, non-zero hybridization between s and $p_{x'}$ or $p_{y'}$ orbitals occurs only at the nearest neighbor pairs and beyond.

Fig. 4.5 shows the calculated FS. At the crudest level of the theory with the *s*-*p* and $p_{x'}$-$p_{y'}$ hybridizations ignored, the bands that generate the FS can be thought of as two one dimensional bands of $p_{x'}$ and $p_{y'}$ characters respectively. The FS for this case is shown as dotted lines in the figure. When the equally important *s*-*p* and $p_{x'}$-$p_{y'}$ hybridizations are included, the relative positions of the bands, some of which are previously degenerate, change, and the resulting FS becomes that shown by the solid lines. As pointed out in Ref. [94], the theoretical nesting vector can be viewed as originating from the perfect nesting vector of the two one dimensional FS's. In the figure, we show the CDW obtained by TEM diffraction spots [87], $\sim 0.143\Gamma$Y(X). One can see that this wavevector approximately nests the theoretical FS. This nesting vector for the final FS is similar to the vector that nests the two one dimensional bands at the same time, 0.125ΓY(X). This idea, maximal nesting of underlying 1 dimensional bands, is exactly that of the hidden 1 dimensionality which we will discuss in Chapter 5. Compared to the case of the purple bronzes discussed in Chapter 5, the current case has a bigger deviation from underlying one dimensionality.

4.4 Valence Band ARPES

Fig. 4.6 shows angle resolved photoemission EDC's at normal emission as a function of photon energy, obtained at the SRC. As Eq.'s 1.3 and 1.4 show, changing photon energy corresponds to changing momentum component $k_z = k_\perp$ perpendicular to surface. To know the range of $k_\perp$ that is covered by our photon energy range using these equations, we need to know the value of the inner potential V_o. A common way of obtaining this value is actually by measuring the dispersion as a function of $k_\perp$ and associating any observed periodicity with the Brillouin zone size. In other words, our lack of disper-

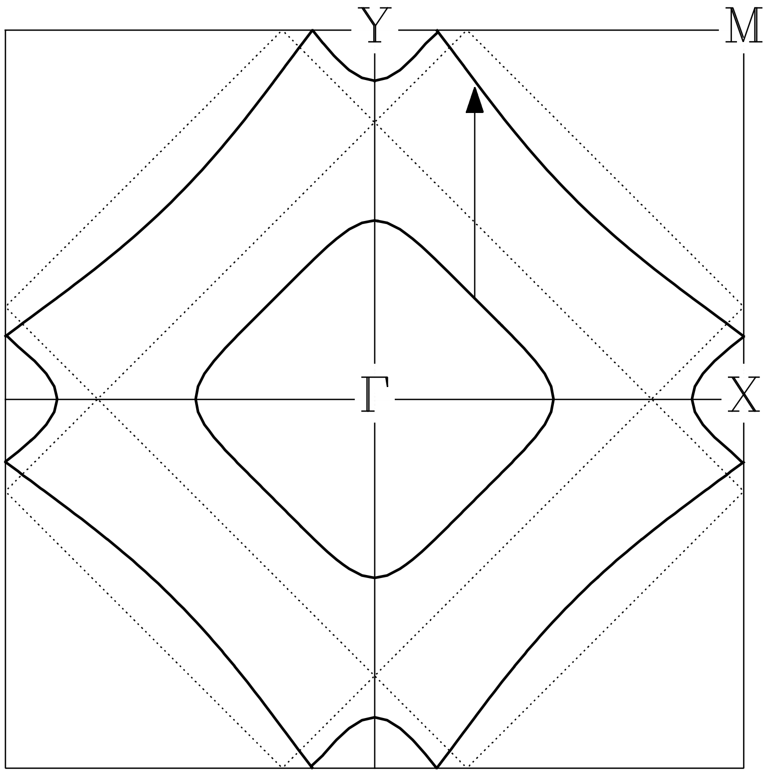

Figure 4.5: Theoretical FS for $SmTe_3$ shown in the first Brillouin zone. The solid lines show the FS calculated for the single Te layer within the extended Hückel tight binding method. The dotted lines are the one dimensional FS's for $p_{x'}$ and $p_{y'}$ bands and are obtained by turning off the *s*-*p* and $p_{x'}$-$p_{y'}$ hybridizations. The arrow represents one of the nesting vectors obtained by the TEM diffraction [87]. The other TEM nesting vector is obtained by rotating the arrow by 90 degrees.

sive features perpendicular to the surface means that we cannot determine V_o using this method. Typically V_o is about 10 eV, and a conservative upper bound could be taken as 20 eV. The size of the Brillouin zone along the surface normal is 0.244 Å^{-1}. One finds that $h\nu = 14\,\mathrm{eV} \rightarrow 18.4\,(25.9)\,\mathrm{eV}$ covers the repeat distance along the normal direction for $V_o = 10\,(20)\,\mathrm{eV}$. Therefore, we are probing more than one Brillouin zone in Fig. 4.6. Within the framework of section 1.1, ARPES as a function of photon energy probes band dispersions perpendicular to cleavage surface. Our data do not show any dispersion, suggesting that there is no band dispersions along the surface normal. This is consistent with the quasi-2 dimensional structure resulting from the layered structure of SmTe$_3$. However, one should also keep in mind that in general a one dimensional density of states effect (section 1.2) could hide the dispersion perpendicular to the surface.

Fig. 4.7 shows ARPES dispersions along the ΓM direction parallel to the cleavage plane, obtained at SSRL. The alignment was such that the ΓM direction is approximately horizontal (x axis in Fig. 1.1) with ϕ_N (Eq. 1.11) $= 11^o$. The small curvature of the momentum space path for varying θ at $\phi = \phi_N$ due to finite ϕ_N is noticeable in the inset. In contrast to the normal emission data, this data set shows strongly dispersing peaks. The closest approach to E_F of the dispersing ARPES peaks occurs at $\theta = 7^o \sim 9^o$ and $55^o \sim 53^o$, with the lowest binding energy ≈ 240 meV. As the momentum value moves toward the M point, these peaks flatten very quickly ($\theta = 13^o \sim 15^o$ and $\theta = 51^o \sim 49^o$) at binding energy $\approx$ 0.67 eV, and the intensity fades away. While this happens, another flat dispersion appears at binding energy ≈ 0.96 eV. As the first peak fades away, the second peak starts to disperse quickly to high binding energy, merging into the region of general high intensity at binding energy 1.6 $\sim$ 2.9 eV at the M point.

A convenient way to represent the band dispersion information contained in ARPES data is to make a continuous scale map. Fig. 4.8 shows a gray-scale map representation of Fig. 4.7. Arrows point to the regions where the two flat bands exchange weights as discussed just above. This figure suggests that these two bands originate from a single parabolic band which is gapped at the pointed regions. We will discuss the origin of this gap later in this section. Here we note that the map representation makes it easy to observe the reflection symmetries with respect to the points Γ and M.

Fig. 4.9 shows EDC's along the ΓM direction taken at the SRC. The sample was oriented so that the ΓX direction is parallel to the horizontal axis. The data are quite

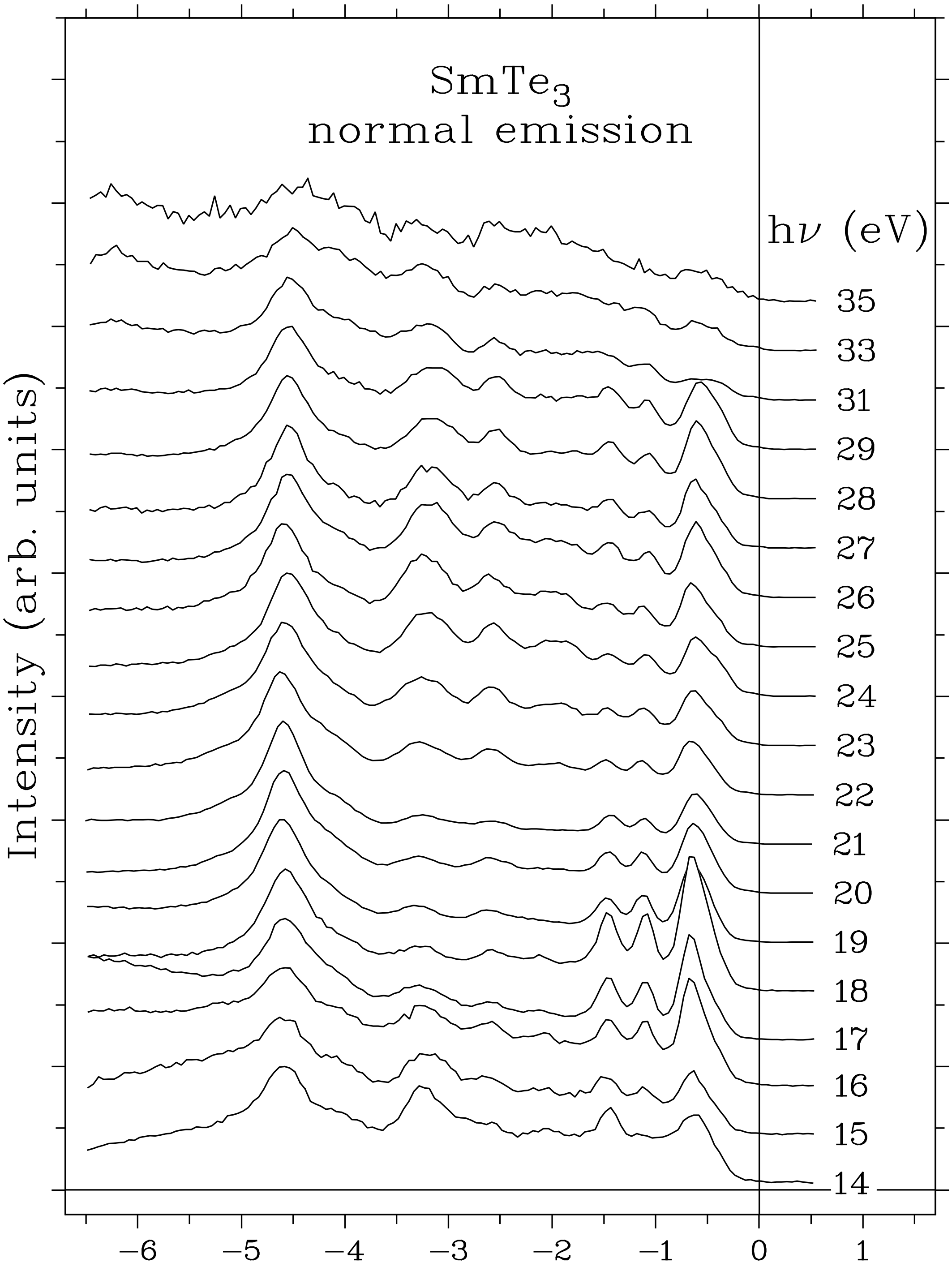

Figure 4.6: Normal emission spectra of SmTe$_3$ as a function of photon energy.

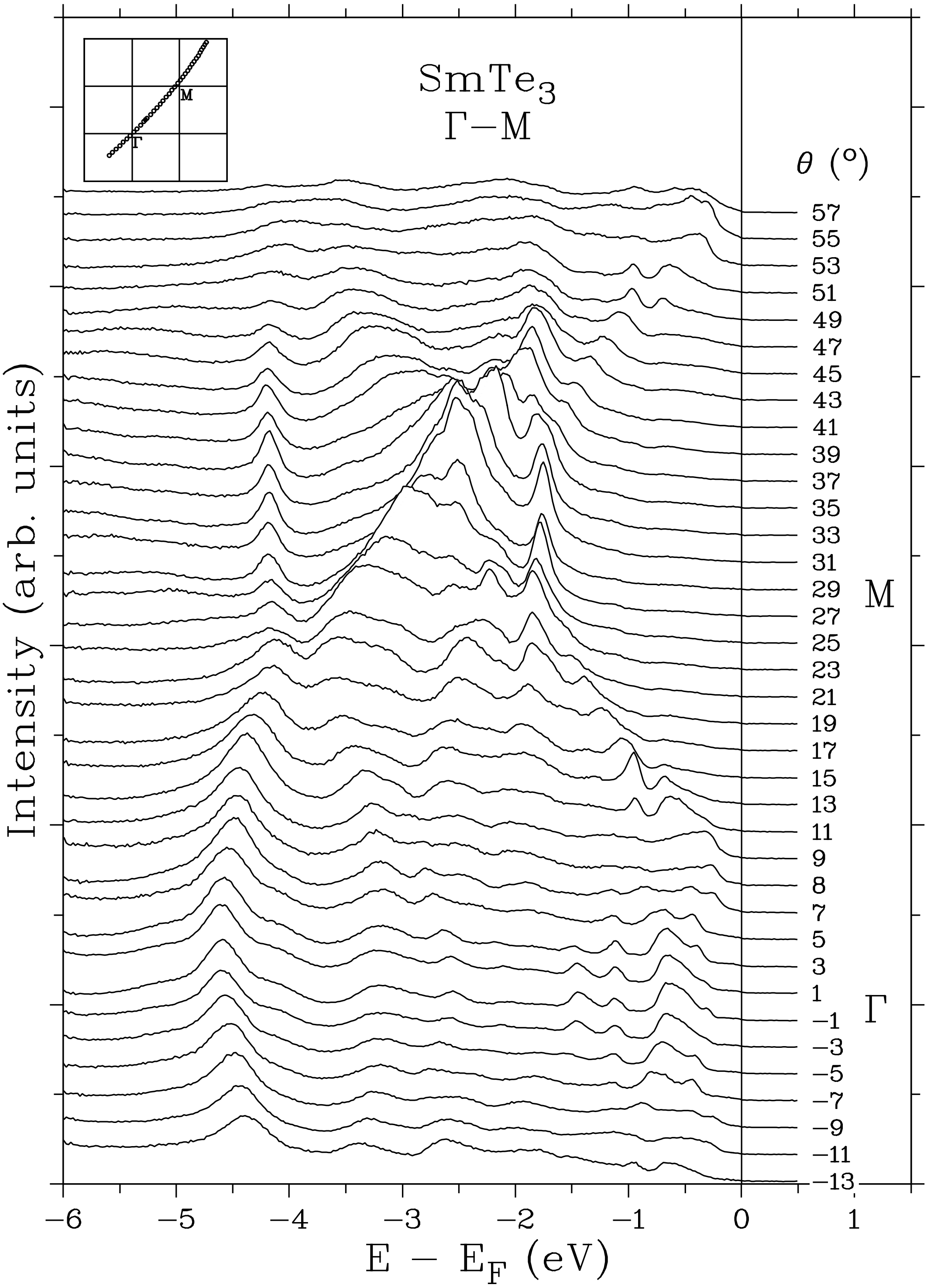

Figure 4.7: EDC's obtained for SmTe$_3$ showing dispersions along the ΓM direction, with $h\nu = 22.4$ eV, $T = 30$ K, and ΔE (instrumental energy resolution) = 34 meV FWHM. The sample was aligned so that the horizontal axis (x axis in Fig. 1.1) is parallel to ΓM direction.

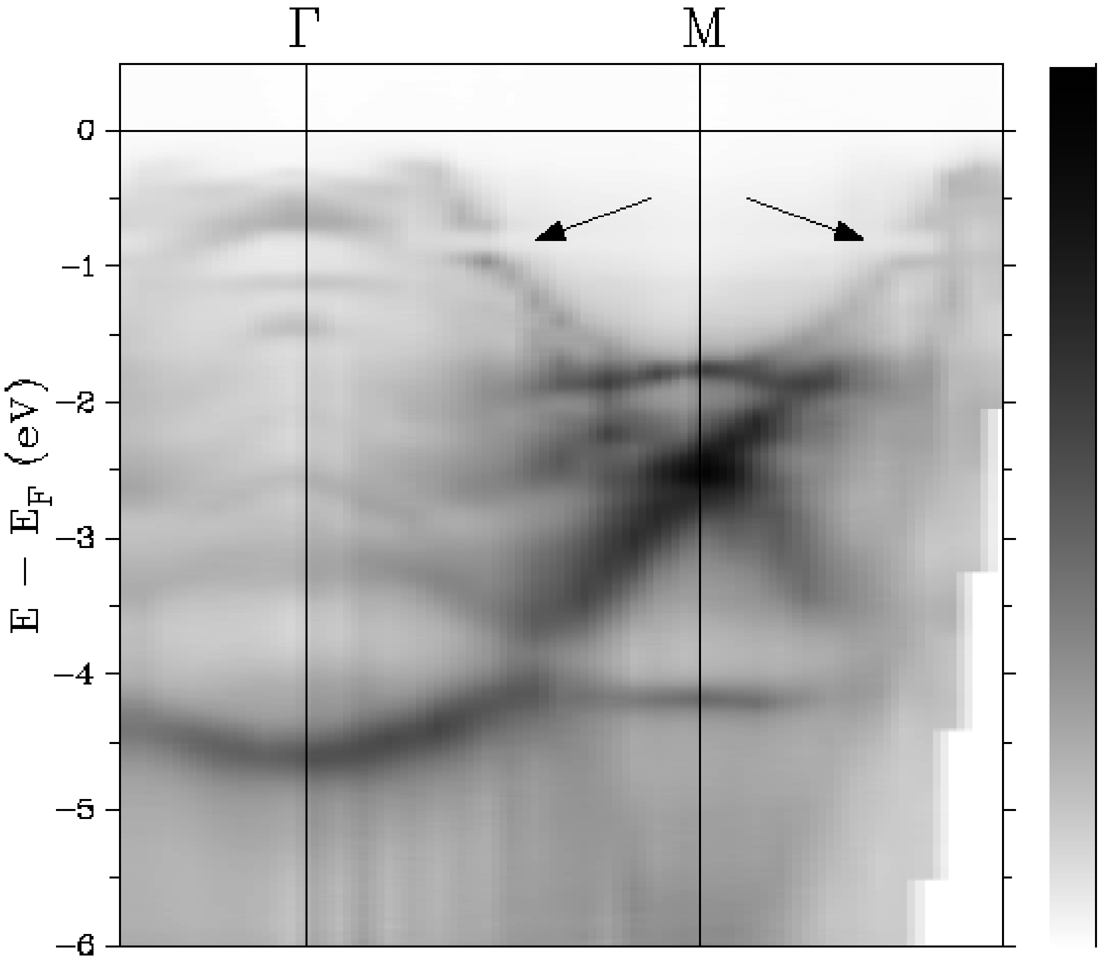

Figure 4.8: Gray scale map of $SmTe_3$ ARPES data along ΓM. The data set is the same as Fig. 4.7.

similar to the SSRL data except for broader peak widths due to the worse energy resolution, signifying no strong polarization dependence arising from the different sample orientations. With the poorer resolution, one sees that the near E_F peak has become quite structureless and at its closest approach to E_F ($(\theta, \phi) = (6,10)$ and $-(6,2)$) has a tail extending to E_F. This "leakage" of weight from a finite binding energy peak to E_F due to instrumental energy broadening is of importance in interpreting the Fermi energy intensity map to be discussed in the next section.

Fig.'s 4.10 and 4.11 show dispersions along other symmetry directions, ΓX, ΓY, XM and YM. These data show a very similar set of spectra for the ΓX and ΓY directions, and also for the XM and YM directions. Basically this is consistent with the near tetragonal symmetry of the SmTe$_3$ crystal. Fig. 4.12 summarizes the SRC data in a gray scale map., with an arrow pointing to the same gap feature observed in the SSRL data, pointed out above.

We now try to compare the experimental dispersions with the band theory. We assign the majority of the bands observed experimentally so far to the Te $5p$ bands. The reasoning is as follows. As we showed above that Sm is trivalent, we do not expect to see Sm $4f$ peaks in this binding energy range. Furthermore, at this low photon energy, the photoemission crossection [9] of Sm $4f$ states is negligible compared with that of Te $5p$. Therefore, the dispersions plotted here are coming from Te *5s* and *5p*, with some possible admixture of Sm *5d* and *6s* character. We also rule out the observation of Te $5s$ bands in this energy region as follows. First, the calculated atomic photoemission crossection [9] for the Te $5s$ orbital is two orders of magnitude smaller than the crossection of the Te $5p$ orbital. Second, at higher photon energies (hν = 40 eV and 70 eV) Te $5s$ bands are observed to lie at $\sim$ 11 eV binding energy, in a good agreement with the Te $5s$ band observed for TiTe$_2$ [95]. The value of 11 eV binding energy is similar in magnitude to the binding energy value of 12.9 eV used in the band calculation.

Fig. 4.13 shows the comparison of our ARPES data with the band theory of the last section. The theoretical Te $5p$ bands, the upper 6 bands in Fig. 4.4, were scaled down by a factor of 0.28 relative to E_F. This scaling factor was determined by identifying and roughly matching a pair of a theoretical band and an experimental band. The theoretical band is the one that has the p_x character along XM and the $s + p_{x'}$ character along the MΓ. This band shows a parabolic shape centered at the M point. The chosen experimental match for this band is the one that shows a similar parabolic intensity profile centered at the M point except for the gaps at E_F and at $\approx$ 0.8 eV binding energy

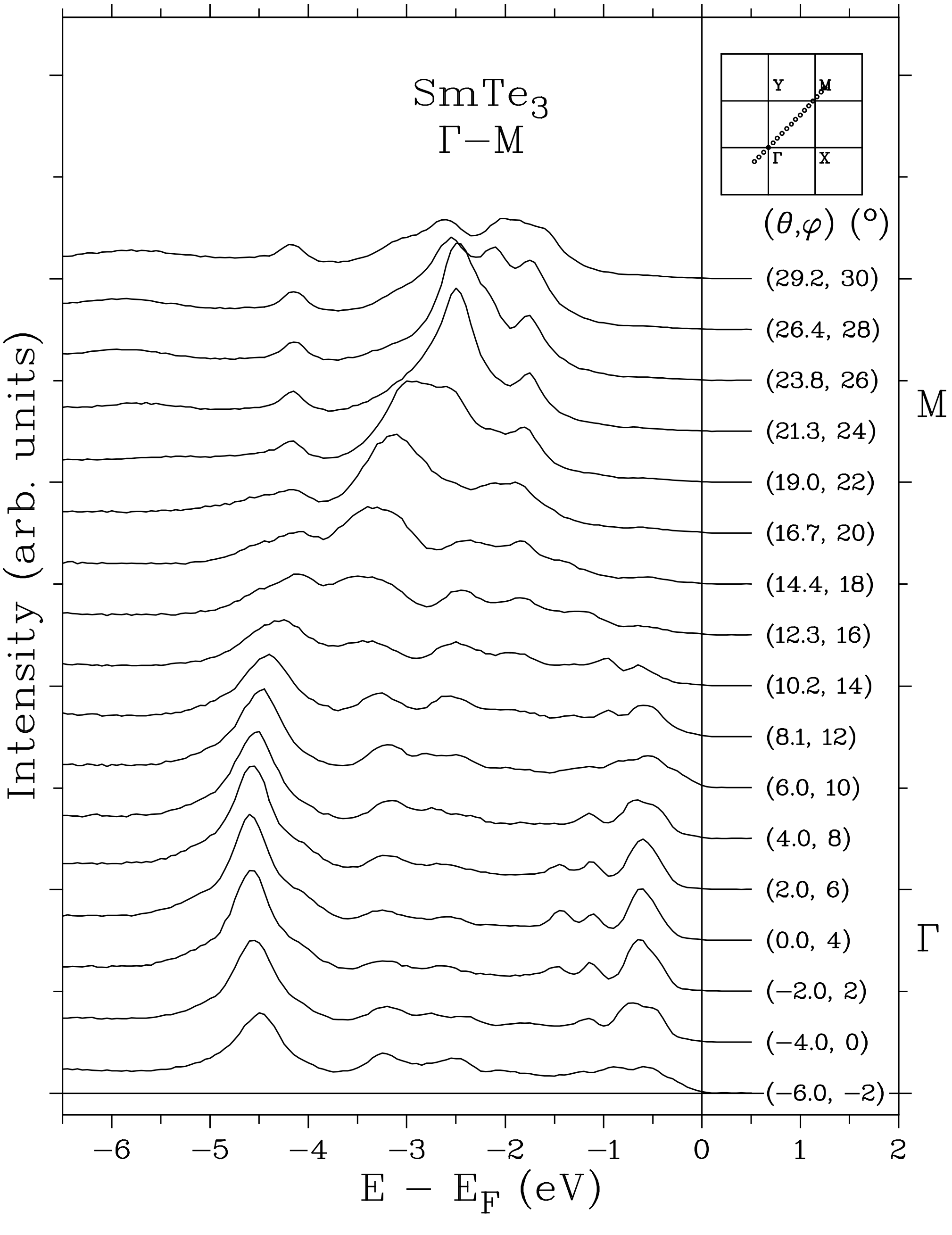

Figure 4.9: ARPES EDC's along ΓM for SmTe$_3$ taken with $h\nu = 21.2$ eV, $T = 25$ K, and ΔE =125 meV FWHM. The surface normal direction is given by $(\theta_N, \phi_N) = (0^o, 4^o)$.

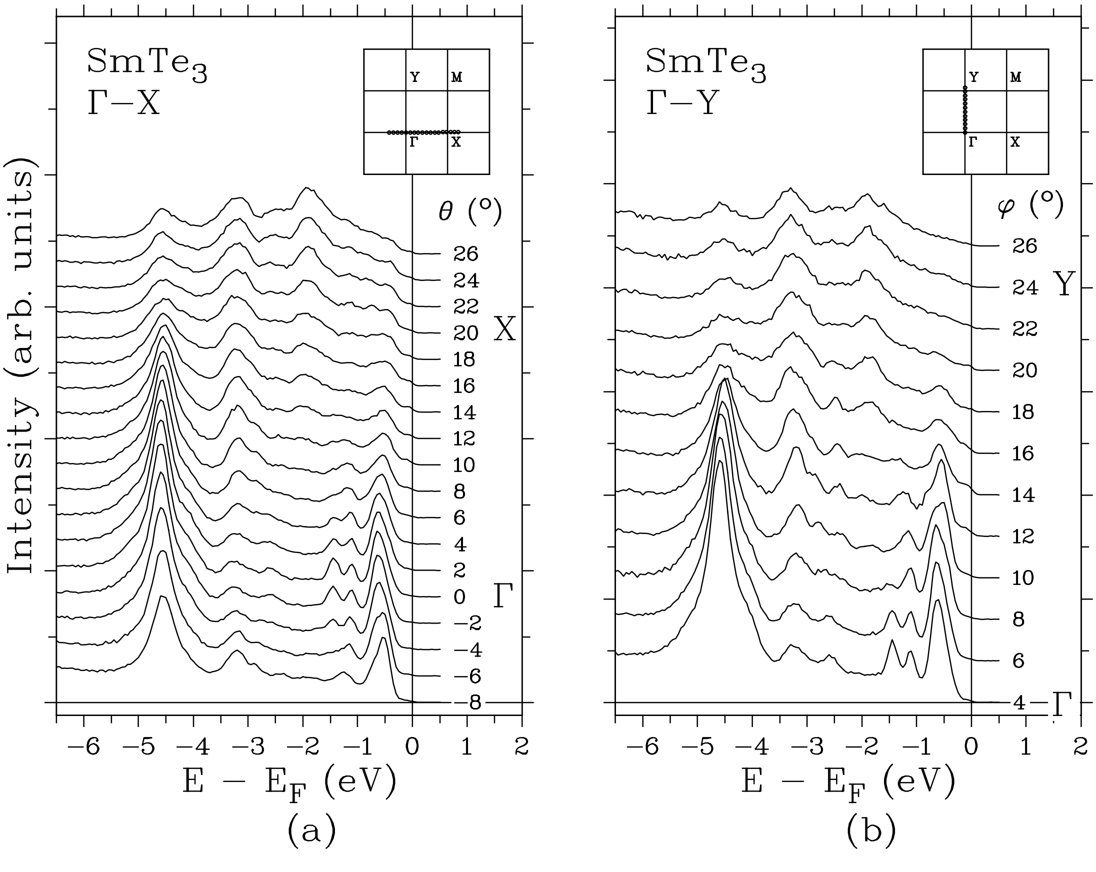

Figure 4.10: ARPES EDC's along ΓX and ΓY for $SmTe_3$. Experimental conditions other than angles are the same as in Fig. 4.9.

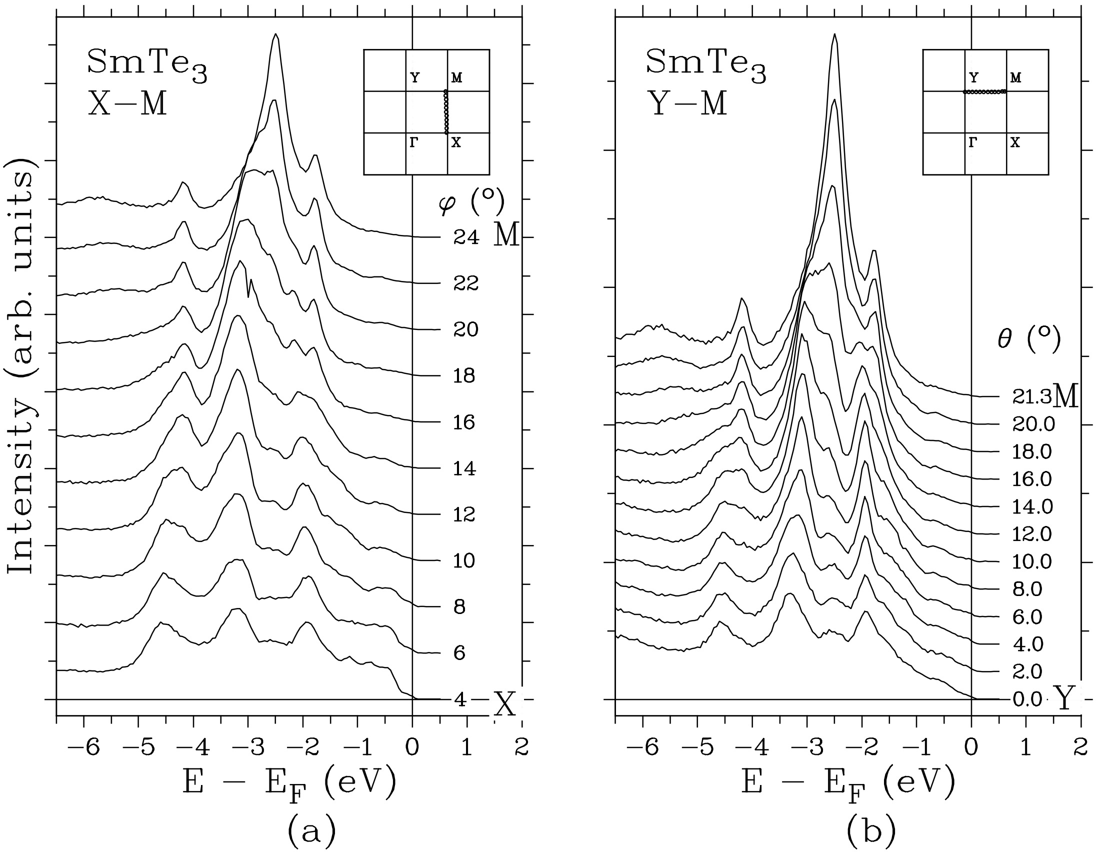

Figure 4.11: ARPES EDC's along XM and YM for SmTe$_3$. Experimental conditions other than angles are the same as in Fig. 4.9.

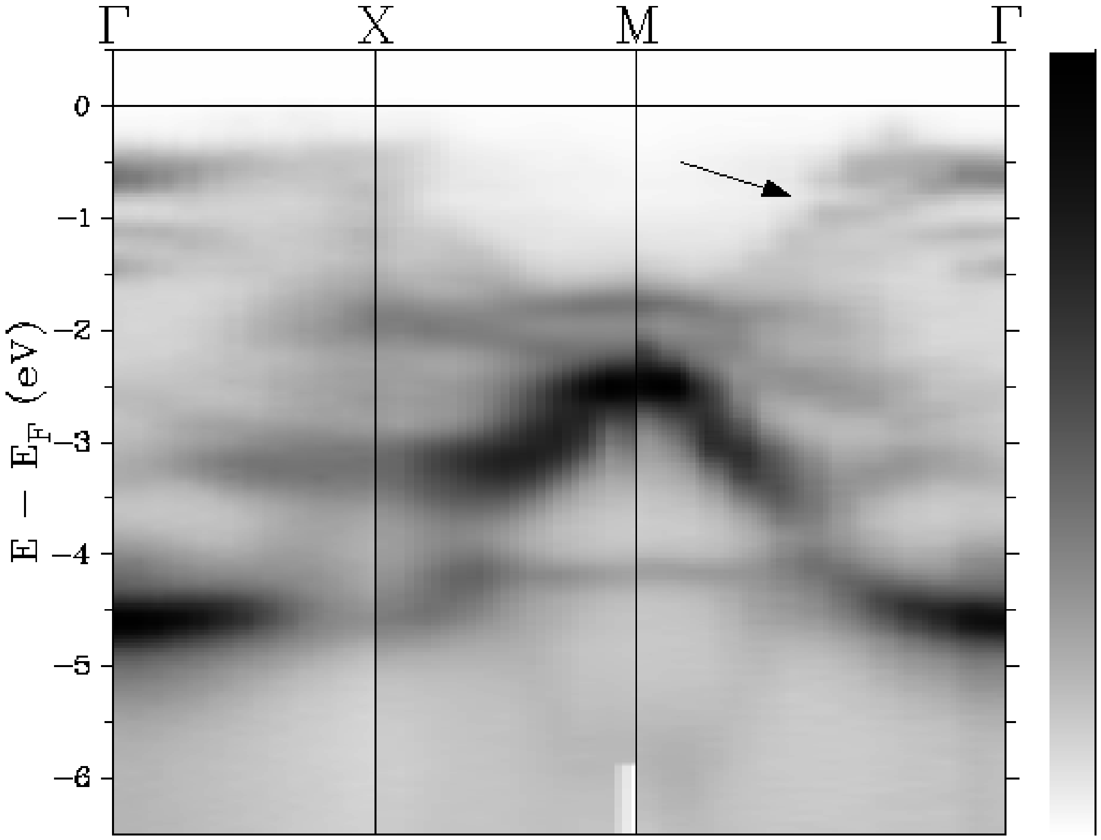

Figure 4.12: Gray scale map representation of ARPES along the path Γ-X-M-Γ for SmTe$_3$.

as pointed out above. By this scaling we also associate the band that is observed at ≈ 1.8 eV binding energy at the M point with the theoretical p_z band. One of the theoretical p_z bands lies in close proximity to the experimental band at binding energy $\approx$ 1.1 eV binding energy at Γ. Unfortunately, the spectra do not show enough continuity to associate this experimental band with the $\approx$ 1.8 eV binding energy peak at the M point. It is interesting to note that near Γ the flat feature at $\approx$1.1 eV is accompanied by another feature at 1.5 eV at Γ. Also, near M the flat band at $\approx$1.8 eV is accompanied by a band at $\approx$ 2.1 eV. A possible scenario is that these bands originate from the theoretical lower binding energy p_z band, split by the lowered crystal symmetry of the $\mathrm{SmTe_3}$ unit cell. However, the overall comparison of the band theory and the experiment is rather incomplete. Generally speaking the experimental dispersions along ΓX and MΓ are much weaker than in the theory, signalling that additional mechanisms such as symmetry lowering due to the full crystal field or CDW nesting must be invoked. In our comparison, the bands at binding energies greater than 2.5 eV are implicitly assumed to be the filled Te $5p$ bands of the SmTe layer. This could be checked by a band calculation for a complete unit cell.

So far, no discussion has been made about the states near the Fermi level, except to point out the gap observed along the ΓM direction. This is because, due to inadequate resolution and inadequate surface quality, most of the near E_F peaks are not clearly resolved in the spectra shown so far. A better measurement of the near E_F features was made successfully, and we will show the data in the next section. However it is worth pointing out already in this section that a Fermi energy intensity map similar to the one in the next section was obtained at the SRC on the same sample surface that gave the spectra shown so far. In particular, a 2 fold symmetric E_F intensity distribution, which in the next section we relate to an anisotropic CDW gap opening, is also observed. Therefore, the inequivalence of the ΓX and ΓY directions, and also of the XM and YM directions, only shows up in the near E_F states.

From the point of view of the CDW formation, it is an interesting question whether any band splitting at a finite binding energy relative to the simple band theory of the last section is due to the CDW. A dramatic band splitting over the entire bandwidth due to the CDW was observed for example in $\mathrm{TaS_2}$ [96]. A good candidate for such an effect in the current data set is the gap feature pointed to by an arrow in the map of Fig.'s 4.8 and 4.12. In order to answer this question, in Fig. 4.14 we plot the theoretical bands along the path Γ-X-M-Γ and along the paths that are translated by $\pm\boldsymbol{q}_{CDW}$ from

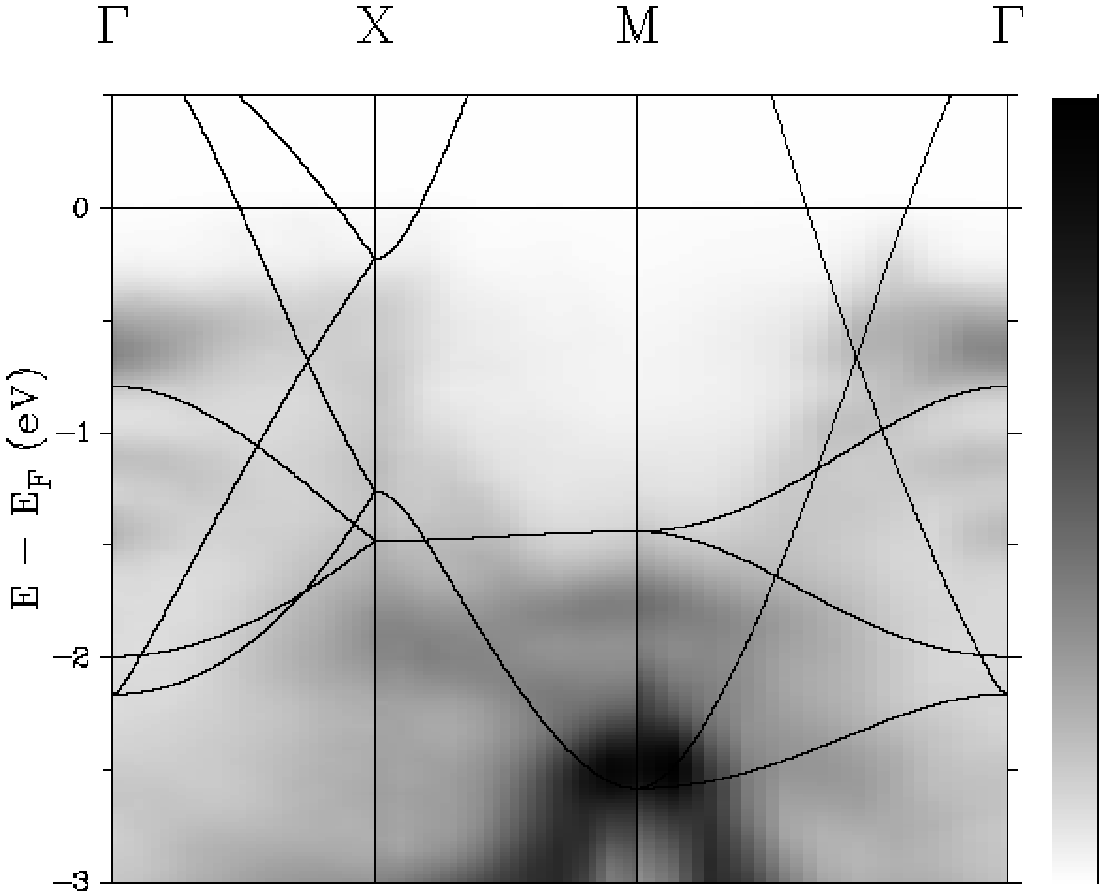

Figure 4.13: Comparison of SmTe$_3$ ARPES with band theory.

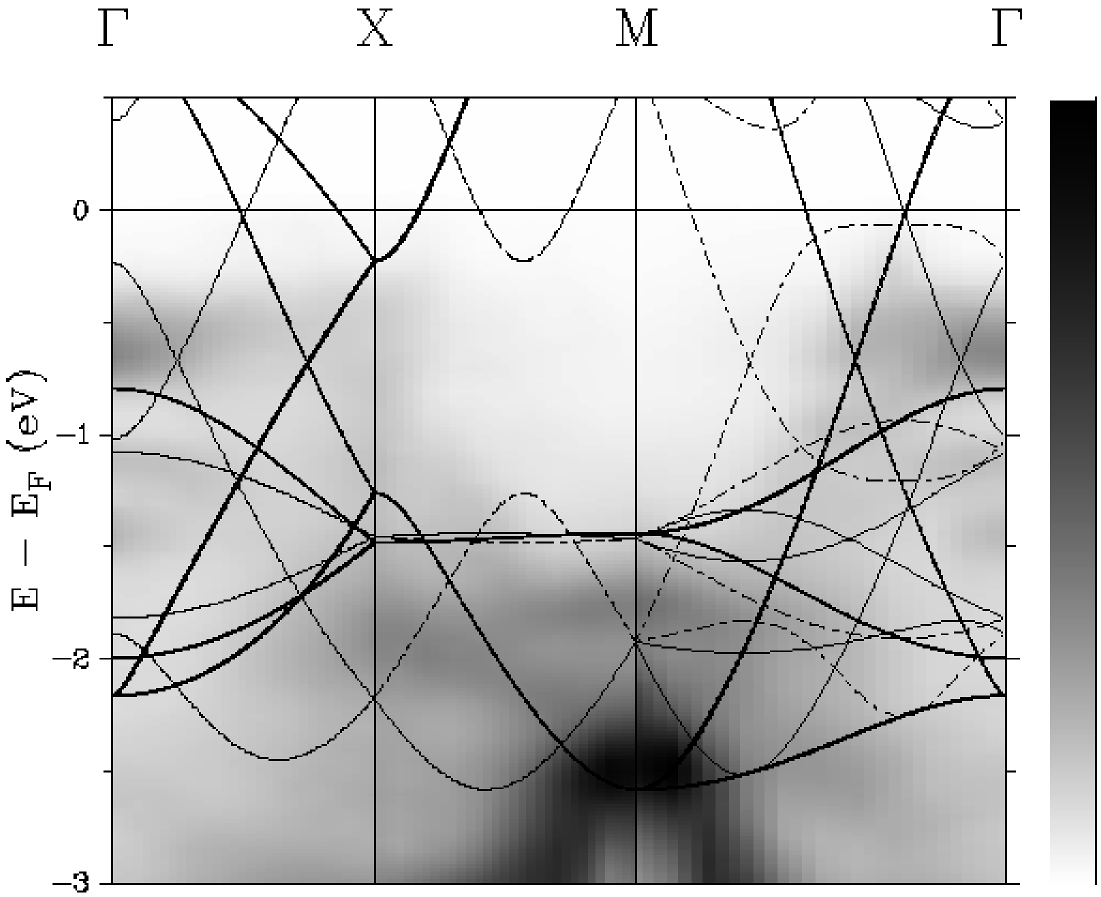

Figure 4.14: Comparison of SmTe$_3$ ARPES with CDW band theory. Thick solid lines are band theory along Γ-X-M-Γ, thin solid lines are band theory along the path shifted by $\boldsymbol{q}_{CDW}$ (arrow in Fig. 4.5) from Γ-X-M-Γ and dash-dotted lines are band theory along the path shifted by $-\boldsymbol{q}_{CDW}$ from Γ-X-M-Γ. Note that the bands for the paths shifted by $\pm\boldsymbol{q}_{CDW}$ from Γ-X are completely degenerate.

the path Γ-X-M-Γ. In principle, for an incommensurate CDW, there are an infinite number of interacting states at a given momentum. However, the strongest interaction effect is expected to occur for the pair of states connected by $\pm\boldsymbol{q}_{CDW}$. In this figure, we notice that no band overlap is induced at the binding energy ≈ 0.8 eV by the $\pm\boldsymbol{q}_{CDW}$ nesting. In fact, up to the band shifting of $\pm 3\boldsymbol{q}_{CDW}$.there is no overlap of bands at this energy position. Therefore, we conclude that the band splitting at ≈ 0.8 eV is not due to CDW nesting. Rather, it seems to be due to the mixing of the $p_{x'}$ and $p_{y'}$ bands due to the full crystal field of SmTe$_3$. A complete band calculation would be necessary for a more detailed comparison of the experimental band structure with theory and a more thorough discussion of possible CDW effects at finite binding energies.

4.5 Fermi surface and CDW gaps

In this section, we present the Fermi energy intensity maps and EDC's near E_F. Data taken in this section were obtained at the Ames/Montana beamline at the SRC, but on a different cleavage surface than the data of the last section. Due to minimizing the time between the cleave and the measurements of the near E_F states, in order to prevent surface degradation, and possibly also due to a better surface exposed by cleaving, rich detail of the near E_F structures were recorded. The experiment was done at room temperature. Photon energies of 21.2 eV and 17 eV were used with total instrumental energy resolution of 140 meV FWHM and 50 meV FWHM for the map and the EDC's respectively.

The FS geometry has been studied by making a momentum space E_F intensity map, a method introduced for the high temperature cuprate superconductors [97]. In our experimental geometry, shown in Fig. 1.1, the map is obtained by sweeping angles ϕ (angle between the photoelectron momentum and its projection p_{xz} in the xz plane) and θ (angle between the z axis and p_{xz}). The FS pattern is generated because the intensity at E_F reaches a local maximum when a dispersing peak passes through the FS. However a real ARPES experiment is characterized by a window with momentum and energy widths Δk and ΔE, set by instrumental angle and energy resolution, respectively. A dispersing peak contributes to a local maximum in the intensity map to the extent that the peak occupies the window, considering also the peak's intrinsic energy broadening and the relevant Fermi function. Depending on the specific details, a peak dispersing near to but not crossing E_F could contribute to the map, by either more or less than a peak actually crossing E_F. For the data presented below, gapped states near E_F do contribute to the intensity map, but less than the ungapped states.

Fig.'s 4.15 (a)-(c) show E_F intensity maps. The logarithm of the intensity was used to enhance the weaker part of the image. The data are overplotted with the two-dimensional (2-D) Brillouin zone of the crystal, labelled with notation for a 2-D rectangular lattice. The full map (a) was generated by xy reflections of the raw data of map (b). The reflection symmetries, which are observed to hold in the raw data of (b), are valid symmetry operations for the orthorhombic crystal shown in Fig. 4.1.

In Fig. 4.15 (a) we include in the lower left quadrant the theoretical FS as described in section 4.3. We note again that the slight difference in the a and c lattice parameters (Fig. 4.1 caption) is included in the calculation but is not visible in the results, which appear as perfectly four-fold symmetric. A detailed comparison of the theory and the

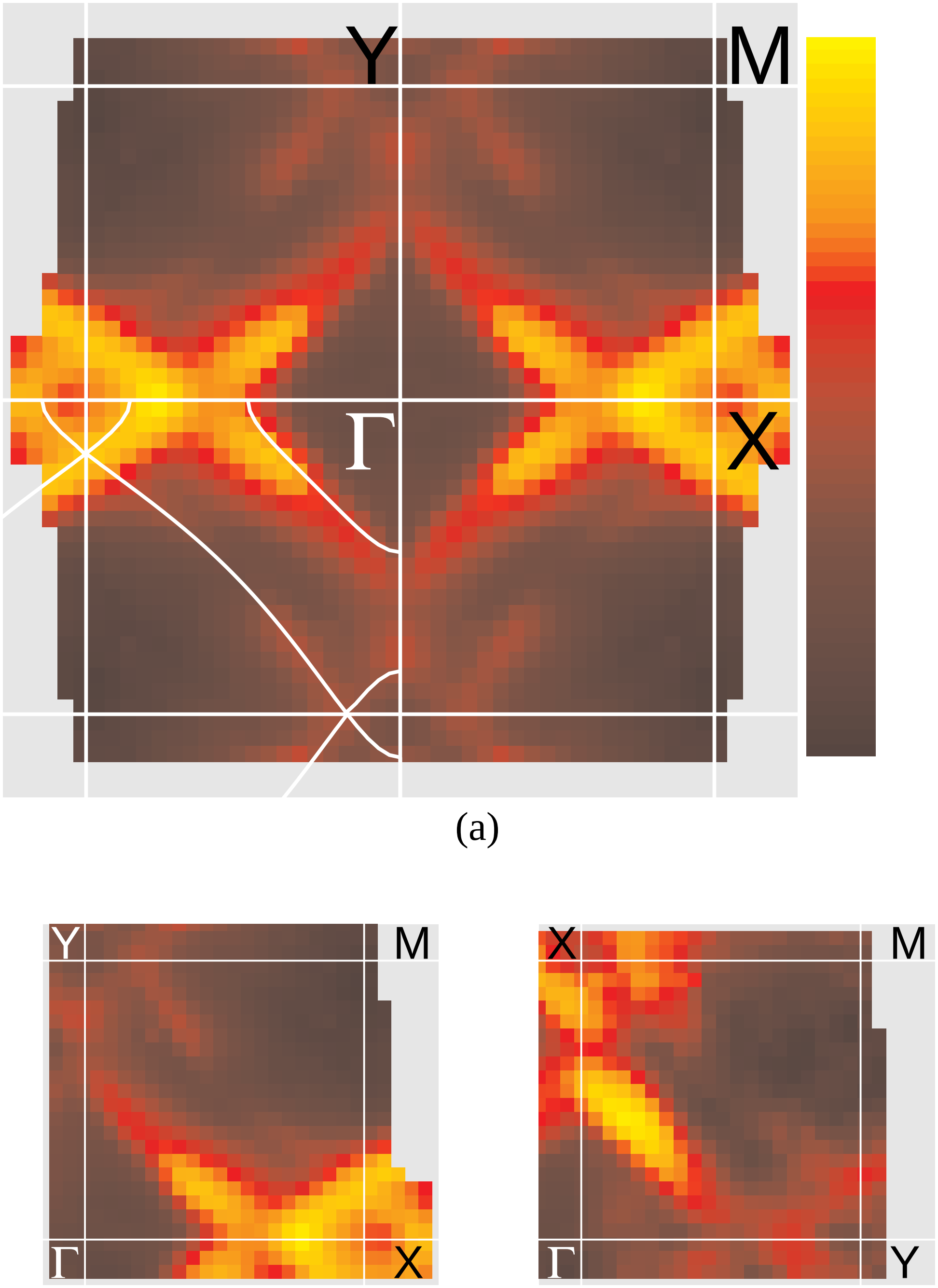

(a)

(b)

(c)

Figure 4.15: (a) Fermi energy intensity map of $SmTe_3$. The lengths of ΓX and ΓY could be either π/a and π/c or π/c and π/a. A theoretical FS is shown in the third quadrant. (b) Raw data for the map of (b). (c) Map taken after the sample was rotated by 90 degrees in the xy plane and then re-cleaved. In maps (a) and (b), ΓX and ΓY are parallel to x and y in Fig. 1.1, and in map (c), ΓY and ΓX are parallel to x and y. The maps of (b) and (c) consist of 725 and 723 data points, respectively.

experiment will be made below. For now, we simply note that there is a good general correspondence between all theoretical and experimental features, even though four-fold symmetry was not assumed in generating the experimental map. But, as we remarked above, one should not unconditionally interpret the pattern as showing the actual FS and it is noteworthy that in spite of its four-fold *shape*, the *intensity* variation is strongly two-fold symmetric.

One could conjecture that the two-fold symmetry involves the photoemission process in some way, e.g. selection rules involving the electron collection direction relative to the photon polarization. To test this possibility, maps (b) and (c) were taken for two sample orientations differing by 90^o, by remounting and recleaving the same crystal. In both cases the pattern is bright near the ΓX line and dim near the ΓY line. This shows unambiguously that the two fold symmetry is an intrinsic property of the crystal, not an extrinsic effect due to the photoemission process. We now show valence band EDC's which show *why* this two-fold symmetry occurs.

Fig. 4.16 shows ARPES spectra taken immediately after making the map of Fig. 4.15 (a). Consistent results were obtained from a smaller set of EDC's taken after making the map of Fig. 4.15 (c). The $\boldsymbol{k}$ values of the EDC's are shown as circles on the map. Along X→ Γ (Fig. 4.16) (a) three peaks (A,B,C) cross E_F at positions marked by the filled circles. We attribute the A-B splitting to the coupling between the Te layers. Along Y→ Γ, however, the three equivalent peaks (A′,B′,C′) show gaps. It might be noted that there exists a small amount of weight, especially near 20.1 %, within the gap. We will discuss this in the Appendix 1. The size of the gap for electron removal is about 300 meV for A′ and C′. The B′ peak tends to merge with A′ and we infer a similar gap size for both. Except for this gap vs. crossing aspect, however, the same general behaviors obtain for all the observed peaks in the EDC's for the two directions. A similar description holds along X→M and Y→M in Fig. 4.16 (b), where the gap size is 300 meV for the peak A′ and 260 meV for the peak B′. Other weakly dispersing peaks and shoulders at $\sim$ 500 meV to 700 meV below E_F are plausibly ascribed to Te p states in the insulating SmTe layer.

The origin of the two fold symmetric intensity variation is now clear. For example, the large gaps along ΓY displace the dispersing peaks nearly out of the energy window $\Delta \mathrm{E} = 140\mathrm{meV}$ so that the pattern is dim. Along ΓX with no gaps the pattern is bright. The four-fold symmetric shape of the map pattern is then interpreted as showing the "FS" – i.e., the FS that we would have obtained if there had been no gap – which we

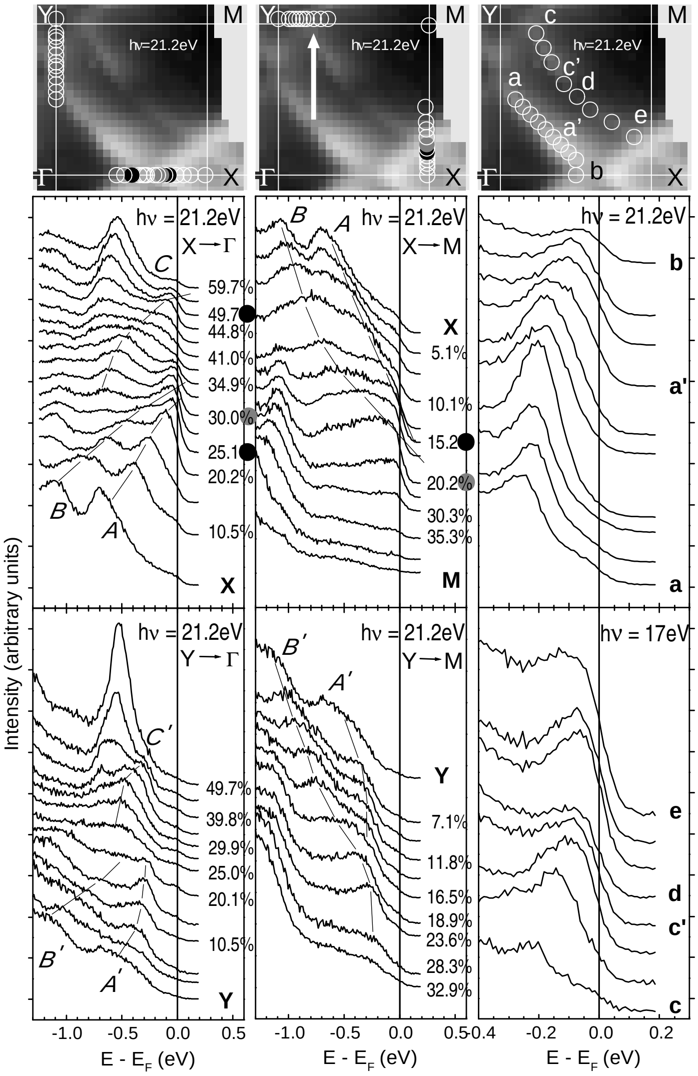

(a) (b) (c)

Figure 4.16: Near E_F ARPES spectra for various cuts in momentum space. Each circle in the map corresponds to a spectrum in the plots below the map. The filled circles represent Fermi energy crossing points determined from dispersions. The size of the circles represents the size of the **k** resolution due to the finite angle resolution of the spectrometer. In (a) and (b), the **k** value for each spectrum is given in terms of the percentile distance along each symmetry line. In the map of (b), we show a nesting wave vector, consistent with our experiment and the TEM result [87]. (c) shows the gap anisotropy. The photon energy $h\nu = 21.2$ eV for all spectra except the lower stack of (c), where $h\nu = 17$ eV to obtain adequate intensity near point d. All spectra are normalized to the photon flux, but each panel has a different overall scale.

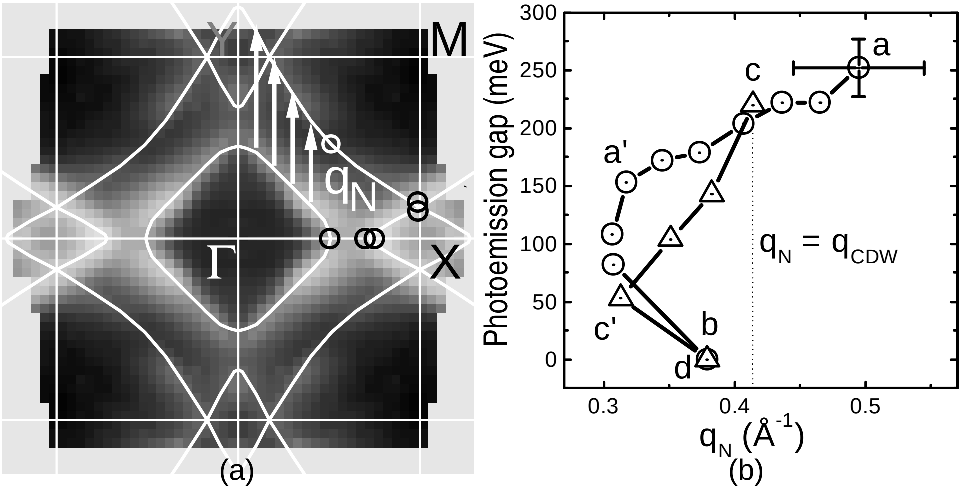

Figure 4.17: Experimentally deduced FS and gap anisotropy of SmTe$_3$. (a) E_F crossing points (circles) from EDC's, experimental "FS" (white line), and nesting vectors (arrows), $\boldsymbol{q}_N$, connecting "FS" pieces plotted over the E_F intensity map. (b) Electron removal gaps on the two "FS" pieces plotted as a function of q_N. The gap values are taken from the data of Fig. 4.16 (c). Representative error bars are shown.

will give the precise shape of below. These findings connect naturally to a CDW picture, with nesting wave vector as indicated in the map of Fig. 4.16 (b), as advertised near the end of the last section. This wave vector is precisely the $\boldsymbol{q}_{CDW}$ obtained from the TEM result [87], and gives the maximal nesting for our "FS." Fig. 4.16 (c) shows the gap anisotropy tracked over the two nested pieces of "FS." Along the outer "FS," c→e, the emission intensity near d happens to be very weak at the photon energy used for the map and so these EDC's were taken instead at photon energy 17eV where the ARPES matrix element for the states is much larger. Note that the gap vanishes at d exactly where geometric nesting with the inner "FS" ceases. For the inner "FS," a→b, the pattern becomes bright near b as the peak moves toward E_F into the energy window and the same would happen for the outer "FS" near b in a map taken at 17eV. In short, our data show clearly the presence of the CDW state of SmTe$_3$. Further, the data imply a single $\boldsymbol{q}_{CDW}$ at least over the ARPES sampling area ($\approx 0.1mm^2$) and depth (≈ 15Å). One can speculate that the crystal's slight orthorhombicity and the direction of $\boldsymbol{q}_{CDW}$ are firmly linked, but large domains with $\boldsymbol{q}_{CDW}$ along either ΓX or ΓY [87] is another possible scenario.

Fig. 4.17 (a) shows FS crossings (circles) obtained from EDC's. Taking four-fold symmetry as approximately correct now, these crossings can be mapped to regions with gaps and used as anchor points to construct an experimental "FS" shown as white lines. For simplicity, the small A-B splittings have been ignored. This "FS" then determines

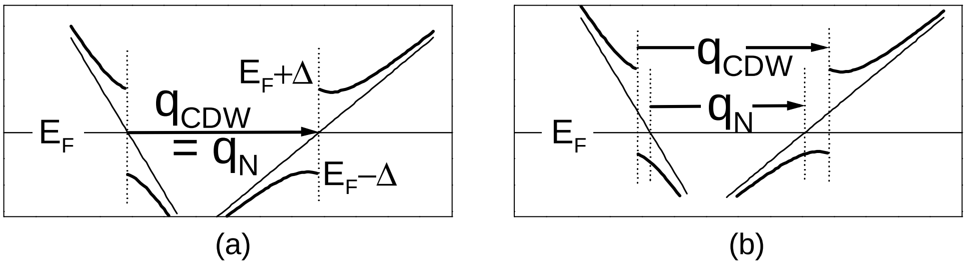

Figure 4.18: Schematic diagrams showing two band CDW mixing when (a) $q_N = q_{CDW}$ and (b) $q_N < q_{CDW}$. Δ mixes two states in the unperturbed bands (straight lines) connected by $\boldsymbol{q}_{CDW}$, resulting in the gapped CDW bands shown as thick lines. The CDW bands are then folded back (not shown) according to the new periodicity.

the nesting wave vectors (arrows), $\boldsymbol{q}_N$, which are *not* constant along the "FS." This means that in general $\boldsymbol{q}_N \neq \boldsymbol{q}_{CDW}$, i.e. we have an imperfect nesting. Fig. 4.17 (b) shows the electron removal gaps for the two paths a-b and c-d in Fig. 4.16 (c) as a function of q_N. In general the two gaps are unequal. However, they *are* equal when $\boldsymbol{q}_N = \boldsymbol{q}_{CDW}$. Other notable aspects of the data, as revealed by the plot of Fig. 4.17 (b), are the roughly linear behavior of the electron removal gaps along the two paths a-a′ and c-c′, and the sudden drop of the electron removal gaps along the two paths a′-b and c′-d despite the fact that $\boldsymbol{q}_N$ moves closer to $\boldsymbol{q}_{CDW}$.

4.6 CDW model

Based on our experimental observations, a minimal model of the CDW for SmTe$_3$ can be built as follows. The FS is taken to be the "FS" (white lines) in Fig. 4.17 (a). This FS defines an imperfect nesting condition as discussed in the last section. For each pair of nested FS points $\boldsymbol{k}$ and $\boldsymbol{k}+\boldsymbol{q}_{CDW}$ we define a 2×2 degenerate matrix eigenvalue problem with off diagonal matrix element Δ_k. For simplicity, we assume that Δ_k is k-independent and that the bands are linear with slopes (i.e. Fermi velocities) different on the different FS pieces but uniform within each FS piece.

Fig. 4.18 (a) illustrates the textbook scenario [40] of perfect nesting, as described in section 2.3, of two bands. Because the inner FS band of Fig. 4.16 (a) nests with an outer FS band that is the reflection, through the Y-M axis, of the one seen dispersing in Fig. 4.16 (a), the two nesting bands have opposite slopes, as shown. Furthermore, we take the magnitudes of the slopes to be different because along the Γ-X axis they are observed to be different, as we will discuss further below in this section, and because the different magnitudes is an essential ingredient in comparing the model calculation with the data in the following. In our data, the case of Fig. 4.18 (a) is rather an exception than a rule, because of the imperfect nesting. Fig. 4.18 (b) shows the imperfect nesting situation where $q_N < q_{CDW}$.

With the imperfect nesting condition, the question of how the system would "pick" the vector $\boldsymbol{q}_{CDW}$ becomes nontrivial. In the following, we show how an answer to this question can be obtained and how well it explains the $\boldsymbol{q}_{CDW}$ of SmTe$_3$. Let us first examine Fig. 4.18 (b). When considered alone, the nesting in this figure would be energetically unfavorable. Instead, it would be more favorable if $q_{CDW}=q_N$ as in Fig. 4.18 (a) so that in the CDW state the lower CDW band is completely filled and the upper CDW band completely empty. Because this is impossible, another mechanism has to be invoked, namely that of the electron-hole compensation between the regions of momentum space with $q_N > q_{CDW}$ and $q_N < q_{CDW}$. In this scenario, the number of holes that would exist in the lower CDW band for the case $q_N < q_{CDW}$ is equal to the number of electrons that would exist in the upper CDW band for the case $q_N > q_{CDW}$, so that the most energetically favorable condition, i.e. a completely filled lower CDW band and a completely empty upper CDW band, is realized across the nesting FS. For each nesting vector $\boldsymbol{q}_{CDW}(\boldsymbol{k})$, the number of holes (if $q_N < q_{CDW}$) or electrons (if $q_N > q_{CDW}$) is given by $2|q_{CDW}-q_N(\boldsymbol{k})|L/(2\pi)$, where the front factor 2 stands for the spin degeneracy and L is the system length. Therefore, the electron-hole compensation condition is summarized as $\sum_{q_\mathrm{N}<q_\mathrm{CDW}} (q_{CDW}-q_N(\boldsymbol{k}))\, L/\pi = \sum_{q_\mathrm{N}>q_{CDW}} (q_N(\boldsymbol{k})-q_{CDW})L/\pi$, i.e.

$$\sum_{q_N<q_{CDW}} (q_{CDW} - q_N(\boldsymbol{k})) = \sum_{q_N<q_{CDW}} (q_N(\boldsymbol{k}) - q_{CDW}).$$

Indeed we find that this condition is satisfied to within 4% for our nesting “FS”, as shown in Fig. 4.19.

Now we discuss the details of our 2×2 CDW nesting model. The two linear bands can be defined as $\epsilon_1(k) = -v_1 k$ and $\epsilon_2(k) = v_2(k - q_N)$. The origins of the momentum and energy are of no consequence in the following discussion, and therefore the chemical potential is taken to be 0 and k_F for the band 1 is taken to be 0. The CDW interaction mixes a state at band 1 with momentum k with another at band 2 with momentum $k + q_{CDW}$. The matrix to diagonalize is then

$$\begin{bmatrix} -v_1 k & \Delta \\ \Delta & v_2(k-\delta q) \end{bmatrix},$$

where $\delta q \equiv q_N - q_{CDW}$. The eigenvalues are

$$\frac{1}{2}\left[(v_2 - v_1)k - v_2\delta q \pm \sqrt{\{(v_2+v_1)k - v_2\delta q\}^2 + 4\Delta^2}\right].$$

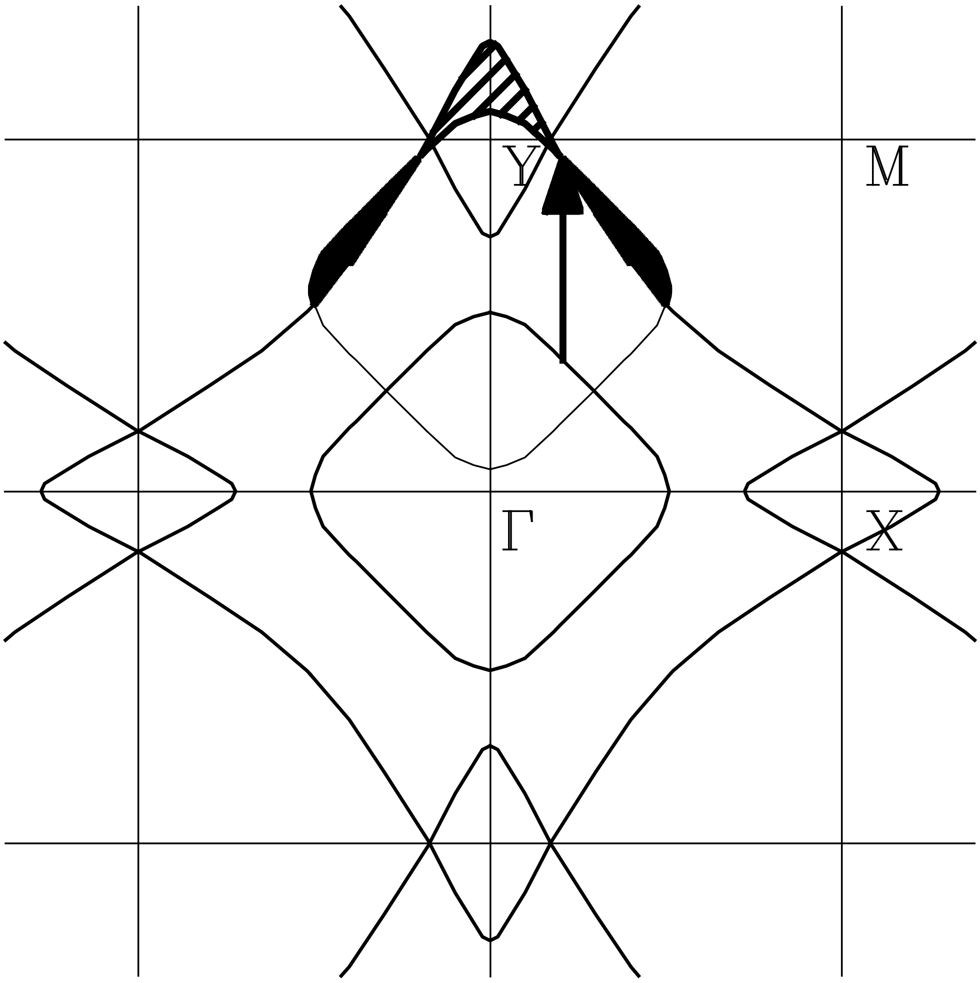

Figure 4.19: Electron-hole compensation in imperfect nesting implied by our experimentally determined FS (solid lines). The dotted line shows the central FS piece translated by q_{CDW} (arrow). The electron-hole compensation requires that the shaded area (hole region) is equal to the hatched area (electron region). This is satisfied with a very high accuracy ($< 4\%$) for our FS.

Our primary interest is in the smaller eigenvalue because it defines the electron removal gap, and furthermore we are concerned with its values at momenta 0 and q_N, i.e. at the FS. They are obtained by inserting 0 and δq into k:

$$\begin{aligned}\Delta_1 &= \frac{1}{2}\left[v_2\delta q + \sqrt{(v_2\delta q)^2 + 4\Delta^2}\right], \\ \Delta_2 &= \frac{1}{2}\left[v_1\delta q + \sqrt{(v_1\delta q)^2 + 4\Delta^2}\right].\end{aligned} \tag{4.1}$$

where Δ_1 and Δ_2 are the photoemission gaps at the FS for the band 1 and the band 2 respectively. With $v_1 \neq v_2$, $\Delta_1 \neq \Delta_2$ unless $\delta q = 0$, as happens for SmTe$_3$. The size of Δ is estimated to be $\approx$ 200 meV from Fig. 4.17 (b). Taking this value to be the Δ in the mean field relation $2\Delta = 3.52k_BT_c$, one obtains $T_c \approx 1300$ K, even larger than the melting temperature 1096 K [86], making SmTe$_3$ truly a "high temperature CDW material."

In the vicinity of $\delta q = 0$, i.e. for $q_N \approx q_{CDW}$,

$$\begin{aligned}\Delta_1 &\approx \Delta + \frac{1}{2}v_2\delta q, \\ \Delta_2 &\approx \Delta + \frac{1}{2}v_1\delta q,\end{aligned} \tag{4.2}$$

i.e., Δ_1 and Δ_2 are linearly dependent on δq, as observed for SmTe$_3$. Without an extra source of information for determining v_1 and v_2, these two equations enable an empirical determination of Fermi velocities of the inner FS and the outer FS if we identify Δ_1 as the PES gap for the inner FS and Δ_2 for the outer FS. Because this equation is true only for $|v_{1,2}\delta q| \ll 2\Delta$, we first consider the range $\delta q = -0.038$ Å^{-1} to 0.024 Å^{-1}, i.e. the close vicinity of q_{CDW}. In this range, we obtain $v_1 \approx 5.0$ eVÅ and $v_2 \approx 1.3$ eVÅ. One can also estimate the Fermi velocities for the full range, i.e. from the a$'$ point to the a point, where δq ranges from -0.095 Å^{-1} to 0.082 Å^{-1}, and from the c$'$ point to the c point, where δq ranges from -0.100 Å^{-1} to 0.001 Å^{-1}. In this range, we obtain $v_1 \approx 3.5$ eVÅ and $v_2 \approx 1.1$ eVÅ. The result that the discrepancy between the two estimates is bigger for v_1 than for v_2 reflects the fact the Δ_1 is more linear from the a$'$ point to the a point than Δ_2 is from the c$'$ point to the c point. In fact, the value of $v_1 \approx 5.0$ eVÅ implies $|v_1\delta q| \approx 0.5$ eV at the c$'$ point, bigger than $2\Delta \approx 0.4$ eV, whereas the value of $v_2 \approx 1.3$ eVÅ implies $|v_2\delta q| \leq 0.12$ eV $= 0.3(2\Delta)$ from the a point to the a$'$ point. Therefore, in view of the exact solution for Δ_2 in Eq. 4.1, it is not surprising that as the c$'$ point is reached Δ_2 deviates somewhat from the small δq linear behavior and flattens out. Note that this discussion hinges on the assumption that the Fermi velocities are constant for each nesting piece of FS. It is difficult to judge the validity of this assumption without more information, but at the level of the current semi-quantitative discussion in this paragraph, there seems not be any strong motivation to question the assumption.

The behavior of the gaps for the paths a′-b and from c′-d cannot be discussed by the FS shape alone, but also requires the knowledge of the symmetry properties of the bands. Study of band symmetry properties in section 4.3 shows that near the point b the character of the inner FS band crosses over from $p_{x'}$ to $p_{y'}$ (see Fig. 4.4 for the definitions of the x' and the y' axes), while near the point d the character of the outer FS band continues to be $p_{x'}$. Due to this symmetry change, we expect that from a′ to b and from c′ to d, even though q_N becomes constant and then increases again, the gap will nonetheless continue to decrease before going to zero abruptly at b and d, as occurs in Fig. 4.17 (b).

Thus this simple two-band model reproduces many of the experimental observations in Fig. 4.17 (b). However, it is not difficult to realize that a multi-band model, including the double Te layer and the SmTe layer, is necessary for a fuller description of the data. This can be seen by closely examining the dispersion data along ΓX and ΓY. Because of the approximate four-fold symmetry, a successful theory of the nested bands along ΓY should start with un-nested bands deduced from our EDC's along ΓX. Fig. 4.20 shows the dispersions along ΓX and ΓY. The notations for the dispersions along these directions are the same as in Fig. 4.16. We also show the bands along ΓX shifted in momentum space by $\pm\boldsymbol{q}_{CDW}$. These are the bands that interact directly with the bands along ΓX via CDW matrix elements to produce the bands along ΓY. That this interaction cannot be simplified to a 2×2 matrix problem is obvious from the figure. Specifically, the band A cannot become the band A′ just by interacting with the band C″. Similarly, the band C cannot become the band C′ just by interacting with the band A″. Rather, with a matrix element $\Delta \approx 200$ meV between the bands A and C″ and between the bands C and A″, the band A would become the band A‴ and the band C would become the band C‴. It therefore seems that we need some other mechanism by which the bands A‴ and C‴ are pushed up by ≈ 150 meV to become the bands A′ and C′ respectively. How such mechanism can be derived can be known only from a detailed band calculation, including the double Te layer and the SmTe layer, and the calculation of CDW matrix elements.

Another piece of information that can be obtained from the dispersions along ΓX

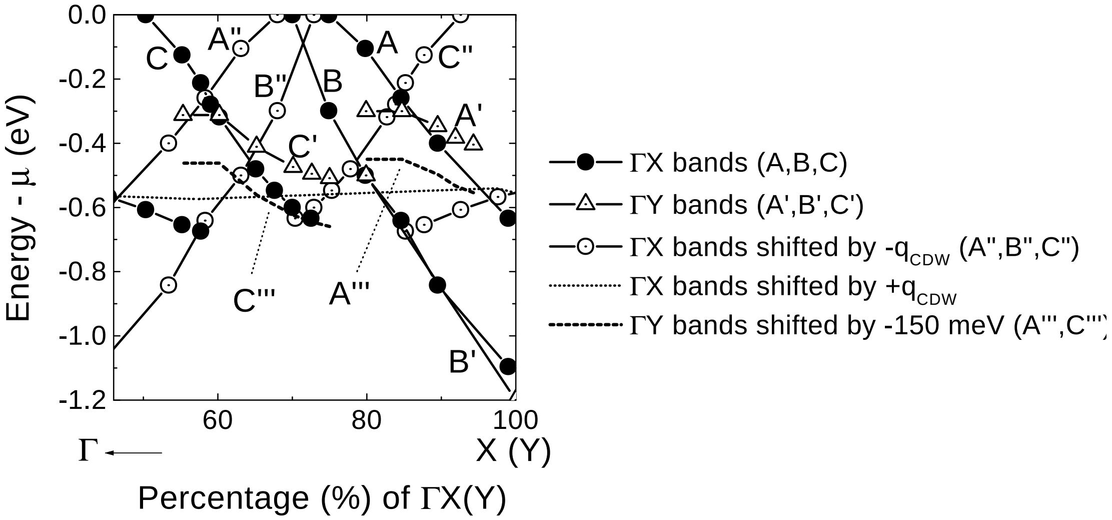

Figure 4.20: Experimentally determined initial and final states of CDW for the bands along ΓX and ΓY.

is the Fermi velocities. By linear fits near the chemical potential, they are estimated to be $v_A \approx$ 3.7 eVÅ, $v_B \approx$ 5.7 eVÅ and $v_C \approx$ 4.2 eVÅ. In view of Eq. 4.2, v_1 is identified with v_C and v_2 with v_A or v_B. There are differences between the Fermi velocity for the inner FS (v_C) and the Fermi velocity for the outer FS (v_A and v_B), although the differences are smaller in magnitude than those between the velocities estimated using Eq. 4.2 above, i.e. $(v_1, v_2) \approx (3.5, 1.1)$ (eVÅ, eVÅ) or $(v_1, v_2) \approx (5.0, 1.3)$ (eVÅ, eVÅ). Depending on whether to take v_A or v_B as v_1, even the sign of $v_1 - v_2$ changes along ΓX. Therefore, it seems that even though we take our 2×2 matrix model seriously near the region $q_N = q_{CDW}$ it cannot be extended to the X(Y) point. Related to this is the fact that the electron removal gaps are both $\approx$ 300 meV for the inner and the outer FS pieces along ΓY, a fact that does not compare well with the behaviors along the paths a′-a and c′-c in Fig. 4.17 (b). A further challenge to a full theory is the apparent absence of any emission intensity from the "back-folded" bands in the gapped EDC's of Fig. 4.16 (a,b). Such intensity was identified in recent ARPES studies of superconductor gap formation [98].

4.7 Conclusions

In conclusion, we have presented a detailed ARPES study on the FS shape and the anisotro-pic gap of SmTe$_3$, a high temperature incommensurate CDW compound. The experimental "FS" shows an excellent agreement in shape with an extended Hückel tight binding band theory and shows a nesting property consistent with the TEM diffraction pattern [87]. The big gap size ≈ 200meV implies a high transition temperature and enables a very detailed gap anisotropy study. The latter is discussed in terms of an imperfect nesting condition and the symmetry properties of the bands. Our results vividly illustrate how incommensurate CDW nesting occurs in a real quasi-2D material.

My role in the work described in this chapter was to measure all the data, to analyze them, to calculate and understand the band structure, and to build the imperfect nesting model.

Appendix 1

The gapped spectra in Fig. 4.16 display small but nonzero spectral weight near E_F. There are many possible mechanisms that could lead to the PES peak's linewidth tail: thermal CDW fluctuations, simple phonon broadening, the photoelectron lifetime or possibly some non-**k**-conserving scattering. We also calculate that when the gapped state above E_F is at its closest approach to E_F, as in the 20.1 % spectrum of Fig. 4.16 (a), the thermal occupation of its tail at 300 K can produce the weak but observable PES peak just at E_F. We show this calculation here, because it is somewhat unconventional and turns out to be closely related to the imperfect nesting picture presented in the text. Along the Γ-Y direction the electron addition gap is smaller than the electron removal gap in our imperfect nesting picture. Therefore, the unoccupied state is close to E_F. For the observed electron removal gap size of 300 meV for peak A′ and our experimental value of the CDW matrix element $\Delta \approx 200$ meV, we estimate the electron addition gap size to be $2\Delta - 300 \approx 100$ meV. At 300K the Fermi-Dirac function gives a broadening of 50 meV HWHM, a considerable fraction of this electron addition gap. Fig. 4.21 shows our simulation for a CDW gap treated with the usual BCS-like theory, as explained in section 2.3. We have used a non-zero linewidth roughly like that seen in photoemission. For $\epsilon(k) = -100$ meV, the point of closest approach to E_F, or for $\epsilon(k) = 0$ meV, the small photoemission peak near E_F is much like that observed in the 20.1% spectrum. Nevertheless, we stress that this is only a qualitative plausibility argument, and to make it more in quantitative agreement with the experiment we need a complete multi-band imperfect nesting theory, which we lack at this stage.

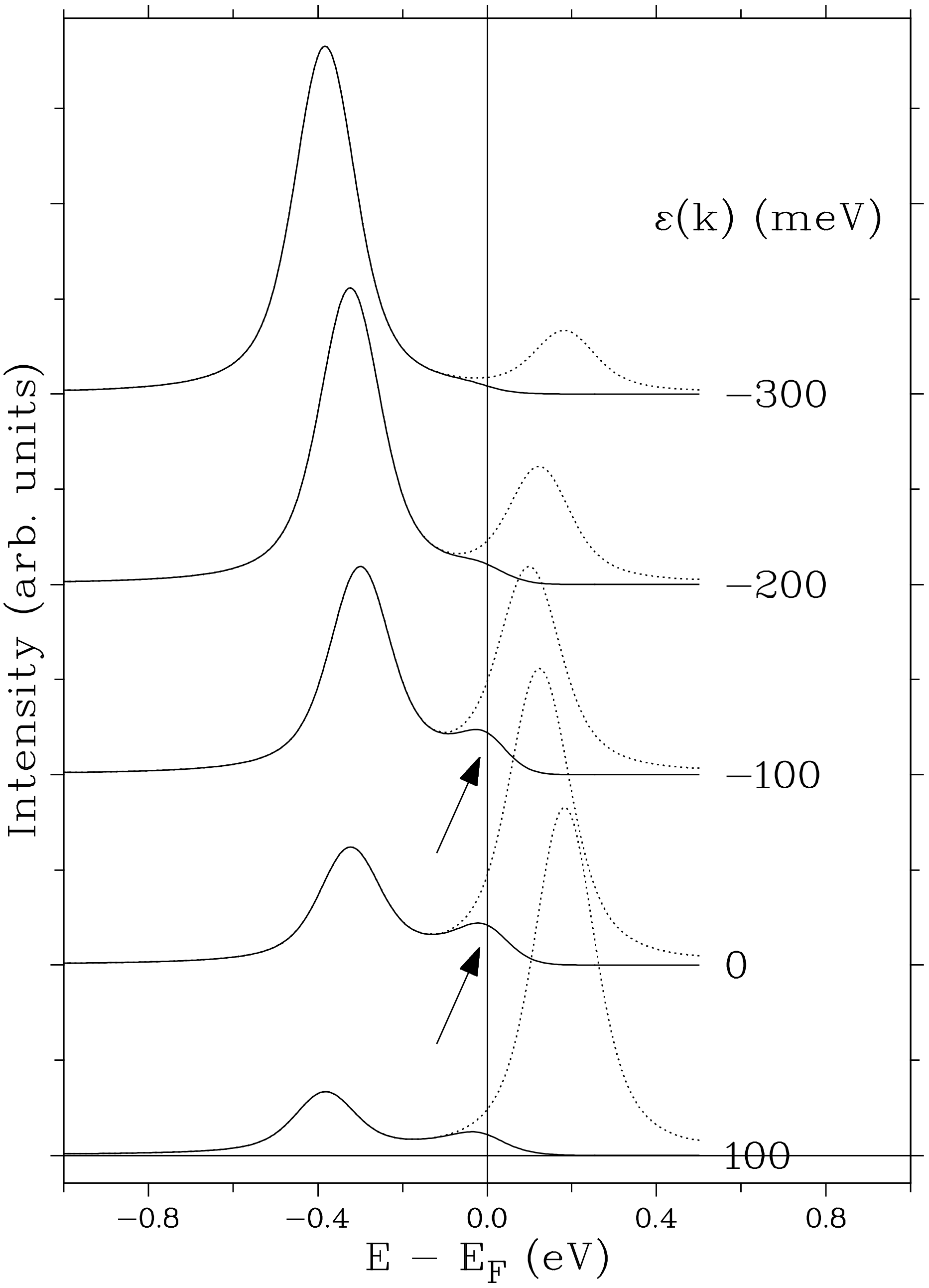

Figure 4.21: Schematic CDW lineshape for imperfect nesting situation. Theory is the mean-field CDW theory in section 2.3, but with nesting occurring 100 meV below E_F. CDW matrix element Δ of 200 meV is used. Theory is broadened with Gaussian and Lorentzian shapes of 200 meV FWHM each, to give broadened one electron spectral functions shown as dotted lines. Multiplication of the Fermi-Dirac function for room temperature and an additional 50 meV FWHM Gaussian broadening gives the spectra in solid lines.

Chapter 5

$NaMo_6O_{17}$ and KMo_6O_{17}: Hidden one dimensionality

This chapter is an expansion of the journal article: "Direct Fermi-surface image of hidden nesting for $NaMo_6O_{17}$ and KMo_6O_{17}", G.-H. Gweon, J.W. Allen, J.A. Clack, Y.-X. Zhang, D.M. Poirier, P.J. Benning, C.G. Olson, J. Marcus and C. Schlenker, Phys. Rev. B **55**, R13353 (1997).

We report direct FS images obtained with ARPES for $NaMo_6O_{17}$ and KMo_6O_{17} above the charge density wave transition temperatures. We also report ARPES spectra of the valence band. The images imply a FS based on three underlying quasi-one-dimensional (quasi-1D) surfaces. Thus it agrees in detail with that expected in the "hidden nesting," or "hidden one dimensionality," picture of Whangbo *et al.* [99], but differs greatly from a FS deduced in a previous study by Breuer *et al.* [100], which found only two underlying quasi-1D surfaces. We point out anomalous lineshapes observed for an isolated band crossing E_F.

5.1 Introduction

The molybdenum bronzes are a family of quasi-low dimensional materials with the general formula $A_xMo_yO_z$, where A is an alkali metal or thallium. As recently reviewed [102], many of these materials display CDW formation, where the CDW wavevector **q** is determined by the topology of the FS and so can be either commensurate or incommensurate with the underlying lattice. As described in section 2.3, the essential requirement is for substantial portions of the FS to be separated by the same wavevector q_{CDW}, a CDW "nesting" wavevector. When the CDW forms below some transition temperature T_c, the nested portions of the FS are destroyed by the development of gaps in the single particle electronic structure. Depending on whether or not the entire FS is destroyed, a metal–semiconductor or metal–metal transition occurs at T_c. The so-called "purple bronzes"[1], $NaMo_6O_{17}$ and KMo_6O_{17}, are quasi-two dimensional (quasi-2D) materials with metal–metal transitions and commensurate CDW formation at T_c's of 120K and 80K, respectively.

It is apparent that determining the FS topology of these materials is central to an understanding of their CDW's. If the topology is known, possible nesting vectors can be determined and compared to the CDW vectors measured by diffraction techniques. Ideally one wants a theoretical FS which has been directly verified experimentally. On the theory side, the very large numbers of atoms in their unit cells have precluded density functional calculations for the molybdenum bronzes[2], but FS's have been obtained by tight binding methods [105, 99]. Experimentally, the most direct method of determining the global FS topology important for nesting properties is that of ARPES. Two complementary methods can be used. Either one can follow the dispersion with wavevector **k** of a spectral peak in the ARPES EDC's and observe the **k** value at which it crosses E_F and then disappears, or one can directly image the FS by making a **k**-space intensity map of the ARPES emission just at E_F. The latter method has been useful in studies of the superconducting cuprates [97]. In the chapter, we use both methods, but heavily rely on the map method for the FS geometry.

Fig. 5.1 shows the schematic crystal structure of KMo_6O_{17}. The crystal symmetry for KMo_6O_{17} is $P\bar{3}$ (trigonal) [106], with an improper 6-fold rotation (S_6) symmetry around the *c* axis. The figure shows the projection of the crystal structure along the *a* axis of the hexagonal unit cell. The crystal symmetry of $NaMo_6O_{17}$ is $C2$ (monoclinic) [107]. However, the crystal structure for $NaMo_6O_{17}$ can be seen as that of KMo_6O_{17} with a very small monoclinic distortion, which is of little importance for our study. The basic ingredients of KMo_6O_{17} is the Mo oxide slabs, whose perpendicular cuts are shown in the figure, and K^+ ions sandwiched between the Mo oxide slabs. These K^+ ions donate conduction electrons to the Mo sites. As shown in the figure, each Mo oxide slab has 4 layers consisting of MoO_6 octahedra and two outer layers consisting of MoO_4 tetrahedra. By corner sharing, these octahedra and tetrahedra span an infinite 2 dimensional slab. However, there is no bonding between the neighboring slabs. Bond

---

[1] For $NaMo_6O_{17}$, we use the chemical formula determined by crystallographic refinement [103], but note that the more conventional formula is $Na_{0.9}Mo_6O_{17}$.

[2] However, new techniques especially suitable for large unit cell compounds are being developed and was applied to the blue bronze [104].

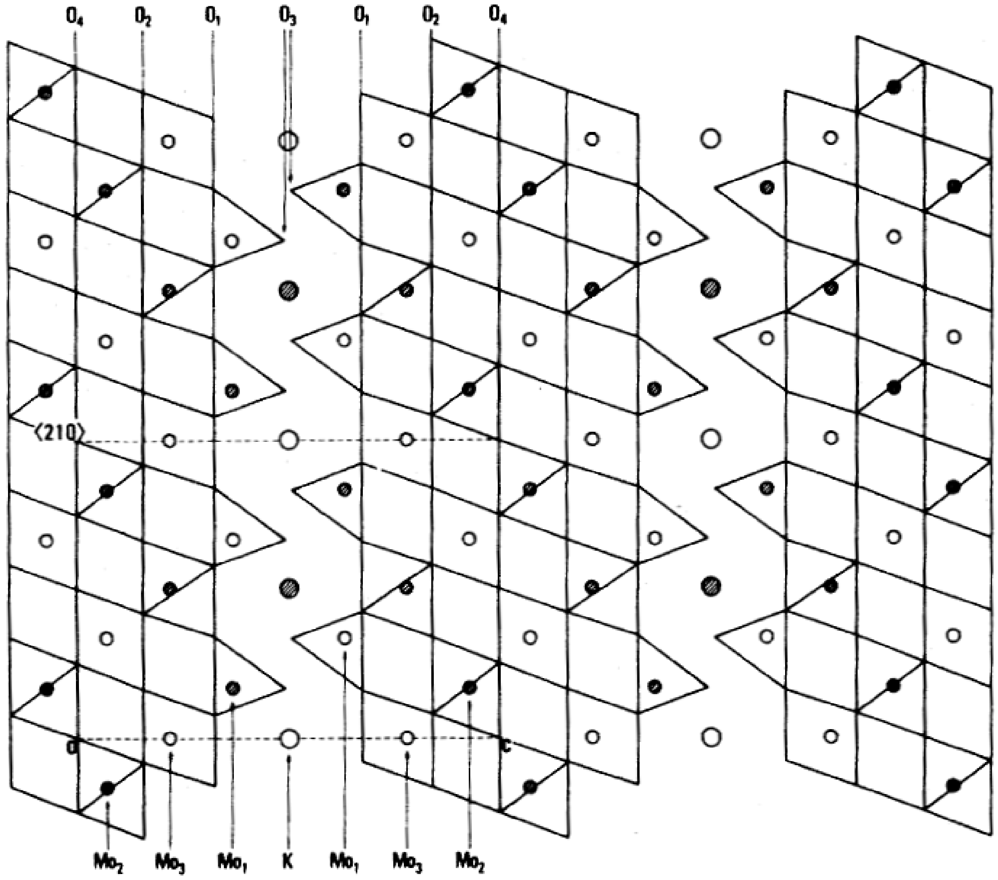

Figure 5.1: Crystal structure of KMo_6O_{17} viewed along the crystallographic *a* axis. The big circles are K^+ ions, the small circles Mo ions and the vertices O ions.

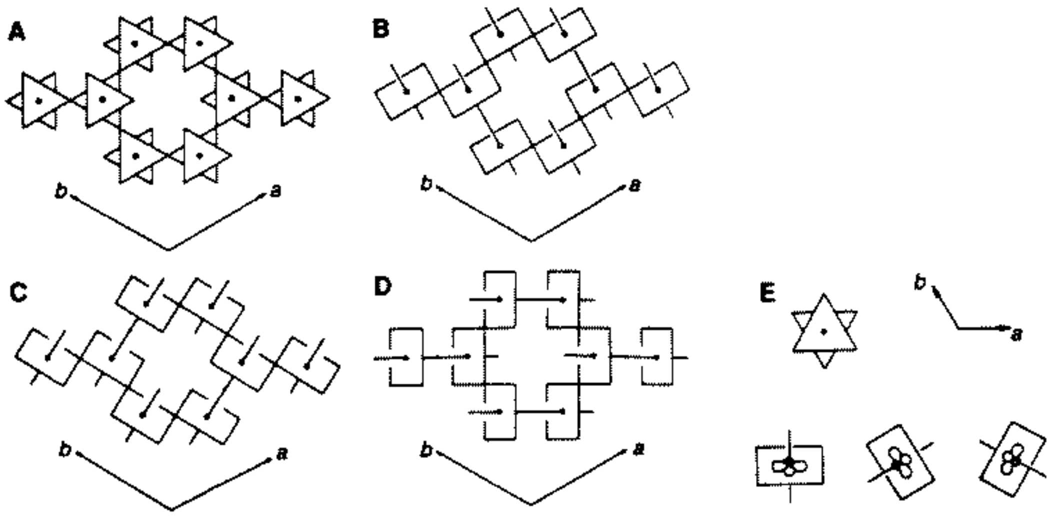

Figure 5.2: Crystal structure of the conducting MoO layers of KMo_6O_{17}. A, B, C,. and D are different representations of the structure of the two innermost MoO layer of Fig. 5.1. E shows the Mo t_{2g} orbitals that hold the conduction electrons.

length analysis [106] shows that the conduction electrons reside mostly in the Mo ions in the two innermost MoO$_6$ layers: the valency for Mo ions are +5.1, +5.8 and +6.0 for Mo$_2$, Mo$_3$ and Mo$_1$ in Fig. 5.1, respectively. Fig. 5.2 shows the crystal structure of the two innermost layers, which governs the electronic properties of the crystal, viewed here as one looks down onto the layer, i.e. viewed along the *c* axis of the hexagonal unit cell. The S$_6$ symmetry of the crystal is obvious for the central object in A. The same crystal structure is decorated differently in B, C and D to clearly show the edge-sharing MoO$_6$ chains that are aligned along *a, b,* and *a+b* directions respectively. These three MoO$_6$ chains are equivalent by the crystal symmetry of this substructure. In E, the lowest lying Mo *d* orbitals are plotted.

The electronic structure of NaMo$_6$O$_{17}$ is expected [105] to be essentially the same as that of KMo$_6$O$_{17}$ and it is reported that [99] both give the same CDW wavevectors in X-ray scattering studies. These materials are particularly interesting for FS imaging studies because their quasi-2D electronic structures can usefully be regarded as being composed of quasi-1D chains (Fig. 5.2) forming a triangular pattern. That is, in the band theory the quasi-2D electronic structure has its origin in the three 1 dimensional bands originating from the three t_{2g} orbitals of Fig. 5.2 E with hopping matrix elements confined in the three MoO$_6$ chains of Fig. 5.2 B, C and D respectively.

The FS calculated by band theory on a Mo$_6$O$_{17}$ slab is shown in Fig. 5.3. The FS can be visualized as three pairs of parallel lines, the pairs being oriented at 120^o to one another. The connectivity and final details of the actual FS are determined by small hybridization gaps which open at the crossing points of the lines. If long segments of the quasi 1-D FS survive intact, the optimum nesting vector is the same as that for no hybridization, i.e., one of the three which simultaneously connect the two lines of two of the three pairs. The wavevector thus identified explains the experimentally observed wavevectors [108, 99] very well. Both of our FS images are in remarkable overall agreement with this elegant and useful visualization, a concept called "hidden nesting," originated by Whangbo et al.[99]. In sharp contrast, the first report [100] on hidden nesting in NaMo$_6$O$_{17}$ emphasized very significant disagreements between the observed and expected FS's. Possible factors contributing to the large difference in the two results are mentioned below. In our opinion the concept of "hidden nesting" could be better called "hidden 1 dimensionality (1D)," because CDW nesting occurs on the real 3 dimensional FS rather than on the hidden 1 dimensional FS. Therefore, our choice of the title of this chapter.

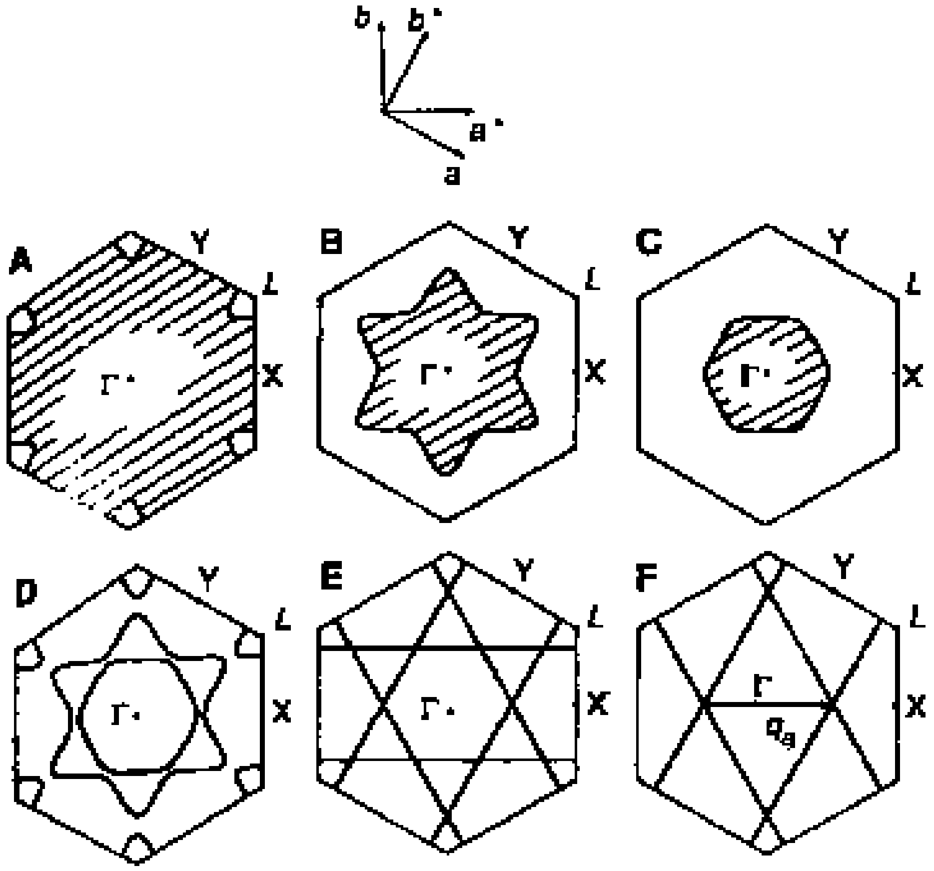

Figure 5.3: Hidden 1D picture of KMo_6O_{17} and $NaMo_6O_{17}$. The three 2D FS's calculated for the Mo_6O_{17} layer by extended Hückel tight binding calculations are shown in A, B, C, and D. For the most part, the FS can be approximated to three 1D FS's shown in E. The CDW nesting vector, here denoted as q_a, is determined by the maximal nesting condition shown in F. Relative to the rest of this chapter, the Brillouin zone notations here are translated to X=M, L=K′ and Y=M′. From Ref. [99].

The calculated bands along the high symmetry directions are shown in Fig. 5.4. This band calculation from Ref. [105] precedes that of the hidden 1D theory of Ref. [99]. In the latter paper, only the FS calculation was given, while in the former paper, both the band calculation and the FS calculation were reported. The two FS calculations are not exactly the same. The difference lies in the central FS piece which is close to a circle in the older calculation rather than to a hexagon. This means that the hidden 1D picture is not satisfied by the original FS calculation and therefore by the band calculation shown in Fig. 5.4. The FS piece for which the two calculations differ arises from the most shallow band dispersion around Γ which has binding energy 0.12 eV at the Γ point. Note also that this band is separated by as much as 0.17 eV from the other two degenerate bands at Γ, due to the interchain coupling.

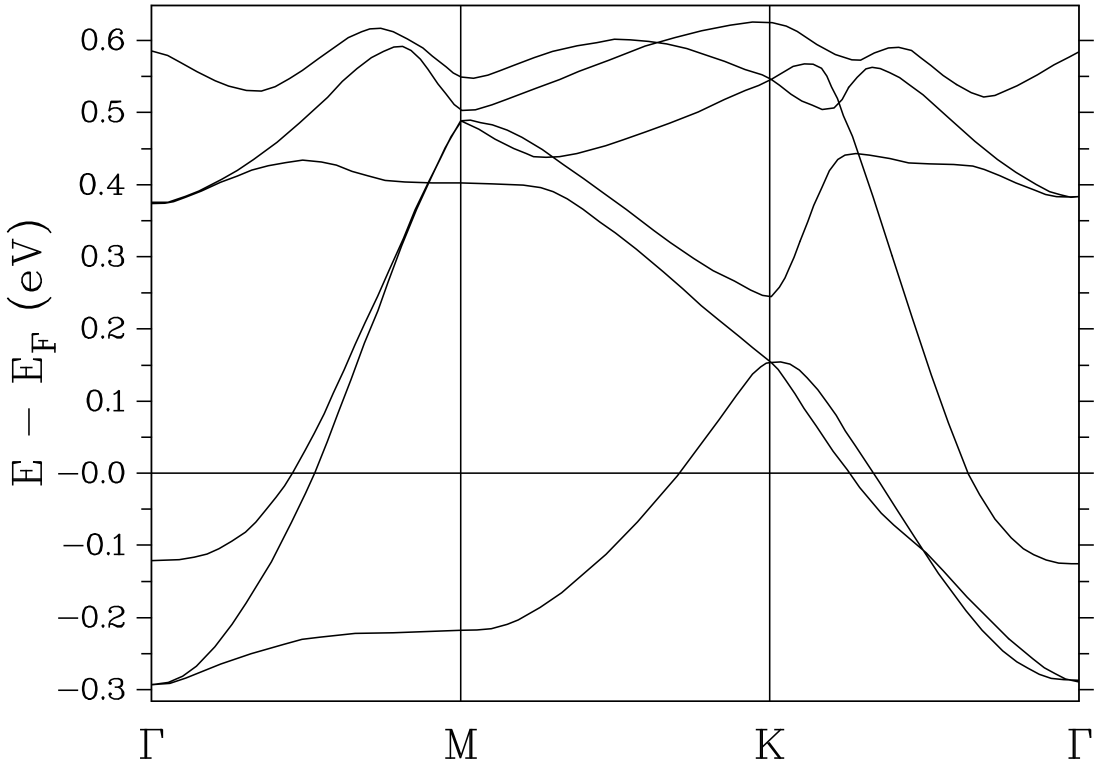

Figure 5.4: Band calculation for KMo$_6$O$_{17}$ using the extended Hückel tight binding model. Data digitized from Ref. [105].

5.2 Experimental

Single crystalline samples of the purple bronzes were grown by our collaborators in Grenoble, France using the electrolytic reduction technique as described in Ref. [106]. A typical sample dimension was 1 mm × 1 mm (rectangular or triangular shape) with thickness $<$ 0.2 mm. In the Laue pictures that we have taken for sample orientation, and in ARPES spectra, the monoclinic distortion for NaMo$_6$O$_{17}$ is not noticeable. However, X-ray crystallography [103] on our NaMo$_6$O$_{17}$ samples does show the well-known monoclinic symmetry.

The ARPES measurements were done at the Ames–Montana beamline of the Synchrotron Radiation Center (SRC) at the University of Wisconsin, except for one set of EDC's (Fig. 5.9) taken at the beamline 5 of the Stanford Synchrotron Radiation Laboratories (SSRL). The samples were introduced into the analysis chamber, which was kept at pressure smaller than 5×10^{-11} Torr. The top layers of the material were cleaved off to expose clean surfaces by levering against a post glued onto the sample. The sample surface was irradiated with monochromatic ultraviolet synchrotron radiation, and the resulting photoelectrons were then energy analyzed with a 50mm radius hemispherical analyzer. The photoemission data reported here are all normalized with respect to the photon flux, which was monitored constantly. The full angular acceptance of the analyzer lens is 2^o. The Fermi energy and the instrumental energy resolution were determined from EDC scans on a clean Pt or Au surface. The photon energies, temperatures, and combined photon and analyzer resolutions are reported with each data set below. The temperature was always kept above the CDW transition temperatures. Under similar conditions, we have reproduced EDC's on 3 cleaved surfaces of $NaMo_6O_{17}$ and on 2 of KMo_6O_{17}.

In our ARPES setup, the sample orientation was fixed and different **k** values were sampled by rotating the analyzer. To obtain the Fermi energy intensity map, the kinetic energy of the analyzer was fixed to be the E_F value known from the Pt edge scan, and the analyzer was rotated away from the normal in two perpendicular directions in steps of 1^o (corresponding to $\Delta k = 0.037\text{Å}^{-1} \sim \Gamma\text{M}/18$) while the intensity was recorded. Our method is slightly different from the usual one [97] which involves rotating the sample with fixed analyzer. By rotating the analyzer, the image is not modulated by the dependence of the ARPES matrix element on photon incidence angle, which was fixed at $\sim 45^o$ in our geometry.

5.3 Results

Fig. 5.5 shows the Fermi energy intensity maps. Using equations 1.3 and 1.4, the momentum inside the crystal parallel to the cleaved surface is easily calculated. The map is shown in this two dimensional **k** space. In Fig.'s 5.5 (a) and 5.5 (b), one third of the map, enclosed between the two white lines, represents the raw data set consisting of 783 and 445 data points respectively, and the remainder of the map was generated as described below. To enhance the contrast, the intensity was plotted in log scale. In the sudden approximation of photoemission theory [7] as described in Section 1.1, the intensity is given by the product of the photoemission matrix element and the spectral function. Thus we interpret the local maxima of the data as showing lines of FS, but give no particular significance to the strong intensity variation, which arises from the **k**-dependence of the matrix element and the details of which will vary with the incident photon angle and energy.

To generate the complete maps the raw data sets must be extended by symmetry. Therefore, three-fold rotations were applied to both data sets, and the full maps were created, using the bilinear interpolation method, on a regular **k** grid, a cell of which corresponds to approximately one data point. These rotations are symmetry opera-

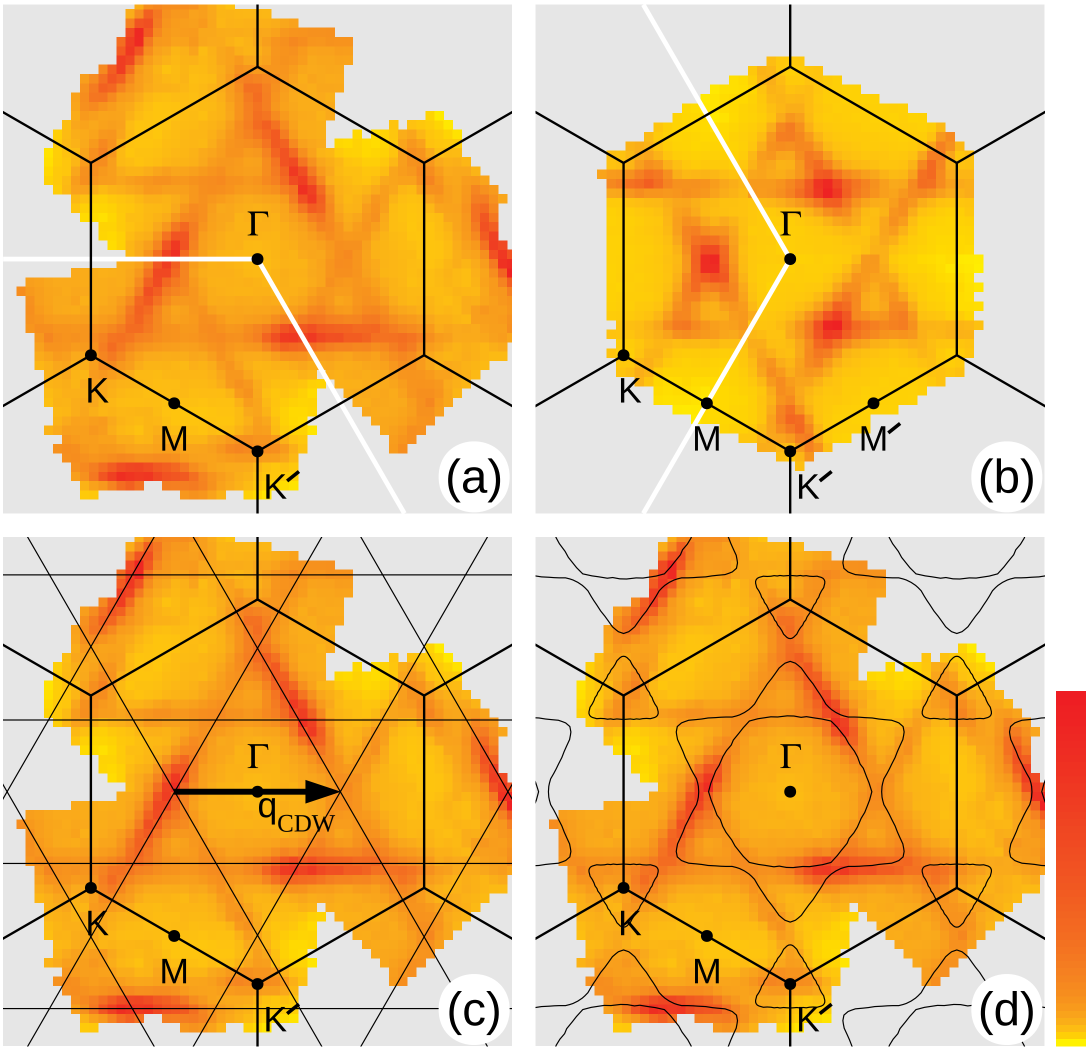

Figure 5.5: (a) Fermi energy intensity map for NaMo$_6$O$_{17}$, obtained at T=300K and with hν=22eV and total energy resolution of 150meV. The measured data are one third of the map (enclosed in the two white lines), the rest of which was generated by three-fold rotations. (b) Same map for KMo$_6$O$_{17}$ at T=150K and with hν=22eV and total energy resolution of 100 meV. (c) Hidden 1D FS's from Ref. [99] for KMo$_6$O$_{17}$ and our data for NaMo$_6$O$_{17}$. One of the three equivalent measured CDW wavevectors, from Ref.'s [108,99], is shown as an arrow. (d) The FS's from the tight binding calculation from Ref. [99] for KMo$_6$O$_{17}$ and our data for NaMo$_6$O$_{17}$.

tions for KMo_6O_{17}, and approximately so for $NaMo_6O_{17}$. The validity of their use for $NaMo_6O_{17}$ is strengthened by the existence of the same motifs in the two raw data sets, i.e. three lines of FS oriented at 120°. Furthermore, the internal consistency of the procedure is shown by the perfect matching of different parts of the data set at the intersections of the rotated segments. Overplotted in the figure is the quasi-2D hexagonal Brillouin zone, for which the Γ to M and Γ to K distances are 0.66 and 0.76 $Å^{-1}$, respectively, the same for both compounds to this accuracy.

The resulting patterns for the two materials are essentially identical, and the dominant feature is three pairs of lines defining a central hexagon. There are two subtle differences. First, the intensity variations of the FS's for the two maps show some *complementary* differences. Namely, the central hexagon is more complete in the $NaMo_6O_{17}$ map, while outer lines are more complete in the KMo_6O_{17} map. The reason for these differences may be the different sample orientations. The $NaMo_6O_{17}$ crystal was aligned so that $K'\Gamma$ was approximately vertical, i.e. normal to the photon incidence plane, whereas for KMo_6O_{17}, $K\Gamma$ was vertically aligned. For $NaMo_6O_{17}$, one may also notice that the weaker line of two parallel lines become very strong in the adjacent zone, forming a bright image in the outer area of the map, and vice versa [12, 13]. This exchange of intensity is reminiscent of the "photoemission structure factor effect" as found in graphite [12,13], an effect arising from the interference of electron waves emanating from different atoms in a unit cell. From this interchange of the intensities, again one can be confident that both lines persist across the entire zone. The second difference between the two maps is the size of the FS. When the centroid of the patterns is taken to define the FS, then the FS of $NaMo_6O_{17}$ is about 10 % larger than that of KMo_6O_{17}. The origin of this difference is an open question. The slight differences in the unit cell dimensions are a much smaller effect and so do not account for this FS size difference. To know the origin of the difference, more measurements on different cleave surfaces seem to be necessary, because different cleaves may leave slightly different amounts of Na or K on the surface, leading to the different FS sizes measured by photoemission.

From the three pairs of lines, one concludes that there are three quasi-1D bands, each half-filled (i.e., occupying half of the first Brillouin zone), and inter-related by 3 fold rotations. This is exactly what is predicted by the hidden 1D idea for the quasi-2D purple bronzes [99]. In Fig.'s 5.5 (c) and 5.5 (d), we compare our map with the theoretical FS's calculated for KMo_6O_{17}. We compare the theory with our $NaMo_6O_{17}$ map, because there exists a published work [100] on this material, and in principle one expects a bigger discrepancy, if any, for NaMo$_6$O$_{17}$ because of its monoclinic distortion.

Fig. 5.5 (c) shows the comparison of our measured FS map with the theoretical FS obtained by neglecting interchain hybridization. The two agree at the quantitative level. Also shown as an arrow is the CDW wavevector measured in X-ray diffuse scattering and electron diffraction studies [108, 99]. This wavevector nests "perfectly"[3] two of the three pairs of 1D FS's. In Fig. 5.5 (d) we have overplotted on our map the calculated 2D FS [99] resulting from interchain hybridization gaps. In general the agreement is again remarkable. The gap along Γ-K is resolved in the map, as shown by a slight local minimum, visible with careful examination, at the point where the two lines cross each other near K. It appears that the FS is slightly closer to the K point than in the calculation, so that the gap is slightly under-estimated. This aspect of the data can perhaps be better observed in the EDC's, discussed below. Along Γ-M the gap is not observed, entirely consistent with a predicted splitting which corresponds to only 1^o, less than the resolution of the image. So far, the only obvious feature not discussed is the streak at the K′ point. We will discuss this extrinsic feature later. Now we discuss the EDC's.

Fig. 5.6 shows an overview of the valence band and the conduction band for near normal emission, in general agreement with the previously reported work [109] on the same energy scale. The spectrum is typical of all the Mo bronzes studied in this thesis, and consists of two parts, a region of strong intensity below binding energy $\sim$ 2.5 eV and a small "foot" of intensity near the Fermi energy. The first has a strong O $2p$ character, and the second has a strong Mo $4d$ character. The general characteristics of this valence band structure reminds one of the similar situation found in high temperature superconducting cuprates [110], although the atomic characters of the bands for the two materials are different and more significantly the foot structure, which is most interesting, is not as clearly separated from the stronger intensity region in the cuprates as in the bronzes.

Fig. 5.7 shows the EDC's for NaMo$_6$O$_{17}$, for the same surface and conditions as for the FS image, taken along three lines of high symmetry. Either from the band calculation or the FS map in Fig. 5.5, one expects to see three conduction bands crossing the Fermi level. The FS map shows two unresolved crossings at $\sim$ 55% of ΓM, one crossing at $\sim$ 86% of $\mathrm{M}K$, and three crossings at $\sim$ 12%, $\sim$ 29% and $\sim$ 60% of KΓ. Peak dispersions corresponding to these crossings can be discerned, as shown by the broken lines

---

[3] One should note however that the FS lines do not lie exactly at the centroid of the FS pattern in Fig. 5.5 (c). For KMo$_6$O$_{17}$(Fig. 5.5 (b)), however, the lines, if drawn, do lie close to the centroid. In this sense, the comparison with the theory is better for KMo$_6$O$_{17}$ than for NaMo$_6$O$_{17}$.

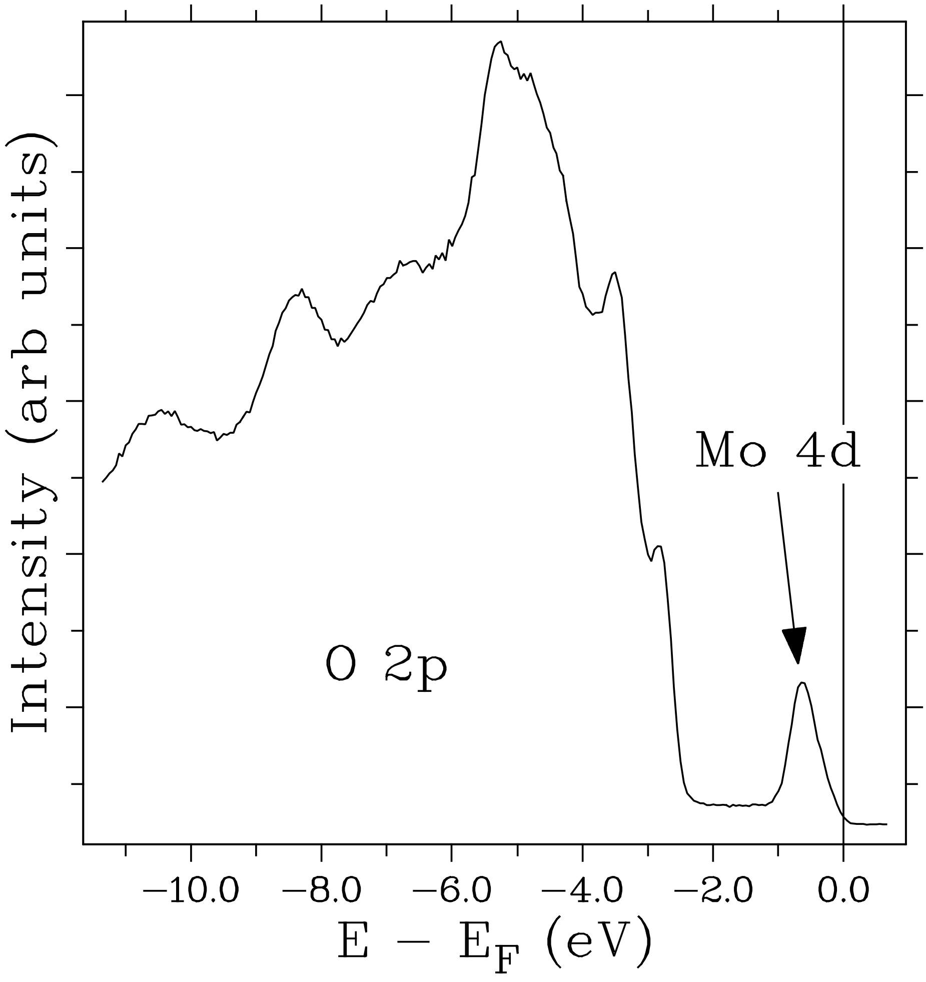

Figure 5.6: An overview scan of $\mathrm{NaMo_6O_{17}}$ over the valence band and the conduction band, taken at T=300 K and with hν = 22 eV and total energy resolution of 250 meV. Angles are near normal emission, $(\theta, \phi) = (-0.5, 2)$ relative to the normal angle.

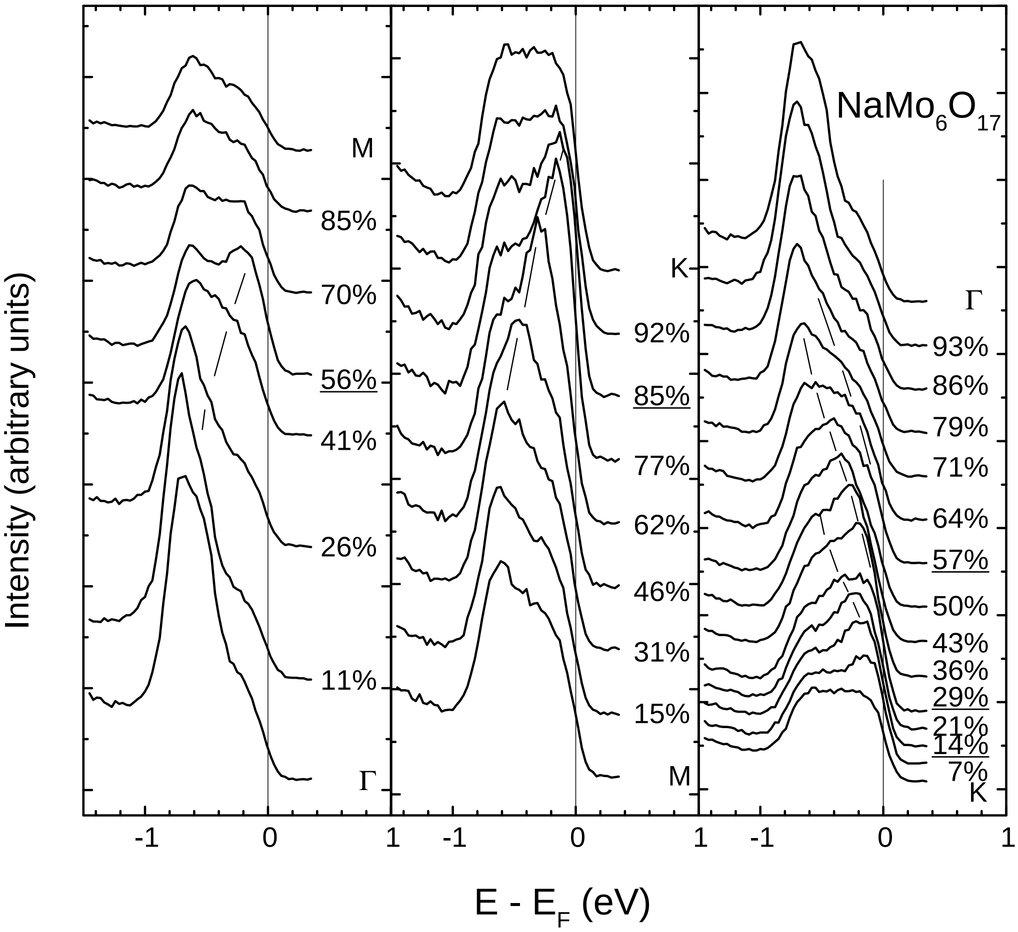

Figure 5.7: ARPES EDC's of NaMo$_6$O$_{17}$ along the three symmetry lines, taken on the same surface as in Fig. 5.5 (a) with the same conditions, i.e. at T = 300K and with hν = 22 eV and total energy resolution of 150 meV. The percentage denotes the relative distance along the line in each set. Broken lines are guide to the eyes for dispersing features which can be identified with strong input from the FS map. Underlined are the angles closest to the Fermi level crossings.

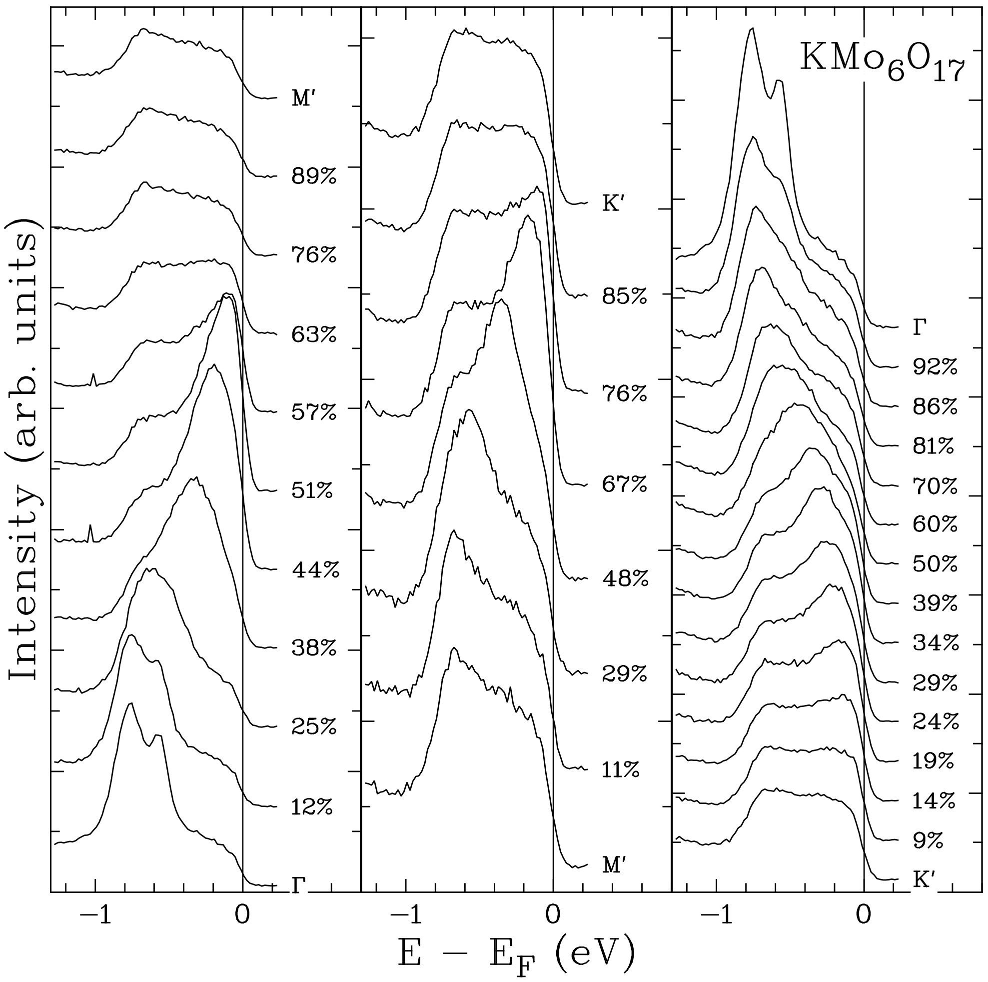

Figure 5.8: ARPES EDC's for $\mathrm{KMo_6O_{17}}$ taken along the three symmetry lines, taken on the same surface as in Fig. 5.5 (b) with the same conditions, i.e. at T = 150K and with $h\nu = 22$ eV and total energy resolution of 100 meV.

in Fig. 5.7. Along KΓ, the crossing nearest Γ is more easily seen in the map, while the separation of the two crossings nearer K is more easily seen in the EDC's. A direct comparison to the EDC's shown in Ref. [100] is not possible because they are for different parts of **k** space and different photon energies were used. But it can be noted that only two bands crossing E_F are reported in Ref. [100].

Fig. 5.8 shows a set of EDC's for $\mathrm{KMo_6O_{17}}$. The data are quite similar to the $\mathrm{NaMo_6O_{17}}$ data in the sense that they show three bands crossing the Fermi level, all resolved along the K′-Γ direction, two of them degenerate along the Γ-M′ direction, and the third one observed to cross singly along the M′-K′ direction. Like the maps, the EDC's show essentially the same behaviors for the two materials, except for the different positions of Fermi level crossings, most easily noticed in the M′K′ cut data, where the 76 % spectrum is closest to the Fermi level crossing. Having the crossings closer to Γ than for $\mathrm{NaMo_6O_{17}}$ means a smaller FS, in consistency with the finding based on the map above.

In comparing Fig. 5.8 with Fig. 5.7, an assumption is made that the path Γ–M–K–Γ is equivalent to the path Γ–M′–K′–Γ. This is a reasonable assumption because the 6 fold symmetry of the FS *shape* is reproduced remarkably well by our data. Note that the S_6 crystal symmetry implies that the **k** space sampled for a given photon energy in general has only 3 fold rotational symmetry unless the photon energy was fortuitously set to sample near $k_z = 0$ plane, where a strict 6 fold symmetry holds. However, if the band structure is 2 dimensional so that it does not have any k_z dependence, then it will show 6 fold symmetry independent of k_z. On the other hand, it is to be noted that the intensity of the FS pattern is not expected to, and does not, show the 6-fold symmetry even for the 2 dimensional electronic structure of the conduction band because the intensity also involves the photoemission final state which is fully 3 dimensional, and thus is expected to show only 3 fold symmetry.

However, there is one feature that apparently breaks the 6 fold symmetry of the FS shape: the streak observed for NaMo$_6$O$_{17}$ only at the K′ point but not at the K point. This streak is inconsistent with the hexagonal symmetry of the central part of the pattern and does not connect naturally to the rest of the pattern, suggesting it is not intrinsic to the single crystal. Indeed, further studies for other sample surfaces, specifically of the K′ region, repeatedly show the same pattern as for the K point, like KMo$_6$O$_{17}$. We show such a study in Fig. 5.9. The data in this figure were obtained at the beamline 5-3 of the SSRL. Here, one can easily notice the perfect agreement of the data along the MK′ direction with those along the MK direction in Fig. 5.7. This observation is also confirmed by a map taken at the SRC, which despite low signal/noise ratio due to high resolution shows the same absence of any pattern at both K and K′ points. One likely source of such an extrinsic feature is that it is a displacement of the bright parallel image in the outermost part of the map. Because of the large analyzer angle from the surface normal, we are most susceptible here to picking up some intensity from a part of the surface which may have a slightly different orientation. Another point to be made about Fig. 5.9 is that the size of the background here is much smaller than that in Fig.'s 5.7 or 5.8. This is because the data in Fig. 5.9 were obtained right after cleave but the data in Fig.'s 5.7 or 5.8 were obtained after the surface has degraded a little due to the lengthy E_F intensity map measurement.

In Fig.'s 5.7, 5.8, and 5.9, it is easily recognized that the lineshape at Γ is progressively better resolved. This is due to the progressively better total energy resolution, which helps to resolve the doublet structure at 0.75 eV and 0.55 eV binding energies.

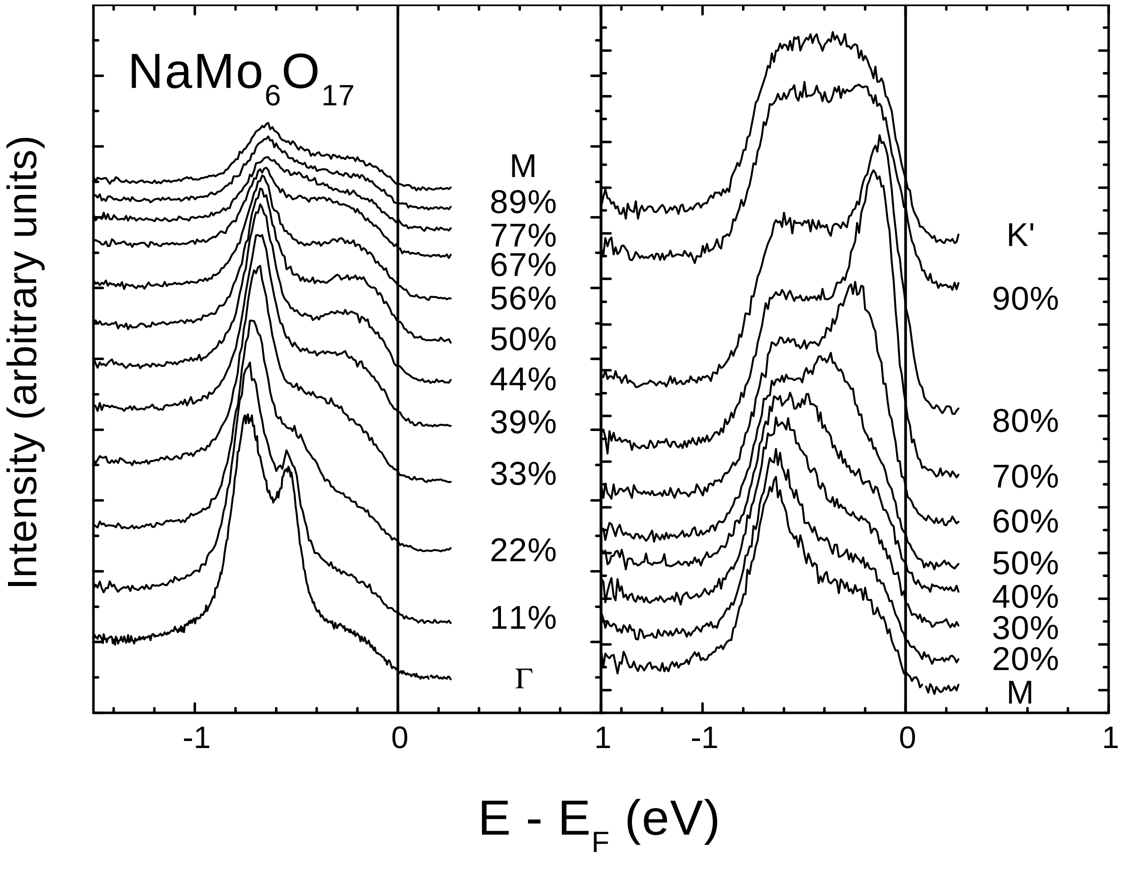

Figure 5.9: ARPES EDC's for NaMo$_6$O$_{17}$ along the path Γ–M–K′ taken at T = 300 K and with hν = 22.4 eV and total energy resolution of 43 meV.

As discussed above, the qualitative behaviors of the three bands are quite identical with those of the band calculation, and therefore these two peaks are identified with the doubly degenerate bands at 0.29 eV binding energy and the non-degenerate band at 0.12 eV binding energy in the band theory, respectively. In this comparison, two differences are obvious. First, the overall band width is apparently underestimated in the calculation. Taking the doublet peak as the reference, the ratio is 0.75/0.29 = 2.6. This ratio is of importance in assessing the reliability of the extended Hückel calculations on other Mo bronzes, performed by the same group and used to compare with our ARPES results in the following chapters. Second, the splitting between the two peaks is overestimated by the calculation. The ratio between the lower binding energy and the higher binding energy is 0.73 in the experiment in substantial disagreement with 0.41 of the theory. As discussed in section 5.1, the larger this ratio is, the closer to the non-interacting 1D bands the band structure is. In addition, we should also remember from the discussion above that this band calculation (Fig. 5.4) produces a central FS piece which is quite different from a hexagon. Therefore, it is quite likely that in the calculation of Fig. 5.4 the hybridization between the 1D bands is overestimated and as a result the splitting between the two peaks at Γ is overestimated.

The ARPES lineshapes observed along the M(M′)K(K′) direction is particularly interesting. Here, a single band well separated from other bands crosses Fermi energy, an ideal condition for lineshape studies in ARPES. However, the lineshapes are truly anomalous in that there is always a significant weight at binding energy ~ 0.7 eV and that the lineshape after the Fermi level crossing, e.g. at the K point, shows a distinct Fermi edge and an overall “hat”-like lineshape. Apart from the intensity drop at the high binding energy, the overall lineshape of this “foot” is actually quite similar to the lineshape observed for the superconducting cuprates [20, 110]. As remarked earlier, an important difference between the cuprates and the bronzes is the energy separation of the “foot” intensity and the big valence band structure. It is this aspect that enables the total lineshape including the eventual drop of the intensity at high binding energy to be observed for the current sample, but not for the cuprates.

The lineshape at the K point for the purple bronzes is so abnormal in fact that in the initial stages of the research it contributed very much to a state of confusion regarding the mapping of the experimental dispersions to the theory. Only after the **k** space map was taken, which gave confidence in the band calculation, did it became clear how the data should be interpreted. However, further study is necessary to determine if the lineshapes near the K point actually represent the hole spectral function, and if so, whether they are a clear sign of electron-electron interactions. It is an intriguing question whether a theory similar to the two pole causal self energy theory which was used successfully in Section 3.3 is capable of producing the anomalous lineshape here. One cannot help but notice the apparent similarity of the anomalous lineshapes observed for $\mathrm{TiTe_2}$ near the M point, and for the purple bronzes near the K point, although a clear difference is that in the former case the spectral function is for an occupied state while for the latter it is for an unoccupied state.

The overall topology of the FS image obtained in this work differs substantially from one published previously [100]. The comparison is shown in Fig. 5.10. The authors in Ref. [100] obtained Fermi level crossing points, marked by filled circles in (a), from EDC's and then used operations of xy ($x \perp \Gamma\mathrm{K}'$, $y \parallel \Gamma\mathrm{K}'$) reflections and translations for the hexagonal symmetry to obtain the full picture. They then deduced two types of FS structures from the data, an elliptical piece around Γ and diamond shaped pieces along axes parallel and perpendicular to the direction of the monoclinic distortion, as shown in (b). They could relate this FS to only two sets of quasi-1D FS's, each line of which was found to intersect edges of two adjacent diamonds at an angle of $\approx 6^{\circ}$. Though parallel, the two intersected edges are displaced by $\approx 0.15\text{Å}^{-1}$, so that the three lines being related as parts of a quasi-1D FS are not actually collinear. The large difference from the calculated FS was attributed to the monoclinic distortion of $\mathrm{NaMo_6O_{17}}$ relative to the higher symmetry of $\mathrm{KMo_6O_{17}}$ used in the calculation [99]. This reported difference is so large that the central feature of the hidden 1D concept is lost, i.e. for the supposed FS of the actual material, best nesting between straight sections would occur *not at the observed CDW wavevector, but at wavevectors parallel to the diamond edges*. Also, the reduced rotational symmetry is inconsistent with the overall hexagonal translational symmetry. However, our image shows *three* sets of *weakly hybridized* quasi-1D FS's, implying a FS with hexagonal symmetry and collinear straight sections, almost perfectly consistent with the theoretical one [99]. It is important to note that the essential difference lies in the raw data which show, in our case, all three quasi-1D FS's at 120° to each other, but in Ref. [100], FS objects coming from only two bands. Therefore, even the use in Ref. [100] of xy reflections to extend the data did not result in the correct FS pattern. One could view that the large difference in the FS topologies finally obtained by this study and by the study of Ref. [100] arises essentially from the fact that the authors in Ref. [100] failed to observe a FS line segment, dim in our map,

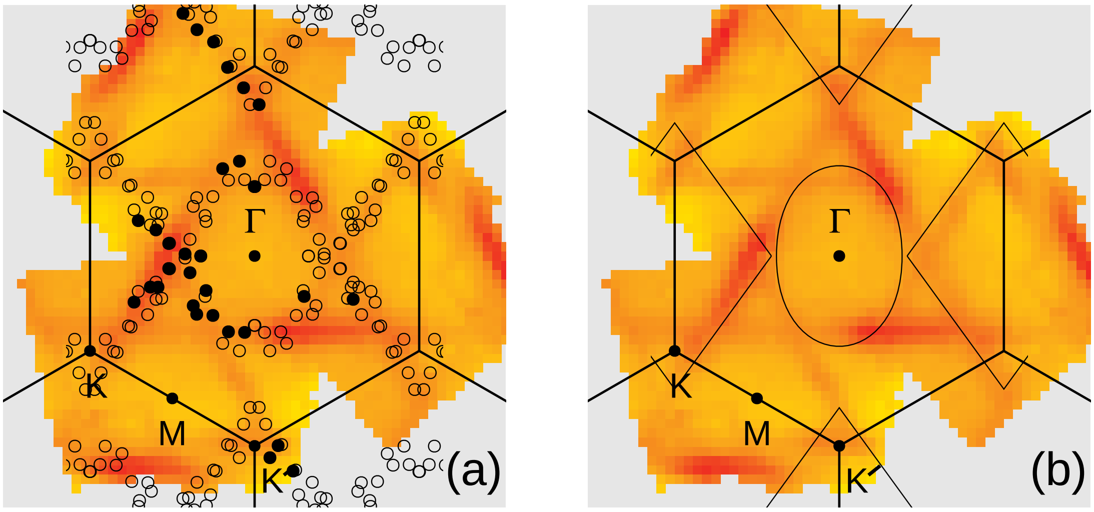

Figure 5.10: Comparison of the NaMo$_6$O$_{17}$ Fermi energy intensity map with FS obtained by Breuer *et al.* [100]. In (a), the circles correspond to the Fermi level crossing points obtained in Ref. [100], and in (b), the lines are the FS deduced in Ref. [100].

connecting the central piece and the pattern around the K′ point.

In this work relative to that of Ref. [100], the observation of collinear straight sections arising from three quasi 1-D FS's, one of which was previously unobserved, may have couple of origins. (1) The photon energy used may be serendipitous for obtaining a non-vanishing ARPES matrix element for observing all the FS features. (2) The complementary use of the map method gives additional information on the locations of FS crossings through more **k** sampling and a view of the overall FS pattern, the contrast of which can be enhanced by use of a logarithmic scale.

Finally we comment on angle integrated photoemission spectra on the 2D purple bron-zes. The data are shown in the next chapter (Fig. 6.6) with the data for the 1D blue bronze, K$_{0.3}$MoO$_3$. Here, a contrast can be easily noticed between the Na purple bronze and the blue bronze – a clear Fermi edge for the one and a smooth power-law-like onset for the other. Looking further ahead, we also point out that the 1D purple bronze, Li$_{0.9}$Mo$_6$O$_{17}$, shows a power law behavior (Fig. 7.10) much like that of the blue bronze, but qualitatively differently from that of the 2D purple bronzes. Consistent with the Fermi edge for the 2D purple bronze, examination of the purple bronze EDC's shows that for the spectra of the E_F crossings, there is substantial weight at E_F. In this respect the quasi-2D purple bronzes are like the quasi-2D high T_c cuprates, even though the two differ in that a considerable body of spectral and transport evidence has been assembled that the latter are NFL materials.

5.4 Conclusions

We have made E_F intensity maps of the quasi-2D purple bronzes, $\mathrm{NaMo_6O_{17}}$ and $\mathrm{KMo_6O_{17}}$. The intrinsic features of the two maps are almost identical, and imply a FS which is substantially different from that in a previous report [100], but which is in remarkably good agreement with nearly all aspects of the hidden 1D picture [99] for these materials. Specifically, the image shows three quasi-1D bands with nearly straight FS sections and only small hybridization induced splittings. The observed nesting wavevector can be understood as the wavevector for optimal nesting of the quasi-1D FS's. Anomalous ARPES lineshapes are found for an isolated band crossing E_F. The novel hidden one dimensionality poses an interesting question of how the Luttinger liquid state of 1D chains are modified by the 2D couplings. Theoretical studies [60, 65, 66] of the effects of higher dimensionality often consider weakly coupled 1D chains, although usually parallel chains rather than the more complex arrangement here.

My role in the work described in this chapter was to measure all the data, to analyze them and to compare them with Breuer *et al.*'s result.

Chapter 6

$K_{0.3}MoO_3$: CDW material with a non-Fermi liquid CDW

This chapter is an expansion of the $K_{0.3}MoO_3$ part of the journal publication: "Fermi surfaces and single-particle spectral functions of low-dimensional inorganic non-cuprate compounds: the molybdenum bronzes", G.-H. Gweon, J.W. Allen, R. Claessen, J.A. Clack, D.M. Poirier, P.J. Benning, C.G. Olson, W.P. Ellis, Y.-X. Zhang, L.F. Schneemeyer, J. Marcus and C. Schlenker, J. Phys. Condens. Matter **8**, 9923 (1996).

In this chapter, $K_{0.3}MoO_3$, a prototypical quasi-1D CDW material is studied with photoemission. In the normal state above the CDW transition temperature, angle integrated photoemission spectra show an absence of the Fermi edge in contrast to the situation with the higher dimensional bronzes. Small weight at E_F is also a general feature of ARPES spectra. Nevertheless, the E_F intensity map shows a FS pattern in good agreement with the previously measured CDW wavevector. By lineshape modeling of the CDW fluctuation effect, I argue that the generally weak intensity at E_F in this material cannot be explained by CDW fluctuations. Rather, this aspect of the data is better explained by a LL theory based on the spin-independent TL model. We also discuss issues that arise when the LL theory is compared with experiment.

6.1 Introduction

$K_{0.3}MoO_3$, the so-called blue bronze, has been studied by many researchers because of its CDW properties and the availability of large (a few *mm* × a few *mm*) single crystalline samples. Although a great deal is known about its CDW properties, the character of its normal state above the CDW transition is not clear. In this section, we

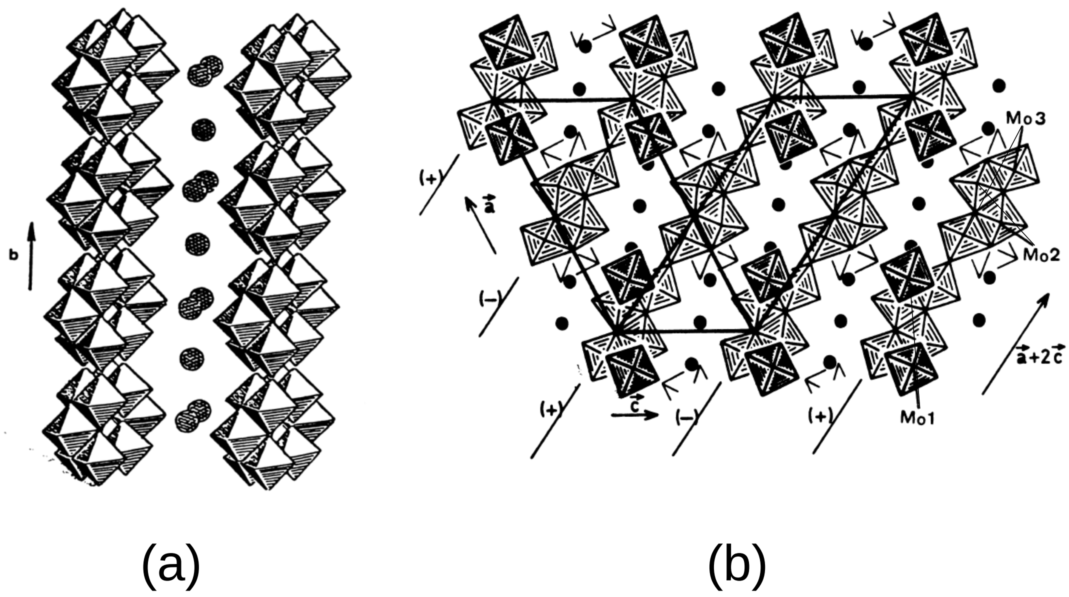

Figure 6.1: Crystal structure of $K_{0.3}MoO_3$. (a) View of quasi-1D chains along the *b* axis. From Ref. [112]. (b) Projection of the structure onto *ac* plane. That is, in this figure, the *b* axis is perpendicular to the paper. From Ref. [113].

summarize known physical properties and previous PES measurements.

Fig. 6.1 shows the crystal structure of the blue bronze. Like the other Mo bronzes studied in this thesis the basic building block of this material is the MoO_6 octahedron. In Fig. 6.1 (a) the chain structure along the *b* direction is easily noticeable. The repeating unit of the chain is $Mo_{10}O_{32}$, consisting of 10 distorted MoO_6 octahedra which share corners or edges with each other. Among the 10 octahedra, 8 make two layers of a 4 octahedra group, containing the Mo2 and Mo3 ions in Fig. 6.1 (b). The other 2, which contains the Mo1 ions in Fig. 6.1 (b), are attached to the sides of the group of 8. This unit repeats along the *b* direction to form a chain, as shown in Fig. 6.1 (a), and the chains form a 2 dimensional $Mo_{10}O_{30}$ slab by corner sharing of the octahedra, as shown in Fig. 6.1 (b). Between the slabs are sandwiched the K ions which play the role of gluing the layers to form a 3 dimensional crystal structure, as well as providing electrons to the Mo sites, the Mo2 and Mo3 ions, to make the material conducting. The unit formula for the blue bronze is $K_6Mo_{20}O_{60}$. The overall crystal symmetry is $C2/m$ (monoclinic), and the lattice parameters are given by $a = 18.249$ Å, $b = 7.560$ Å, $c = 9.855$ Å, and $\beta = 117.3^o$ [111].

The blue bronze shows quasi-one dimensional electronic properties, as evidenced by the resistivity [114] and the optical properties [115]. The resistivity perpendicular to the *b* axis is greater than that along the *b* axis by a factor of 10 to 100. The blue bronze undergoes a metal-semiconductor transition [114, 116] with a lattice modulation [117] at T_c=180K. Its CDW wavevector, studied by X ray diffraction [117] and neutron scattering [118], is unusual in that it shows a temperature dependence. Its b^* axis component gradually increases from ≈0.72 b^* at 180 K to ≈0.75 b^* near 100 K, below which it stays nearly constant at ≈0.75 b^*. The CDW transition at 180 K is also seen in the magnetic susceptibility [119, 120], which shows an abrupt decrease as the temperature is changed from above to below the transition. Interestingly, the magnetic susceptibility in the metallic phase is not constant as expected for a normal Fermi liquid, but shows an activated behavior up to the highest measured temperature of 720 K with an apparent gap of $\Delta \approx 24$ meV deduced from a fit [119] in the temperature range of $T = 200$ K $\sim$ 300 K. J. Voit drew attention to this apparent spin-charge separation, i.e. a metallic charge channel (resistivity) and a gapped spin channel (Pauli susceptibility), was noticed by J. Voit [121], and suggested that a LL behavior is observed for the blue bronze. However, early on, Pouget *et al.* [122] conjectured a flat band ≈ 56 meV above the Fermi energy to explain the temperature dependent CDW wavevector. At the same time, they argued that this band is responsible for the abnormal spin susceptibility in the metallic phase. This argument was also supported by a band calculation [123] which found a band giving rise to a high density of states just above the Fermi energy. We will discuss this band calculation result shortly. However, one should note that this extended Hückel tight binding band calculation was the only one available until very recently, because of the great difficulty of performing calculations for a material with such a large unit cell. A new first principles LDA band calculation [104] does in fact show some substantial differences, one of which is the absence of the unoccupied band just above E_F. Therefore, the origin of the T dependent CDW wavevector and the apparent spin-charge separation is still an unresolved issue.

Fig. 6.2 shows the theoretical tight binding bands calculated for the blue bronze. Fig. 6.2 (a) shows the hexagonal Brillouin zone for the $Mo_{10}O_{30}$ layer. A more convenient tetragonal unit cell is also shown in the figure. Here, ΓX is parallel to the b or b^* axis, and the X point is given by (b^* /2, 0). In Fig. 6.2 (b) the one dimensional bands for the $Mo_{10}O_{32}$ chain are shown. The calculated bands for the $Mo_{10}O_{30}$ slab in Fig. 6.2 (c) show substantial amounts of dispersion perpendicular to the chain. The FS is shown in Fig. 6.3. From the two pieces of FS and their curvatures, a nesting vector that connects one FS to the other is identified, as shown in the figure, and is in reasonable quantitative agreement with the wavevector measured by X ray diffraction [117]. It should also be noted that if the full three dimensional structure of the blue bronze is considered

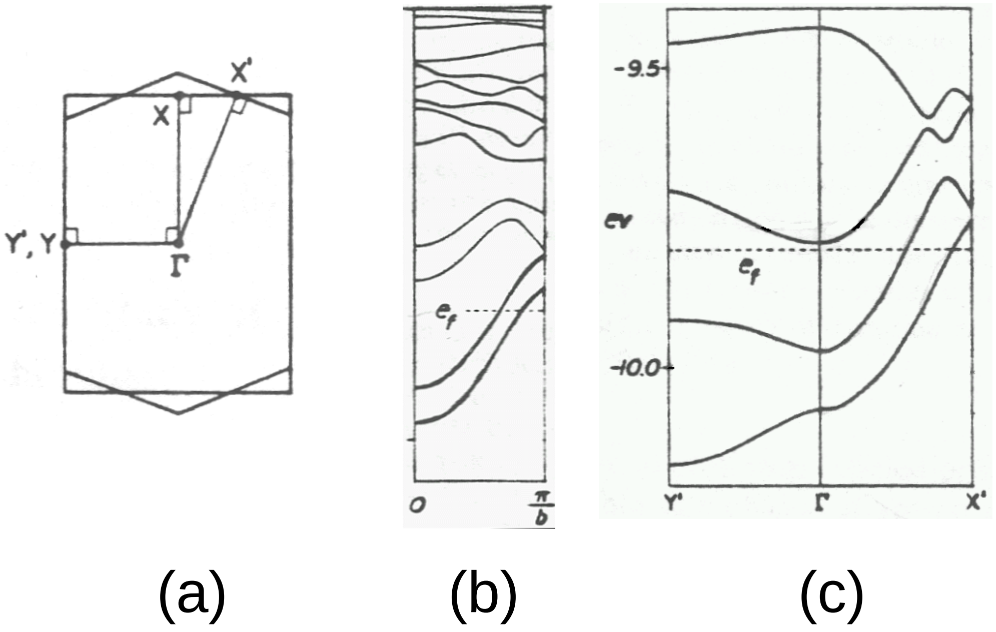

Figure 6.2: Band calculation for $K_{0.3}MoO_3$, taken from Ref. [123]. (a) Brillouin zone for the $Mo_{10}O_{30}$ slab. (b) Low lying d block bands for $Mo_{10}O_{32}$ chain. (c) Low lying d block bands for $Mo_{10}O_{30}$ slab.

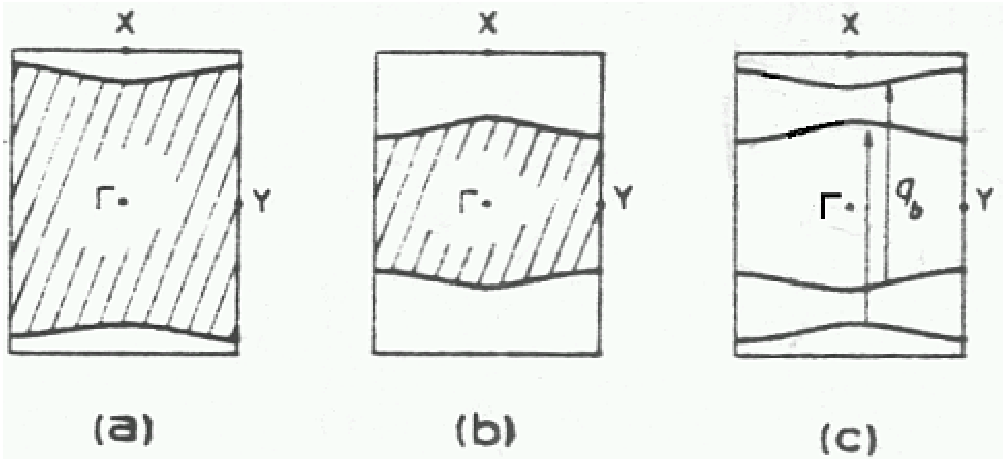

Figure 6.3: FS of $K_{0.3}MoO_3$, calculated for the $Mo_{10}O_{32}$ slab. From Ref. [123]. Shaded regions are occupied with electrons. (c) shows nesting of the two FS's.

then the unit cell contains twice as many MoO_6 octahedra as the $Mo_{10}O_{30}$ layer or the $Mo_{10}O_{32}$ chain. Therefore, each band shown in Fig. 6.2 is expected to show a small amount of splitting if some 3 dimensional coupling exists. Note also that Fig. 6.2 (c) shows an unoccupied band just above E_F near the Γ point – the feature discussed in the previous paragraph.

From the PES point of view, the blue bronze is one of many quasi-1D materials which do not show a Fermi edge in PES, while being nonetheless metallic in their transport properties. The previous angle integrated PES data for the blue bronze were shown in Fig. 1.7. Many quasi-1D materials which show the absence of the Fermi edge also show CDW transitions. Examples are the blue bronze, Ta_2Se_8I [29, 21] and TTF-TCNQ [124]. Therefore, the electron-phonon interaction should be included in a realistic model of the electronic properties of these materials. As is carefully discussed in Ref. [28], the electron-phonon interaction could lead to a suppression of spectral weight at the Fermi energy, through pseudo-gap formation due to CDW fluctuations. The latter was the topic discussed in section 2.3. However, a generically non-FL state in 1 dimension is that of the LL, discussed in section 2.4. An experimental issue to consider in assessing these different mechanisms is the surface degradation [125] which could also the explanation of the vanishing E_F weight. Because the **k**-resolved spectral function contains much more detailed information for distinguishing among these different mechanisms, obtaining ARPES spectra for this class of materials is crucial.

Fig. 6.4 shows a previous ARPES study in the metallic state. Here, a single broad peak is observed to disperse in the 1D direction. It shows an E_F crossing with a value of k_F in good agreement with the wavevector $2k_F$ of the CDW lattice distortion as determined by the X-ray diffraction [117]. Note that the spectra have a large background in the energy range 1 eV to 2 eV below E_F. In the present study we have obtained spectra with very low backgrounds, enabling the observation of two features which disperse toward E_F in the 1D direction. We attribute the low backgrounds in large measure to minimizing photon induced sample damage by taking precautions based on studies by Breuer *et al* [125]. Their results, reproduced in Fig. 6.5, show a defect structure growing at ~ 2 eV binding energy and a shift towards high binding energy of the near-E_F peak as the sample is damaged by the photon.

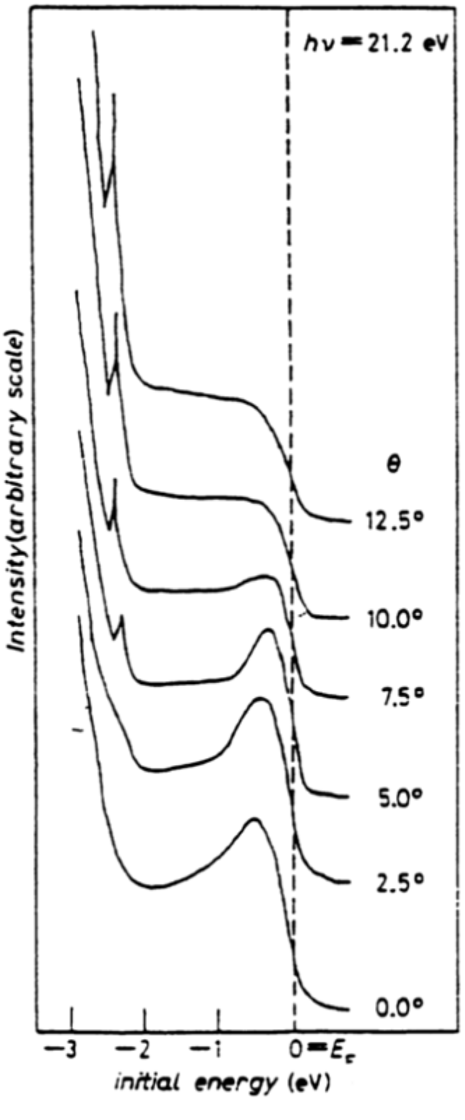

Figure 6.4: ARPES EDC's of the blue bronze by Veuillen *et al* [126].

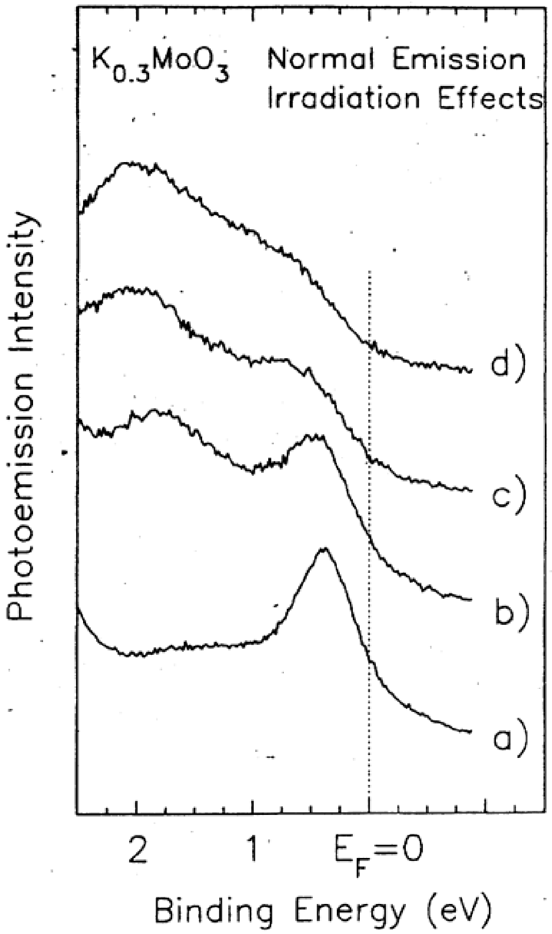

Figure 6.5: Sample damaging effect of photon irradiation on the blue bronze as reported by Breuer *et al.* in Ref. [125]. (a) Cleaved. (b) 20 h exposure at $h\nu = 18$ eV. (c) 60 min exposure at $h\nu = 60$ eV. (d) 145 min exposure at $h\nu = 60$ eV.

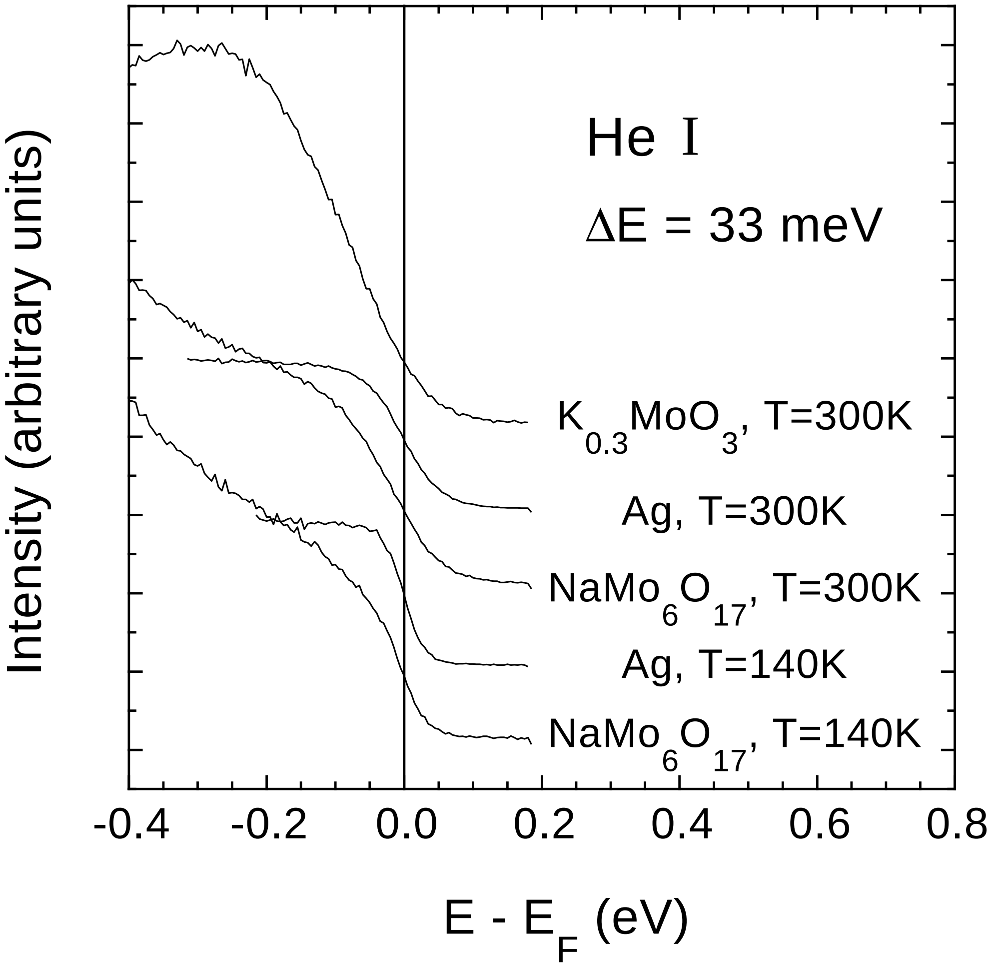

Figure 6.6: Angle integrated PES spectra of $K_{0.3}MoO_3$ and $NaMo_6O_{17}$ taken at 300K and 140K. He I line (21.2eV) was used for the photon source. Overall instrumental energy resolution was 33meV FWHM. Spectra for Ag are shown for comparisons. Note the absence of a Fermi edge only for $K_{0.3}MoO_3$.

6.2 Experimental

ARPES data were taken at the Ames-Montana beamline of the SRC and at beamline 5-1 of the SSRL. Angle integrated PES data were taken in the home lab. Single crystal samples were prepared by our collaborator at Bell Laboratories by electrolyzing fused-salt mixtures [127], and were cleaved *in situ* in ultra-high vacuum chambers having a base pressure better than 2.0 $\times 10^{-10}$ Torr. The sample temperature was between 220K and 300K, well into the metallic phase. The angular resolution of the electron spectrometers was $\sim 2^{o}$ full acceptance. Samples were oriented by Laue diffraction. The cleavage plane of the blue bronze crystal is $(\bar{2}01)$, i.e. parallel to the $Mo_{10}O_{30}$ plane.

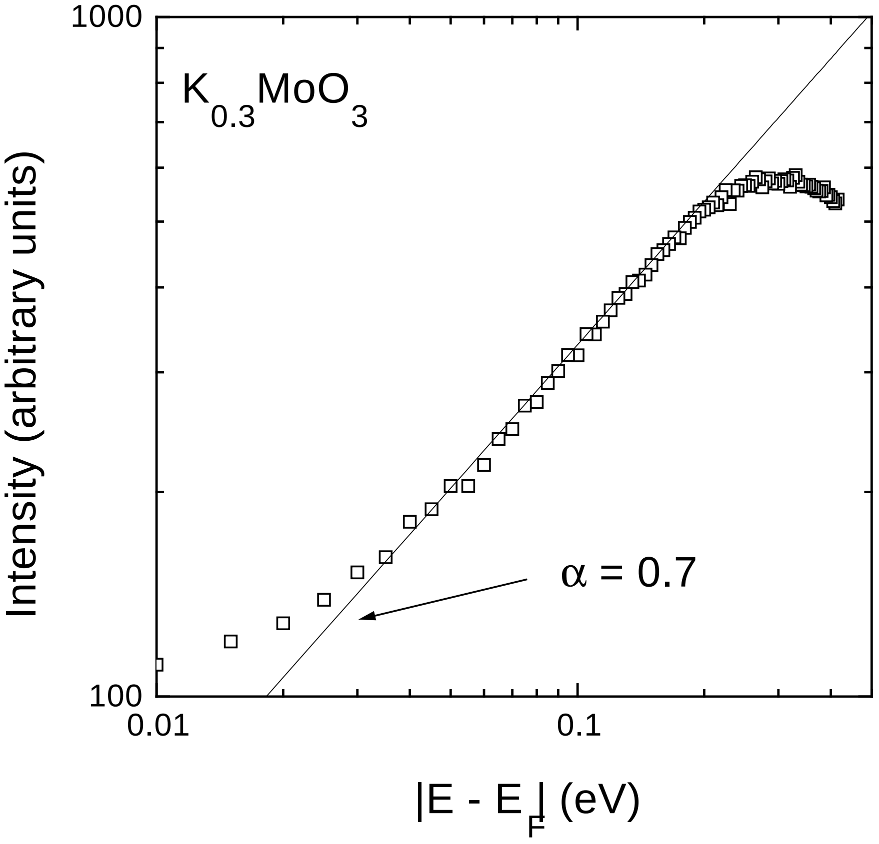

Figure 6.7: Power law fit of the blue bronze angle integrated photoemission spectrum shown in 6.6.

6.3 Results

To begin, we look at the angle integrated photoemission spectrum in Fig. 6.6, taken at 300 K. For comparison, we also show spectra of the 2D Na purple bronze and Ag, taken at T=300 K and at 140 K. The spectrum for the blue bronze is similar to that of a previous study shown in Fig. 1.7, and shows a smooth onset of the spectral function at E_F. In contrast, the Na purple bronze, which has hidden one dimensionality but is a quasi 2D metal, shows a Fermi edge with the width scaling correctly with the temperature, in much the same way as that for Ag. An alternative scenario for the angle integrated photoemission spectrum is the power law behavior of the LL theory. Fig. 6.7 shows a power law fit of the spectrum. For the binding energy range from 30 meV to 150 meV, a linear behavior is found in the double log plot, from which we deduce a power law behavior of $\propto \omega^{0.7}$. From the data of Fig. 1.7 one obtains a similar behavior, $\propto \omega^{0.9}$.

Given the lack of a Fermi edge in the PES spectrum, one may wonder if a FS can be observed. The answer is 'yes', as shown by the direct FS image for $K_{0.3}MoO_3$ in Fig. 6.8. The actual data set consists of the right half of the image and the full image has been produced by reflection about the ΓY line. As for the purple bronze image of Fig. 5.5, the details of the intensity distribution along its bright parts arise from the ARPES matrix element. But one can clearly see four lines of FS, consistent with those expected from band theory, which are shown by the dashed lines. Both of the two experimental pieces of FS lie closer to the vertical X axis than in the theory. We interpret the experimental feature lying essentially on the vertical X axis as the unresolved image of the two lines symmetrically disposed on both sides of the axis, as the two lines of the theoretical FS in the figure, and very close to it. The curvature of the lines shows the departure from one-dimensionality and judging by their centroids, the departures of the experimental features are less than that of the theory. That is, the experimental FS is more 1 dimensional than the theoretical FS. The projection of the experimental CDW wavevector onto the plane of Fig. 5.5 is shown by the arrow. The length of the arrow is in excellent agreement with that required for good nesting, i.e. twice the distance from Γ to the midpoint of the two pieces of FS in half the zone, and is longer than that implied by the theoretical FS. As a final point concerning this figure, it appears by eye that the FS image for the blue bronze is more diffuse than that of the purple bronze in Fig. 5.5, which may reflect the lack of weight near E_F in the PES spectrum and also in the ARPES EDC's, which we discuss next.

Fig. 6.9 shows ARPES spectra along the *b* direction, taken at the SRC with photon

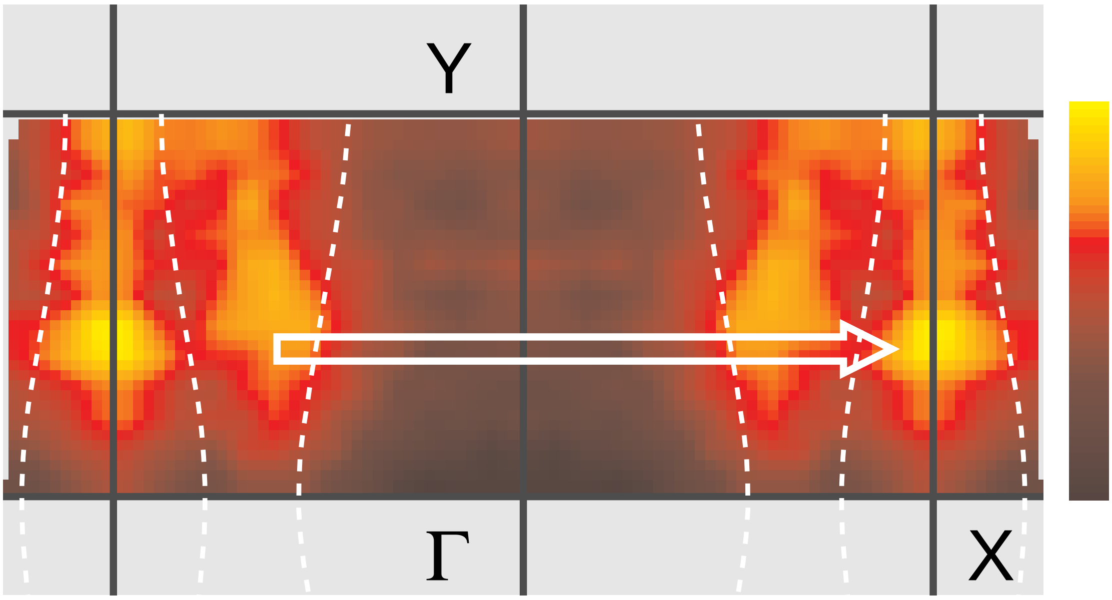

Figure 6.8: Fermi energy intensity map for $K_{0.3}MoO_3$ obtained at 300K with 17eV photons. Overall instrumental resolution was 150meV FWHM. The measured data are the right half of the map, while the left half was obtained by reflection, a symmetry operation for the crystal. ΓX is parallel to the crystallographic b axis, the easy axis. Four almost linear FS's are observed. The dotted lines are the FS's shown in Fig. 6.3. The measured CDW wavevector, from Ref. [117], is shown as an arrow.

energy 17 eV and energy resolution of 140 meV. The only hint of photon-induced sample damage [125] is a slight peak near 2 eV which appears only in spectra taken after the sample surface has begun to age. The symmetrical dispersion of the two marked features about the Γ and X points gives confidence that they are both intrinsic. The high binding energy feature disperses much more rapidly than the low binding energy feature. E_F crossings after 12^o (k_b=0.37 $Å^{-1}$) and 8^o (k_b=0.25 $Å^{-1}$) are implied by the two dispersions, respectively, as expected for a metallic state and consistent with the Fermi energy intensity map. However, the carefully calibrated E_F position falls on the leading edges of the spectra nearest E_F such that their E_F weights, although nonzero, are anomalously smaller than usually found, e.g. in Fig. 3.3, for E_F crossings.

Fig. 6.10 shows the dispersions perpendicular to the b axis, along the two directions [102] and ($\bar{2}01$). In Fig. 6.10 (a) the total angle span of 10^o encompasses the entire first Brillouin zone in the [102] direction. We show the spectra for $k_b = 0.25$ $Å^{-1}$ where both peaks are easily seen for all the angles. No dispersion can be detected in the data. The spectra in Fig. 6.10 (b) were measured close ($\theta = 4^o$) to normal emission, with the k-value along the ($\bar{2}01$) direction being varied by changing the photon energy. Without knowing the inner potential V_o in Eq. 1.4 we cannot determine the precise k-values along the ($\bar{2}01$) direction but if the parameter is less than 20 eV, as is nearly always so,

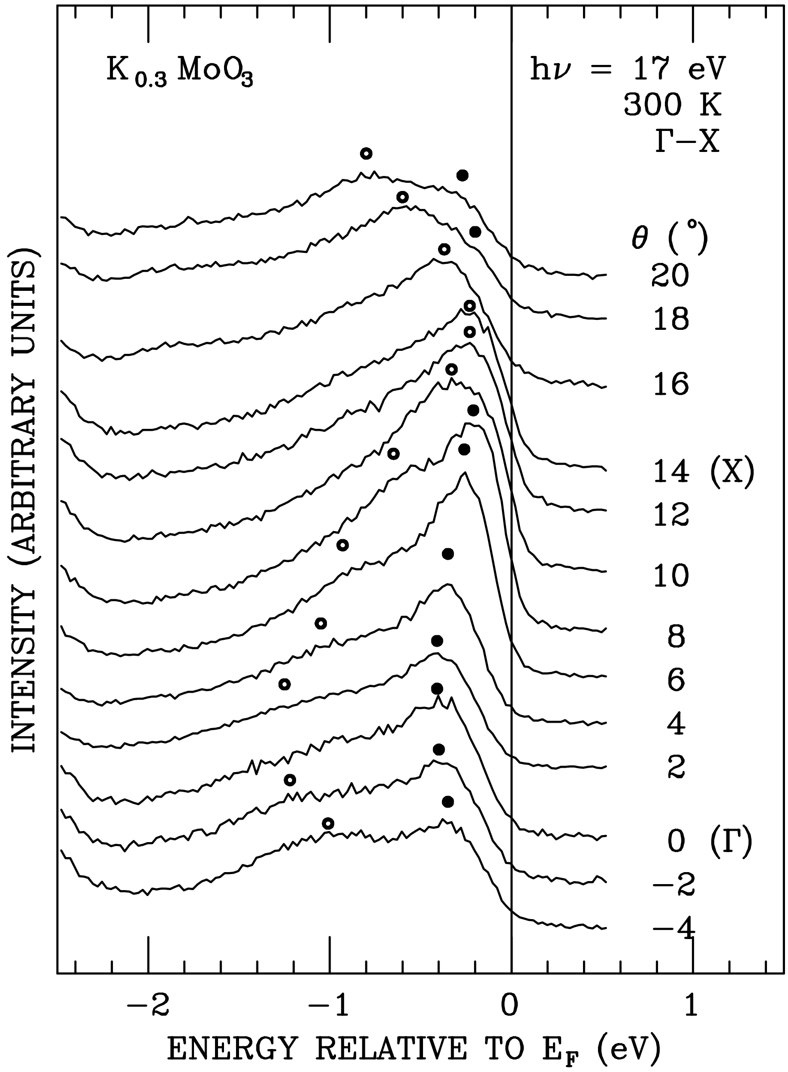

Figure 6.9: ARPES of the conduction band region for k varying along the *b* axis. θ is the angle between the surface normal and the electron analyzer. The X point k_b value is 0.42 Å^{-1}, with $\theta \approx 14^{\text{O}}$. The resolution (FWHM) is 140 meV. Filled and open circles are drawn on the peak maxima.

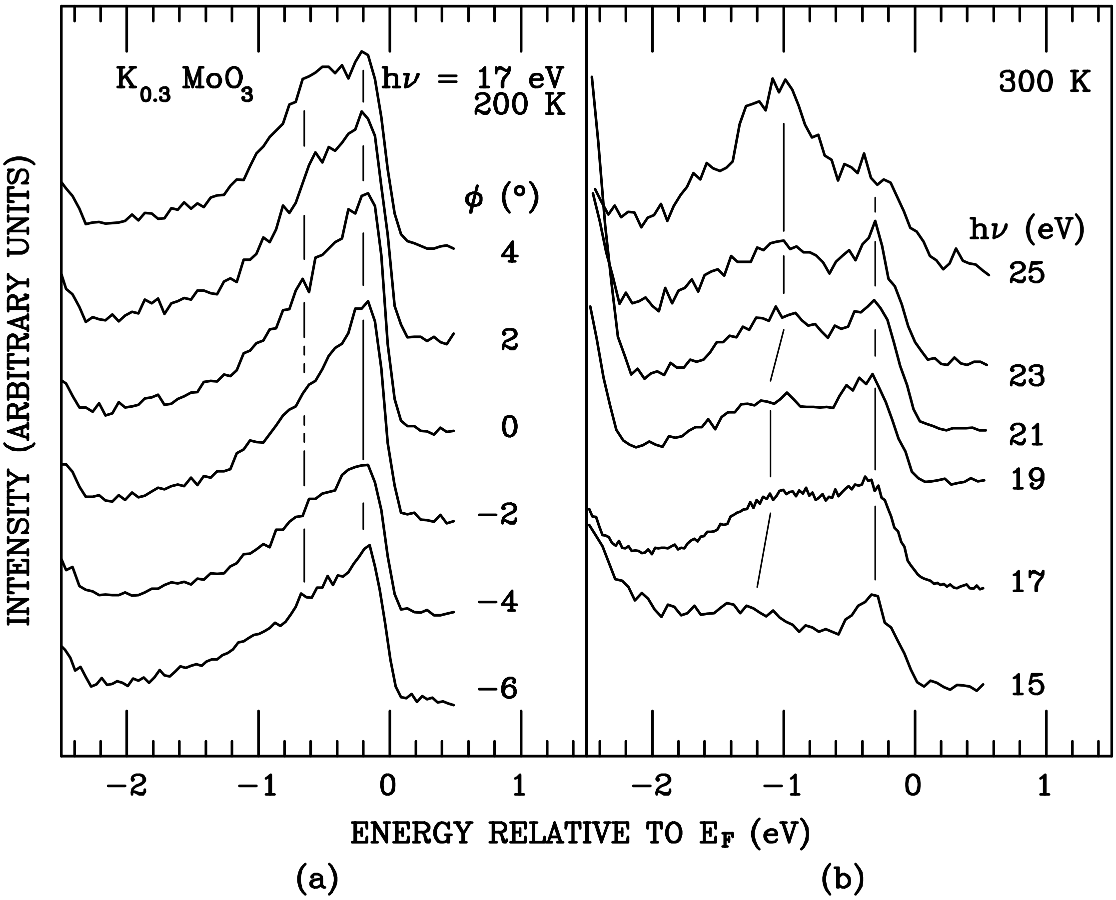

Figure 6.10: ARPES of the conduction band region for k varying along directions perpendicular to the b-axis . (a) the [102] direction, with $k_b = 0.25$ Å^{-1} ($\theta = 8^{o}$), and (b) the ($\bar{2}01$) direction, with $\theta = 4^{o}$. The short vertical lines are a guide to the eye.

then the data span at least 60% of the first Brillouin zone in this direction. The small variation of k_b arising from the slight deviation from the surface normal fully accounts for the only hν-dependence of the line positions in the spectra, i.e. the small shift of the high binding energy peak due to its large k_b dispersion.

In Fig. 6.11 we show the dispersions along the b axis taken with 20 eV photons at the SSRL and at the SRC with energy resolutions of 40 meV and 100 meV respectively. First of all, one can note the exceptionally low background of this set of spectra. The background shows no sign of sample damage of the kind reported in Ref. [125]. The marked features in Fig. 6.11 show the same dispersions as those in Fig. 6.9, and for k-values where the spectrum has its closest approach to E_F, the weight at E_F is again unusually low. One may observe that the E_F weight relative to the peak height is largest near the X point. Exactly at the X point, the fast dispersing band has already crossed E_F. However, the close proximity of this E_F crossing to the X point implies that the band is just above E_F.

Fig. 6.12 shows the energies of the ARPES peak maxima from several sets of our data. Interpreting the nearest E_F peaks to obtain accurate values for k_F probably requires a detailed analysis with an appropriate theoretical lineshape. Important here is the comparison with the results of a tight binding band calculation [20] over the entire Brillouin zone. One sees that the high binding energy peak is about 5 times further from E_F than the calculated bands, with an absolute energy difference of up to 1eV. The energy of the low binding energy peak is about a factor of 2 larger than the calculated binding energies. We will discuss these findings in more detail later. Now we discuss the general features of the ARPES lineshapes.

In order to understand the ARPES lineshapes of the blue bronze, it is important to assess the extent of CDW fluctuations. Evidences of CDW fluctuations are easily found for the blue bronze. For example, the gaps measured by the resistivity [40], the optical conductivity [40] and the magnetic susceptibility [119], imply the ratio of $2\Delta(0)/T_c \approx 5 \sim 8$, significantly higher than 3.52 for the mean field theory of Eq. 2.21. CDW fluctuations are directly observed in the X ray diffraction experiments as diffuse scattering [128]. From the widths of the diffraction intensity peaks, the correlation lengths along the b direction, the [102] direction and the $(\bar{2}01)$ direction have been deduced. For example, from the temperature dependence of the correlation lengths it is found that the 3D ordering sets in at ≈ 200 K, above which 2D fluctuations dominate. This is a concrete example of the qualitative picture of dimensional cross-over in the

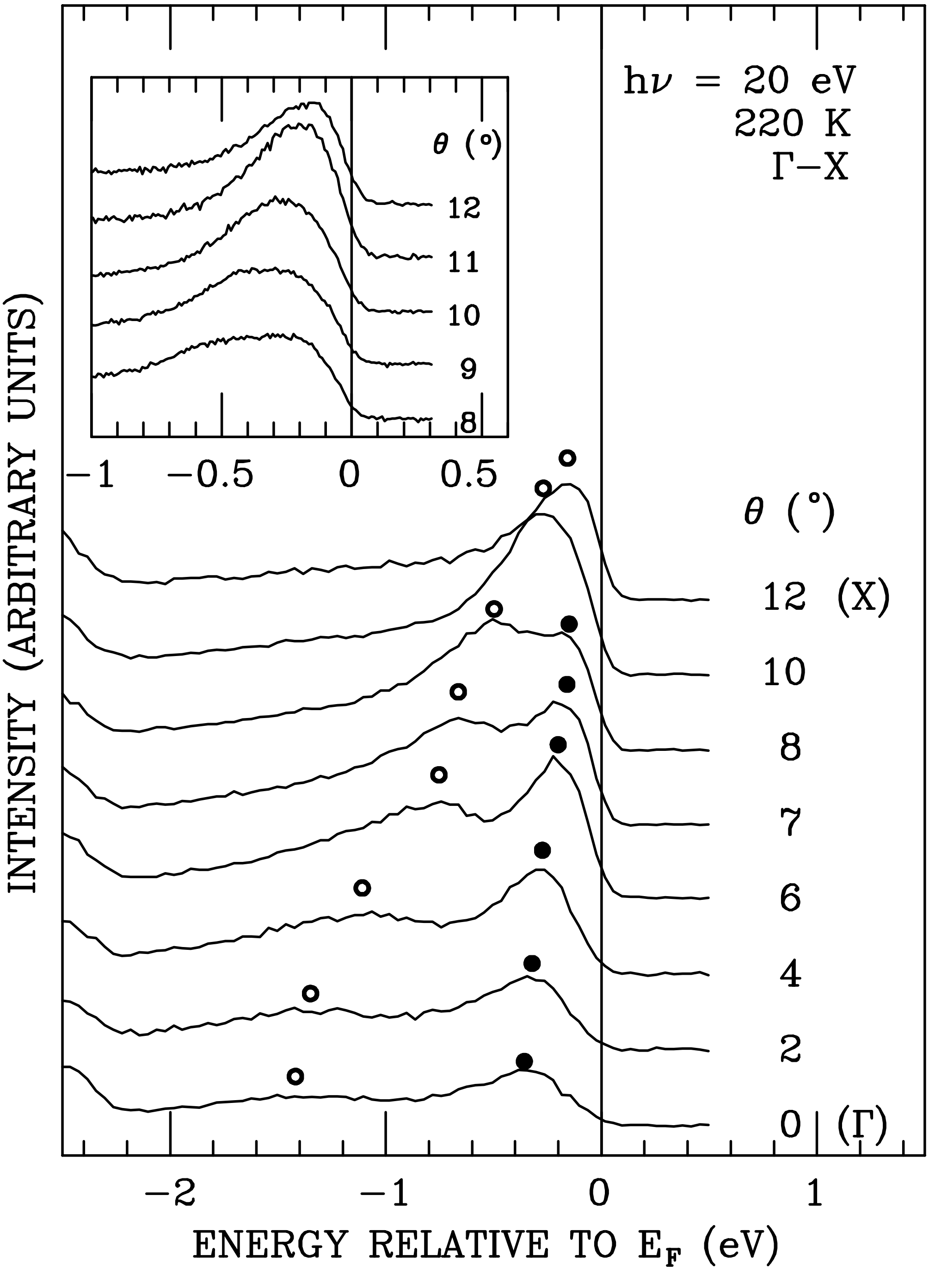

Figure 6.11: ARPES of the conduction band region for k varying along the *b* axis. The sample cleave, temperature, and photon energy differ from the data of Fig. 6.9. The resolution is 100 meV. The inset shows data taken at SSRL with hν=20.2 eV and a resolution of 40 meV.

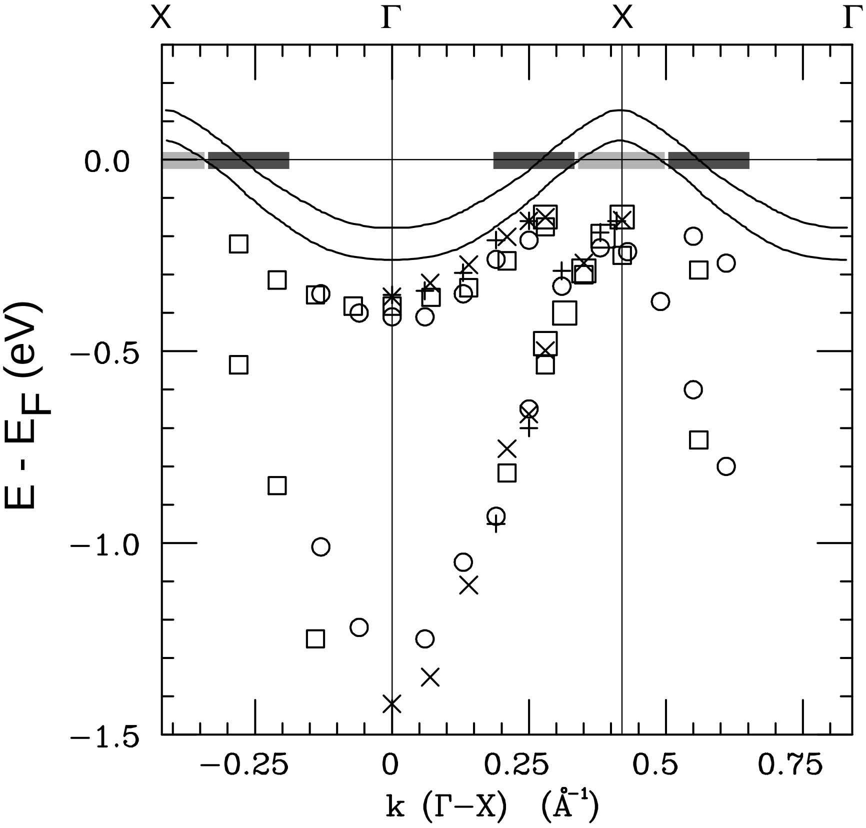

Figure 6.12: Comparsion of the ARPES peak maxima and the theoretical bands (solids lines) calculated in Ref. [123]. Circles: SRC, hν=17 eV (data of Fig. 6.9). Crosses: SRC, hν=20 eV (data of Fig. 6.11). Pluses: SRC, hν=17eV (same cleave as for Fig. 6.11). Boxes: SSRL, hν=20.2 eV (big boxes, data of inset of Fig. 6.11; small boxes, data of spectra not shown here). The gray bars at the Fermi energy show the location of the E_F crossings deduced from Fig. 7. Approximate FWHM's, parallel to ΓX, of the FS "peaks" in the image are indicated.

fluctuation regime, as presented in section 2.3. Due to its anisotropy, both 1D to 2D crossover and 2D to 3D crossover exists in the blue bronze. For the temperature range of our ARPES experiment, 220 K $\sim$ 300 K, the correlation length along the b direction varies from $\approx$ 50 Å to $\approx$ 30 Å. An important question to ask is, how much do the fluctuations affect the ARPES lineshapes?

Using the theory of Rice and Strässler as described in section 2.3, we argue that the ARPES lineshapes observed for the blue bronze cannot be ascribed to CDW fluctuations (alone). In order to know the α and f for the Rice and Strässler theory of section 2.3, we need to know v_F, ψ, and T_{MF}. We estimate these parameters as follows. First, v_F is estimated from Fig. 6.12 by using the gray bars as a guide. We get, $v_F \approx 3$ eVÅ for the slowly dispersing band and ≈ 4 eVÅ for the fast dispersing band. Due to the uncertainty of the k_F values, the uncertainties of these velocities are estimated to be $\approx \pm 0.5$ eVÅ. Second, the mean square fluctuation of the order parameter ψ is estimated to be the $T = 0$ gap as measured by the optical conductivity [40], $\approx$ 700 K = 60 meV. This is an estimated conservative upper bound for ψ. In reality, this value is likely to be smaller. For example, the effective gap above 200 K, and up to 300 K, was deduced in Ref. [119] from the activated behavior of the spin susceptibility to be about half of the $T = 0$ gap. Third, T_{MF} is obtained from the $T = 0$ gap as 2×700 K $/3.52 = 390$ K, from Eq. 2.21. To make a conservative estimate, we calculate for the smallest value of α, which means the strongest tendency to form a pseudo-gap. Therefore, we use $v_F = 3$ eVÅ, $\psi = 60$ meV and $\xi = 50$ Å, and get $\alpha = 3/(0.06 \times 50) = 1$ from Eq. 2.24. For f, the 3 dimensional coupling parameter, we get $\approx$ 5.3 by inserting $T_c = 180$ K and $T_{MF} = 390$ K into Eq. 2.25.

Fig. 6.13 shows the ARPES spectra calculated with these parameters, and assuming a linearly dispersing band with $v_F = 3$ eVÅ. In addition, the experimental angular resolution and energy resolution are taken into account by assuming Gaussian resolution functions for W_k and W_ω in Eq. 1.9. The temperature was taken to be 220 K, in consistency with the choice of ξ. In Fig. 6.13 (a), the energy resolution corresponding to the inset of Fig. 6.11 was used, and in Fig. 6.13 (b) the energy resolution corresponding to the main figure of Fig. 6.11 was used. Note that the only substantial difference between the general situations of the calculation of Fig. 6.13 and the experiment of Fig. 6.11 is the assumed linearity of the band. Because the bands near k_F are expected to be linear, we can make meaningful comparisons of the near k_F spectra. If we make such a comparison, a large difference between the theory and the experiment is readily noticeable.

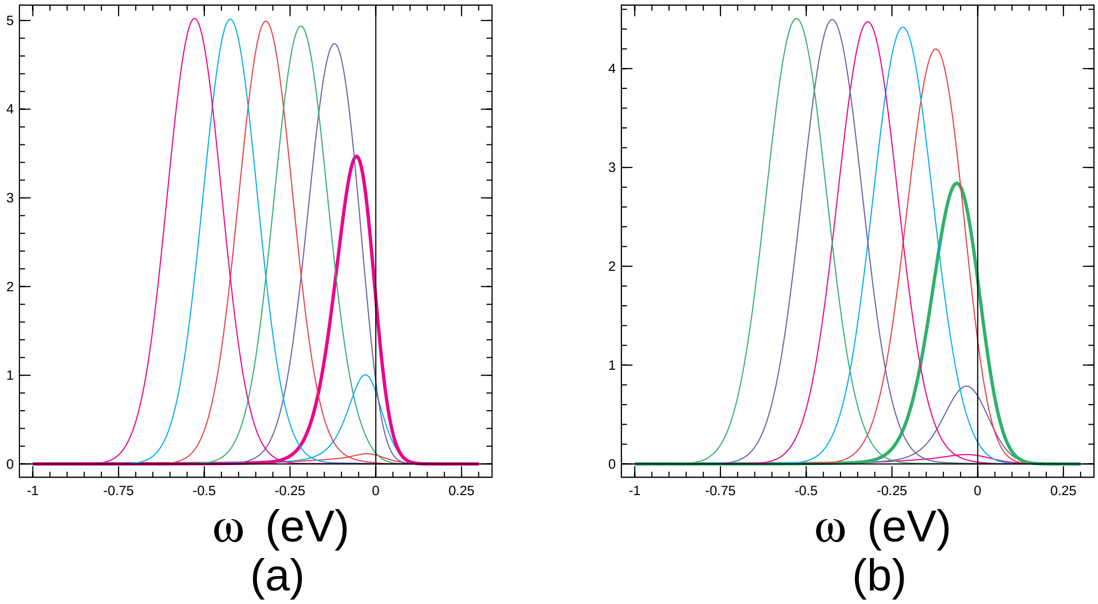

Figure 6.13: ARPES spectra calculated with CDW fluctuations, for the blue bronze at 220 K, and with energy resolution of 40 meV FWHM ((a)) and 100 meV FWHM ((b)). Linear dispersion is assumed, and the momentum increment for successive spectra corresponds to the angle increment of 1^o. k_F spectrum is plotted as thick line. See the text for discussion.

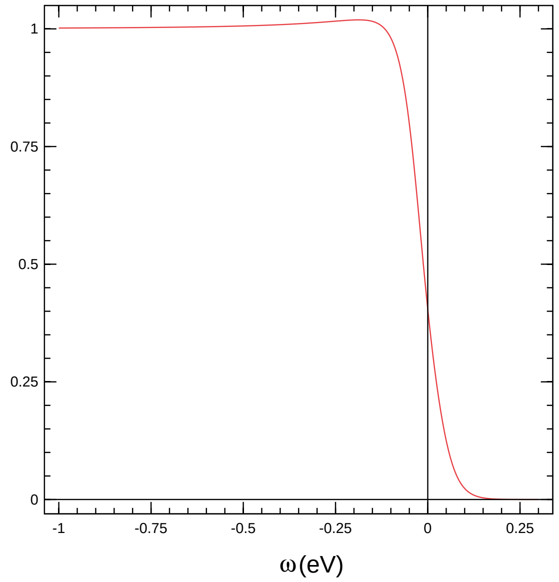

Figure 6.14: **k**-integrated spectrum calculated with CDW fluctuations for the blue bronze at 300 K, and with energy resolution of 33 meV. See the text for more discussion.

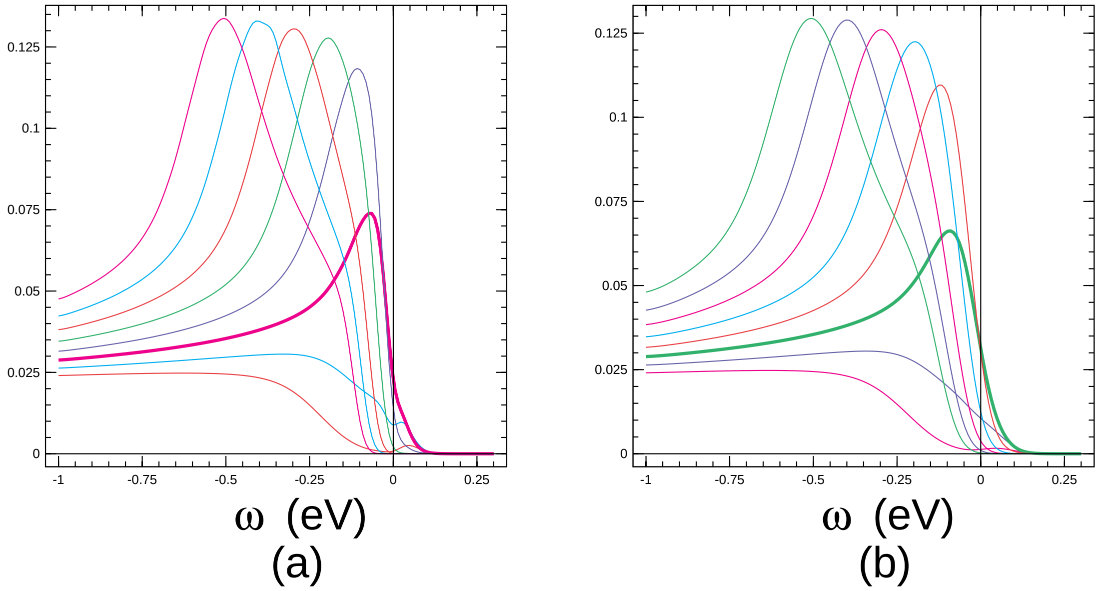

Figure 6.15: ARPES spectra calculated with the TL model for the blue bronze. The information in the caption of Fig. 6.13. For more discussion see the text.

The spectral weight at E_F in the inset of Fig. 6.11 is very small compared to that of the peak. However, the E_F weight at the E_F crossing in Fig. 6.13 is more than half of the peak height. Furthermore, after the crossing, the spectral weight at E_F is as much as 80 % of the peak height. In short, the relative strength of the E_F intensity to the peak height is far too small in the experiment to be explained by the CDW fluctuation theory. The conclusion is strengthened by the fact that we have been most conservative in the selection of the theoretical parameters. It is quite likely that our estimate of α is about a factor of 2 or more too large. If we included this correction, the comparison between the experiment and the theory would be even worse. However, in practice such a correction is found to be irrelevant for the current parameter values. Specifically, the doubling or halving of α or f does not change the final result substantially enough to change the general quality of the comparison.

One can also calculate the **k**-integrated spectrum and compare it with the angle integrated PES in Fig. 6.6. Fig. 6.14 shows the calculation. In this result, not only is there a clear Fermi edge, although slightly shifted to high binding energy, but also there is a small peak at 100 $\sim$ 200 meV binding energy due to the pileup of intensity following the formation of the pseudo gap. In the experiment, none of these features are observed.

Another candidate for producing a low weight at E_F is the LL. Fig. 6.15 shows ARPES spectra calculated within the spin-independent TL model (cf. section 2.4). Specifically Eq. 45 of Ref. [58] was used to calculate the spectral function, the same as for the Li purple bronze analysis of Chapter 7. The parameters used for this TL model are $\alpha = 0.7$, $v_F = 0.66$ eVÅ, and $r_c = 0.1$Å. The α value was taken from Fig. 6.7. The v_F value was chosen so that the final spectra show peaks which disperse with velocity 3 eVÅ, as in Fig. 6.13. The steps to determine this v_F are the following. First, let us remember from section 2.4 that for k within the FS there are two singularities on the photoemission side of the spectral function. They are at $v_c(k - k_F)$ and $v_s(k - k_F)$ with singularity indices $\alpha_c/2+\alpha_s-1/2$ and $\alpha_s/2+\alpha_c-1/2$, respectively (cf. Eq. 2.34). Noting that $\alpha_s = 0$ for the spin-independent interaction, one sees that the spin density singularity at $v_s(k - k_F)$ is divergent (a peak) for $\alpha_c < 1/2$ but goes to 0 for $\alpha_c > 1/2$ (a step singularity). Second, let us also remember that for spin-independent interactions there is a special relationship coupling between α and β_c, given by Eq. 2.29. For $\alpha = 0.7$, this relation gives $\beta_c = 4.6$. Combining these two facts, the general description of the spectral function for $1/2 < \alpha < 1$ is a peak dispersing with velocity $\beta_c v_F$ and a step edge dispersing with velocity $\beta_s v_F$. In order to reproduce the dispersing peak with velocity 3 eVÅ, we are therefore forced to choose $v_F = 0.66$ eVÅ, which is what we used above. Finally, the r_c value was chosen so that the calculated spectral functions are well within the validity limit of the universal LL behavior [58]. We defer the discussion of the importance of r_c to the next chapter. Here we merely note that the choice of its exact value is irrelevant as long as it gives the correct behavior in the spectral function. In the calculation of Fig. 6.15, the same angular resolution function and energy resolution function were used as that for Fig. 6.13.

The theoretical spectra in Fig. 6.15 are definitely an improvement over those of Fig. 6.13 in the comparison with the experiment. The weight at E_F is always less than half the peak height. It happens that for the 100 meV energy resolution the k_F spectrum shows an E_F intensity which is almost half the peak height. Experimentally, the spectrum at angle 8^o in Fig. 6.11 does show E_F weight somewhat close to half the peak height, but not as much as in the theory. The same situation occurs if we calculate the TL lineshapes for velocity 4 eVÅ, suitable for the fast dispersing band, and compared the theoretical $k = k_F$ spectrum with the spectrum at angle 12^o. One might imagine that some combination of the two models – LL and CDW fluctuations – would cooperatively decrease the weights at E_F to make them agree better with the experiment. In fact, the Luther Emery model [129] may be such a possibility. This model includes an attractive $2k_F$ scattering in addition to the interactions of TL model. As a result, the spin channel is gapped and the charge channel remains metallic. Such a model would also describe the apparent spin-charge separation, as pointed out by Voit [121]. Because removing an electron requires removing both charge and spin excitations, the spin gap would appear as a gap in the one electron spectral function. Another possibility to improve the agreement between the TL theory and the experiment is to increase α.

Another point of the comparison is that in the TL lineshape there is an intrinsic asymmetry while the CDW fluctuation lineshape shows very symmetric peaks except perhaps near the E_F crossing. The reason for the latter is that the CDW fluctuation theory does not have any interaction other than the electron-phonon $2k_F$ scattering, which is strong only near k_F due to the FS nesting condition. Therefore, for k away k_F, the lineshape becomes practically that of the non-interacting limit, a delta function. The Gaussian lineshapes found for most of the angles in Fig. 6.13 reflect just the convolution of the experimental Gaussian k resolution function and the experimental Gaussian ω resolution function. The experimental lineshapes in Fig. 6.11 are definitely asymmetric. Therefore, also in this respect, the TL model is better. However, one should also note that the lineshape asymmetry is a common feature of electron-electron interaction models, including the FL model discussed in section 2.2.

It is an interesting finding that in the comparison of the LL model with the experimental results we are forced to use $\beta_c = 4.6$, a number very close to ~ 5, the ratio of the theoretical band and the fast dispersing band in Fig. 6.12. In fact, in early stages of the research, we took this ratio seriously and speculated that this fast dispersing peak is the charge peak of the TL model, and that the slowly dispersing peak is the spin peak of the TL model. This line of thinking was abandoned after the map of Fig. 6.8 was taken, because the observation of the two clearly separated lines of FS in Fig. 6.8 is in good general correspondence to band theory and is also hard to reconcile with the predicted behavior of the spin peak and the charge peak of the TL model, which cross E_F at the same momentum value. Also, the spin singularity for $\alpha > 1/2$ is not peaky, as discussed above – another fact hard to reconcile with the data. In the current thinking, a point of view could be taken that the two peaks in ARPES both correspond to charge peaks of the TL model, one for each band. It could be further speculated that the edge at $v_s(k - k_F)$ is smoothed by 2D or 3D kinematics. However, it is then rather uncertain how to explain the ratio of 2 for the dispersions of the theoretical slow band and the experimental slow band. The situation is made worse due to the uncertainty of the band calculation. A new band calculation [130] by the same group who reported the bands in Fig. 6.2 has produced bands which are only a factor of 2 narrower than those in the experiment, both for the slow band and for the fast band. More recently, a first-principle LDA calculation, done for the full 3D crystal, showed 4 fully split bands, two of which are nearly degenerate and show about half the bandwidth of the slow ARPES band, with the other two also being nearly degenerate and showing about the *same* bandwidth as that of the fast ARPES band. Thus the uncertainty of the band calculation is entangled with the issue of the relevance of LL state of the blue bronze, from the ARPES point of view and also from the other points of view discussed in the introduction.

6.4 Conclusions

In summary, we have measured the FS and ARPES lineshapes of $K_{0.3}MoO_3$, a prototypical quasi-1D CDW material. We find a good agreement of the FS nesting with that implied by the previously known CDW wavevector. The lineshapes show generally low weight at E_F, both in angle integrated and angle resolved PES. We find that this low weight at E_F is explained better by the LL scenario than by the fluctuating CDW scenario. However, other aspects of the TL lineshape comparison indicate that further generalization including 3 dimensional coupling effects is necessary. Also, resolving the differences among the available band calculations would be highly desirable. It seems likely that a full model including both LL and CDW effects will be necessary to describe the physics of the blue bronze.

My role in the work described in this chapter was to measure all the data, to analyze them, to interpret them and to do spectral function calculations for the Rice and Strässler CDW fluctuations theory and the TL model.

Chapter 7

$Li_{0.9}Mo_6O_{17}$: non-CDW non-Fermi liquid

This chapter essentially reproduces the journal article: "Non-Fermi-Liquid Single Particle Line Shape of the Quasi-One-Dimensional Non-CDW Metal $Li_{0.9}Mo_6O_{17}$: Comparison to the Luttinger Liquid", J.D. Denlinger, G.-H. Gweon, J.W. Allen, C.G. Olson, J. Marcus, C. Schlenker and L.S. Hsu, Phys. Rev. Lett. **82**, 2540 (1999).

Unlike the other bronzes studied in the previous 2 chapters, the existence of a charge density wave in $Li_{0.9}Mo_6O_{17}$ is precluded by its the known properties. By angle resolved photoemission spectroscopy, we show that its electronic properties are near perfect one dimensionality, in a good agreement with band theory. The non-Fermi liquid lineshapes obtained for $Li_{0.9}Mo_6O_{17}$ are a unique example so far that can be meaningfully compared with known non-Fermi liquid metal models in 1 dimension. Without concern about competing CDW effects, we point out strong similarities of the lineshapes with predictions of the Tomonaga-Luttinger model, but also significant differences.

7.1 Introduction

The so-called Li purple bronze, $Li_{0.9}Mo_6O_{17}$, is a material with a quasi-one-dimensional (quasi-1D) electronic property like the blue bronze. Its composition is much like the quasi-2-dimensional (quasi-2D) purple bronzes, $NaMo_6O_{17}$ and KMo_6O_{17}. However, there are several distinguishing physical properties that make $Li_{0.9}Mo_6O_{17}$ more interesting. First of all, its electronic structure is the most one dimensional. Second, it is superconducting below ≈ 1.9 K. Superconductivity is not found for other bronzes.

Third, its higher temperature phase transition at ≈ 24 K cannot be classified as a CDW transition. The absence of a CDW means that the $2k_F$ electron-phonon interaction is not important. Regardless of the origin of the transition, its temperature is still much less than the CDW temperatures of the blue bronze or the quasi-2D purple bronzes, allowing spectra to be taken much further above the transition. Fourth, it shows a distinctly linear resistivity from 24 K to room temperature, much like high temperature superconductors, and consistent with expectation for Luttinger liquid theory.

Thus far ARPES of non-CDW quasi-1D metals has not obtained dispersing lineshape data which could be compared meaningfully with many-body theories such as LL theory. Most of the non-CDW quasi-1D metals are organic and for these metals **k**-integrated weight suppression near E_F occurs [131], but dispersing features have not been observed [132]. $Li_{0.9}Mo_6O_{17}$ is unusual as a quasi-1D inorganic metal which appears to be free of strong electron-phonon effects, as discussed further below, and which shows suppressed E_F photoemission weight. In this chapter, we report the detailed non-Fermi liquid (NFL) lineshape of the dispersing excitation which defines the FS for $Li_{0.9}Mo_6O_{17}$. Obtaining the lineshape data was enabled by taking precautions to minimize photon-induced sample damage[1] and by studying a region in **k**-space where the near-E_F ARPES intensity is especially large, as determined by first making a **k**-space map of the ARPES intensity near E_F. The properties of $Li_{0.9}Mo_6O_{17}$ strongly argue that the NFL behavior has a purely electronic origin, giving this set of data a special current importance.

Fig. 7.1 (a) shows the crystal structure, solved by Onoda *et al* [107]. The space group is $P2_1/m$ (monoclinic), and its unit cell is given by $a = 12.762$ Å, $b = 5.523$ Å, $c = 9.499$ Å, and $\beta = 90.6^o$. In this figure, the crystal structure is shown as it is projected on the ac plane. The empty circles and hatched circles represent the atoms at $y = b/4$ and $3b/4$ respectively. Despite the similar chemical formula, the crystal structure is different in an essential way from the structure of the quasi-2D purple bronze (Fig. 5.1). In contrast to the well separated Mo oxide slabs in the quasi-2D purple bronzes, the Li purple bronze has a more three dimensional structure, composed of thinner Mo oxide slabs connected by the Mo oxide "bridges" as well as the Li ions. The bond length analysis [107] shows that the valencies for the Mo ions are 5.05 (Mo_1), 5.72 (Mo_2), 5.76 (Mo_3, Mo_5, Mo_6) and 5.01 (Mo_4). Fig. 7.1 (b) shows the same plot as Fig. 7.1 (a) with a 90^o rotation. The MoO_6 octahedra containing Mo_1 and Mo_4, and thus important for

---

[1] See Ref. [125]. The SRC Seya monochromator has a negligible amount of 2nd order light of energy higher than ~ 35 eV, due to its low energy grating.

electron transport, are marked with hatches. In this figure, the isolated group of 4 octahedra, consisting of 2 Mo_1's and 2 Mo_4's, is easily recognized. Fig. 7.1 (c) shows a three dimensional view of a Mo oxide slab of Fig. 7.1 (b). Along the b direction, each group of 4 octahedra forms a zigzag infinite chain as shown in Fig. 7.1 (d). This chain is essential in understanding the electronic structure of the Li purple bronze.

Fig. 7.2 shows the calculated band structure [133]. The bottom 4 Mo $4d$ bands are of greatest interest. Among them, 2 bands are crossing the Fermi level along the b direction and the other 2 bands are completely filled. These bands are essentially those of the Mo_4O_{18} chains shown in Fig. 7.1 (d), modified somewhat by the couplings between the adjacent Mo_4O_{18} chains, mostly in the c direction. The calculated dispersion along the a direction is essentially 0.

Fig. 7.3 shows the FS calculation [133]. The two pieces of FS's come from the two bands crossing the Fermi level in Fig. 7.2. They are practically indistinguishable. The two crossing bands are two one dimensional bands from the upper and lower "decks" in Fig. 7.1 (d). The band orbitals near the Fermi level crossing are the (x^2-y^2) orbitals in Fig. 7.1 (d). It is very important that, by symmetry, the two (x^2-y^2) orbitals in the upper and the lower decks in Fig. 7.1 (d) cannot have any coupling mediated by $2p$ orbitals of the O ions that bridges the two decks. For a similar reason, the coupling between the adjacent Mo_4O_{18} chains are nearly zero as well for the two bands. Therefore, the calculated FS's are perfectly degenerate and perfectly one dimensional. The FS is given by $k_y = 0.45\Gamma Y$.

Not surprisingly, the resistivity of Li purple bronze [134] shows a strong one dimensional anisotropy. At room temperature, the conductivity ratio is given by $\sigma_b : \sigma_a : \sigma_c = 250 : 10 : 1$ [134]. The temperature dependence of the resistivity is as follows. As T is reduced from 300 K, the resistivity decreases linearly all the way down to $T_X \approx 24$ K, at which point it shows a rapid upturn. This upturn stops at ≈ 1.9 K, and then the material becomes superconducting. The two anomalies also show up in the specific heat measurement [135], where two similarly shaped anomalies signalling broad 2nd order phase transitions are found at these temperature values. The absence of any anomaly in the magnetic susceptibility [134, 136] associated with the 24 K transition argues against its possible CDW nature, although it was recognized [134] that the same absence occurs for a well known CDW compound $NbSe_3$. More definitive evidence against a CDW comes from infrared optical spectroscopy which does not show any gap opening [137] despite its routine capability [138] to detect CDW or spin density wave (SDW)

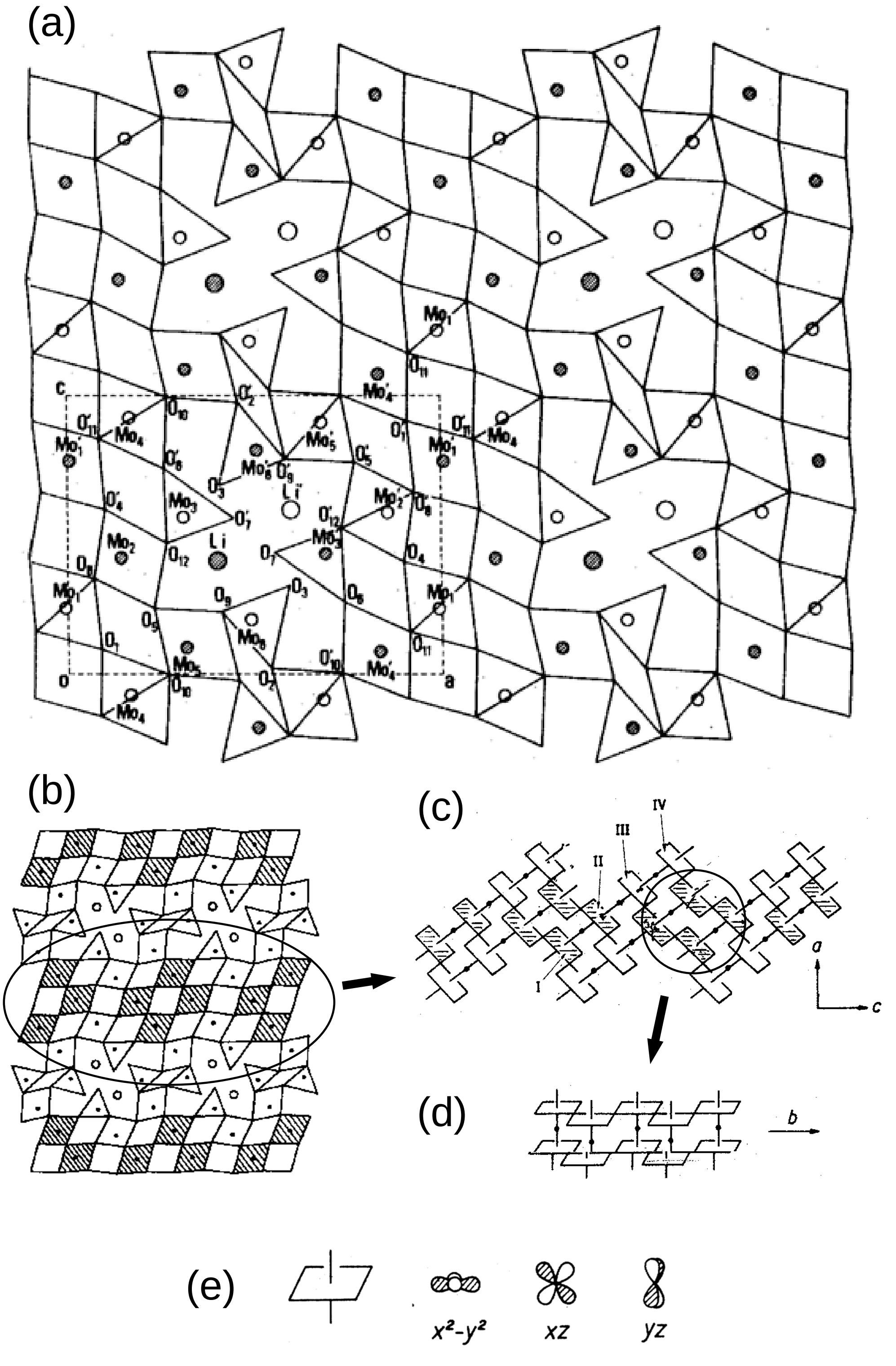

Figure 7.1: Crystal structure of Li$_{0.9}$Mo$_6$O$_{17}$. See text for discussion. From Ref.'s [107] and [106].

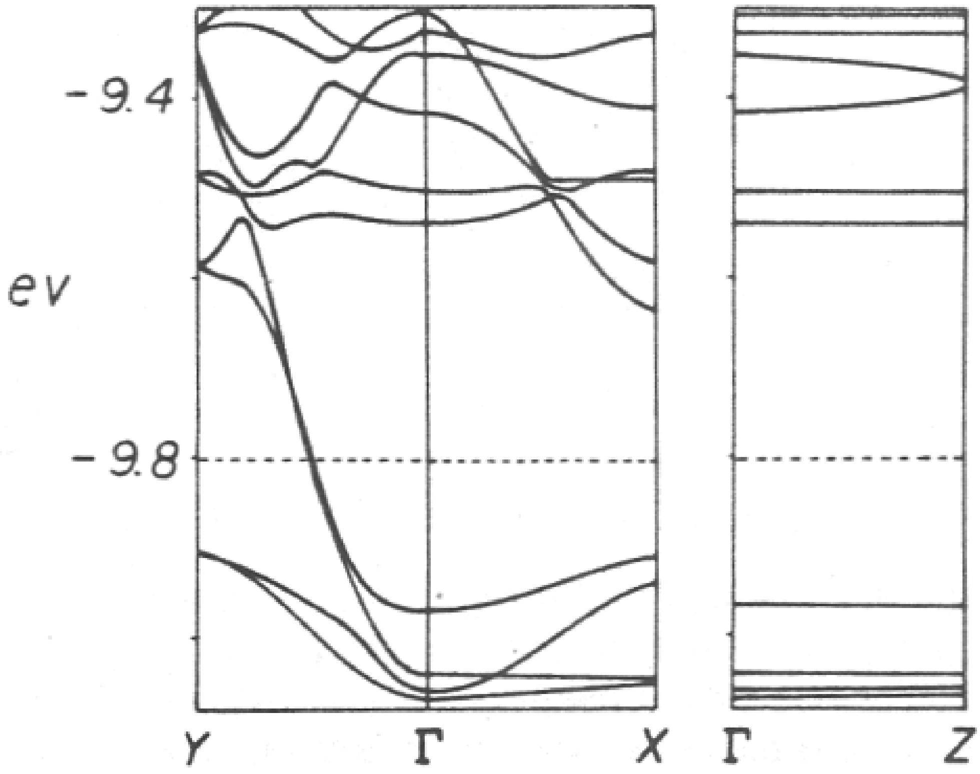

Figure 7.2: Band calculation for the Li purple bronze in extended Hückel approximation. $\Gamma = (0,0,0)$, $X = (c^*/2,0,0)$, $Y = (0,b^*/2,0)$ and $Z = (0,0,a^*/2)$. The dotted lines mark the Fermi energy position. From Ref. [133].

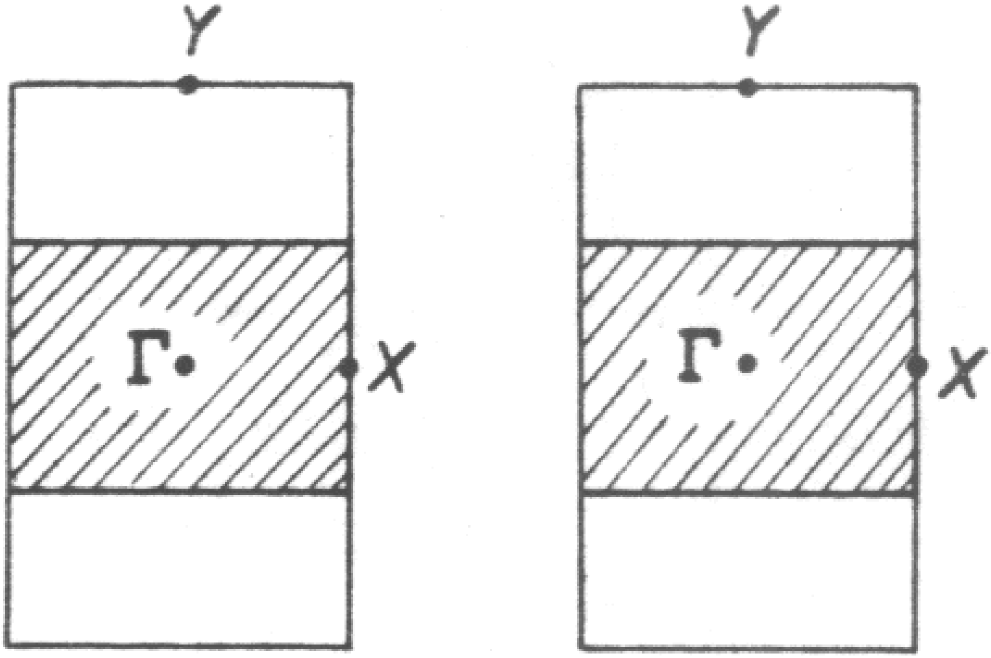

Figure 7.3: Theoretical FS for the Li purple bronze. From Ref. [133].

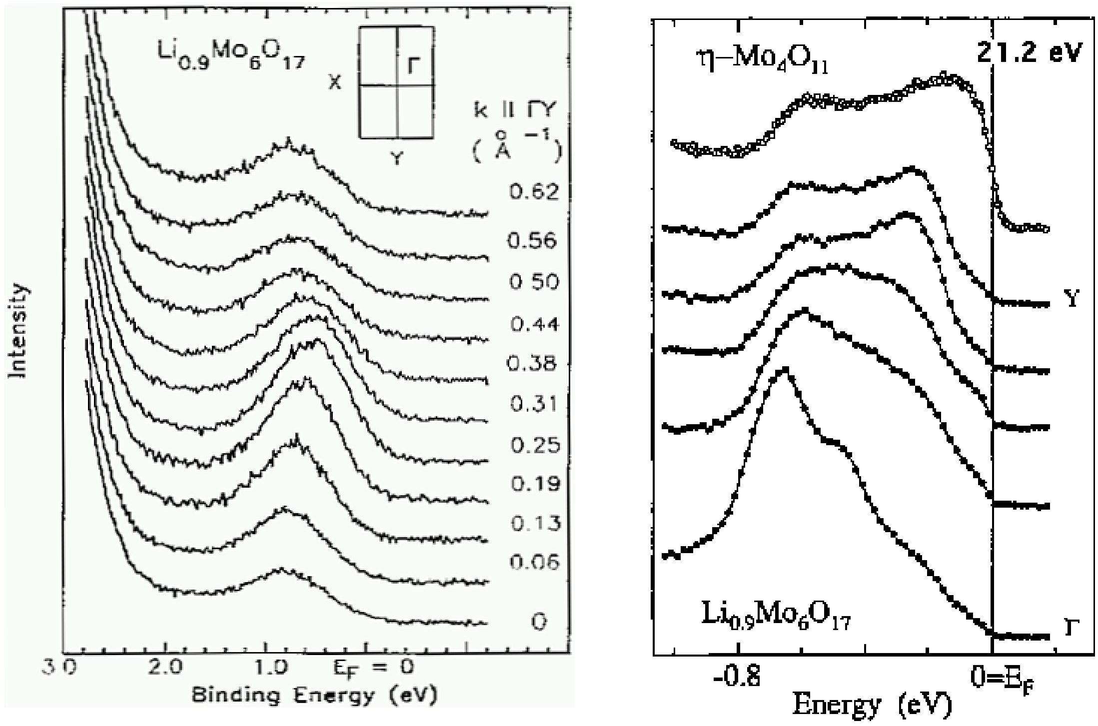

(a) (b)

Figure 7.4: Previous ARPES studies on the Li purple bronzes. (a) ARPES EDC's along ΓY by K. Smith *et al* [139]. (b) A similar set by Grioni *et al.* [140], compared with a spectrum for η–Mo$_4$O$_{11}$.

gaps. The minimum energy down to which the measurement was made, 1 meV, sets an upper limit of (11.6/3.52)≈3K for a mean field CDW or SDW transition temperature. Therefore, it is likely that electron-phonon interactions are of less importance in this material than in other bronzes. Related to this observation is the aforementioned T-linear resistivity down to 24 K. Although electron-phonon interactions do imply [2] linear resistivity, it is only for temperatures above $\sim \Theta_D$, the Debye temperature, which is estimated to be 365 K [135] or 410 K [136] for the Li purple bronze. Therefore, it is likely that the electron-electron interaction is important to interpret the T dependence of the resistivity. An important thing to remember, regardless of the origin of the 24 K phase transition, is that its low transition temperature means that one can study the lineshape at a temperature more than 10 times the transition temperature at room temperature, a very favorable condition to study the lineshapes in the normal metallic state without being influenced by thermal fluctuations, strong in 1-D as discussed in section 2.3.

A FS study by photoemission has been reported [139], where the FS was deduced from 300K EDC's. The EDC's in this work are shown in Fig. 7.4 (a). The EDC's, reported only for the ΓY direction, show for all **k**-values a broad background feature which develops a weak shoulder that moves toward E_F as one moves away from Γ. In the vicinity of the **k**-value (0.35 Å) interpreted as the E_F crossing, the weak shoulder loses intensity, leaving again the broad background feature. This background feature can be interpreted as an uncertain mix of a complex lineshape which reflects the total occupied bandwidth, as seems to occur for the Na- and K-purple bronzes, and also of a peak arising from the other bands shown in Fig. 7.2, which disperse halfway toward E_F but do not cross it. In fact, the predicted dispersion of these other bands is roughly consistent with the dispersion of the weak shoulder. Since there is an almost complete absence of spectral weight at E_F in all the spectra, to a degree even greater than that seen in the blue bronze, the main evidence for an E_F crossing is the intensity change of the weak shoulder. Intensity changes of this size are known to arise from the variation of the ARPES matrix element and so it is very difficult to be sure that a FS has actually been observed. In Fig. 7.4 (b), we show data taken by Grioni *et al.* [140]. Here, better energy resolution and maybe a better surface exposed by the cleave result in spectra with well-defined structures. However, the intensity near the Fermi energy is only suggestive of a peak, and the number of spectra is too few to enable a meaningful discussion of FS. Note the very strong suppression of weight at E_F for the Li purple bronze observed in this data set.

7.2 Experimental

Single-crystal samples were grown by our collaborators in Grenoble, France using the electrolytic reduction technique as described in Ref. [135]. The ARPES was performed at the Ames/Montana beamline of the Synchrotron Radiation Center (SRC) at the University of Wisconsin and at the beamline 5 of the Stanford Synchrotron Radiation Laboratories (SSRL). Samples oriented by Laue diffraction were mounted on the tip of a helium refrigerator and cleaved *in situ* at a temperature of 30K just before measurement in a vacuum of $\approx 4 \times 10^{-11}$ Torr (SRC) and 2×10^{-10} Torr (SSRL), exposing a clean surface containing the crystallographic *c*- and quasi-1D *b*-axes. All the data are normalized to the photon flux. The instrumental resolution ΔE and E_F were calibrated with a reference spectrum taken on a freshly sputtered Pt foil (SRC) and evaporated Au (SSRL). Energy resolutions ranged from 43 meV to 150 meV. The angular resolution for the spectrometer was $\pm 1^\circ$, which amounts to ±7% of the distance from Γ to Y in the Brillouin zone. The **k**-space near-E_F intensity map was made by detecting electrons

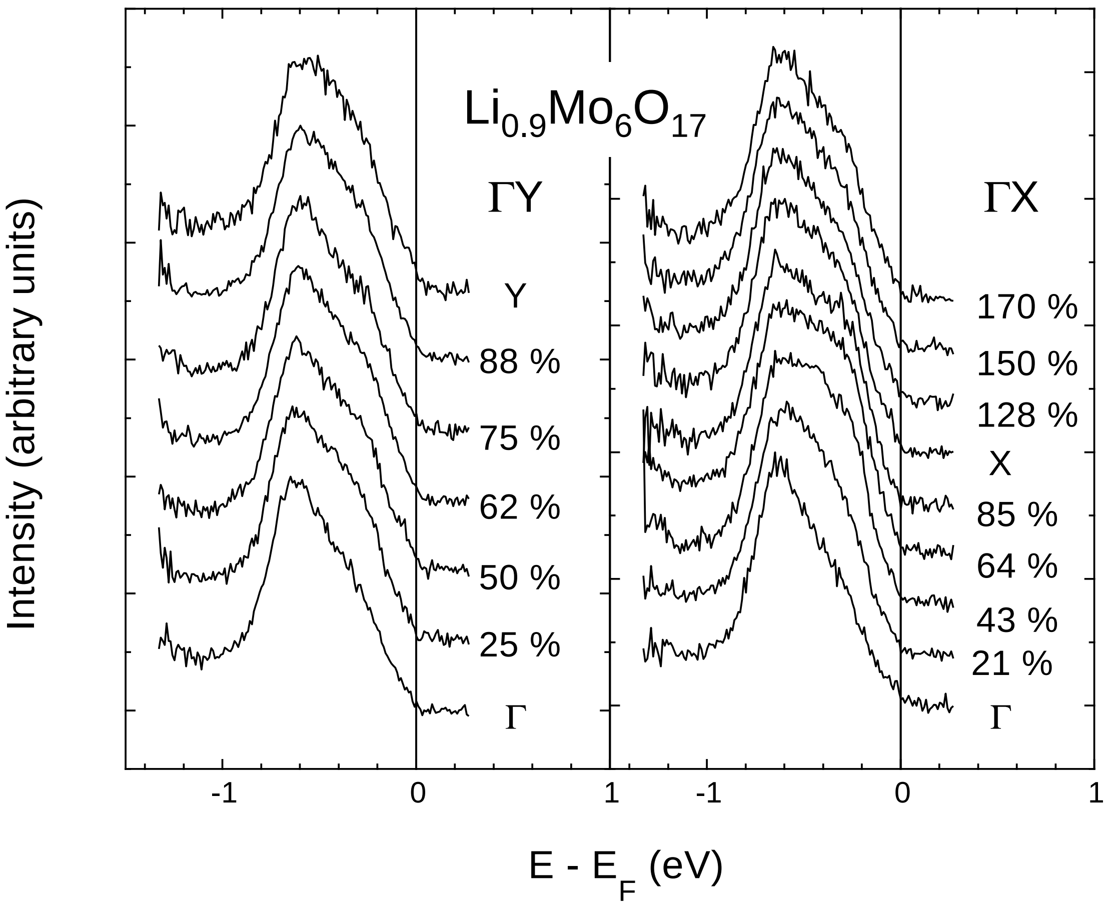

Figure 7.5: ARPES EDC's along ΓY and ΓX. The measurement was made at 32K with overall instrumental energy resolution of 43meV and photon energy of 20.2eV.

over the range ΔE=150 meV, centered 50 meV below E_F, and sweeping analyzer angles along two orthogonal directions relative to the sample normal, in steps of 1^o for θ and 2^o for ϕ in Fig. 1.1. As discussed already in section 1.1, one can show from Eq.'s 1.3 and 1.4 that such sweeps move the **k**-vector on a spherical surface with a radius which depends on the kinetic energy and hence on the photon energy. In an idealized geometrical description, one observes the intersection of this spherical surface and the FS. In a more realistic spectroscopic description, the FS pattern is generated because the intensity at E_F reaches a local maximum when a dispersing peak passes sufficiently near the angle/energy resolution window, for given temperature and peak lineshape. The momentum inside the solid is determined by Eq.'s 1.31.4 with a nominal inner potential (V_o) value of 10 eV.

7.3 Results

Fig. 7.5 (b) shows EDC's we have taken for $Li_{0.9}Mo_6O_{17}$, along ΓX and ΓY, obtained at the SSRL. In the hopes of observing sharper features and clearer dispersion than that of Fig. 7.4 (a), the data were taken at a much lower temperature and with considerably better resolution. Unfortunately, although the high binding energy onset of the background feature is indeed much sharper than in the data of Ref. [139], the dispersing shoulder along the parallel direction is no clearer. As with the data in Fig. 7.4 (a), there is no weight at E_F, making an E_F crossing for the shoulder very difficult to identify. One can see that the spectra for the perpendicular ΓX direction also show a very similar dispersing shoulder. For this direction, where an E_F crossing is not expected from the theory, the shoulder must be interpreted as the bands which, for this direction also, disperses halfway to E_F but do not cross it. We concluded that, without having a direct FS image, the primary source of confidence that the correct FS has actually been found for this material in Ref. [139] is not the EDC's that have been obtained, but instead the general success of the tight binding theory for the Mo bronzes, and perhaps also the simplicity of the predicted FS. In the rest of this chapter, we discuss the results obtained at the SRC, taken subsequently to the work shown in Fig. 7.4 (b), which also does not show the dispersive band, in spite of having sharper features.

Fig. 7.6 shows the set of data taken along the same directions as for Fig. 7.5. As in the previous figure, it is easily noticed that the spectral features are dominated by the bands that are not crossing the Fermi energy. However, dispersions for these bands are observed more clearly in this data. Furthermore, along ΓY, but not along ΓX, there is a distinct low binding energy shoulder-like feature that exists for $k_{\Gamma Y} \leq 55$ %. As the momentum value moves away from Γ this feature branches off from the main peak to disperse to the Fermi energy before losing intensity at > 55 %. Therefore, the current data clearly identifies a new feature. We attribute the better quality of the current data to the judicious selection of the photon energy, as we will discuss below, and possibly a better surface exposed by cleaving. In the following, we will show that the new shoulder-like feature is a band that crosses the Fermi level and contributes to the FS formation.

Fig. 7.7 (a) shows the projection onto the $\boldsymbol{k}_{||}$ plane of our near-E_F intensity map made at a temperature of 30K by varying both analyzer angles for fixed hν=24 eV. Fig. 7.7 (b) shows the projection onto the $k_\perp$/Γ-Y plane of a map made at 200K by fixing one analyzer angle, while varying the other angle and also the photon energy.

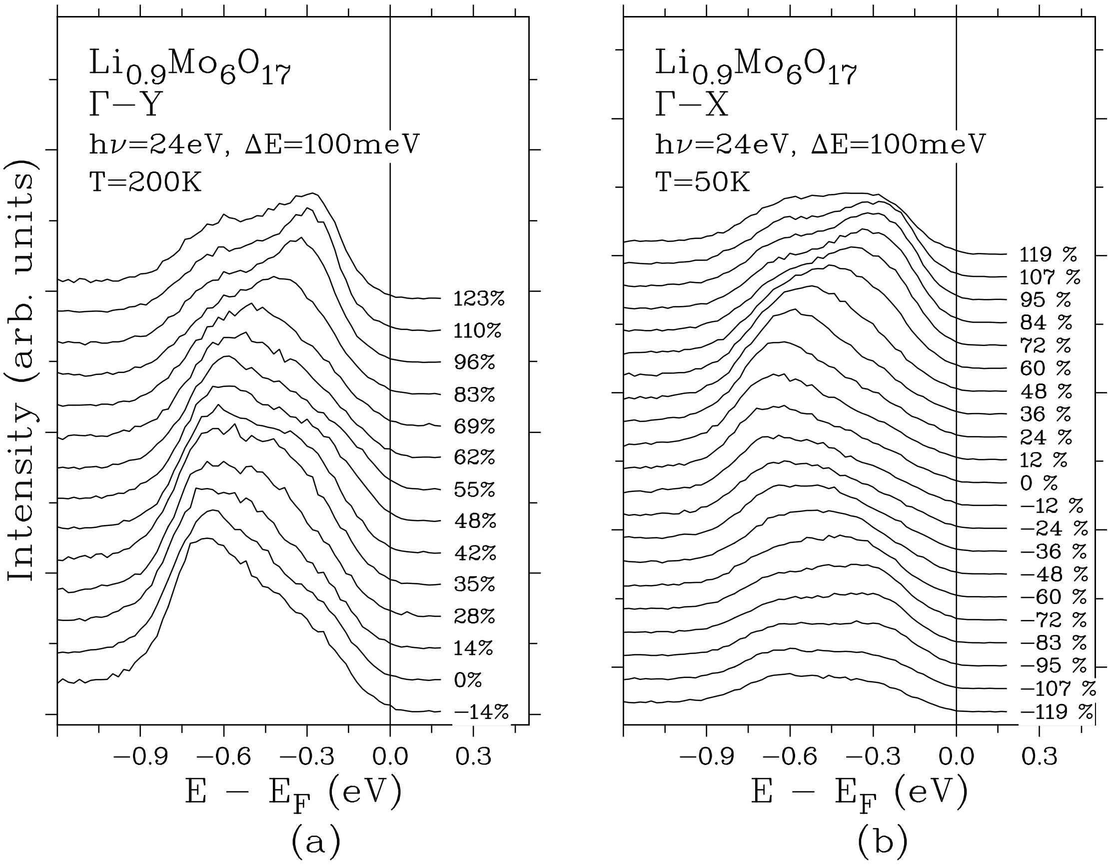

Figure 7.6: ARPES EDC's along ΓY and ΓX.

The spherical arcs for each photon energy are easily seen, and an arrow shows the arc corresponding to the fixed photon energy of the map of Fig. 7.7 (a). The straightness of the FS segments in both maps shows that this material fulfills very well the band theory prediction of being quasi-1D. The Fermi wave-vector k$_F$ defined by the center of the left hand FS segment is 2k$_F$ $\approx$ 0.57Å^{-1}, somewhat larger than the band theory [133] value [2] of 0.51 Å^{-1}. Most significant for the rest of this chapter is the existence of bright spots where the ARPES matrix element for the states near E_F is maximum and where the dispersing peak lineshape can best be studied.

Fig. 7.8 (a) shows a sequence of spectra taken at 200K $\approx 8T_X$ along a line 0.06Å^{-1} below an X-M Brillouin zone boundary and passing through the FS at one of the bright points, as indicated in Fig. 7.7 (a). The band calculation shown in Fig. 7.2 is juxtaposed with the data for an easy comparison. Over the corresponding k-range along Γ-Y, the calculation of Fig. 7.8 (b) shows two bands merging and crossing E_F together. We identify the two dispersing peaks of Fig. 7.8 (a) with these two bands, since both the

---

[2] Ref. 139 found larger dispersion perpendicular to the sample surface than we do and a different 2k$_F$ $\approx$ 0.7 Å^{-1}. Both differences can be attributed to our better resolution of the near-E_F peak which defines the FS.

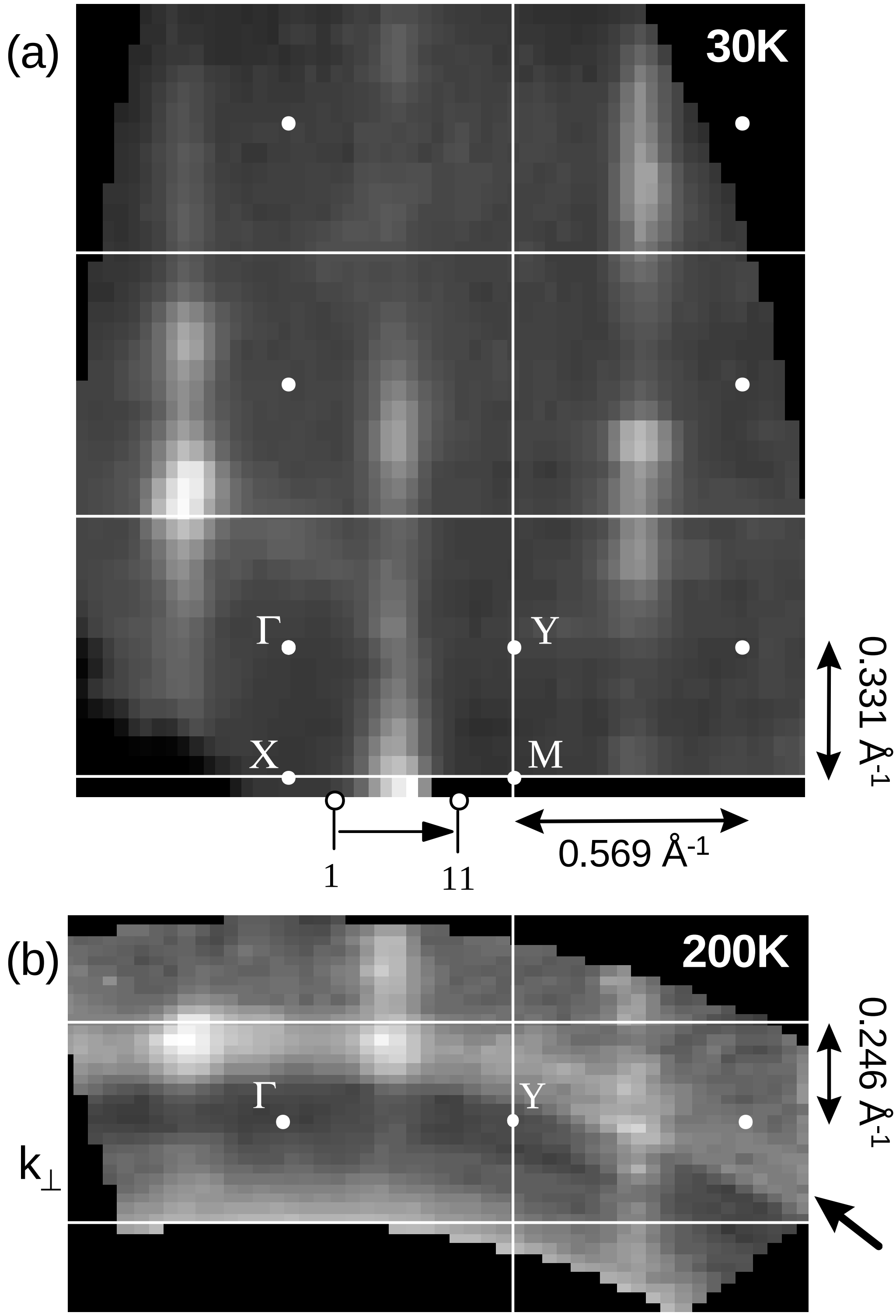

Figure 7.7: Near-E_F intensity map of $Li_{0.9}Mo_6O_{17}$. (a) $\boldsymbol{k}_{||}$ plane projection for hν=24 eV with variation of two detector angles. (b) $k_\perp/\Gamma$-Y plane projection for varying hν=15-32 eV and one detector angle. The thick arrow in (b) indicates the arc corresponding to hν=24 eV used in (a). In both maps, image contrast has been enhanced by dividing the data by the data heavily smoothed to retain only slowly varying cross-sectional dependences.

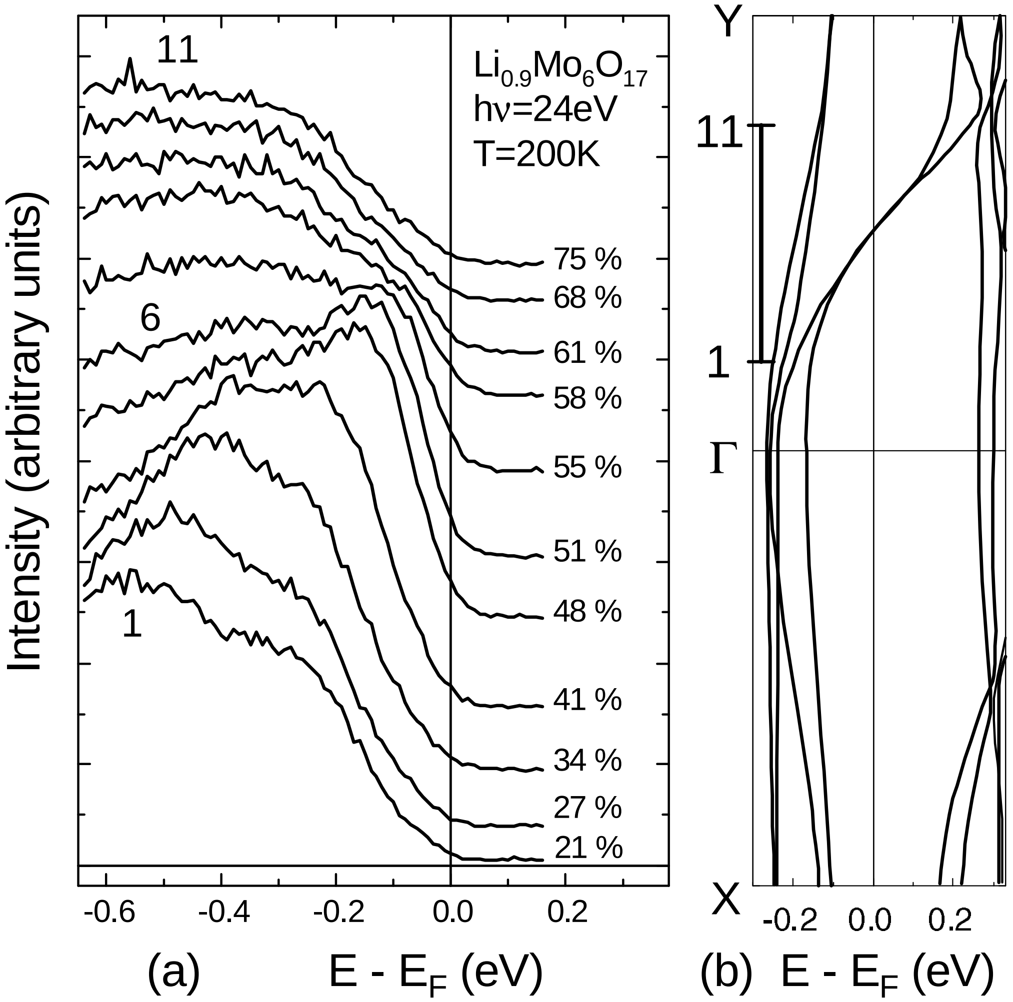

Figure 7.8: (a) ARPES spectra showing FS crossing along the path, marked with an arrow in Fig. 7.7 (a), that passes through a bright spot of the image. For each spectrum, the corresponding momentum value parallel to ΓY is given as a percentage of the length of ΓY. Total energy resolution ΔE is 50 meV FWHM. (b) Tight binding band calculation [133] showing bands along X–Γ–Y. The bar shows the range of $k_{\Gamma Y}$ explored in (a).

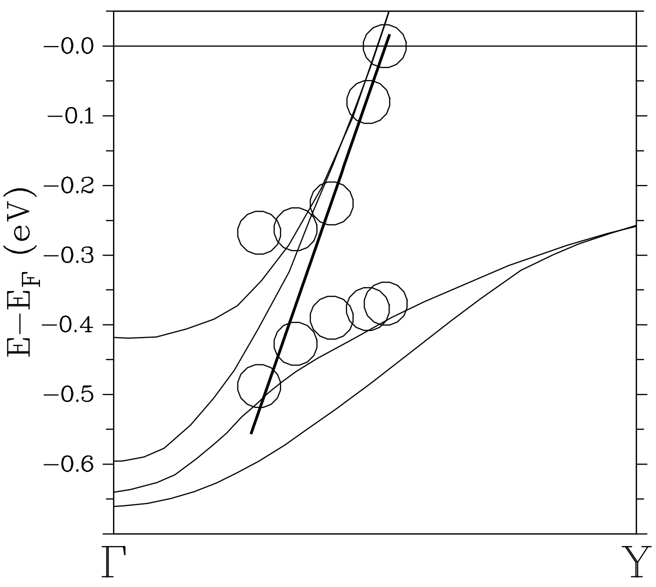

Figure 7.9: ARPES dispersions near E$_F$ crossing for $Li_{0.9}Mo_6O_{17}$. Band theoretical calculation (Fig. 7.2, scaled by 2.5) is shown for comparison. The circles correspond to peak positions extracted from spectra 2 to 6. Thick line, to be used later for lineshape modeling, shows a linear approximation of the dispersing feature.

calculation and our quasi-1D FS image show that the two bands disperse very weakly along Γ-X. The calculated bands which do not cross E_F are very weak for the special path of Fig. 7.8 (a), but can still be seen as a small peak or general humping ~ 400 meV below E_F in spectra 4 to 11. As we saw earlier in Fig. 7.6, these bands are easily seen along Γ-X and Γ-Y. Thus we find a good general agreement with band theory except that the bandwidth is about two and a half times the calculated value, as has also been found for the other molybdenum bronzes in the previous two chapters.

Fig. 7.9 show the peak positions extracted from the spectra 2 to 6 of Fig. 7.8 (a), and compares them with the calculated bands. In this figure, we have chosen the momentum value for spectrum 6 as the Fermi level crossing point, and therefore put its peak position at the Fermi energy. This interpretation is in large part based on the lineshape analysis which we will describe below, and assigns the experimental value of 2k$_F$=0.59 Å^{-1}. This value is also well within the "error bar" given by the width of the pattern of our Fermi energy intensity map. Since LL models assume linear dispersion around E_F, it is noteworthy that this aspect of the band theory is observed over an energy range of 200 meV for one band and 500 meV for the other, as represented by the line of Fig. 7.9.

Before discussing the lineshape of the E_F-crossing peak in detail, we now look at the angle integrated photoemission spectra taken in the home lab. Fig. 7.10 shows angle integrated photoemission spectra taken at two different temperatures. The 300 K data

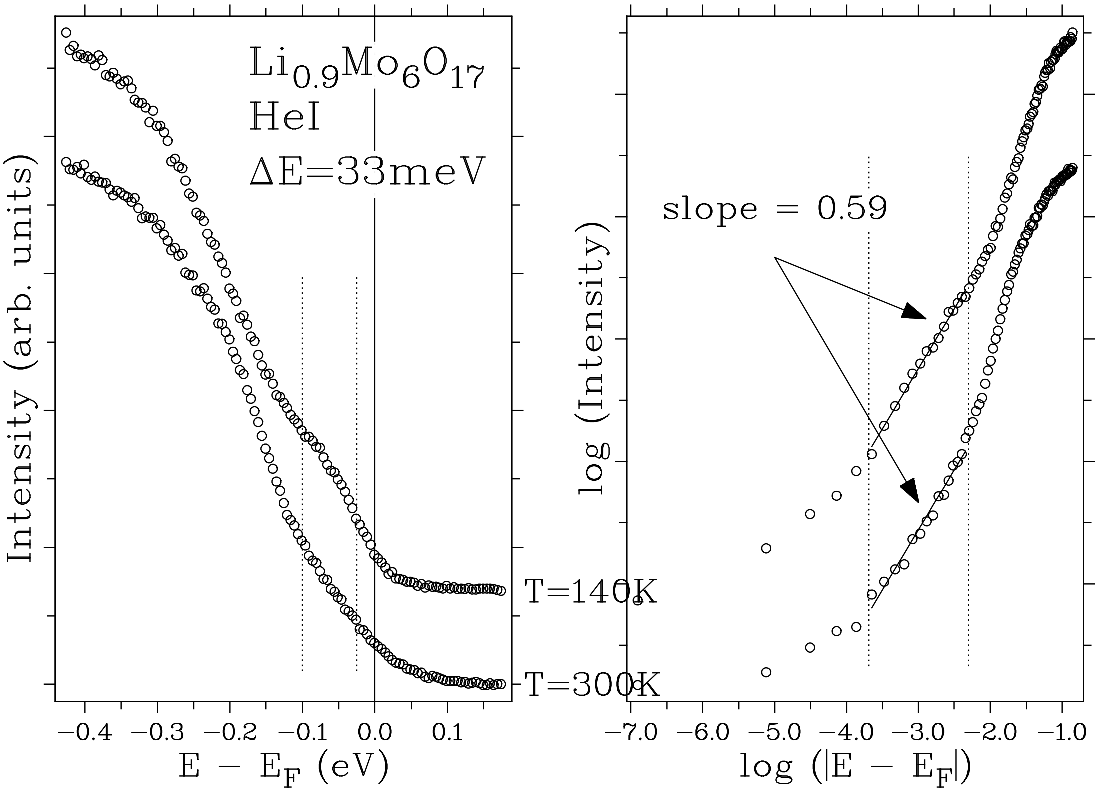

Figure 7.10: Angle integrated photoemission spectra of $Li_{0.9}Mo_6O_{17}$ taken at T = 300 K and 140 K.

were taken both before and after the 140 K data, and were completely identical. Therefore the small temperature dependence observed in this figure is an intrinsic behavior, and is thought to arise from thermal broadening of the spectral function. The main point of observation here is the absence of a clear Fermi edge, as in the blue bronze but different from the quasi-2D purple bronze (Fig. 6.6). In the right panel we show the log-log plot of the same data set. We observe a linear behavior from 25 meV up to 100 meV with slope of 0.59 for both cases. From the LL point of view, this signifies the anomalous dimension, α of 0.59. Although the power law behavior exists down to the chemical potential in the pure one dimensional LL theory at T = 0, in a real case it is expected [142] to be valid only at a finite energy above an energy scale given by finite temperature, experimental energy resolution, or small interchain hopping. We find this energy scale to be 25 meV empirically. This energy scale is certainly the same order of magnitude as the temperatures and the energy resolution. The interchain hopping parameter is also expected to be similar in magnitude or smaller, based on our flat FS's. Later in this section, we will also comment on the upper bound of the fit. We now go back to the ARPES data.

Of greatest interest is the detailed lineshape of the dispersing peak defining the FS.

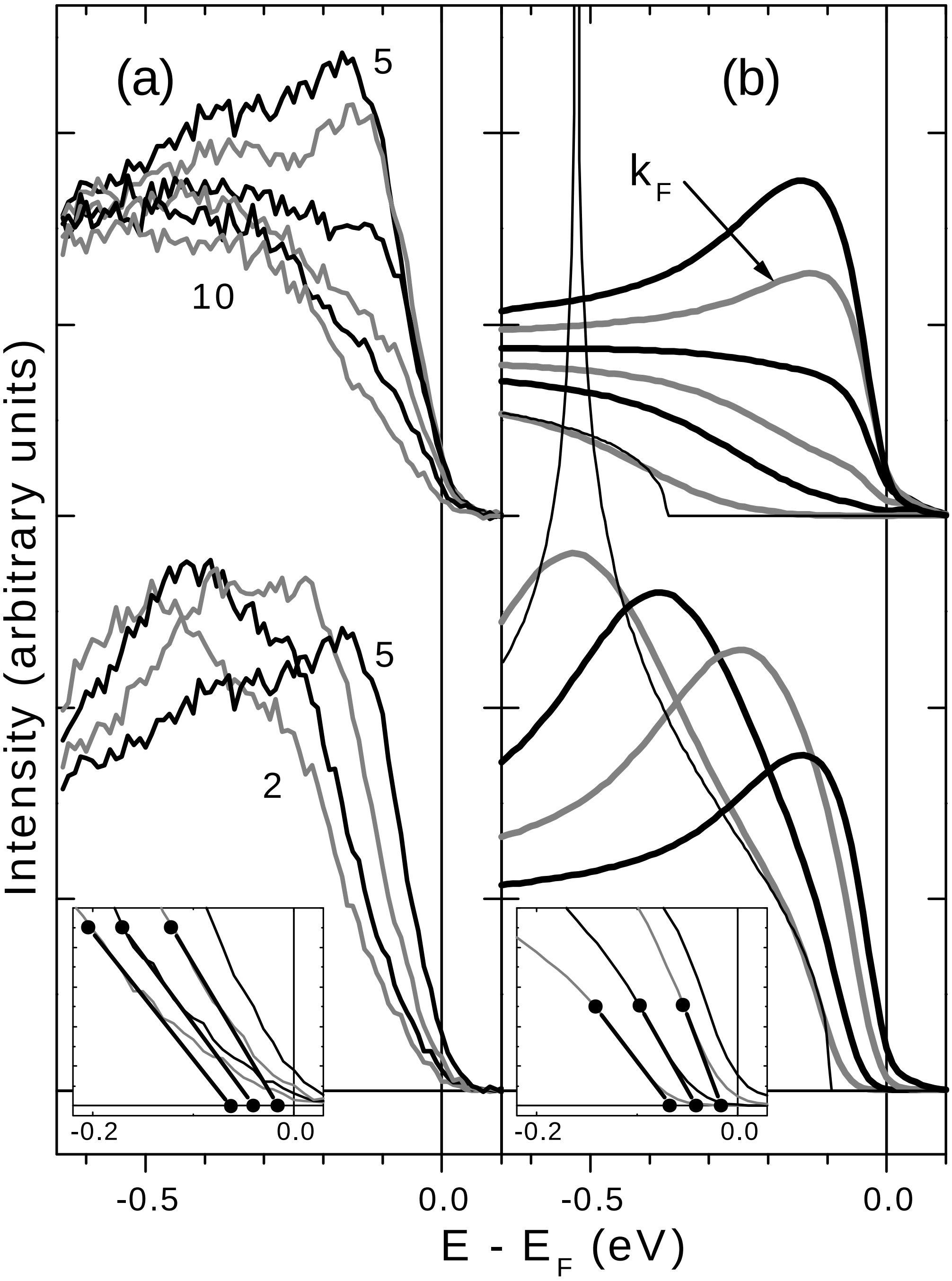

Figure 7.11: (a) Spectra of Fig. 7.8 (a) replotted for a close examination of lineshapes. Inset shows a detailed view of the spectral line shape approaching E_F, with lines drawn to emphasize a hint of 1D onset behavior. (b) Tomonaga-Luttinger (TL) model spectra, calculated to be compared with (a), as described in text. Inset shows the spinon edge singularity onsets.

Fig. 7.11 (a) shows the spectra overplotted so as to emphasize the defining behavior of the leading edge of the lineshape. The peaks move toward E_F until the leading edge shows a point of closest approach, after which the intensity then drops. Within the experimental resolution, very little intensity develops at E_F. In spectra 2 through 5 one sees the leading edge shift toward E_F up to a certain limit, "the wall," and in spectra 5 through 10 one sees the intensity fall, first without a change in the leading edge, and then accompanied by a shift of the leading edge away from E_F. A set of spectra taken at 50K is identical with respect to all these features.

In the absence of any LL lineshape theory including interactions between two bands, we apply lineshapes calculated for the one-band Tomonaga-Luttinger (TL) model, discussed in section 2.4, to the two degenerate bands crossing E_F. Fig. 7.11 (b) shows TL lineshapes for a spin independent repulsive interaction [58] and singularity index $\alpha = 0.9$. This choice of the value for α instead of 0.59 from angle integrated photoemission is discussed in the next paragraph. The thick lines are spectra including our angle and energy resolutions. The thin lines accompanying two of the spectra show the purely theoretical curves without including the experimental resolutions. The k-values and format are exactly the same as for Fig. 7.11 (a). Before discussing the considerable similarity to the experimental data for the behavior of the leading edge, we first describe the generic theoretical features. As discussed already in 2.4, the LL has no single particle excitations, and the removal or addition of an electron results entirely in the generation of combinations of collective excitations of the spin and charge densities, known as spinons and holons, respectively. In this TL model the spinon dispersion is that of the underlying band, v$_F$k with Fermi velocity v$_F$, and the holon dispersion is βv$_F$k where β depends on α and is > 1. For the lower group of spectra, with k inside the FS, there is an edge singularity onset at a non-zero low energy and then a rise to a power law singularity peak at higher energies. These sharp features are greatly broadened by the experimental resolutions and, except for the slight shoulder of curve 2, the spinon features of the theory curves are simply the leading edges of the lineshapes. The movements with k of the low energy onset and of the peak reflect the dispersions of the spinons and holons, respectively. That the onset occurs at a non-zero energy for k$\neq$k$_F$ is a direct consequence of the restrictive kinematics of 1 dimension (1-D). For the four lowest members of the upper set of curves, k lies outside the FS. The k-dependence of the non-zero singular energy onset in this case reflects the holon dispersion.

We now discuss the choice of parameters and the comparison to experiment, for

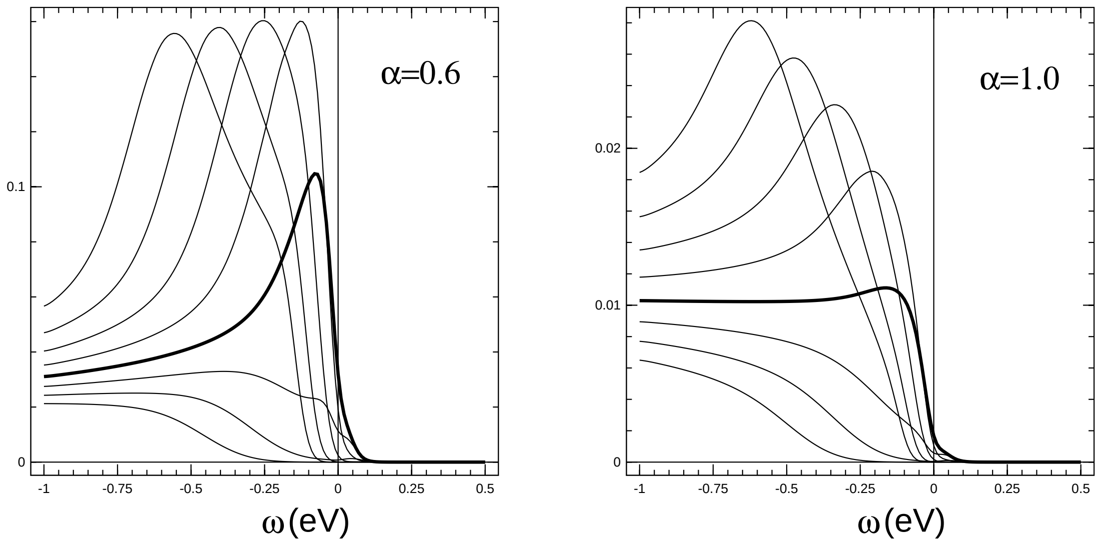

(a) (b)

Figure 7.12: TL model spectral functions calculated with the same parameters as Fig. 7.11 (b), except for different values for α, v_F and momentum increment. v_F is chosen for each α so that βv_F is invariant. The momentum increment for successive spectra corresponds to the angle increment of 1^o. k_F spectrum is plotted as thick line.

which we associate the spectral peaks with the rapidly dispersing holon features and the leading edges with the slowly dispersing spinon features. We consider a range of $\alpha > 1/2$ because for $\alpha < 1/2$ the low energy edge singularity takes the form of a peak, as shown in Fig. 2.11, which is obviously not present in the data. Each α determines a β and v$_F$ is chosen so that βv$_F$k matches the experimental peak movements, linear to ≈ 500 meV below E_F for one peak, but only ≈ 200 meV below E_F for the other, so that the lowest energy peak in data curves 1 to 3 has no theoretical counterpart. One finds that for the broadened spectra, as α increases from 1/2, (a) the peak maximum as k approaches k$_F$ decreases more rapidly, and (b) the amount of E_F weight relative to the spectrum maximum in the k=k$_F$ spectrum decreases. This is demonstrated in Fig. 7.12. The α value of 0.59 from Fig. 7.10 is nicely greater than 1/2. For α = 0.59 ($\beta = 4$) the behavior of (a) is similar to experiment but the value for (b) is about twice the experiment value of $\approx 16\%$. For α = 0.9 ($\beta = 5$), it is noticeable that the behavior of (a) is faster than in experiment, but the fractional amount of E_F weight for the k=k$_F$ spectrum is only slightly greater than in experiment. With the choice α = 0.9 and $\hbar$v$_F$ = 0.7 eVÅ, the theory curves reproduce semiquantitatively the variation of the leading edge in spectra 2 to 5, the "wall" behavior in spectra 5 to 7, the loss of a peaky upturn at E_F from spectrum 6 to 7 as k passes beyond k$_F$, and qualitatively the movement of the leading edge away from E_F for spectra 8 to 10. The agreement of the intercepts given by the

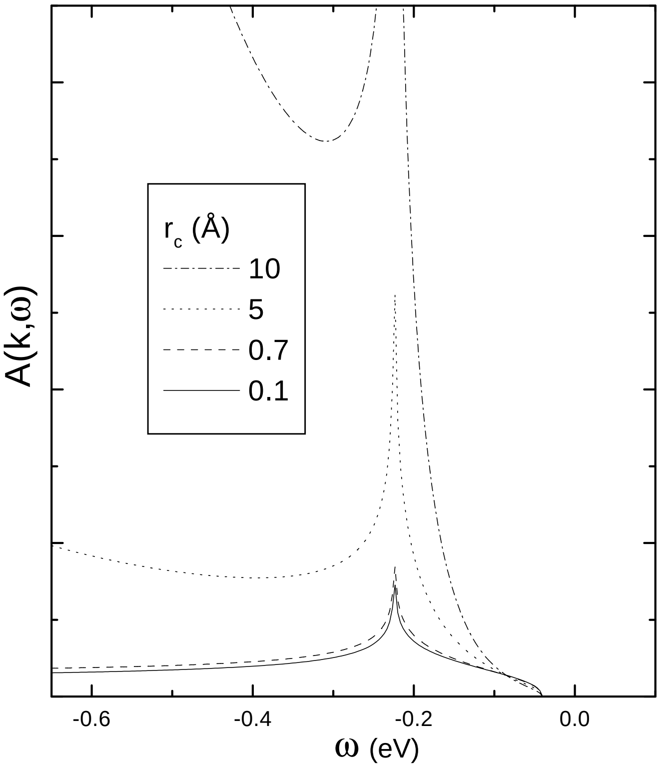

Figure 7.13: r_c dependence of the Tomonaga-Luttinger spectral function. Other input parameters are the same for the simulated spectrum 4 of Fig. 7.11.

straight line extrapolations shown in the two insets indicates a remnant in the data of the theoretical onset behavior of 1-D kinematics, and even a semi-quantitative agreement with the β value. The general goodness of the agreement for spectra 5 through 7 leads us to take the value of 2k$_F$=0.59 Å^{-1} from spectrum 6 as a better determination of 2k$_F$ than the slightly smaller value deduced above from the center of the FS image.

Another parameter that is necessary for the calculation is the so-called r_c [58], briefly mentioned in section 2.4. This parameter determines the momentum scale $1/r_c$ and the energy scale v$_F/r_c$ below which the low energy LL lineshapes are valid. For the comparison in Fig. 7.11, we have chosen the parameter of 0.1 Å. The justification of this value is as follows. First, for the momentum values and the energy values covered in Fig. 7.11, any value of r_c less than 0.7 produces spectra that are substantially the same. This point is illustrated in Fig. 7.13. Here, one sees the pathological feature of an exponentially increasing high binding energy intensity for large r_c and also that comparison to the data cannot distinguish values between 0.1 Å and 0.7 Å. So, for Fig. 7.11, we chose the small value of $r_c = 0.1$ Å, to be conservative relative to the theory's validity. Second, we can estimate r_c using the interchain Thomas-Fermi screening theory of Ref. [60]. The essential results of Ref. [60] were summarized at the end of Section 2.4. For our experimental value of v_F = 0.7eVÅ the theory coupling parameter $g = e^2/(\pi\hbar v_F) = 6.6$, and so $r_c = 1/\kappa = a_\perp/\sqrt{8\pi g} = a_\perp/13$. The complicated array of the linear chains in $Li_{0.9}Mo_6O_{17}$ means that an effective value of $a_\perp$ for a square array of linear chains has to be evaluated for estimating r_c. $a_\perp$ for $Li_{0.9}Mo_6O_{17}$ ranges from 3.7 Å to 12.8 Å. This yields the upper and lower bounds of r_c to be 0.3 Å and 1.0 Å, respectively. By this estimate r_c is probably larger than the value that we chose, and could be similar to the typical Thomas-Fermi values, e.g. 0.55 Å and 0.67 Å for Cu [1] and Na [2], respectively. It is also interesting in this context to notice from Fig. 1 of Ref. [60] that this theory gives for $g = 6.6$ a value of α (γ_{cb} in the notation of Ref. [60]) ≈ 1.2. This is even larger than our value of 0.9. Viewed from this theory, then, the fact that our α value is much larger than the value 1/8 for the 1-D Hubbard model is due to the long range nature of the interaction and the 3-D coupling via Coulomb interaction [60]. The r_c parameter of 0.3∼1.0 Å with v_F = 0.7eVÅ implies an energy scale of $0.7 \sim 2.3$ eV and momentum scale of $1.0 \sim 3.3$ Å^{-1}, enough to cover the entire range of Fig. 7.11. The range energy scale is much larger than the upper cutoff of the power law fit in Fig. 7.10. One should note in this comparison that the shallower band of the two bands that cross E_F shows peaks dispersing non-linearly in the spectra 1–4, as pointed out above. Also, after the E_F crossings of the two bands, the other bands that do not cross E_F disperse toward E_F and show peaks near E_F, as discussed with Fig. 7.6. Because these near E_F peaks, which are not relevant to the LL analysis, are at $0.2 \sim 0.3$ eV, the upper cutoff of the power law fit of ≈ 0.1 eV in Fig. 7.10 is reasonable.

Looking in more detail, differences between the theory and the experiment can be seen. First, considering the insets of Fig. 7.11, the amount of experimental weight in the energy range from E_F to the theory onset definitely exceeds that for the corresponding broadened theory curve. This could reflect the ultimate 3-D character of the material relaxing the restrictive 1-D kinematics, consistent with the increasing magnitude of the disagreement as **k** moves further from the FS and the available phase space increases. We also report that the only difference between the spectra at 200K and 50K is a subtle change at lower temperature such that the leading edge extrapolates more to E_F. At present this small temperature dependence is a tentative finding which requires further study, but might hint at a departure from LL behavior, perhaps an increased 3-D character, due to some lingering effects of whatever processes are important in the phase transition at T_X. In any case, we note that this temperature dependence is opposite to that expected [141] for the case of a pseudogap associated with gap formation (e.g.

CDW or SDW) at T_X. Second, the magnitude of the edge movement for experimental spectra 8 to 10 is much less than in the theory, probably due to the interfering presence in the spectra of the contributions from the two bands further below, and not crossing, E_F. Thus the detailed differences can plausibly be attributed to the oversimplifications of the TL model, e.g. its one-band nature and its strict 1-D character, relative to the experimental situation.

7.4 Conclusions

In summary we have presented spectra which are currently unique in showing the lineshape of the dispersing excitation that defines the FS for interacting electrons in a quasi-1D non-CDW metal. We have compared the data to the lineshape in the TL model of the LL. Although there are important differences in detail, nonetheless there is a remarkable similarity between theory and experiment for the anomalous behavior of the leading edge of the lineshape. In the TL model this behavior has its origin in the underlying charge-spin separation of the LL scenario. Previous ARPES reports [143] of charge-spin separation have been for quasi-1D materials where a Mott-Hubbard insulator precludes the LL. This is the first such report for a quasi-1D metal and provides strong motivation for further study of Li$_{0.9}$Mo$_6$O$_{17}$ using other techniques.

My role in the work described in this chapter was to measure the SSRL data, to participate in the analysis of the SRC data, to measure the angle integrated PES data, to calculate the TL lineshapes, and to compare them with the SRC data.

Chapter 8

Conclusions and future directions

Conclusions

In this thesis, I presented an ARPES study of the electronic structure of various inorganic quasi-low dimensional materials. ARPES gives a direct access to the single particle Green's function, a quantity of central importance in the many body theoretical understanding of solids. ARPES is usually done in two modes – the EDC mode and the map mode. In the EDC mode, energy distribution curves are obtained to give ARPES lineshapes. In a simple view, the ARPES lineshape is proportional to the imaginary part of the Green's function. In the map mode, an intensity map is measured as a function of angles. In particular, an E_F intensity map is very useful for studying the FS geometry. A summary of the ARPES principle and previous work that prompted this thesis work was given in Chapter 1.

From the outset, my interest was to distinguish between the normal FL and non-FL using ARPES. Theoretically, it is well accepted that in one dimension the FL theory is replaced by the LL theory. In P.W. Anderson's point of view, LL is not only restricted to one dimension but also strongly possible in higher dimensions, e.g. in 2D Hubbard model. Another state preferred in one dimension is the CDW state. It is known that CDW fluctuations, strong because of the one dimensionality, also show non-FL behaviors. A summary of key concepts of FL, LL and CDW were given in Chapter 2.

My study focussed on quasi-2D and quasi-1D materials, ranging from weakly 3 dimensional samples, e.g. $TiTe_2$, to strongly 1 dimensional samples, e.g. $Li_{0.9}Mo_6O_{17}$, and aimed to discern differences between them. I studied, with collaborators, many organic and inorganic materials. The organic materials, however, were generally a failure because the surface degraded quickly under the exposure to the synchrotron radiation.

On the other hand, inorganic samples had more stable surfaces and produced good ARPES data. The key results from the inorganic samples were reported in chapters 3 to 7. These chapters were organized in the order as the effective dimensionality of the sample decreases.

In Chapter 3, I reported ARPES spectra for the Ti $3d$ band of TiTe_2, measured at 25 K and 300 K. The 300 K ARPES spectra are very unusual and show the Ti $3d$ band peak to move *across* E_F. This feature enables a very accurate determination of $\mathbf{k}_F$. This value is compared with the $\mathbf{k}_F$ values determined by other methods that are commonly used by ARPES researchers. The value agrees well with the values determined by the methods based on $n(\mathbf{k})$, but disagrees with the values determined by the minimum peak position or the minimum peak width of the 25 K spectra. I also report lineshape fits on the original 25 K ARPES spectra, measured and lineshape-fitted by Claessen *et al.* The new fit uses the Matho FL model which is analytically well behaved in contrast to the original Taylor FL model. The new model gives a good fit and is also capable of fitting the lineshapes for the entire range of $\mathbf{k}$. Under certain assumptions, the energy dependence of the self energy can be compared with the temperature dependence of the resistivity. The Matho self energy shows much better agreement with the resistivity than the Taylor FL self energy. The $\mathbf{k}_F$ values found from the 300 K dispersion and the lineshape fits of 25 K spectra are different by about 8 %. Possible origins of this discrepancy include a temperature dependent $\mathbf{k}_F$ or a missing ingredient in the fit model. A preliminary analysis indicates the possibility of the latter.

In Chapter 4, SmTe_3, a quasi-2D high temperature CDW compound, is studied. Resonant photoemission shows no sign of the well-known Sm^{2+} multiplet structure. Therefore, I conclude that Sm is trivalent, in good agreement with the estimate made from the magnetic susceptibility by E. DiMasi *et al.* Valence band ARPES spectra show a quasi-2D electronic structure. The general 4 fold symmetry of this electronic structure is in agreement with the band theory on the double Te layer. However, near E_F, the electronic structure revealed by maps and EDC's shows a reduced symmetry and a highly anisotropic CDW gap. The big gap size $\approx$ 200meV implies a transition temperature even higher than the melting temperature. Based on the experimental FS shape measured by the ARPES map and the group theoretical properties of the band theory, a simple model of imperfect nesting can be built. This model qualitatively explains the gap anisotropy and reproduces the CDW nesting wavevector measured by E. DiMasi *et al.* within 4 %.

In Chapter 5, quasi-2D purple bronzes, $NaMo_6O_{17}$ and KMo_6O_{17}, were studied using E_F intensity maps and EDC's. The intrinsic features of the two maps are almost identical, and imply a FS which is substantially different from that in a previous report by K. Breuer *et al.*, but which is in remarkably good agreement with nearly all aspects of the hidden 1D picture by M. Whangbo *et al.* for these materials. Specifically, the image shows three quasi-1D bands with nearly straight FS sections and only small hybridization induced splittings. The observed nesting wavevector can be understood as the wavevector for optimal nesting of the quasi-1D FS's. Anomalous ARPES lineshapes are found for an isolated band crossing E_F. Even for **k** outside FS, the lineshape shows a substantial weight distribution over the entire bandwidth. Especially, the presence of a small peak at the band minimum energy for *all* measured **k** values is a great puzzle.

In Chapter 6, I reported the FS and ARPES lineshapes of $K_{0.3}MoO_3$, a prototypical quasi-1D CDW material. I find a good agreement of the FS nesting with that implied by the previously known CDW wavevector. The lineshapes show generally low weight at E_F, both in angle integrated and angle resolved PES. I find that this low weight at E_F is explained better by the LL scenario than by the fluctuating CDW scenario. However, other aspects of the TL lineshape comparison indicate that further generalization including 3 dimensional coupling effects is necessary. Also, resolving the differences among the available band calculations would be highly desirable. It seems likely that a full model including both LL and CDW effects will be necessary to describe the physics of the blue bronze.

In Chapter 7, I presented ARPES spectra which are currently unique in showing the lineshape of the dispersing excitation that defines the FS for interacting electrons in a quasi-1D non-CDW metal. I have compared the data to the lineshape in the TL model of the LL. Although there are important differences in detail, nonetheless there is a remarkable similarity between theory and experiment for the anomalous behavior of the leading edge of the lineshape. In the TL model this behavior has its origin in the underlying charge-spin separation of the LL scenario. This is the first such report for a quasi-1D metal and provides strong motivation for further study of $Li_{0.9}Mo_6O_{17}$ using other techniques.

Future directions

Understanding of non-FL features in ARPES spectra of quasi-1D materials are only beginning. Here are some topics that I think are worth pursuing.

1. **High resolution lineshape studies**. The ARPES community is currently beginning to enjoy a significant boost in the energy resolution and the angular resolution, due to the construction of high flux beamlines using insertion devices and the progress of the electron analyzer technology. As opposed to the 2^o angular resolution and 35 meV energy resolution, which are the best resolutions utilized in this thesis work, the angular resolution $\leq 1/2^o$ and the energy resolution of $\leq$ 10 meV are becoming available. With these dramatically better resolution, one can hope to observe more lineshape details than ever before. Especially, new lineshape data on $TiTe_2$, $K_{0.3}MoO_3$ and $Li_{0.9}Mo_6O_{17}$ will deepen our understanding of FL and non-FL lineshapes.

2. **Density or doping dependences**. For $Li_{0.9}Mo_6O_{17}$, I identified some features of the TL model, i.e. spin edge singularities and charge peaks. One way to corroborate this finding is to control the α value and to see if the features behave as expected. As we make the α value smaller, we expect spin and charge features to become sharper. If α becomes less than $1/2$ then the spin feature is expected to become a peak. At the same time we expect the spin and charge singularities move closer to each other in energy as α gets smaller. Following the theory of Ref. 60, one expects to be able to change α by changing the carrier density, thus changing the screened Coulomb potential and possibly v_F as well. There is a possibility in sample growth technique to make the electron density change in the Li purple bronze. Another way to change the anomalous dimension is to introduce impurities [144] or boundaries [145]. These two theories are equivalent in the sense that they predict the same α_B near the impurity or the boundary. Doping of the blue bronze and the Li purple bronze, either by substituting K with, say, Rb, or by substituting Mo with W, should be quite interesting in this regard. Possibly different behaviors with magnetic impurities and non-magnetic impurities would be very interesting in view of testing the spin and charge separation. For the blue bronze, it is already known [146] that heavy doping with W results in the reduction of the CDW transition temperature and the eventual quenching of the CDW transition. Even purely from the CDW point of view, it would be interesting to see spectroscopically how the electronic structure changes.

3. **Temperature dependence**. Only preliminary results have been obtained so far for the ARPES temperature dependence on the blue bronze, quasi-2D purple bronzes, and the Li purple bronze. A temperature dependent ARPES experiment

is somewhat challenging, because temperature cycle accelerates surface degradation, and because often the photon spot moves to a different point of the sample surface due to the contraction or the elongation of the sample holder. The latter can be a problem if the sample is warped or consists of domains. Gap opening is signaled in the blue bronze, but it also accompanies the surface degradation. For 2D purple bronzes, interesting preliminary results indicate that temperature dependence of the CDW gap is momentum dependent. For the Li purple bronze, the small temperature dependence between 50 K and 200 K reported in the last paragraph of section 7.3 needs to be reproduced. Also, our preliminary result shows no gap opening between 20 K and 30 K. Although this is consistent with the optical measurement, it also needs to be reproduced. In general, temperature dependent ARPES on these materials are important to measure the CDW gaps (blue bronze, quasi-2D purple bronzes), and to judge whether the origin of the non-FL lineshape is thermal fluctuations or LL state.

4. **Lineshape analysis** The Anderson-Ren [23] type lineshape analysis on the ARPES spectra presented in this thesis is very interesting and also very intriguing. This lineshape, characterized by a **k**-independent power law tail, has been suggested to describe the ARPES spectra of high temperature superconductors. It is found that all the bronze samples studied in this thesis show the Anderson-Ren type lineshapes when the spectra are scaled appropriately. In contrast, $TiTe_2$ data cannot be described by the Anderson-Ren type lineshape. One common aspect of the bronze samples studied in this thesis is their (hidden) one dimensionality of the electronic structure. It is then quite interesting that the Anderson-Ren lineshape is in fact a model of a 1D LL lineshape modified by 2D kinematics, a seemingly appropriate model for the bronzes also. Although currently there is no microscopic understanding of the Anderson-Ren lineshape, documenting the empirically found lineshapes and their density/doping/temperature dependence would be quite interesting. A possible theoretical starting point to simulate the Anderson-Ren lineshape is to integrate the 1D LL lineshape or to use a phenomenological power law self energy [35]. It may be hoped that one can eventually understand the lineshapes of the high temperature superconductor (Fig. 1.5) and the bronzes within a single model.

5. **New samples** In addition to changing the properties of the existing samples, entirely new kinds of samples should be tried. Candidates are carbon nanotubes

and artificial structures on semiconductor surfaces, such as In wires grown on Si [147]. Experimental studies of the CDW properties and LL behaviors of these materials are very scarce. Especially, carbon nanotubes are fascinating 1D materials for which LL properties [148] and very low CDW transition temperatures [149] are predicted. While the current sample quality is not ideal for an ARPES investigation, an angle integrated high energy resolution PES study combined with the state-of-the-art sub-micron spatial resolution could already give a significant amount of information. It may be hoped that the continous sample quality improvement leads to a successfull ARPES experiment on the nanotubes.

Bibliography

[1] C. Kittel, *Introduction to Solid State Physics* (6th ed. John Wiley and Sons, 1986).

[2] N.W. Ashcroft and N.D. Mermin, *Solid State Physics* (Holt, Rinehart and Winston, 1976).

[3] L.D. Landau, Sov. Phys. JETP **30**, 1058 (1956); **32**, 59 (1957).

[4] *Photoemission in Solids*, eds M. Cardona and L. Ley (Springer-Verlag, 1978).

[5] S. Hüfner, *Photoelectron spectroscopy: principles and applications* (2nd ed. Springer, 1996).

[6] F.J. Himpsel, Adv. Phys. **32**, 1 (1983).

[7] L. Hedin and S. Lundqvist, *Solid State Physics*, Vol. 23, eds H. Ehrenreich, D. Turnbull and F. Seitz (Academic, New York) p. 1. (1969).

[8] T. Miller, W.E. McMahon, and T.-C. Chiang, Phys. Rev. Lett. **77**, 1167 (1996).

[9] J. Yeh and I. Lindau, Atomic Data and Nuclear Data Tables **32**, 1 (1985).

[10] E. Dietz, H. Becker and U. Gerhardt, Phys. Rev. Lett. **36**, 1397 (1976).

[11] J. Hermanson, Solid State Comm. **22**, 9 (1997).

[12] H. Daimon, S. Imada, H. Nishimoto and S. Suga, J. Elec. Spectro. Rel. Phenom. **76**, 487 (1995).

[13] E.L. Shirley, L.J. Terminello, A. Santoni and F.J. Himpsel, Phys. Rev. B **51**, 13614 (1995).

[14] D.A. Shirley, Phys. Rev. B **5**, 4709 (1972).

[15] S. Tougaard and P. Sigmund, Phys. Rev. B **25**, 4452 (1982); S. Tougaard, Phys. Rev. B **34**, 6779 (1986).

[16] N.V. Smith, Comm. Cond. Matt. Phys. **15,** 263 (1992).

[17] W. Bardyszewski and L. Hedin, Physica Scripta **32**, 439 (1985).

[18] N.V. Smith, P. Thiry and Y. Petroff, Phys. Rev. B **47**, 15476 (1993).

[19] For example, see F. Reinert, R. Claessen, G. Nicolay, D. Ehm, S. Hüfner, W.P. Ellis, G.-H. Gweon, J.W. Allen, B. Kindler and W. Assmus, Phys. Rev. B **58**, 12808 (1998).

[20] C.G. Olson, R. Liu, D.W. Lynch, R.S. List, A.J. Arko, B.W. Veal, Y.C. Chang, P.Z. Jiang and A.P. Paulikas, Phys. Rev. B **42**, 381 (1990).

[21] R. Claessen, C. Wilde, F. Reinert, S. Hüfner, G.-H. Gweon, J.W. Allen, D.M. Poirier and C.G. Olson, Phys. Rev. B. **56**, 12643 (1997).

[22] A. Terrasi, M. Marsi, H. Berger, G. Margaritondo, R.J. Kelly and M. Onellion, Phys. Rev. B **52**, 5592 (1995).

[23] P.W. Anderson and Y. Ren in *High Temperature Superconductivity*, eds. K.S. Bedell, D. Coffey, D.E. Meltzer, D. Pines and J.R. Schrieffer (Addison-Wesley, Redwood City, 1990) p. 3; P.W. Anderson, Physica B **199-200**, 8 (1994)

[24] C.M. Varma, P.B. Littlewood, S. Schmitt-Rink, E. Abrahams and A.E. Ruckenstein, Phys. Rev. Lett. **63**, 1996 (1989).

[25] G.A. Sawatzky in *High Temperature Superconductivity*, eds. K.S. Bedell, D. Coffey, D.E. Meltzer, D. Pines and J.R. Schrieffer (Addison-Wesley, Redwood City, 1990) p. 297.

[26] L.-Z. Liu, R.O. Anderson and J.W. Allen, J. Phys. Chem. Solids **52**, 1473 (1991)

[27] R. Claessen, R.O. Anderson, J.W. Allen, C.G. Olson, C. Janowitz, W.P. Ellis, S. Harm, M. Kalning, R. Manzke and M. Skibowski, Phys. Rev. Lett. **69**, 808 (1992).

[28] B. Dardel, D. Malterre, M. Grioni, P. Weibel, Y. Baer and F. Lévy, Phys. Rev. Lett. **67**, 3144 (1991).

[29] Y. Hwu, P. Alméras, M. Marsi, H. Berger, F. Lévy, M. Grioni, D. Malterre and G. Margaritondo, Phys. Rev. B **46**, 13624 (1992).

[30] A.L. Fetter and J. D. Walecka, *Quantum Theory of Many-Particle Systems* (McGraw-Hill, 1971).

[31] J.M. Luttinger, Phys. Rev. **121**, 942 (1961).

[32] E. Müller-Hartman, Z. Phys. B **76**, 211 (1989).

[33] R.D. Mattuck, *A Guide to Feynman Diagrams in the Many-body Problem* (2nd ed. McGraw-Hill, 1976).

[34] See, e.g., J.W. Negele and H. Orland, *Quantum Many Particle Systems* (Addison-Wesley, Menlo Park, 1988).

[35] K. Matho, J. Phys. Chem. Solids **56**, 1735 (1995).

[36] R. E. Peierls, *Quantum Theory of Solids* (Oxford, 1955).

[37] F.R.S. Fröhlich, Proc. R. Soc. London Ser. **A223**, 296 (1954).

[38] T.M. Rice and G.K. Scott, Phys. Rev. Lett. **35**, 120 (1975).

[39] R. Liu, C.G. Olson, W.C. Tonjes and R.F. Frindt, Phys. Rev. Lett. **80**, 5762 (1998).

[40] G. Grüner, *Density Waves in Solids* (Addison-Wesley 1994).

[41] N.D. Mermin and H. Wagner, Phys. Rev. Lett. **28**, 1133 (1966).

[42] P.C. Hohenberg, Phys. Rev. **158**, 383 (1967).

[43] D.J. Scalapino, M. Sears and R.A. Ferrell, Phys. Rev. B **6**, 3409 (1972).

[44] P.A. Lee, T.M. Rice and P.W. Anderson, Phys. Rev. Lett. **31**, 462 (1973).

[45] M.J. Rice and S. Strässler, Solid State Comm. **13**, 1389 (1973).

[46] M.V. Sadovskii, Sov. Phys. JETP **50**, 989 (1979).

[47] R.H. McKenzie and D. Scarratt, Phys. Rev. B **54** R12709 (1996).

[48] O. Tchernyshyov, Phys. Rev. B **59** 1358 (1999).

[49] R.H. McKenzie and J.W. Wilkins, Phys. Rev. Lett. **69**, 1085 (1992).

[50] P.W. Anderson, *The Theory of Superconductivity in the High-*T_c *Cuprates* (Princeton University Press, 1997).

[51] F.D.M. Haldane, J. Phys. C **14**, 2585 (1981).

[52] D.L. Cox, Phys. Rev. Lett. **59**, 1240 (1987); P. Nozieres and A. Blandin, J. Phys. (Paris) **41**, 193 (1980).

[53] J.M. Luttinger, J. Math. Phys. **4**, 1154 (1963); D.C. Mattis and E.H. Lieb, J. Math. Phys. **6**, 304 (1965); A. Luther and I. Peschel, Phys. Rev. B **9**, 2911 (1974).

[54] K. Schönhammer and V. Meden, Amer. J. Phys. **64**, 1168 (1996); K. Schönhammer, cond-mat/9710330.

[55] J. von Delft and H. Schoeller, Annalen der Physik **7**, 225 (1998).

[56] P.W. Anderson, Phys. Rev. Lett. **18**, 1049 (1967).

[57] P.W. Anderson, Phys. Rev. Lett. **64**, 1839 (1990); Phys. Rev. Lett. **65**, 2306 (1990).

[58] V. Meden and K. Schönhammer, Phys. Rev. B **46**, 15753 (1992).

[59] J. Voit, Phys. Rev. B **47**, 6740 (1993).

[60] P. Kopietz, V. Meden and K. Schönhammer, Phys. Rev. Lett. **74**, 2997 (1995).

[61] K. Schönhammer and V. Meden, Phys. Rev. B **47**, 16205 (1993).

[62] J. Voit, Rep. Prog. Phys. **58**, 977 (1995).

[63] H.J. Schulz, Int. J. Mod. Phys. **B5**, 57 (1991).

[64] K. Penc, F. Mila and H. Shiba, Phys. Rev. Lett. **75**, 894 (1995).

[65] H.J. Schulz, J. Phys. C **16** 6769 (1983).

[66] M. Fabrizio and A. Parola, Phys. Rev. Lett. **70**, 226 (1993).

[67] R. Claessen, R.O. Anderson, G.-H. Gweon, W.P. Ellis, J.W. Allen, C. Janowitz, C.G. Olson, Z.X. Shen, V. Eyert, M. Skibowski, K. Frimelt, E. Bucher and S. Hüfner, Phys. Rev. B **54**, 2453 (1996).

[68] K. Koike, M. Okamura, T. Nakanomyo and T. Fukase, J. Phys. Soc. Jpn. **52**, 597 (1983)

[69] D.K.G. de Boer, C.F. van Bruggen, G.W. Bus, C. Coehoorn, C. Haas, G.A. Sawatzky, H.W. Myron, D. Norman and H. Padmore, Phys. Rev. B **29**, 6797 (1984).

[70] Th. Straub, R. Claessen, P. Steiner, S. Hüfner, V. Eyert, K. Frimelt and E. Bucher, Phys. Rev. B **55**, 13473 (1997).

[71] D.S. Dessau, Z.-X. Shen, D.M. King, D.S. Marshall, L.W. Lombardo, P.H. Dickinson, J. DiCarlo, C.-H. Park, A.G. Loeser, A. Kapitulnik and W.E. Spicer, Phys. Rev. Lett. **71**, 2781 (1993).

[72] M. Randeria, H. Ding, J.-C. Campuzano, A. Bellman, G. Jennings, T. Yokoya, T. Takahashi, H. Katayama-Yoshida, T. Mochiku and K. Kadowaki, Phys. Rev. Lett. **74**, 4951 (1995).

[73] M.C. Schabel, C.-H. Park, A. Matsuura, Z.-X. Shen, D.A. Bonn, R. Liang and W.N. Hardy, Phys. Rev. B **57**, 6107 (1998).

[74] J.W. Allen, G.-H. Gweon, R. Claessen and K. Matho, J. Phys. Chem. Solids **56**, 1849 (1995).

[75] N.E. Bickers, D.L. Cox and J.W. Wilkins, Phys. Rev. B **28**, 4315 (1983).

[76] S. Harm, R. Dürig, R. Manzke, M. Skibowski, R. Claessen and J.W. Allen, J. Elec. Spectro. Rel. Phenom. **68**, 111 (1993).

[77] P. Allen and N. Chetty, Phys. Rev. B **50**, 14855 (1994).

[78] K. Matho, preprint.

[79] C.W. Greeff, H.R. Glyde and B.E. Clements, Phys. Rev. B **45**, 7951 (1992).

[80] I.H. Inoue, I. Hase, Y. Aiura, A. Fujimori, Y. Haruyama, T. Maruyama and Y. Nishihara, Phys. Rev. Lett. **74**, 2539 (1995); I.H. Inoue, Y. Aiura, Y. Nishihara, Y. Haruyama, S. Nishizaki, Y. Maeno, T. Fujita, J.G. Bednorz and F. Lichtenberg, J. Elec. Spec. Rel. Phenom. **78**, 175 (1996).

[81] P. Lloyd, J. Phys. C **2**, 1717 (1969).

[82] E. DiMasi, B. Foran, M.C. Aronson and S. Lee, Chem. Mater. **6**, 1867 (1994).

[83] Z.-X. Shen, D.S. Dessau, B.O. Wells, D.M. King, W.E. Spicer, A.J. Arko, D. Marshall, L.W. Lombardo, A. Kapitulnik, P. Dickinson, S. Doniach, J. DiCarlo, T. Loeser, and C.H. Park, Phys. Rev. Lett. **70**, 1553 (1993); H. Ding, M.R. Norman, J.C. Campuzano, M. Randeria, A.F. Bellman, T. Yokoya, T. Takahashi, T. Mochiku and K. Kadowaki, Phys. Rev. B **54**, 9678 (1996).

[84] B. Dardel, M. Grioni, D. Malterre, P. Weibel, Y. Baer, and F. Lévy, J. Phys. Condens. Matter **5**, 6111 (1993).

[85] A. Terrasi, M. Marsi, H. Berger, F. Gauthier, L. Forró, G. Margaritondo, R.J. Kelley and M. Onellion, Z. Phys. B **100**, 493 (1996).

[86] P. Villars and L.D. Calvert, *Pearson's Handbook of Crystallographic Data for Intermetallic Phases*, 2nd ed. vol. 4, ASM International (1991).

[87] E. DiMasi, M.C. Aronson, J.F. Mansfield, B. Foran and S. Lee, Phys. Rev. B **52**, 14516 (1995).

[88] J.W. Allen, S.-J. Oh, O. Gunnarsson, K. Schönhammer, M.B. Maple, M.S. Torikachvilli and I. Lindau, Adv. Phys. **35**, 275 (1987), and references therein.

[89] J.W. Allen, L.I. Johansson, I. Lindau and S.B. Hagstrom, Phys. Rev. B **21**, 1335 (1980).

[90] D.M. Wieliczka and C.G. Olson, unpublished.

[91] R. Hoffmann, J. Chem. Phys. **39**, 1397 (1963); M.-H. Whangbo, R. Hoffmann and R.B. Woodward, Proc. R. Soc. London Ser. A **366**, 23 (1979). M.-H. Whangbo, M. Evain, T. Hughbanks, M. Kertesz, S. Wijeyesekera, C. Wilker, C. Zhen and R. Hoffmann, EHMACC program for extended Hückel molecular and crystal calculations.

[92] B. Foran, Ph. D. thesis, University of Michigan (1996).

[93] E. Canadell, Y. Mathey, M.-H. Whangbo, J. Amer. Chem. Soc. **110**, 104 (1988).

[94] E. DiMasi, B. Foran, M.C. Aronson and S. Lee, Phys. Rev. B **54**, 13587 (1996).

[95] R. Claessen, R.O. Anderson, J.W. Allen and C.G. Olson, unpublished.

[96] F. Zwick, H. Berger, I. Vobornik, G. Margaritondo, L. Forró, C. Beeli, M. Onellion, G. Panaccione, A. Taleb-Ibrahimi and M. Grioni, Phys. Rev. Lett. **81**, 1058 (1998).

[97] P. Aebi, J. Osterwalder, P. Schwaller, L. Schlapbach, M. Shimoda, T. Mochiku and K. Kadowaki, Phys. Rev. Lett. **72**, 2757 (1994).

[98] J.C. Campuzano, H. Ding, M.R. Norman, M. Randeria, A.F. Bellman, T. Yokoya, T. Takahashi, H. Katayama-Yoshida, T. Mochiku and K. Kadowaki, Phys. Rev. B **53**, R14737 (1996).

[99] M.-H. Whangbo, E. Canadell, P. Foury and J.-P. Pouget, Science **252**, 96 (1991).

[100] K. Breuer, C. Stagerescu, K.E. Smith, M. Greenblatt and K. Ramanujachary, Phys. Rev. Lett. **76**, 3172 (1996).

[101] *Low-Dimensional Electronic Properties of Molybdenum Bronzes and Oxides*, ed. C. Schlenker (Kluwer Academic Publishers, 1989).

[102] J. Dumas and C. Schlenker, Int. J. Mod. Phys. B **7**, 4045 (1993).

[103] J.L. de Boer and A. Meetsma, private communication.

[104] H. Kim, U.V. Waghmare, E. Kaxiras, Bull. Amer. Phys. Soc. **44**, 526 (1999).

[105] M.-H. Whangbo, E. Canadell and C. Schlenker, J. Am. Chem. Soc. **109**, 6308 (1987).

[106] H. Vincent, M. Ghedira, J. Marcus, J. Mercier and C. Schlenker, J. Sol. State Chem. **47**, 113 (1983).

[107] M. Onoda, Y. Matsuda and M. Sato, J. Sol. State Chem. **69**, 67 (1987).

[108] C. Escribe-Filippini, K. Konaté, J. Marcus, C. Schlenker, R. Almairac, R. Ayroles and C. Roucau, Phil. Mag. B **50**, 321 (1984).

[109] K. Terashima, H. Matsuoka, K. Soda, S. Suga, R. Yamamoto and M. Doyama, J. Phys. Soc. Japan **57**, 2557 (1988).

[110] Z.-X. Shen and D.S. Dessau, Phys. Rep. **253**, 1 (1995).

[111] J. Graham and A.D. Wadsley, Acta Crystallogr. **20**, 93 (1966).

[112] M. Ghedira, J. Chenavas, M. Marezio and J. Marcus, J. Solid State Chem. **57**, 300 (1985).

[113] J.P. Pouget in Ref. [101].

[114] R. Brusetti, B.K. Chakraverty, J. Devenyi, J. Dumas, J. Marcus and C. Schlenker in *Recent Developments in Condensed Matter Physics*, Vol 2, edited by J.T. Devreese, L.F. Lemmens, V.E. Van Doren and J. Van Royen (Plenum, New York, 1981) p. 181.

[115] G. Travaglini, P. Wachter, J. Marcus and C. Schlenker, Solid State Comm. **37**, 599 (1981).

[116] W. Fogle and J.H. Perlstein, Phys. Rev. B **6**, 1412 (1972).

[117] J.P. Pouget, S. Kagoshima, C. Schlenker and J. Marcus, J. Physique **44**, L-113 (1983).

[118] C. Escribe-Filippini, J.P. Pouget, R. Currat, B. Hennion and J. Marcus, *Lecture Notes in Physics* **217** (Springer Verlag) p. 71 (1985).

[119] D.C. Johnston, Phys. Rev. Lett. **52**, 2049 (1984).

[120] R.S. Kwok, G. Grüner and S.E. Brown, Phys. Rev. Lett. **65**, 365 (1990).

[121] J. Voit, J. Phys. (Cond. Matt.) **5**, 8305 (1993); and private communication.

[122] J.P. Pouget, C. Noguera, A.H. Moudden and R. Moret, J. de Physique **46**, 1731 (1985).

[123] M.H. Whangbo and L.F. Schneemeyer, Inorg. Chem. **25**, 2424 (1986).

[124] F. Zwick, D. Jérome, G. Margaritondo, M. Onellion, J. Voit and M. Grioni, Phys. Rev. Lett. **81**, 2974 (1998).

[125] K. Breuer, K.E. Smith, M. Greenblatt and W. McCarroll, J. Vac. Sci. Tech. A **12**, 2196 (1994); and private communication with K.E. Smith.

[126] J.Y. Veuillen, R.C. Cinti and E. Al Khoury Nemeh, Europhys. Lett. **3**, 355 (1987).

[127] A. Wold, W. Kunnmann, R.J. Arnott and A. Ferretti, Inorg. Chem. **3**, 545 (1964).

[128] S. Girault, A.H. Moudden and J.P. Pouget, Phys. Rev. B **39**, 4430 (1989); J.P. Pouget, B. Hennion, C. Escribe-Fillippini and M. Sato, Phys. Rev. B **43** 8421 (1991).

[129] A. Luther and V.J. Emery, Phys. Rev. Lett. **33**, 589 (1974).

[130] M.H. Whangbo, private communication.

[131] B. Dardel, D. Malterre, M. Grioni, P. Weibel, Y. Baer, J. Voit and D. Jérôme, Europhys. Lett. **24**, 687 (1993).

[132] F. Zwick, S. Brown, G. Margaritondo, C. Merlic, M. Onellion, J. Voit and M. Grioni, Phys. Rev. Lett. **79**, 3982 (1997).

[133] M.-H. Whangbo and E. Canadell, J. Am. Chem. Soc. **110**, 358 (1988).

[134] M. Greenblatt, W.H. McCarroll, R. Neifeld, M. Croft and J.V. Waszczak, Solid State Comm. **51**, 671 (1984).

[135] C. Schlenker, H. Schwenk, C. Escribe-Filippini and J. Marcus, Physica **135**B, 511 (1985).

[136] Y. Matsuda, M. Sato, M. Onoda and K. Nakao, J. Phys. C **19**, 6039 (1986).

[137] L. Degiorgi, P. Wachter, M. Greenblatt, W.H. McCarroll, K.V. Ramanujachary, J. Marcus and C. Schlenker, Phys. Rev. B **38**, 5821 (1988).

[138] For examples, see G. Travaglini and P. Wachter, Phys. Rev. B **30**, 1971 (1984) (CDW) or L. Degiorgi, M. Dressel, A. Schwartz, B. Alavi and G. Grüner, Phys. Rev. Lett. **76**, 3838 (1996) (SDW).

[139] K.E. Smith, K. Breuer, M. Greenblatt and W. McCarroll, Phys. Rev. Lett. **70**, 3772 (1993).

[140] M. Grioni, H. Berger, M. Garnier, F. Bommeli, L. Degiorgi and C. Schlenker, Phys. Scripta **T66**, 172 (1996).

[141] R.H. McKenzie, Phys. Rev. B **52**, 16428 (1995).

[142] K. Schönhammer, private communication.

[143] C. Kim, A.Y. Matsuura, Z.-X. Shen, N. Motoyama, H. Eisaki, S. Uchida, T. Tohyama and S. Maekawa, Phys. Rev. Lett. **77**, 4054 (1996); H. Fujisawa, T. Yokoya and T. Takahashi, Solid State Comm. **106**, 543 (1998).

[144] C.L. Kane and M.P.A. Fisher, Phys. Rev. B **46**, 15233 (1992).

[145] S. Eggert, H. Johannesson and A. Mattsson, Phys. Rev. Lett. **76**, 1505 (1996).

[146] L.F. Schneemeyer, F.J. DiSalvo, S.E. Spengler and J.V. Waszczak, Phys. Rev. B **30**, 4297 (1984).

[147] T. Abukawa, M. Sasaki, F. Hisamatsu, T. Goto, T. Kinoshita, A. Kakizaki and S. Kono, Surf. Sci. **325**, 33 (1995).

[148] R. Egger and A.O. Gogolin, Phys. Rev. Lett. **79**, 5082 (1997); C. Kane, L. Balents and M.P.A. Fisher, Phys. Rev. Lett. **79**, 5086 (1997).

[149] J.W. Mintmire, B.I. Dunlap and C.T. White, Phys. Rev. Lett. **68**, 631 (1992).